
Cavity Solitons and Frequency Combs via Vectorial and Counterpropagating Light in Optical Resonators

Graeme Neil Campbell

First supervisor: Prof. Gian-Luca Oppo
Second supervisor: Dr Gordon Robb

CNQO (Computation, Nonlinear and Quantum Optics)
Department of Physics
University of Strathclyde, Glasgow

A thesis presented for the degree of
Doctor of Philosophy

May 1, 2025

This thesis is the result of the author's original research. It has been composed by the author and has not been previously submitted for examination which has led to the award of a degree.

The copyright of this thesis belongs to the author under the terms of the United Kingdom Copyright Acts as qualified by University of Strathclyde Regulation 3.50. Due acknowledgement must always be made of the use of any material contained in, or derived from, this thesis.

Signed: Graeme Neil Campbell
Date: May 1, 2025

Abstract

In this thesis, we concern ourselves with generation of frequency combs in ring and Fabry-Pérot resonators possessing intracavity fields of; vectorial field components, counterpropagating field components or a combination of the two, with a wide range of applications including telecommunication, spectroscopy and quantum technologies. For counterpropagating fields in the ring resonator, we characterise the formation of robust stationary states formed by light plateaus separated by two local switching fronts. Such states are due to nonlocal cross coupling and allow for frequency combs to switch from one field to the other by simply tuning the input laser frequency. Exact expressions for the distance between fronts and for plateau powers are provided which demonstrate an unusual high degree of control over pulse and plateau duration upon changes of one of the input laser frequencies, where light plateaus are generally self-starting for a wide range of parameters. In the Fabry-Pérot resonator, ranges of existence and stability are determined for dark cavity solitons, where we find that nonlocal coupling leads to strongly detuned dark cavity solitons when compared with ring resonators. This shift is a consequence of the counterpropagation inherent to Fabry-Pérot resonators. The existence and stability of dark soliton solutions are dependent on the size and number of solitons in the cavity due to nonlocal coupling. Long-range interactions between vectorial dark cavity solitons are induced by the formation of patterns via spontaneous symmetry breaking of orthogonally polarised fields. Turing patterns of alternating polarisations form between adjacent solitons, pushing them apart such that a random distribution of solitons spontaneously reach equal equilibrium distances, which enhances the two-component frequency comb through the formation of regular soliton crystals ('self-crystallisation'). This phenomenon generalises to both Fabry-Pérot and ring resonator systems, where in addition, we discuss the possibility of vectorial dark-bright solitons demonstrating nontrivial breathing dynamics.

Acknowledgements

First and foremost, I would like to express my deepest gratitude to my supervisor, Gian-Luca Oppo, for his continuous support, guidance, and encouragement throughout my research.

I am grateful to my colleagues and friends at the Max Plank institute for the science of light, for their camaraderie, advice, and insightful discussions. Working alongside such a talented and motivated group of individuals has been an incredibly rewarding experience.

This research was supported by funding from the EPSRC DTA Grant No. EP/T517938/1 and the Del'Haye group at the Max Plank institute for the science of light.

To my family, I thank you for your patience and understanding throughout this journey.

Author's Bibliography

Publications for peer-reviewed journals

- **G. N. Campbell**, S. Zhang, L. D. Bino, P. Del'Haye, and G.-L. Oppo, Counter-propagating light in ring resonators: Switching fronts, plateaus, and oscillations, *Phys. Rev. A*, **106**, 043507, (2022).
- **G. N. Campbell**, L. Hill, P. Del'Haye, and G.-L. Oppo, Dark solitons in Fabry-Pérot resonators with Kerr media and normal dispersion, *Phys. Rev. A*, **108**, 033505, (2023).
- L. Hill, E.-M. Hirmer, **G. N. Campbell**, T. Bi, A. Ghosh, P. Del'Haye, and G.-L. Oppo, Symmetry broken vectorial Kerr frequency combs from Fabry-Pérot resonators, *Commun. Phys.*, **7**, 82, (2024).
- A. Ghosh, A. Pal, L. Hill, **G. N. Campbell**, T. Bi, Y. Zhang, A. Alabbadi, S. Zhang, G.-L. Oppo, and P. Del'Haye, Controlled light distribution with coupled microresonator chains via Kerr symmetry breaking, *Photon. Res.*, **12**, 2376-2389, (2024).
- **G. N. Campbell**, L. Hill, P. Del'Haye, and G.-L. Oppo, Frequency comb enhancement via the self-crystallization of vectorial cavity solitons, *Opt. Express*, **32**, 37691-37702, (2024).

Publications in the process of submission

- **G. N. Campbell**, L. Hill, P. Del'Haye, and G.-L. Oppo, Vectorial solitons in Fabry-Pérot resonators with normal dispersion, (2025).

Conference oral presentations

- **G. N. Campbell**, S. Zhang, L. D. Bino, P. Del'Haye, and G.-L. Oppo, Bistability of light plateaus and oscillatory states for counterpropagation in ring resonators, Optica advanced photonics congress, Amsterdam, The Netherlands, (2022).
- **G. N. Campbell**, L. Hill, P. Del'Haye, and G.-L. Oppo, Single field light plateaus for counterpropagation in ring resonators, Photon 2022, Nottingham, UK, (2022).
- **G. N. Campbell**, L. Hill, P. Del'Haye, and G.-L. Oppo, Self-crystallization of dark vectorial solitons in Fabry-Pérot resonators, CLEO, San Jose, USA, (2023).

- **G. N. Campbell**, L. Hill, P. Del'Haye, and G.-L. Oppo, Control of frequency comb spacing via self-crystallization of dark vectorial solitons in Kerr resonators, Optica advanced photonics congress, Québec, Canada, (2024).

Conference poster presentations

- G.-L. Oppo, **G. N. Campbell**, G. Morigi, F. Rosati, and G. Robb, Optomechanical self-structuring and the Brownian mean field transition, ColOpt 724. WE-Heraeus-Seminar "Collective effects and non-equilibrium quantum dynamics", online seminar, (2021).
- G.-L. Oppo, **G. N. Campbell**, G. Morigi, F. Rosati, and G. Robb, Optomechanical self-structuring and the Brownian mean field transition, Wavecomplexity international networking event, online seminar, (2021).
- **G. N. Campbell**, L. Hill, P. Del'Haye, and G.-L. Oppo, Comparison of dark temporal cavity solitons in Fabry-Pérot and ring resonators with normal dispersion, CLEO/Europe-EQEC, Munich, Germany, (2023).
- **G. N. Campbell**, L. Hill, P. Del'Haye, and G.-L. Oppo, Dark temporal cavity soliton pairs in Fabry-Pérot resonators with normal dispersion and orthogonal polarizations, CLEO/Europe-EQEC, Munich, Germany, (2023).

Contents

Abstract	ii
Acknowledgements	iii
Author's Bibliography	iv
List of Figures	x
1 Introduction	2
1.1 Motivations	3
1.2 Objectives	4
1.3 Layout of the thesis	4
2 Theory of Temporal Cavity Solitons in Ring Resonators with Normal Dispersion	8
2.1 Introduction	9
2.2 Whispering gallery mode microresonators	9
2.2.1 Micro-cavity devices	9
2.2.2 Guided mode solutions	10
2.2.3 Birefringence and polarisation mode dispersion	14
2.2.4 Propagation losses	15
2.3 Fundamentals of ring resonators	16
2.3.1 Coupling via evanescent fields	16
2.3.2 Resonance enhancement	17
2.3.3 Coupling efficiency	18
2.3.4 Cavity finesse and quality factor	19
2.4 The propagation of light in nonlinear dielectric waveguides	20
2.4.1 Nonlinear atomic polarisation	20
2.4.2 Chromatic dispersion	21
2.4.3 Longitudinal waveguide propagation equation	22
2.5 Modelling the ring resonator	26
2.6 The longitudinal Lugiato-Lefever equation	27
2.7 Stationary solutions of the Lugiato-Lefever equation with normal dispersion	33
2.7.1 Optical bistability of homogeneous solutions	33
2.7.2 The existence and stability of exponentially localised solutions	36
2.8 Conclusion	39

3	Symmetry Breaking in Unidirectionally Driven Ring Resonators	41
3.1	Introduction	42
3.2	Modelling orthogonal polarisation field components in the ring resonators	42
3.3	Spontaneous symmetry breaking of homogeneous stationary solutions	45
	3.3.1 Instabilities when neglecting group-velocity dispersion	45
	3.3.2 Symmetry breaking Turing patterns	46
3.4	Spontaneous symmetry breaking of vectorial dark solitons	49
3.5	Self-crystallisation of temporal cavity solitons	51
3.6	Partial self-crystallisation of temporal cavity solitons	53
3.7	Vectorial dark-bright solitons	57
3.8	Conclusion	60
4	Counterpropagating Light in Bidirectionally Driven Ring Resonators	62
4.1	Introduction	63
4.2	Modelling the counterpropagation of light in ring resonators	64
4.3	Homogeneous steady states	70
4.4	Two switching fronts and dark soliton steady states	73
4.5	Distance of two stationary switching fronts	78
4.6	Evolution towards the two switching-front solutions	84
4.7	Oscillatory dynamics and bistability with front stationary states	87
4.8	Conclusions	91
5	Dark Solitons in Fabry-Pérot Resonators	94
5.1	Introduction	95
5.2	Fundamentals of Fabry-Pérot resonators	96
	5.2.1 The Fabry-Pérot cavity	96
	5.2.2 Resonance enhancement	98
	5.2.3 Coupling efficiency	99
	5.2.4 Cavity finesse and quality factor	99
5.3	The Fabry-Pérot model	100
5.4	Homogeneous solutions and fast time dynamics	104
	5.4.1 Homogeneous stationary solutions	105
	5.4.2 Plateau solutions	105
5.5	Linear stability analysis of plateau solutions in slow time	107
	5.5.1 Turing pattern instability	107
	5.5.2 Homogeneous instability of plateaus	108
5.6	Localised solutions	109
	5.6.1 Switching fronts and their dynamics	110
	5.6.2 Dark cavity solitons	114
5.7	Oscillatory dynamics of dark solitons	117
5.8	Conclusions	119

6	Spontaneous Symmetry Breaking in Fabry-Pérot Resonators	122
6.1	Introduction	123
6.2	Modelling the Fabry-Pérot resonator with polarisation consideration	124
6.2.1	Derivation of the Fabry-Pérot model with vectorial electric field	124
6.2.2	Equation of the Fabry-Pérot with a single field component	131
6.3	Homogeneous stationary states	131
6.3.1	Linear stability of the homogeneous stationary states	132
6.3.2	Spontaneous symmetry breaking codimension-2 bifurcation	134
6.4	Spontaneous symmetry breaking of vectorial dark solitons	139
6.4.1	Codimension-2 bifurcation of vectorial dark solitons	139
6.4.2	Linear stability analysis of the plateau for Turing pattern formation	141
6.4.3	Spontaneous symmetry breaking in the presence of nonlocal coupling	143
6.5	Self-crystallisation of vectorial dark solitons	144
6.6	Partial crystal formation	147
6.7	Vectorial dark-bright solitons	150
6.7.1	Vectorial dark-bright solitons in Fabry-Pérot resonators	150
6.7.2	Nonlocal coupling of oscillating vectorial dark-bright solitons	153
6.8	Vectorial cavity soliton distribution in parameter space	158
6.9	Conclusion	159
7	Conclusion	161
A	Linear Stability Analysis of Counterpropagating Light in Ring Resonators	163
A.1	Linear stability analysis of the modal amplitudes	163
A.2	Linear stability of homogeneous stationary states to step function perturbations	165
A.3	Linear stability of plateaus connected by step functions	167
A.4	Self starting two switching front stationary states when scanning detuning	171
A.5	Fast time dynamics of plateau solutions	173
B	Linear Stability Analysis of the Fabry-Pérot Resonator	175
B.1	Linear stability analysis of homogeneous stationary states	175
B.2	Linear stability analysis of plateau states connected by step functions	177
C	Numerical Methods	179
C.1	Constraints on simulation step sizes	179
C.2	Fourier split-step integration method for nonlocally coupled Lugiato-Lefever equations	180
C.3	Crank-Nicolson integration method for nonlocally coupled Lugiato-Lefever equations	183
	Bibliography	185

List of Figures

2.1	Schematics of different whispering gallery mode microresonator geometries	9
2.2	waveguide-cavity coupling	16
2.3	Resonances of a linear ring cavity	18
2.4	Resonances of a nonlinear cavity: optical bistability curves of the Lugiato-Lefever equation	35
2.5	Switching front of the Lugiato-Lefever equation	37
2.6	Local solutions of the Lugiato-Lefever equation	38
3.1	Unidirectionally driven ring resonator with two polarisations	44
3.2	Spontaneous symmetry breaking ‘bubble’ of homogeneous stationary solutions	45
3.3	Spontaneous symmetry breaking of homogeneous and soliton stationary states	47
3.4	Spontaneous self-organisation of vectorial dark solitons to regularly spaced dark soliton crystal	52
3.5	Multistability of soliton crystals	54
3.6	Spontaneous self-organisation of vectorial dark solitons to local crystal	55
3.7	Regular soliton crystal unit cells	56
3.8	Dark-bright vectorial solitons in ring resonator	58
3.9	Dual combs of dark-bright vectorial solitons in ring resonator	59
3.10	Oscillation of dark-bright vectorial solitons	60
4.1	Bidirectionally pumped ring resonator	65
4.2	Homogeneous stationary states of counterpropagating fields	69
4.3	Homogeneous stationary states of counterpropagating fields and linear stability eigenvalues	71
4.4	Switching front dynamics resulting in light plateau stationary solutions	74
4.5	Example light plateau solutions for different values of detuning	76
4.6	Bright solitons stabilised by nonlocal coupling	77
4.7	$2N$ switching fronts formed from noise in a long cavity	79
4.8	Approximation and estimation of the Maxwell point	80
4.9	Plateau power obtained semi-analytically given knowledge of the Maxwell point	81
4.10	Light plateau solutions for different values of the dispersion	82
4.11	Approximated size of the light plateau solutions when scan of the detuning	83
4.12	Analytically determined path of evolution of light plateau solutions	85
4.13	Velocity of switching fronts	86

4.14	Bistability of oscillations in fast time and slow time	88
4.15	Argand plot of bistable oscillations	88
4.16	Scan of slow time oscillations of the homogeneous stationary solutions . . .	90
4.17	Instability of light plateau to slow time oscillations of the plateaus	91
5.1	Schematic representation of a Fabry-Pérot	96
5.2	Resonance enhancement in Fabry-Pérot resonators	98
5.3	Fabry-Pérot configuration	104
5.4	Plateau stability in slow time within the Fabry-Pérot cavity	110
5.5	Switching front and dark soliton trajectories in the Argand plane	111
5.6	Homogeneous stationary states and dark soliton solutions of the Fabry-Pérot resonator in comparison with the ring resonator	112
5.7	Switching front dynamics in a Fabry-Pérot resonator	113
5.8	Location in parameter space of dark soliton solutions of the Fabry-Pérot . .	115
5.9	Interaction of stationary dark solitons	116
5.10	Oscillatory dynamics of Dark solitons within a Fabry-Pérot cavity	118
5.11	Trace of oscillating dark solitons	119
5.12	Example frequency combs of dark solitons in ring resonator	120
6.1	Fabry-Pérot cavity with two orthogonal polarisation field components . . .	125
6.2	Linear stability eigenvalues of polarisation degenerate homogeneous stationary solutions of the Fabry-Pérot cavity	135
6.3	Codimension-2 bifurcation of the homogeneous and vectorial dark soliton stationary states	137
6.4	Example symmetry broken Turing patterns and vectorial dark solitons . . .	138
6.5	Extended range of existence of symmetry broken vectorial dark solitons . .	143
6.6	Self-crystallisation of three vectorial dark solitons in a Fabry-Pérot resonator	145
6.7	Partial crystal formation in a Fabry-Pérot resonator	148
6.8	Regular soliton crystal unit cells	149
6.9	Displaced bifurcation of three vectorial dark solitons	150
6.10	Vectorial dark-bright solitons of the Fabry-Pérot resonator	151
6.11	Interaction of stationary vectorial dark-bright solitons	153
6.12	Anti-synchronisation of vectorial dark-bright solitons	154
6.13	Synchronisation of vectorial dark-bright solitons	156
6.14	Synchronisation of multi-peek vectorial dark-bright solitons	157
6.15	Vectorial dark-dark and dark-bright soliton distribution in parameter space	158
A.1	Linear stability eigenvalues of the HSS, indicating instability to two front stationary states	168
A.2	Linear stability eigenvalues of the two front stationary states	171
A.3	Detuning scan of counterpropagating fields	172

Chapter 1

Introduction

1.1	Motivations	3
1.2	Objectives	4
1.3	Layout of the thesis	4

1.1 Motivations

In this thesis, we concern ourselves with the optical Kerr effect. This phenomenon was first discovered by Kerr [1, 2] in 1875 and describes a nonlinear optical effect in which the refractive index of the medium changes proportionally to the intensity of the applied electric field. The Kerr effect is responsible for various nonlinear optical phenomena, including self-focusing, self and cross phase modulation, third harmonic generation, modulation instability and four wave mixing (FWM), of which the latter phenomenon finds itself at the centre of increasing attention. FWM describes the interaction between different frequency components of light, mediated by the nonlinear medium, leading to the generation of new frequencies. This redistribution of energy into frequency sidebands leads to the formation of a coherent set of equally spaced spectral lines around the driving frequency. The resulting spectra is known as a frequency comb. The generation of optical frequency combs [3] is an active area of research due to the wide range of practical applications that span across various fields including telecommunication [4, 5], spectroscopy [6, 7], quantum technology [8, 9] and in the fundamental studies of complex dissipative structures. In 2006, critical developments in the area of frequency comb generation won the Nobel Prize in Physics [10], owing to their importance.

A very high intensity field is required to observe significant contributions from the Kerr effect. Microresonators provide an exceptional platform for inducing optical nonlinearities due to their ability to enhance the optical power circulating within the resonator. This is due to constructive interference between the the cavity mode and the incident field, inducing an intracavity field of significantly higher power than the driving field. Microresonators are designed to confine light via mechanisms such as whispering gallery modes (WGM) or Fabry-Pérot resonances, resulting in strong optical confinement to a small mode area. Such devices allow light to circulate the resonator many times before escaping the cavity, effectively increasing the interaction length between the light and the material. As such, nonlinear effects can be achieved at remarkable low driving power. Optical frequency combs were first observed monolithic microresonators in [11], and have henceforth seen great interest.

In the temporal domain, frequency combs take the form of a periodic temporal structure, such as a train of optical pulses. Temporal cavity solitons (TCS) [12, 13] can be key elements for broadband optical frequency combs [14]. TCSs are a special class of cavity solitons that originate in dissipative optical resonators under the action of external driving, diffraction [15, 16] and/or group velocity dispersion [17–23], where generally optical structures may occur in the longitudinal direction (temporal patterns) or along the transverse directions (spatial patterns). Here, the Kerr effect introduces an intensity dependant refractive index, crucial to the formation of solitons. The change in the refractive index will be greatest at the peak of the intensity such that, as the light propagates, the Kerr effect acts to increase the peak intensity and narrow its intensity profile. An electric field of Gaussian transverse profile will experience a lensing effect, whereby the Kerr effect induces an optical path similar to a convex lens [25]. In the case of a spatial pattern, soliton formation occurs due to the balance of Kerr nonlinear interaction (self-focusing) and diffraction (defocusing) [15, 16]. In this thesis, we restrict our investigation to phenomena in which the transverse components of the electric field do not change significantly

in time. In doing so, we may consider the electric field component which evolves over the longitudinal coordinate. For an optical pulse with temporal profile, the Kerr effect is also present, as the change in refractive index is largest at the centre of the pulse compared to the leading and trailing components. Here, nonlinear self-focusing occurs longitudinally, shortening the pulse duration. Soliton formation is then reliant on the balance of Kerr nonlinear interaction (self-focusing) and chromatic dispersion (defocusing).

Bright TCSs were first observed in macroscopic fibre ring resonators [17]. Kerr nonlinearity is induced in optical silica fibres due to the small mode area of the fibre cross section and the long interaction length of a spool of fibre. Shortly after, bright TCS were observed in WGM microresonators [18]. Now, ring resonator geometries are regularly used for the generation of optical frequency combs via bright TCS. More recently, dark TCSs have been investigated in the regime of normal group velocity dispersion and observed in fibre ring [19] and micro-ring [20–23] resonators. As opposed to bright TCSs, dark TCSs form a localised dip in power on a high power continuous wave background, and can be used to generate frequency combs with higher power conversion efficiency [23]. In both cases, light propagation in ring resonators is well described by the longitudinal version of the Lugiato-Lefever equation (LLE) [24]. The LLE originally described the transverse, dissipative spatial structures in passive optical systems with diffraction and was later adapted to describe pattern formation along the cavity length [26–28]. Furthermore, the generation of bright TCSs has recently been experimentally demonstrated in microresonators with Fabry-Pérot geometry [29]. This has expanded the design space for microresonator application in frequency comb generation.

1.2 Objectives

This thesis aims to present new and interesting optical phenomenon achievable in experimentally realisable microresonators displaying third order nonlinearity (Kerr effect) via analytical and numerical methods. We give particular attention to novel methods of frequency comb generation via temporal cavity solitons and patterns in the regime of normal group velocity dispersion. By considering configurations of ring and Fabry-Pérot geometry, we study temporal pattern formation in intracavity fields composed of; orthogonal polarisation components, counterpropagating components, or a combination of the two. We derive microresonator models of generalised Lugiato-Lefever equation form, in which the interaction of field components presents as self- and cross-phase modulation originating from the Kerr nonlinearity. Though the derivation and analysis of our models, this thesis aims to provide analytical and numerical results which forms a theoretical basis to guide future experimental implementation.

1.3 Layout of the thesis

Chapter 2

We provide a review of the physics of high finesse ring resonators. The material presented in this chapter will facilitate the results of subsequent chapters, providing the relevant

theoretical background required of frequency comb generation in Kerr resonator. We begin with a review of the of whispering gallery microresonator [30, 31]. Whispering gallery modes are presented for cylindrical geometry, while a broader discussion on resonator geometries and material compositions used in experiment is given. Next we discuss the operation of micro-ring resonators, and their useful features. A general description of the the physics of light matter interaction in Kerr nonlinear mediums with normal group velocity dispersion [32–34] is given, which culminates in a detailed derivation of the longitudinal LLE [28]. This model has been used to great success to describe the propagation of light in ring resonators. Finally, we discuss the existence and stability of homogeneous and localised solutions (switching fronts [SF] and dark cavity solitons [DCS]) of the LLE [35].

Chapter 3

We generalise the LLE to include the polarisation properties of the intracavity field following the work of Geddes et al. [36]. The linearly polarised driving laser coupled into the cavity can be transformed such that the intracavity fields may be resolved into components of counter-rotating circularly polarised field components. The now vectorial dark cavity solitons (VDS) [37] of the ring resonator display features in addition to those seen for a cavity with a single field due to the possibility of spontaneous symmetry breaking (SSB) between polarisation components. SSB of the homogeneous stationary states (HSS) has been previously investigated in the ring resonator, whereby a linearly polarised intracavity field suddenly becomes nonlinearly polarised through a small change in control parameter [38]. Here, we present a SSB Turing instability, found in regimes of the normal dispersion, which results in the formation of Turing patterns of alternating polarisations on the high power HSS. SSB of the VDSs result in a useful ‘self-crystallisation’ phenomenon in which an initially random distribution of VDSs spontaneously form a regular soliton crystal (RSC) [39]. The formation of soliton crystals was originally performed using phase gradients to position them into regularly spaced structures [16] and more recently has been demonstrated through perturbations introduced near avoided mode crossings [40–43], or an external modulation [44] of the field. The RSC of our system are a result of a self-organisation mechanism of long range interactions between adjacent VDSs via a SSB of Turing patterns. We conclude this chapter by characterising the formation of vectorial dark-bright solitons (VDBS) in regimes of large symmetry breaking.

Chapter 4

We study the interaction of two counterpropagating intracavity field within a bidirectionally driven, normally dispersive, ring resonator. This system is described by two globally coupled integro-partial differential equations of LLE form [45, 46]. We use the term ‘global coupling’ following [47] to describe nonlinear cross terms that couple a point of the resonator to all other points in the same resonator via integrals that extend over the round trip of the cavity. It is the nature of counterpropagation, and the resulting global coupling, that variations in one field are not necessarily present in the other. Global coupling of the counterpropagating fields is found to result in a class of robust stationary states formed by light plateaus separated by two local(SF). The two SF stationary state forms in only one of two counterpropagating intracavity fields, leaving the other flat in profile. We provide

the expressions for the separation of SFs and plateaus power with respect to the control parameters, and demonstrate an unusually high degree of control over pulse and plateau duration upon changes of one of the input laser frequencies. Light plateau stationary states are self-starting from noise over a large range of parameters due to an instability of the HSSs to inhomogeneous perturbation, resulting from the averaged terms, which allows for frequency combs to switch propagation direction (moving from one field to the other) by scanning the frequency of one field. Finally, we show the presence of nonlinear oscillations of symmetry broken HSS, resulting in a multistability of slow nonlinear oscillations with SF states and continuous wave outputs.

Chapter 5

We continue our discussion of temporal cavity solitons, but at a difference to the ring resonators, we consider a Fabry-Pérot (FP) configuration. Temporal cavity solitons (TCS) within FP resonators has seen significant interest in recent years, where the generation of bright soliton in the anomalous dispersion regime has been demonstrated, first studied theoretically [48, 49] and then demonstrated experimentally in microresonator [29] and macroscopic fibre resonator [50] settings. The generation of frequency combs produced by modulational instabilities and Turing patterns have also been demonstrated [51] along with pulsed driving [52, 53]. In Chapter 5, we model a FP resonator filled with a Kerr nonlinear medium and investigate the inherent counterpropagation of light under normal dispersion conditions. We outline the conditions required for the existence of local structures (switching fronts [SF] and dark cavity solitons [DCS]) and make comparison with the DCSs of the ring resonator. DCSs are found to be detuning shifted with respect to those in a ring resonator by the average power of the field over a round trip of the cavity, where stationary solutions of the FP are described by a modified LLE. Counterpropagation of light is found to induce nonlocal self coupling corresponding to the averaged power of the field over the round trip of the cavity. We compare the stationary solutions of the FP model and their stability with the stationary solutions of LLE [35, 54] for the ring resonator to properly elucidate the effects of the shift in detuning. Nonlocal self coupling of the field introduces long range interactions between distant DCS. We investigate the effects of these interactions using oscillatory DCSs, where we present the spontaneous synchronisation of their oscillations.

Chapter 6

Finally, we consider a high finesse FP resonator as we had previously, but now we generalise the model in consideration of polarisation effects as described by Pitois et al. [55]. We begin by deriving the integro-partial differential equations of the FP [49], which describe the two counter-rotating circular polarised fields over the cavity round trip following from Cole et al. [48]. By performing linear stability analysis on the HSSs of our model, we identify a codimension-2 bifurcation of two distinct SSB bifurcations corresponding to symmetry broken HSSs and Turing patterns of alternating polarisations. This bifurcation structure is found to extend to symmetric vectorial dark solitons (VDS). Due to the possibility of SSB, the now vectorial temporal cavity solitons [37] display additional features to those seen for the single field FP [48, 56]. In particular, VDS are found to undergo a

Turing bifurcation resulting in the formation of patterns of alternating polarisations on the homogeneous plateau separating adjacent VDSs. We discuss in Chapter 3 the spontaneous self-organisation of VDSs due to long rang interactions between adjacent VDSs mediated by Turing patterns. We generalise the ‘self-crystallisation’ mechanism described to the FP resonator, and discuss the differences between these two systems in the generation of regular soliton crystals. We end this chapter by characterising the formation of dark-bright vectorial solitons, where we present non trivial breathing dynamics of VDBS originating from nonlocal coupling.

Chapter 2

Theory of Temporal Cavity Solitons in Ring Resonators with Normal Dispersion

2.1	Introduction	9
2.2	Whispering gallery mode microresonators	9
2.2.1	Micro-cavity devices	9
2.2.2	Guided mode solutions	10
2.2.3	Birefringence and polarisation mode dispersion	14
2.2.4	Propagation losses	15
2.3	Fundamentals of ring resonators	16
2.3.1	Coupling via evanescent fields	16
2.3.2	Resonance enhancement	17
2.3.3	Coupling efficiency	18
2.3.4	Cavity finesse and quality factor	19
2.4	The propagation of light in nonlinear dielectric waveguides	20
2.4.1	Nonlinear atomic polarisation	20
2.4.2	Chromatic dispersion	21
2.4.3	Longitudinal waveguide propagation equation	22
2.5	Modelling the ring resonator	26
2.6	The longitudinal Lugiato-Lefever equation	27
2.7	Stationary solutions of the Lugiato-Lefever equation with normal dispersion	33
2.7.1	Optical bistability of homogeneous solutions	33
2.7.2	The existence and stability of exponentially localised solutions	36
2.8	Conclusion	39

2.1 Introduction

In this chapter, we review the physics and applications of the ring resonator system to provide a theoretical and methodological foundation from which we can understand the results presented in future chapters. This begins in Section 2.2 with a description of the material properties and geometries of the whispering gallery microresonator platform. In particular, we highlight the design considerations which make ring resonator geometries prolific in practice, where a brief overview of the whispering gallery modes (WGM) is given. An overview of optical ring cavity physics is presented in Section 2.3, where we discuss the coupling conditions, resonance enhancement and quality factor required for the enhancement of nonlinear optical effects. The propagation of light in nonlinear dielectric waveguides is characterised in Section 2.4, where we outline the typical separation of the transverse mode profile from the longitudinal evolution of the electric field amplitude of the guided light. In Section 2.5 we provide a description of the ring resonator model and then in Section 2.6 derive the well-known longitudinal Lugiato-Lefever equation (LLE) from first principles [28]. This mean field model, originally derived to describe the transverse directions [24], has been used to great success to describe the propagation of light in high finesse ring resonators along the longitudinal coordinate [26]. Finally, we present typical solitonic solutions of the (LLE) in Section 2.7 using numerical and analytic methods.

2.2 Whispering gallery mode microresonators

2.2.1 Micro-cavity devices

In general, a ring resonator system is composed of a waveguide that forms a closed loop. This may take the form of a loop of optical fibre, or a dielectric media composed of a closed geometry forming a resonant cavity, such as a sphere, disc, etc.. In the latter case, confinement of the light does not require an internal dielectric boundary, instead light propagates close to the outer curved boundary as a optical whispering gallery mode (WGM).

The phenomenon of whispering galleries was first described by Lord Rayleigh in 1912 [57], where he observed that sound waves could travel along curved surfaces with minimal attenuation, allowing high frequency ‘whispers’ to be heard clearly across large distances. This effect was notably observed in dome of St. Paul’s Cathedral in London. The physics

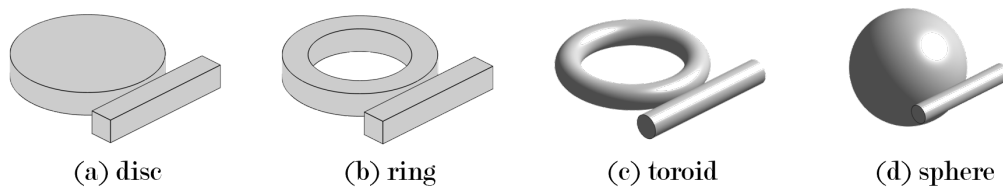


Figure 2.1: Example of whispering gallery microresonator geometries, typically found in practice [3, 31].

of acoustic whispering galleries were later applied to electromagnetic waves, leading to the development of optical WGM resonators. In optical WGM resonators, light is confined by total internal reflection along the boundary of a curved surface at which two dielectrics materials interface. Dielectric optical resonators can be fabricated in various geometries and composed of different materials [3, 58]. Cylindrical (a), ring (b), toroidal (c) and spherical (d) microresonator geometries are shown in Fig. 2.1, where in each case, light is coupled into the cavity via an evanescent field extending from an adjacent bus waveguide. Each waveguide shape is capable of storing the electric field with very low loss over the round trip.

The optical phenomena exhibited by a WGM microresonator is dependant on the material from which it is fabricated. We consider a resonator made of a Kerr nonlinear material, which can achieve normal group velocity dispersion. Amorphous silica glasses, such as silicon nitride (Si_3N_4), are commonly used in integrated photonics and can provide normal dispersion in the visible and near-infrared regions. In addition, silica microresonator have been shown to produce strong Kerr effects. Resonators composed of silica glass are routinely used for the generation of temporal cavity solitons [3, 58]. Confinement of the light is greatly influenced by the ratio of the refractive indices of the core media, composing the resonator, and the cladding media, surrounding the resonator.

2.2.2 Guided mode solutions

WGM solutions have come to represent the family of optical modes associated with microresonators in general [59], and are well covered in the literature for spherical [60], cylindrical [30, 61, 62], and toroidal [62, 63] geometries. Example microresonators of different shapes are shown in Fig. 2.1 for disc (a), ring (b), toroid (c), and sphere (d) cavities, where in each case light propagates azimuthally, confined near the outer curved surface of the cavity due to total internal reflection. The electric fields of the WGM may be decomposed into eigenmode solutions of the Schrödinger equation

$$\nabla^2\psi(\mathbf{x}, t) + \frac{n^2}{c^2}\partial_t^2\psi(\mathbf{x}, t) = 0. \quad (2.1)$$

This is obtained directly from the Maxwells equations [33] in the absence of free charges and currents, where ψ may represent either the electric E or magnetic H field. We assume a low loss resonator with linear atomic polarisation, whereby the dielectric constant may be approximated $\epsilon \approx n^2$. In addition, the refractive index n is assumed to be independent of the cavity coordinates within the medium, such that the optical modes are presumed to maintain their polarisation as they travel through the waveguide. This significantly simplifies Maxwells wave equation where the modal distribution may be obtained by solving a Helmholtz equation, as we will show here.

The solutions of the scalar equation (2.1) belong to two distinct classes; transverse electric (TE) and transverse magnetic (TM). As is conventional for the WGMs of cylinder geometry; TE modes possess an axial magnetic field parallel to the outermost curved surface, whereas TM modes possess an axial electric field parallel to the outermost curved surface. For TE modes, the electric field oscillates within the plane of the cylinder. Hence, these two classes describe optical modes of orthogonal polarisation. In what follows we

consider the electric field component of TM solutions.

This thesis concerns itself with microresonators of cylindrical geometry (specifically micro-ring resonator geometry), in which the height of the resonator is much smaller than the diameter. In this case the dominant axial guiding mechanism will be the refractive index change at the boundary. We begin with a micro-disc resonator, where it is useful to convert to cylindrical coordinates (r, ϕ, h) to obtain solutions for the intensity profile, with radial distance r from the centre of the resonator, azimuth angle ϕ and resonator height h . We assume solutions of the form $E(\mathbf{x}, t) = F(r, h) \exp(i\omega_0 t - im\phi)$, such that we may rewrite Eq. (2.1) as

$$\partial_r^2 F(r, h) + \frac{1}{r} \partial_r F(r, h) + \partial_y^2 F(r, h) + \left[k_0^2 n^2 - \frac{m^2}{r^2} \right] F(r, h) = 0. \quad (2.2)$$

The separation of variables leads to the introduction of the azimuthal mode number m , which corresponds to the number of effective wavelengths the field undergoes as it makes a full revolution around the cavity, and assumes an integer value corresponding to the resonance condition. In order to resolve the WGM solutions, we make the critical assumption that we may perform a separation of variables $F(r, h) = F(r)F(h)$, applicable for microresonators presenting a rotationally symmetric cross-sectional area. From (2.2), we obtain the radial equation

$$\partial_r^2 F(r) + \frac{1}{r} \partial_r F(r) + \left[k_0^2 n_{\text{eff}}^2 - \frac{m^2}{r^2} \right] F(r) = 0, \quad (2.3)$$

with effective index $n_{\text{eff}} = (n^2 - k_y^2/k_0^2)^{1/2}$ defined by the axial confinement wavenumber k_y . The solutions of the Bessel equation (2.3) are Bessel functions of the first J_m and second Y_m kind. We solve Eq. (2.3) both inside the waveguide medium (core) and in its surroundings (cladding), implementing the appropriate boundary conditions. Y_m is singular at the origin, and as such, we only consider the well behaved J_m solutions within the core. Outside of the core, we retain both Bessel functions, which may be expressed in terms of the Hankel functions $H_m^\pm = J_m \pm iY_m$. Hankel functions correspond to inward H_m^- and outward H_m^+ propagating cylindrical waves, of which, we consider only outward propagating waves here. Hence, the solutions of Eq. (2.3) may be expressed as [61, 62],

$$F(r) \propto \begin{cases} J_m(k_0 n_{\text{eff}} r), & \text{if } r \leq R_o, \\ H_m^+(k_0 n_{\text{eff}} r), & \text{if } r \geq R_o, \end{cases} \quad (2.4)$$

and the effective index takes the form within the core $n_{\text{eff}} = (n_{\text{core}}^2 - k_y^2/k_0^2)^{1/2}$ and within the cladding $n_{\text{eff}} = (n_{\text{clad}}^2 - k_y^2/k_0^2)^{1/2}$, where $n_{\text{core}}, n_{\text{clad}}$ are the indices of the disc media and cladding, respectively, with the constraint that $k_0 n_{\text{core}} > k_y > k_0 n_{\text{clad}}$ for guided solutions. Bessel functions of the first and second kind are oscillatory in character, where J_m describes the oscillation of the electric field radially from the centre of the disc. This may be illustrated in the asymptotic limit $k_0 n_{\text{eff}} r \gg 1$, with, [61, 64]

$$J_m(k_0 n_{\text{eff}} r) \approx \sqrt{\frac{2}{\pi k_0 n_{\text{eff}} r}} \cos\{\kappa(r, m)\}, \quad (2.5)$$

where $\kappa(r, m) = k_0 n_{\text{eff}} r - m\pi/2 - \pi/4$. Throughout this thesis, we assume excitation of the fundamental mode of the resonator. This represents the simplest possible mode structure, consisting of a single radial oscillation of the electric field envelope located near the core-cladding boundary, as is commonly implemented in practice. Outside of the core, the electric field decays exponentially from the resonator as an evanescent field. This is described by the Hankel function, which can be expressed in asymptotic limit as,

$$H_m^+(k_0 n_{\text{eff}} r) \approx \sqrt{\frac{2}{\pi k_0 n_{\text{eff}} r}} \exp\{i\kappa(r, m)\}, \quad (2.6)$$

where the effective index takes imaginary form within the cladding $n_{\text{eff}} = i|n_{\text{eff}}|$. The field outside of the resonator medium is commonly expressed in terms of the modified Bessel function of the second kind $K_m \sim \exp(-k_0|n_{\text{eff}}|r)/k_0|n_{\text{eff}}|r$, which in general is defined as $H_m^+(ix) \equiv i^{m+1}K_m(x)\pi/2$. This component of the guiding mode is non-propagating, localised near the core-cladding boundary, and carries zero net power in the direction perpendicular to the waveguide surface. In the presence of another nearby structure (such as a bus waveguide), coupling can occur when the evanescent tails of the two waveguides overlap, and energy can be transferred via optical tunnelling. This is a primary mechanism by which light is coupled into the cavity in practice.

We note that the asymptotic expressions for the Bessel and Hankel functions are appropriate when the radius of the disc is much larger than the wavelength ($k_0 n_{\text{eff}} r \gg 1$). This is generally the case in practice, where typical high- Q microresonator systems have radii 10-500 μm and are driven by lasers of approximate wavelength 1 μm [3, 61].

The axial modes are obtained by solving the equation

$$\partial_y^2 F(y) + k_0^2 [n^2 - n_{\text{eff}}^2] F(y) = 0, \quad (2.7)$$

which was obtained from Eq. (2.2) along with the radial equation (2.3) during the separation of variables, and yields the modal distribution of a slab-like waveguide [61, 62]

$$F(h) \propto \begin{cases} \exp(-qh), & \text{if } h \geq h_0, \\ \cos(ph), & \text{if } -h_0 \leq h \leq h_0, \\ \exp(qh), & \text{if } h \leq -h_0, \end{cases} \quad (2.8)$$

where $p = k_0(n_{\text{core}}^2 - n_{\text{eff}}^2)^{1/2}$, $q = k_0(n_{\text{eff}}^2 - n_{\text{clad}}^2)^{1/2}$, and the core media occupies the domain $|h| \leq h_0, r \leq R_o$, with cladding for $|h| \geq h_0, r \geq R_o$. It is clear to see that the waveguide modes of Eqs. (2.7) are oscillatory within the core, and presents an evanescent tail outside the core in which the electric field exponentially decays, much like the radial confinement. Similar to the radial case, light may be coupled into and out of the resonator via the axial evanescent field, as is common in practice.

In this thesis, single mode operation is assumed. Generally, the number of modes supported by the cavity is dependant on the confinement of the WGM, where waveguides possessing a small cross-sectional area and large core-cladding index difference provide greater confinement of the circulating light. A single mode waveguide only supports the fundamental mode, in which light is confined to either TM or TE modes, and is charac-

terised by a single radial oscillation of the electric field within the disc. Disc resonators are generally multimode by their nature, due to the lack of an inside surface to provide tight confinement of the WGM. For a micro-disc, the radial confinement of the WGM is formally equivalent to a potential well $V(r) \sim (m/nr)^2$ whereby the WGM occupies a local region of high effective radial index, with

$$n_r = \sqrt{n_{\text{eff}} - \frac{m^2}{k_0^2 r^2}}. \quad (2.9)$$

WGMs do not require an inner surface to complete the confinement of the optical mode. Instead light is confined near the perimeter of the cavity due to ‘optical inertia’, inhibiting the field from approaching the centre of the disc. We may define an inner caustic radius $R_{\text{inner}} = m/k_0 n_{\text{core}}$ within which the light possess too great an optical inertia to be confined via total internal reflection. The oscillatory guided mode is bound between the outer surface of the microresonator and this inner caustic radius. For radii below R_{inner} , the electric field may be described in terms of the modified Bessel function of the first kind, defined as $I_m(x) \equiv i^{-m} J_m(ix)$, displaying oscillations of decreasing amplitude as $r \rightarrow 0$, where the field is considered to decay evanescently from the inner caustic radius. We may avoid the exciton of parasitic higher order modes within a micro-disc resonator by removing the interior of the disc, forming a micro-ring resonator. Should the diameter of the inside surface be less than the inner caustic boundary, the ring will continue to support similar whispering gallery modes, but when the radius of the inner surface is greater than the inner caustic, the electric field is forced to be exponentially decaying, leading to greater confinement of the optical mode to a smaller mode area. The radial confinement within a ring can be described as

$$F_{\text{ring}}(r) \propto \begin{cases} I_m(k_0 n_{\text{eff}} r), & \text{if } 0 \leq r \leq R_i, \\ AJ_m(k_0 n_{\text{eff}} r) + BY_m(k_0 n_{\text{eff}} r), & \text{if } R_i \leq r \leq R_o, \\ K_m(k_0 n_{\text{eff}} r), & \text{if } r \geq R_o, \end{cases} \quad (2.10)$$

where $I_m(k_0 n_{\text{eff}} r)$ governs the electric field from the inner surface R_i to the origin. As the origin is no longer within the core, we must reintroduce the now well behaved Bessel function of the second kind into our expression of the electric field within the resonator core, $R_i \leq r \leq R_o$, with constant coefficients A, B . In addition to suppressing higher order modes, the interior surface of the ring leads to greater condiment of the fundamental mode to smaller cross sectional area closer to the outer surface. This leads to stronger light-matter interaction critical for inducing nonlinear optical effects, and reduced losses allowing light to circulate the cavity for longer.

In general, should the diameter of the ring be significantly larger than the width of the waveguide $[(R_o - R_i) \ll R_o]$, we can no longer perform a separation of variables $F(r, h) \neq F(r)F(h)$. In such systems, the cylindrical WGM approximation is unsuitable and we must rely on numerical evaluation of Eq. (2.2) to obtain the modal distribution of the ring [65]. The inability to perform a separation of variables means the resulting mode will be hybridised between TM and TE modes. In this thesis, we make the assumption of quasi-TM or quasi-TE fields. This amounts to the assumption that we may treat the

intracavity field as TM or TE in approximation, even if the modes are partially hybrid. Nonetheless, in certain limits the modal distribution may be approximated analytically. For the rectangular waveguides commonly produced for photonic integrated circuit technologies [3], the radial modal distribution may resemble a straight slab-waveguide [62] similar to the y -direction confinement (2.7), whereas the modal solutions of the micro-toroid resonator can be studied analytically through perturbative methods [63].

2.2.3 Birefringence and polarisation mode dispersion

Here, our investigation pertains to waveguides that are single mode as discussed in Section 2.2.2. Contrary to the name, a single mode waveguide does in fact display two degenerate polarisation modes, TE and TM, which support orthogonally polarised electric field components [34]. In this thesis, we consider two scenarios; either the waveguide preserves the linear polarisation of the driving field (Chapters 4 and 5), or the two polarisation modes are degenerate (Chapters 3 and 6). These two scenarios require different design considerations.

If we presume an ideal case in which the waveguide cross-section has perfect rotational symmetry, a linearly polarised electric field will maintain its polarisation as it travels along the waveguide. In practise, small random variances in the shape of the waveguide along with stress-induced anisotropy and thermal effects break the symmetry of the cross-section, such that the polarisation modes are no longer degenerate. The propagation constant β of each component of the electric field is dependant on its polarisation as a result. This phenomenon is referred to as birefringence. The polarisation components within the birefringent waveguide exchange power as they propagate with beat length $L_B = 2\pi/|\beta_x - \beta_y|$, where β_x, β_y are the wavenumbers of the orthogonal linearly polarised components, and the group velocity dispersion β_2 and nonlinear coefficient γ are the same for both polarisations. This process is particularly important for optical pulses as the intensity profile of an optical pulse which excites both polarisation modes will broaden as orthogonal components of the pulse will propagate at different speeds. This is referred to as polarisation mode dispersion.

One method to ensure the preservation of a linearly polarised state is to fabricate a strong birefringence in the waveguide. By driving light linearly polarised along the axis of smallest propagation constant (the slow axis), polarisation fluctuations due to the coupling between the polarisation modes have negligible effects on the polarisation state. This can be done by introducing a strong geometrical asymmetry, such as a large aspect ratio for the rectangular or elliptical cross section. Micro-ring resonators are natural polarisers due to phase-matching constraints. In particular, birefringence causes the effective refractive index for TE and TM modes to be different, leading to different resonance conditions for each polarisation. This is beneficial should we wish for light to maintain its polarisation as it propagates.

Due to the universality of the generalised Lugiato-Lefever equations presented in this thesis, the polarisation degenerate models may be used for both macroscopic and microscopic resonators. As of now, polarisation degeneracy has only been observed in optical fibres [66] and macroscopic fibre resonators [67, 68]. Optical fibres do not have the tight tolerances of the microresonator which confines light into very a small mode area, allowing

for easier engineering of polarisation degeneracy.

2.2.4 Propagation losses

The optical losses we consider within the ring resonator system are attributed to material absorption, the scattering of light, and characteristically of WGM resonators, bending losses. While losses attributed to absorption and scattering are also present in straight waveguides, bending losses unique to ring resonators, and generally curved waveguides.

Absorption

Absorption losses occur when a portion of the optical power is converted into heat or other forms of energy due to interaction with the material composing the waveguide [3]. In this thesis, we consider silica glass waveguides. This material platform is widely used for optical telecommunication fibres due to their low absorption properties. That said, during the fabrication of microresonators unintentional dopants, defects, or residual fabrication impurities can contribute to absorption losses. Losses to absorption are responsible for thermal effects [69, 70].

Scattering

As light propagates along a resonator, imperfections in the waveguide can cause light to couple out of the guided mode. Such imperfections include variations in material composition or density. This introduces small variation in the refractive index, and is the origin of Rayleigh scattering [71, 72]. Another mechanism of scattering found in ring resonators is associated with residual crystalline structure of the glass. Despite our assumptions of amorphous silica glass, short scale crystalline structures may still be present in the waveguide. Interactions with these crystalline structures may introduce Raman scattering [98] (inelastic scattering of photons by vibrational modes of the medium) or Brillouin scattering [99] (arises from interaction between light and thermally induced acoustic waves). Finally, irregularities at the core-cladding boundary due to fabrication imperfections is another mechanism for scattering. Roughness at the surface of the silica waveguide is particularly important in integrated photonics and etched structures [45, 73–75].

Light scattered by these mechanism will either exit the waveguide, couple to a different optical mode with the same resonant frequency or couple into the same mode travelling in the opposite direction.

Bending losses

The bending losses of a waveguide refer to the loss of optical power due to the curvature of the waveguide. This is due to the fact that components of the light travelling at larger radius within the waveguide travel a larger distance. For microresonators, this introduces a caustic radius at which the azimuthal phase velocity of the whispering gallery modes exceed the speed of light in the cladding, beyond which light escapes the cavity in a radial direction. If we consider a microresonator with cylindrical geometry, this effect can be quantified in the radial refractive index [Eq. (2.9)] which increases in value with greater

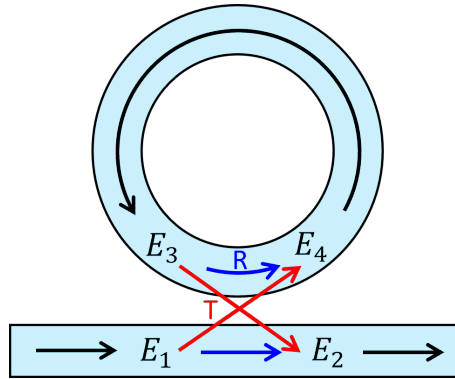


Figure 2.2: Light from the adjacent bus waveguide may enter and leave the cavity via the coupling mechanism (evanescent field for a microresonator, or a beam splitter for a fibre loop ring resonator, etc.). The coefficients of power transmissivity and reflectivity of the electric field are shown as T and R , respectively.

radial distance from the centre of the resonator. We may then define the outer caustic radius at which the guided light radiates as $R_{\text{outer}} = m/n_{\text{clad}}k_0$, beyond which light may exit the guiding mode. For microresonators, the losses associated with the whispering gallery modes can be viewed as a tunnelling of the guided field beyond the boundary formed by the resonator edge and outer caustic radius into a region of lower potential energy. At R_{outer} , the evanescent field protruding from the resonator has azimuthal phase velocity equal to the phase velocity of the cladding, beyond which the field begins to freely propagate radially outwards. For high- Q resonator, the evanescent field extends only a short distance from the surface of the resonator (within a wavelength), and as such the bending losses are small.

Nonetheless, bending losses impose a limit on minimum possible size for a ring resonator, as smaller rings possess greater curvature and therefore higher bending losses. These losses can be mitigated through the design of the rings geometry and material composition. In particular, bending losses can be reduced by selecting a material platform with a large difference in refractive index between the core and cladding. When the step in refractive index between core and cladding is very high, we can achieve a strong confinement of the electric field within the waveguide, which enables light guiding in bends with very small radii without fatal radiation losses. Thus the material choice is of vital importance for microresonator systems.

2.3 Fundamentals of ring resonators

2.3.1 Coupling via evanescent fields

Evanescent field coupling is a key mechanism used to transfer light between optical waveguides and microresonators. As described in Section 2.2.2, the evanescent field is a non-propagating component of the transverse mode, exponentially decaying outside the core. By situating the microresonator sufficiently close to the bus waveguide, their evanescent fields overlap, allowing for energy to transfer from the waveguide to the resonator and

vice versa within the overlapping region. This allows for tunable coupling by setting the separation of the waveguide and microresonator. The general relationship between the incident field E_1 and the transmitted field E_2 within the bus waveguide, along with the circulating fields with the ring cavity entering E_3 and leaving E_4 the coupling region can be represented in the spectral domain by the scattering matrix

$$\begin{pmatrix} E_4 \\ E_2 \end{pmatrix} = \begin{pmatrix} \sqrt{R} & i\sqrt{T} \\ i\sqrt{T} & \sqrt{R} \end{pmatrix} \begin{pmatrix} E_3 \\ E_1 \end{pmatrix}, \quad (2.11)$$

where the coefficients of reflection R and transmission T are real. The coupling coefficients satisfy the relation $T+R = 1$, which amounts to the assumption that there are zero losses at the coupling point. In general, the coupling region extends over a considerable proportion of the ring. This is particularly true for micro-ring resonators, but here we assume a singular coupling point without loss of generality by implementing to appropriate phase matching between the waveguide and resonator as is performed in experimentally. The driving field can be related to the output field through the relation

$$E_3 = ae^{i\theta} E_4, \quad (2.12)$$

where $1 - a$ is the loss of the electric field over a single round trip of the cavity and θ is the phase acquired over the single round trip. The phase shift can be expressed as $\theta = Ln\omega/c = \omega\tau_R$ which represents the radian frequency over the round trip time τ_R . As such, we recognise θ as a normalised frequency detuning between incident field and the cavity with circumference L and refractive index n . Solving Eqs. (2.11) and (2.12) we obtain expressions for the fields

$$E_1 = 1, \quad E_2 = \frac{\sqrt{R}e^{-i\theta} - a}{e^{-i\theta} - a\sqrt{R}}, \quad E_3 = \frac{ia\sqrt{T}}{e^{-i\theta} - a\sqrt{R}}, \quad E_4 = \frac{i\sqrt{T}}{1 - a\sqrt{R}e^{i\theta}}. \quad (2.13)$$

2.3.2 Resonance enhancement

Constructive interference at the coupling point results in a circulating intensity much larger than the incident field. This effect is reliant on the coherence of the deriving field. An incoherent driving field will result in a circulating power equal to the incident power. The significant larger field intensity within the cavity results in dramatically enhanced nonlinear effects. As such, this coherent excitation of the circulation field is highly desirable for application as a strong nonlinear response can be obtained with a driving field of comparatively low input power. The ratio of the incident and circulating field can be determined by solving Eqs. (2.11) and (2.12), yielding

$$\frac{E_3}{E_1} = \frac{1\sqrt{T}ae^{i\theta}}{1 - \sqrt{R}ae^{i\theta}} \quad (2.14)$$

with power ratio

$$\frac{|E_3|^2}{|E_1|^2} = \frac{(1 - R)a^2}{1 - 2\sqrt{R}a \cos(\theta) + Ra^2}. \quad (2.15)$$

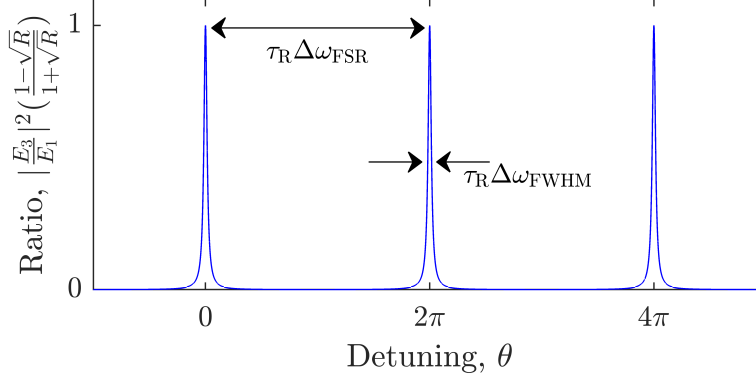


Figure 2.3: Plot of the normalised ratio between incident and circulating field intensities in a high- Q linear cavity without dispersion. Three resonances are visible with linewidth $\Delta\omega_{\text{FWHM}}$, located at detuning values $\theta = 0, 2\pi, 4\pi$ and separated by the free spectral range $\Delta\omega_{\text{FSR}}$.

The theoretical maximum power ratio between the incident and circulating fields is achieved when the incident light is resonant with the cavity. Resonant modes correspond to a phase shift θ that is an integer number m of 2π accumulated over a round trip. As such, the resonances are distributed as $\theta = 2\pi m$ in the frequency domain as is shown in Fig. 2.3. Here we can see that successive resonances in the frequency domain are separated by the free spectral range (FSR) of the cavity defined as $\Delta\omega_{\text{FSR}} = 2\pi/\tau_{\text{R}}$. In the absence of dispersion, these modes are equally spaced in the frequency domain. Under the ideal conditions of low transmission $T \ll 1$, and negligible losses $a \approx 1$ the highest possible power ratio is achieved $|E_3|^2/|E_1|^2 = (1 + \sqrt{R})/(1 - \sqrt{R}) \approx 4/T$. For a power transmission coefficient of 10% ($T = 0.1$), the circulating field $|E_3|^2$ is 40 times larger than the incident field $|E_1|^2$.

2.3.3 Coupling efficiency

Utilising the field expressions (2.13), we may define the coupling efficiency parameter

$$\eta = \frac{|E_1|^2 - |E_2|^2}{|E_1|^2} \Big|_{\theta=0} = \frac{(1 - a^2)(1 - R)}{(1 - a\sqrt{R})^2} \quad (2.16)$$

When a system is tuned to resonance, the energy transfer into the resonator becomes more efficient due to optical impedance matching, maximising power transfer. The strength of resonance enhancement depends on how efficiently light is coupled into the resonator. If coupling is poor, insufficient energy enters the resonator, limiting the enhancement effect.

Critical coupling is achieved when the internal losses of the cavity is equal to the loss due to transmission of the electric field at the coupling point $a = \sqrt{R}$ [30, 76]. Under such conditions, the output field E_2 is zero at resonance as all of the incident light coupled to the ring is stored and lost within the resonator. When the critical coupling conditions are met, the coupling efficacy becomes $\eta = 1$. In practice, achieving critical coupling ensures optimal energy transfer between the bus waveguide and the resonator, maximizing the

performance of the device.

2.3.4 Cavity finesse and quality factor

The cavity finesse is defined as the FSR of the cavity divided by the linewidth of the resonance [taken to be the full width at half maximum (FWHM)] with,

$$\mathcal{F} = \frac{\Delta\omega_{\text{FSR}}}{\Delta\omega_{\text{FWHM}}} \quad (2.17)$$

Using the field expressions (2.13) we may evaluate the FWHM as $E_4(\theta_{\text{FWHM}}) = E_4(\theta = 0)/2$ by assuming a narrow resonance $\cos(\theta) \approx 1 - \theta^2/2$, yielding

$$\Delta\omega_{\text{FWHM}} = \frac{1}{\tau_R} \theta_{\text{FWHM}} = \frac{1 - a\sqrt{R}}{\tau_R \sqrt{a\sqrt{R}}}. \quad (2.18)$$

The cavity finesse is then

$$\mathcal{F} = 2\pi \frac{\sqrt{a\sqrt{R}}}{1 - a\sqrt{R}} \quad (2.19)$$

The cavity finesse quantifies the intensity build-up within the resonator. Physically, this quantity represent the number of round trips (up to a factor of 2π) light travels within the ring, and therefore, the number of times the electric field interacts with the coupling to the bus waveguide.

The quality factor (Q -factor) is defined as 2π times the ratio between the energy stored in the resonator at frequency ω and the energy losses over one cycle cycle of the electric field, which we write as

$$Q = \omega \times \left(\frac{\text{energy stored at } \omega}{\text{power loss per cycle}} \right) = \omega\kappa^{-1} \quad (2.20)$$

This, by definition, is related to the exponential decay rate κ of the cavity. The Q -factor allows us to quantify impact of losses for a resonator system. An alternative definition for the Q -factor in terms of the resonance linewidth is

$$Q = \frac{\omega}{\Delta\omega_{\text{FWHM}}} = \mathcal{F} \frac{\omega}{\Delta\omega_{\text{FSR}}} = \omega\tau_R \frac{\sqrt{a\sqrt{R}}}{1 - a\sqrt{R}} \quad (2.21)$$

The definitions (2.20) and (2.21) are equivalent in the limit of high- Q and allows us to express the Q -factor in terms of observable parameters and the cavity finesse. Physically speaking, the Q -factor quantifies effective interaction time of the propagating light with the cavity. It represents the number of wavelengths light travels within the ring, before being lost due to the interaction with the cavity interior.

The performance of the cavity is quantified though cavity finesse and Q -factor. These properties are used to inform the suitability of the microresonator for its required purpose.

2.4 The propagation of light in nonlinear dielectric waveguides

In this section, we characterise the propagation of light within dielectric waveguides in the presence of Kerr nonlinearity. We begin our discussion with the scalar Maxwell wave equation,

$$\nabla \times \nabla \times \mathcal{E}(\mathbf{x}, t) + \frac{1}{c^2} \partial_t^2 \mathcal{E}(\mathbf{x}, t) = -\mu_0 \partial_t^2 \mathcal{P}(\mathbf{x}, t). \quad (2.22)$$

This equation is derived directly from Maxwell's equations [32–34] and describes the free propagation of the electric field within a dielectric medium, where c is the speed of light in vacuum which is related to the vacuum permittivity ϵ_0 and vacuum permeability μ_0 through the relation $c^2 = 1/\mu_0\epsilon_0$, and \mathcal{P} is the induced atomic polarisation of the medium due to the electric field \mathcal{E} at Cartesian coordinate \mathbf{x} and time t . Here, we assume the electric field maintains a linear polarisation.

2.4.1 Nonlinear atomic polarisation

The response of a dielectric medium under the influence of intense electromagnetic fields becomes nonlinear. This nonlinearity is due to the anharmonic motion of bound electrons of the medium under the action of the propagating light, and as such, the polarisation field \mathcal{P} induced by the electric dipole moment of the atoms is nonlinear with respect to the electric field \mathcal{E} . The atomic polarisation of the dielectric medium can be generalised to the expanded form [32, 33]

$$\mathcal{P}(\mathbf{x}, t) = \epsilon_0 \left[\chi^{(1)} \mathcal{E}(\mathbf{x}, t) + \chi^{(2)} \mathcal{E}^2(\mathbf{x}, t) + \chi^{(3)} \mathcal{E}^3(\mathbf{x}, t) + \dots \right] \quad (2.23)$$

encompassing the relation between the atomic polarisation and the electric field, where $\chi^{(j)}$ is, in general, a tensor of rank $j + 1$ and represents the j th order susceptibility of the medium. It is conventional in the study of nonlinear optics to write the atomic polarisation in terms of its linear and nonlinear components

$$\mathcal{P}(\mathbf{x}, t) = \mathcal{P}_L(\mathbf{x}, t) + \mathcal{P}_{NL}(\mathbf{x}, t). \quad (2.24)$$

The leading contribution to the total polarisation is the linear polarisation, which we define as [32, 33]

$$\mathcal{P}_L(\mathbf{x}, t) = \epsilon_0 \int_{-\infty}^t \chi^{(1)}(t - t') \mathcal{E}(\mathbf{x}, t) dt', \quad (2.25)$$

which is characterised by the linear susceptibility $\chi^{(1)}$, whose effects manifest through the refractive index n and channel attenuation α , and can be expressed in terms of the real and imaginary parts of $\chi^{(1)}$ with,

$$n = 1 + \frac{1}{2} \text{Re}[\chi^{(1)}], \quad \alpha = \frac{\omega}{nc} \text{Im}[\chi^{(1)}], \quad (2.26)$$

respectively. Considering terms of the nonlinear polarisation, the susceptibility tensors of even order vanish in a media possessing an inversion symmetry at the molecular level.

In silica glass waveguides, commonly used in practice, the second order nonlinear susceptibility $\chi^{(2)}$ (and higher order even order terms) have negligible amplitude and may be neglected. Therefore, the lowest order nonlinear effects found in silica glass waveguides originate from the third order term (Kerr nonlinearity) [1, 2]. Here, the Kerr nonlinear term represent the only significant nonlinear contribution, and is responsible for various nonlinear optical phenomena, including self-focusing, self- and cross-phase modulation, third harmonic generation, modulation instability and four wave mixing, as we discuss throughout this thesis. Higher order terms of the nonlinear polarisation are increasingly small in contribution and are hence considered negligible, such that, the nonlinear polarisation can be expressed in terms of the third order susceptibility $\chi^{(3)}$ and total electric field \mathcal{E} as [32, 33]

$$\mathcal{P}_{\text{NL}}(\mathbf{x}, t) = \epsilon_0 \int_{-\infty}^t dt' \int_{-\infty}^t dt'' \int_{-\infty}^t dt''' \chi^{(3)}(t-t', t-t'', t-t''') \mathcal{E}(\mathbf{x}, t') \mathcal{E}(\mathbf{x}, t'') \mathcal{E}(\mathbf{x}, t'''). \quad (2.27)$$

Eqs. (2.25) and (2.27) are derived within the electric dipole approximation and assume that the response of the medium is local. If we further assume that the nonlinear response is instantaneous, we achieve a significant simplification to the nonlinear response, where the time dependence of $\chi^{(j)}$ reduces to Kronecker delta functions, such that the polarisation fields become,

$$\mathcal{P}_{\text{L}}(\mathbf{x}, t) = \epsilon_0 \chi^{(1)} \mathcal{E}(\mathbf{x}, t), \quad (2.28)$$

$$\mathcal{P}_{\text{NL}}(\mathbf{x}, t) = \epsilon_0 \chi^{(3)} \mathcal{E}^3(\mathbf{x}, t), \quad (2.29)$$

by which we neglect the contributions from the Raman effect (molecular vibration).

2.4.2 Chromatic dispersion

In general, the interaction of light with the bound electrons of a dielectric medium, such as silica waveguides, is dependant on the optical frequency ω . This phenomenon is characterised by the frequency dependence of the index of refraction $n(\omega)$ of the medium. Since the refractive index varies depending on the frequency, different spectral components travel through the medium at different velocities $c/n(\omega)$. This phenomenon is known as chromatic dispersion. As a consequence, an optical pulse will experience a spectral broadening along the direction of propagation, increasing the FWHM of the pulse. Even in the absence of nonlinear effects, chromatic dispersion plays a critical role in the propagation of optical pulses within waveguides.

In practice, the functional form of the chromatic dispersion is not typically known. Despite this, we may account for the dispersive effects through an expansion of the frequency dependant propagation constant $\beta = n(\omega)\omega/c$ about the driving frequency ω_0 , with,

$$\beta(\omega) = \beta_0 + \beta_1(\omega - \omega_0) + \frac{1}{2}\beta_2(\omega - \omega_0)^2 + \frac{1}{3!}\beta_3(\omega - \omega_0)^3 + \dots \quad (2.30)$$

where

$$\beta_m = \left. \frac{d^m \beta}{d\omega^m} \right|_{\omega=\omega_0} \quad \text{for } m = 0, 1, 2, 3, \dots \quad (2.31)$$

We neglect higher order terms ($m \geq 3$) of the dispersion (2.30) throughout this thesis. This can be done due to our assumption of a quasi-monochromatic driving field. We define the dispersion coefficients as $\beta_1 = n_g/c = (n + \omega dn/d\omega)/c$ for group index n_g and $\beta_2 = d\beta_1/d\omega$ for the group velocity dispersion. The dispersion coefficients β_1, β_2 characterise the propagation of an optical pulse through the medium, which travels at the group velocity $v_g = c/n_g = 1/\beta_1$, while the pulse broadens as dictated by the group velocity dispersion β_2 . Should the sign of the group velocity dispersion be positive $\beta_2 > 0$, high frequency components of the optical pulse will travel slower than low frequency components. This is known as the normal dispersion regime of the medium. Conversely, if $\beta_2 < 0$, high frequency components of the optical pulse will travel faster than low frequency components, in which case, we are operating in the anomalous dispersion regime. The nonlinear effects exhibited by the medium are greatly effected by the sign of the group velocity dispersion. Much research has been performed in the anomalous dispersion regime, but in this thesis, we expand this research by investigating the normal dispersion regime.

2.4.3 Longitudinal waveguide propagation equation

Maxwell's wave equation can be written in terms of the linear and nonlinear atomic polarisations

$$\nabla^2 \mathcal{E}(\mathbf{x}, t) - \frac{1}{c^2} \partial_t^2 \mathcal{E}(\mathbf{x}, t) = \mu_0 \partial_t^2 \mathcal{P}_L(\mathbf{x}, t) + \mu_0 \partial_t^2 \mathcal{P}_{NL}(\mathbf{x}, t), \quad (2.32)$$

where we have used $\nabla \times \nabla \times \mathcal{E} \equiv \nabla(\nabla \cdot \mathcal{E}) - \nabla^2 \mathcal{E} = -\nabla^2 \mathcal{E}$ (since Gauss's law reads $\nabla \cdot \mathcal{E} = 0$ for dielectric mediums) and the linear and nonlinear polarisation fields are given by Eqs. (2.28) and (2.29). We begin our derivation by making the following assumptions. We assume that the light retains its linear polarisation during its propagation along the fibre. The design considerations of the choice are discussed in Section 2.2.3. Later in Chapter 3 and Chapter 6, we relax this assumption and generalise the polarisation to counter rotating orthogonal circular polarisations. Next, we assume that the field is quasi-monochromatic. This corresponds to the assumption that the spectral width $\Delta\omega$ is of the size $\Delta\omega/\omega_0 \ll 1$, which is centred around the driving frequency ω_0 . Then, the nonlinear polarisation \mathcal{P}_{NL} is assumed to be a small perturbation on the linear polarisation \mathcal{P}_L , where in practice, we find that the contribution of the nonlinear term to the refractive index is $< 10^{-6}$ [32]. Finally, we assume operation within the slowly varying field approximation. This limit prescribes that the electric field amplitude $E(\mathbf{x}, t)$ varies along the longitudinal coordinate and time coordinate much more slowly than the carrier wave, with

$$\left| \frac{\partial E}{\partial z} \right| \ll k_0 |E|, \quad \left| \frac{\partial E}{\partial t} \right| \ll \omega_0 |E|, \quad (2.33)$$

where the total electric field for the single frequency ω_0 is given by

$$\mathcal{E}(\mathbf{x}, t) = \frac{1}{2} [E(\mathbf{x}, t) e^{-i\omega_0 t} + c.c.], \quad (2.34)$$

Here we may work with scalar fields due to our assumption of a linear polarised electric field. Similarly we may write the linear and nonlinear polarisations as

$$\mathcal{P}_L(\mathbf{x}, t) = \frac{1}{2}[P_L(\mathbf{x}, t)e^{-i\omega_0 t} + c.c.], \quad \mathcal{P}_{NL}(\mathbf{x}, t) = \frac{1}{2}[P_{NL}(\mathbf{x}, t)e^{-i\omega_0 t} + c.c.]. \quad (2.35)$$

where $P_L(\mathbf{x}, t)$ and $P_{NL}(\mathbf{x}, t)$ are slowly varying amplitudes of the atomic polarisation field.

By inserting (2.34) into (2.29), the nonlinear polarisation may be expressed in terms of the electric field envelope $E(\mathbf{x}, t)$, with

$$\mathcal{P}_{NL}(\mathbf{x}, t) = \frac{1}{8}\epsilon_0\chi^{(3)}\left[3|E(\mathbf{x}, t)|^2E(\mathbf{x}, t)e^{-i\omega_0 t} + E^3(\mathbf{x}, t)e^{-3i\omega_0 t} + c.c.\right]. \quad (2.36)$$

Eq. (2.36) contains terms which oscillate at the driving frequency ω_0 but also at the third harmonic $3\omega_0$. In general, we may neglect the terms of third harmonic generation, which requires specific engineering to achieve phase matching conditions. Hence, only the first term of (2.36) is relevant here and the second term is discarded. The nonlinear atomic polarisation is then

$$P_{NL} \approx \epsilon_0\epsilon_{NL}E(\mathbf{x}, t), \quad \text{where} \quad \epsilon_{NL} = \frac{3}{4}\chi^{(3)}|E(\mathbf{x}, t)|^2 \quad (2.37)$$

is the contribution of the nonlinearity to the dielectric constant.

To continue our derivation, it is useful to switch to the frequency domain. This is not generally possible due to the nonlinear terms of Eq. (2.32). We work around this by assuming ϵ_{NL} is constant during our derivation. This is a reasonable assumption when considering operation within the slowly varying wave approximation and the perturbative nature of the nonlinear polarisation. Transforming to the Fourier domain, the wave equation (2.32) takes the form of the Helmholtz equation

$$\nabla^2 E(\mathbf{x}, \omega - \omega_0) + \epsilon(\omega)k_0^2 E(\mathbf{x}, \omega - \omega_0) = 0, \quad (2.38)$$

where $k_0 = \omega_0/c$ and Fourier transform of the electric field is given by

$$E(\mathbf{x}, \omega - \omega_0) = \int_{-\infty}^{\infty} E(\mathbf{x}, t)e^{i(\omega - \omega_0)t} dt. \quad (2.39)$$

The dielectric constant is then

$$\epsilon(\omega) = 1 + \tilde{\chi}^{(1)}(\omega) + \epsilon_{NL}, \quad (2.40)$$

which is dependant on the intensity of the electric field due to the contributions of the nonlinear polarisation. The dielectric constant may be used to define the refractive index \tilde{n} and absorption coefficient $\tilde{\alpha}$ with $\epsilon = (\tilde{n} + i\tilde{\alpha}/2k_0)^2$. Due to the third order nonlinearity ϵ_{NL} , these parameters are dependant on the field intensity, with

$$\tilde{n} = n + \bar{n}_2|E|^2, \quad \tilde{\alpha} = \alpha + \bar{\alpha}_2|E|^2, \quad (2.41)$$

where the linear refractive index and absorption coefficient are related to the real and

imaginary parts of $\chi^{(1)}$, as seen in Eqs. (2.26), and the nonlinear index coefficient and two photon absorption coefficient are related to the real and imaginary parts of $\chi^{(3)}$, with $\bar{n}_2 = 3\text{Re}[\chi^{(3)}]/8n$, $\bar{\alpha}_2 = 3\omega_0\text{Im}[\chi^{(3)}]/4nc$, respectively. Utilising methods of variable separation, we write the electric field as

$$E(\mathbf{x}, \omega - \omega_0) = F(x, y)A(z, \omega - \omega_0)e^{i\beta_0 z} \quad (2.42)$$

where F is the transverse mode distribution, A is a slowly varying envelope over the longitudinal coordinate and β_0 is a propagation constant we determine later. This amounts to assuming an electric field solution where the components transverse to the direction of propagation, taken to be z , accumulates phase uniformly. This allows us to resolve Eq. (2.38) into two equations with respect to $F(x, y)$ and $A(z, \omega)$,

$$\nabla_{\perp}^2 F(x, y) + [\epsilon(\omega)k_0^2 - \tilde{\beta}^2] F(x, y) = 0 \quad (2.43)$$

$$2i\beta_0\partial_z A(z, \omega) + [\tilde{\beta}^2 - \beta_0^2] A(z, \omega) = 0 \quad (2.44)$$

where $\nabla_{\perp}^2 = \partial_x^2 + \partial_y^2$ and we have neglected terms of the second order derivative $\partial_z^2 A$ as the envelope $A(z, \omega)$ is a slowly varying function of z (hence $\partial_z^2 A \ll \partial_z A$). Here, $A(z, \omega)$ represents the evolution of the pulse envelope along the longitudinal direction, incorporating the effects of dispersion, nonlinearity, and loss, whereas $F(x, y)$ describes the stationary transverse mode profile, determined by the resonator geometry and material properties.

The wavenumber of the fibre modes $\tilde{\beta}$ is determined by solving the eigenvalue equation (2.43). This equation can be solved through methods of first order perturbation theory where we approximate the dielectric constant as

$$\epsilon = (n + \Delta n)^2 \approx n^2 + 2n\Delta n \quad (2.45)$$

for small a perturbation $\Delta n = \bar{n}_2|E|^2 + i\tilde{\alpha}/2k_0$. Then we may replace ϵ with n^2 in Eq. (2.43), from which we can determine the modal distribution $F(x, y)$ and propagation constant β using methods outlined in Section 2.2.2, where we consider a single mode waveguide presenting the fundamental mode. We then reintroduce the small perturbation Δn to Eq. (2.43), where it is found that Δn does not change the modal distribution $F(x, y)$ from the linear case presented in Section 2.2.2, but the propagation constant becomes

$$\tilde{\beta}(\omega) = \beta(\omega) + \Delta\beta(\omega) \quad (2.46)$$

where

$$\Delta\beta = \frac{\omega^2 n(\omega)}{c^2 \beta(\omega)} \frac{\iint_{-\infty}^{\infty} \Delta n(\omega) |F(x, y)|^2 dx dy}{\iint_{-\infty}^{\infty} |F(x, y)|^2 dx dy}. \quad (2.47)$$

With this, we have completed the formal derivation of the propagation equations up to a perturbation \mathcal{P}_{NL} , where Eqs. (2.43) and (2.44) describe the propagation light through the waveguide in the frequency domain.

We now wish to return to the temporal domain to obtain the propagation equation in

terms of $A(z, t)$ through means on the inverse Fourier transform defined as

$$A(z, t) = \frac{1}{2\pi} \int_{-\infty}^{\infty} A(z, \omega - \omega_0) e^{-i(\omega - \omega_0)t} d\omega. \quad (2.48)$$

Firstly, we rewrite Eq. (2.44) as

$$\partial_z A(z, \omega) = i[\tilde{\beta}(\omega) + \Delta\beta(\omega) - \beta_0]A(z, \omega) \quad (2.49)$$

where we have approximated $\tilde{\beta}^2 - \beta_0^2 \approx 2\beta_0(\tilde{\beta} - \beta_0)$ and used the relation Eq. (2.46). As is apparent in Eq. (2.49), different spectral components of the optical pulse accumulate a phase shift as they propagate along the fibre, which is frequency and intensity dependant. We have discussed this phenomenon previously in Section 2.4.2, where we recognise that the wavenumber function $\beta(\omega)$ is rarely known and so it is useful to expand the wavenumber as a Taylor expansion [Eq. (2.30)]. Neglecting cubic and higher order terms in this expansion due to our assumption of a quasi-monochromatic field, the inverse Fourier transform of the propagation constant yields

$$\mathcal{F}^{-1}\left\{[\beta_1(\omega - \omega_0) + i\frac{1}{2}\beta_2(\omega - \omega_0)^2]A(z, \omega - \omega_0)\right\} = i\beta_1\partial_t A(z, t) - \frac{\beta_2}{2}\partial_t^2 A(z, t). \quad (2.50)$$

In a similar fashion, we may perform a Taylor expansion of the perturbation to the wavenumber $\Delta\beta$, with

$$\Delta\beta(\omega) = \Delta\beta_0 + \Delta\beta_1(\omega - \omega_0) + \frac{1}{2}\Delta\beta_2(\omega - \omega_0)^2 + \dots \quad (2.51)$$

where

$$\Delta\beta_m = \left. \frac{d^m \Delta\beta}{d\omega^m} \right|_{\omega=\omega_0} \quad \text{for } m = 0, 1, 2, 3, \dots \quad (2.52)$$

Due to our previous assumption of a quasi-monochromatic field, we may approximate $\Delta\beta(\omega) \approx \Delta\beta_0 = \Delta\beta(\omega_0)$. Hence, by assuming that the modal distribution does not change significant over the pulse bandwidth and with the previous considerations, we perform an inverse Fourier transformation of Eq. (2.49) to obtain

$$\partial_z A(z, t) + \beta_1 \partial_t A(z, t) + \frac{i\beta_2}{2} \partial_t^2 A(z, t) + \frac{\alpha}{2} A(z, t) = i\gamma |A(z, t)|^2 A(z, t). \quad (2.53)$$

Here, we renormalise A such that the optical power is given by $|A|^2$, where we introduce $|A'|^2 = \epsilon_0 n c A_m |A|^2 / 2$ with mode area $A_m = \iint_{-\infty}^{\infty} |F|^2 dx dy$, and we have dropped the prime notation of the field envelope in Eq. (2.53). We define the nonlinear parameter γ as

$$\gamma = \frac{\omega_0 n_2}{c A_{\text{eff}}}, \quad \text{where } n_2 = \frac{2\bar{n}_2}{\epsilon_0 n c}. \quad (2.54)$$

and the effective mode area of the fibre is

$$A_{\text{eff}} = \frac{(\iint_{-\infty}^{\infty} |F(x, y)|^2 dx dy)^2}{\iint_{-\infty}^{\infty} |F(x, y)|^4 dx dy}. \quad (2.55)$$

2.5 Modelling the ring resonator

The coupling conditions outlined in Section 2.3.1, and the propagation equation (2.53) may be used to model the ring resonator system. At the coupling point ($z = 0$), the circulating field at the beginning of the $m + 1$ round trip is related to the previous by the boundary condition

$$E_{m+1}(z = 0, \tau) = \sqrt{T}S + \sqrt{R}e^{i\theta} E_m(z = 0, \tau), \quad \text{for } m = 1, 2, 3, \dots, \quad (2.56)$$

where S is the incident (driving) electric field. The propagation of light over a round trip of the resonator is governed by the nonlinear Schrödinger equation

$$\partial_z A(z, \tau) + i\frac{\beta_2}{2}\partial_\tau^2 A(z, \tau) + \frac{\alpha_i}{2}A(z, \tau) = i\gamma|A(z, \tau)|^2 A(z, \tau), \quad (2.57)$$

where α_i is the intracavity loss and we have performed a transformation to a frame of reference travelling at the group velocity $\tau = t - z/v_g$ on Eq. (2.53). Together, these equations form an infinite dimensional Ikeda map [77] which can be solved through direct numerical integration. As was first shown by Haelterman [26], this Ikeda map can be expressed as a single partial differential equation with periodic boundary conditions. By assuming a high finesse cavity, the losses of the cavity are weak, and the temporal evolution of the electric field is slow compared to the round trip time τ_R . To characterise the slow variations of the field over successive round trips of the cavity, we introduce a new temporal variable

$$\tilde{t} = \kappa t, \quad (2.58)$$

which we call the slow time. This temporal variable governs the field envelopes evolution at the scale of the cavity photon decay rate $\kappa = \alpha/\tau_R$ where $\alpha = (\alpha_i + T)/2$ is the total losses. In comparison, we refer to our longitudinal temporal variable τ as the fast time

$$\tilde{\tau} = \frac{\tau}{t_{\text{disp}}}\sqrt{2\alpha}, \quad (2.59)$$

which governed the evolution of the electric field over a single round trip. τ governs the temporal structure of dispersive patterns within the resonator, and is normalised by their characteristic time scale $t_{\text{disp}} = \sqrt{|L\beta_2|}$, the dispersion time. The introduction of the slow time and fast time temporal variables allows us to utilise a mean field approach to define a purely temporal electric field envelope $A(t, \tau)$ over the round trip time $0 \leq \tau \leq \tau_R$, which evolves in slow time over many round trips of the resonator and possess periodic boundary conditions. As is shown in [26], this culminate in the well celebrated longitudinal Lugiato-Lefever equation (LLE)

$$\partial_t A(t, \tau) = S - (1 + i\theta)A(t, \tau) + i|A(t, \tau)|^2 A(t, \tau) - i\eta\partial_\tau^2 A(t, \tau), \quad (2.60)$$

where $\eta = \pm 1$ is the sign of the group velocity dispersion, and we define the normalised amplitude, input field and detuning as

$$\tilde{A} = A\sqrt{\frac{\gamma L}{\alpha}}, \quad \tilde{S} = S\sqrt{\frac{\gamma LT}{\alpha^3}}, \quad \tilde{\theta} = (\omega_r - \omega)\kappa^{-1}, \quad (2.61)$$

respectively, where ω_r is the nearest resonance frequency of the resonator to the driving frequency, and we have dropped the ‘ \sim ’ for notational clarity in Eq. (2.60).

In this thesis, we consider exclusively high- Q cavities, wherein the electric field amplitude evolves slowly over many round trips. As such, simulating the microresonator system requires the evaluation of a very large number of round trips, necessary to reach stationary state. From a computational perspective, the Ikeda model requires us to compute the evolution over a single cavity round trip [by direction numerical integration of Eq. (2.57)], then implement the boundary condition [Eq. (2.56)] to obtain the initial condition for the next round trip. This is then repeated for the required number of round trips, and will incur a long computational time in the high- Q limit. Conversely, direct integration methods of the LLE (Appendix C.2 and C.3) can be appropriately performed using slow time steps sizes that encompass multiple round trips of the cavity, dramatically speeding up the computational time. All of the models studied in this thesis are of generalised LLE form. In the next section (Section 2.6) we provide a first principles derivation of the LLE.

We may also model the ring resonator in terms of the cavity modes by performing the modal expansion $A(t, \tau) = \sum_{\mu} a_{\mu}(t) \exp(i\mu\bar{\alpha}\tau)$ such that Eq. (2.60) becomes,

$$\partial_t a_{\mu} = \delta_{\mu,0} S - (1 + i\theta_{\mu}) a_{\mu} + \sum_{\mu', \mu'', \mu'''} \delta_{\mu, \mu' - \mu'' + \mu'''} a_{\mu'} a_{\mu''}^* a_{\mu'''}, \quad (2.62)$$

where $\bar{\alpha} = 2\pi/\tau_R$, $a_{\mu}(t)$ is the amplitude of the cavity mode oscillating at frequency $\omega_0 - \eta\mu\bar{\alpha}$ with mode number μ , and $\delta_{i,j}$ is the Kronecker delta used to implement the four wave mixing momentum condition $\mu + \mu'' = \mu' + \mu'''$. Here, we have redefined the detuning as $\theta_{\mu} = \theta - \eta\mu\bar{\alpha}$, which quantifies the deviation of the resonance frequencies from a dispersion-free equidistant frequency grid as a function of the relative mode number μ . This allows us to explicitly model the formation of frequency comb lines through degenerate and non-degenerate four wave mixing with straight-forward inclusion of arbitrary dispersion and linewidth profiles [18, 53, 78].

2.6 The longitudinal Lugiato-Lefever equation

In this section we derive the equations of the ring resonator following the derivation of Castelli et al. [28]. This derivation of the governing equations of the ring resonator is given to rigorously quantify the contributions of physical effects from first principle.

The total electric field can be expressed as

$$\mathcal{E} = \frac{1}{2} \frac{\hbar \sqrt{\gamma_{\perp} \gamma_{\parallel}}}{d} [\tilde{E}(z, t) e^{-i\omega_0 t + ikz} + c.c.] \quad (2.63)$$

where $\tilde{E}(z, t)$ is the normalised dimensionless electric field envelope propagating along

the longitudinal direction z , d is the modulus of the dipole moment and $\gamma_{\parallel}, \gamma_{\perp}$ are the relaxation rates of the atomic polarisation and population difference of the two-level atom system, respectively. As was discussed in Section 2.2.2 and 2.4.3, we assume a modal distribution which does not change contributively over the slow time, such that, we consider only the longitudinal evolution of the electric field. The electric field injected into the cavity can be written as

$$\mathcal{E}_{\text{in}} = \frac{1}{2} \frac{\hbar \sqrt{T \gamma_{\perp} \gamma_{\parallel}}}{d} [\tilde{S} e^{-i\omega_0 t} + c.c.] \quad (2.64)$$

where \tilde{S} is the amplitude of the field, which we take to be continuous wave.

In the low transmission limit, we assume that $T \ll 1, \alpha' L \ll 1$ (define T and L during the description of the ring) and define the bistability parameter

$$C = \frac{\alpha' L}{2T} \quad (2.65)$$

where α' is the coefficient of absorption, and

$$|\delta_0| = \frac{|\omega_c - \omega_0|}{c/L} \ll 1, \quad \text{defining} \quad \theta = \frac{\delta_0}{T}, \quad (2.66)$$

where ω_0 is the frequency of the input field and ω_c is the frequency of the cavity mode nearest to the input field.

In the low transmission limit, the Maxwell-Bloch equations are (Chapter 11 in [33])

$$\partial_t \tilde{E} + \tilde{c} \partial_z \tilde{E} = -\kappa [(1 + i\tilde{\theta}) \tilde{E} - S + 2C \tilde{P}] \quad (2.67a)$$

$$\partial_t \tilde{P} = -\gamma_{\perp} [(1 + i\Delta) \tilde{P} - \tilde{E} D] \quad (2.67b)$$

$$\partial_t D = -\gamma_{\parallel} \left[\frac{1}{2} (\tilde{E} \tilde{P}^* + \tilde{E}^* \tilde{P}) + D - 1 \right] \quad (2.67c)$$

where P and D are proportional to the atomic polarisation and population difference, respectively, and $\Delta = (\omega_a - \omega_0)/\gamma_{\perp}$ is the atomic detuning parameter with ω_a being the atomic Bohr transition frequency of the two-level atoms. $\tilde{c} = c/n_B$ is the speed of light in the medium, assumed to occupy the entire length of the cavity. If we consider the homogeneous stationary solution of Eqs. (2.67), we obtain the well known equation of optical bistability [33]

$$|S|^2 = |\tilde{E}|^2 \left[\left(1 + \frac{2C}{1 + \Delta^2 + |\tilde{E}|^2} \right)^2 + \left(\tilde{\theta} - \frac{2C\Delta}{1 + \Delta^2 + |\tilde{E}|^2} \right)^2 \right]. \quad (2.68)$$

In the dispersive limit, heuristically defined as the limit in which the frequency of the input field is far detuned from the atomic resonance with $|\Delta| \gg 1$ and $|\tilde{E}|^2/\Delta^2 \ll 1$, Eq.

(2.68) can be approximated as

$$|S|^2 = |\tilde{E}|^2 \left[\left(1 + \frac{2C}{\Delta^2} - \frac{2C|\tilde{E}|^2}{\Delta^4} \right)^2 + \left(\theta - \frac{2C}{\Delta^2} - \frac{2C|\tilde{E}|^2}{\Delta^3} \right)^2 \right]. \quad (2.69)$$

By describing the the dispersive limit in terms of the smallness parameter ϵ with

$$\Delta = \mathcal{O}(\epsilon^{-3}), \quad |\tilde{E}|^2, |\tilde{S}|^2 = \mathcal{O}(\epsilon^{-2}), \quad 2C = \mathcal{O}(\epsilon^{-5}), \quad \theta = \tilde{\theta} + \frac{2C}{\Delta} \quad (2.70)$$

with $\tilde{\theta} = \mathcal{O}(1), \theta = \mathcal{O}(\epsilon^{-2})$ we may redefine

$$S = \sqrt{\frac{2C}{|\Delta|^3}} \tilde{S} = \mathcal{O}(1), \quad |E| = \sqrt{\frac{2C}{|\Delta|^3}} |\tilde{E}| = \mathcal{O}(1) \quad (2.71)$$

such that the homogeneous stationary states at order 0 in ϵ is

$$|S|^2 = |E|^2 \left[1 + (\theta - \eta|E|^2)^2 \right] \quad (2.72)$$

where $\eta = -|\Delta|/\Delta$.

We now implement these consideration into the Maxwell-Bloch equations (Eqs. 2.68), to obtain

$$\partial_t E + \tilde{c} \partial_z E = -\kappa \left[(1 + i\theta)E - S + \frac{2C}{\Delta} (P + iE) \right] \quad (2.73a)$$

$$\partial_t P = -\gamma_{\perp} [(1 + i\Delta)P - \Delta ED] \quad (2.73b)$$

$$\partial_t D = -\gamma_{\parallel} \left[\frac{\eta \Delta^2}{4C} (EP^* + E^*P) + D - 1 \right] \quad (2.73c)$$

where we have introduced the scaled quantities

$$E = \sqrt{\frac{2C}{|\Delta|^3}} \tilde{E}, \quad P = \sqrt{\frac{2C}{|\Delta|^3}} \Delta \tilde{P} \quad (2.74)$$

Since E, P, D are periodic, $E(z = 0, t) = E(z = L, t)$ etc., we can introduce the modal expansions

$$\begin{pmatrix} E(z, t) \\ P(z, t) \\ D(z, t) \end{pmatrix} = \sum_{\mu=-\infty}^{\infty} \begin{pmatrix} f_{\mu}(t) \\ p_{\mu}(t) \\ d_{\mu}(t) \end{pmatrix} e^{-\alpha_{\mu}(t-z/\tilde{c})} \quad (2.75)$$

where $d_{-\mu}^* = d_{\mu}$ and the free spectral range is $\alpha_{\mu} = 2\pi\mu\tilde{c}/L$. Performing a modal expansion

of Eq. (2.73) we may express the μ 'th modal amplitude as

$$\frac{df_\mu}{dt} = -\kappa \left[(1 + i\theta)f_\mu - S\delta_{\mu,0} + \frac{2C}{\Delta}(p_\mu + if_\mu) \right] \quad (2.76a)$$

$$\frac{dp_\mu}{dt} = -\gamma_\perp \left[(1 + i\Delta_\mu)p_\mu - \Delta \sum_{\mu'} f_{\mu-\mu'} d_{\mu'} \right] \quad (2.76b)$$

$$\frac{dd_\mu}{dt} = \gamma_\parallel \left[\frac{\eta\Delta^2}{4C} \sum_{\mu'} (f_{-\mu'} p_{\mu-\mu'}^* + f_{\mu'}^* p_{\mu'-\mu}) + \delta_{\mu,0} \right] - d_\mu(\gamma_\parallel - i\alpha_\mu) \quad (2.76c)$$

where we have defined the atomic detuning at the frequency $\omega_0 + \mu\alpha$

$$\Delta_\mu = \Delta - \frac{\alpha_\mu}{\gamma_\perp} = \frac{\omega_a - (\omega_0 + \alpha_\mu)}{\gamma_\perp}. \quad (2.77)$$

We may determine the effective variation rates of the dynamical variables by completing our definition of the dispersive limit by assuming

$$\frac{|\alpha_\mu|}{\gamma_\perp}, \frac{|\alpha_\mu|}{\gamma_\parallel} = \mathcal{O}(\epsilon^{-2}) \quad (2.78)$$

We find that the variation rate of f_μ is $\mathcal{O}(\kappa\epsilon^{-1})$ and the variation rates for the atomic modal amplitudes are $\gamma_\perp|\Delta| = \mathcal{O}(\gamma_\perp\epsilon^{-3})$ for p_μ , and $\gamma_\parallel\Delta^2/(2C) = \mathcal{O}(\gamma_\parallel\epsilon^{-1})$ for d_0 and $\alpha_\mu\gamma_\parallel = \mathcal{O}(\gamma_\parallel\epsilon^{-2})$ for d_0 for $d_{\mu \neq 0}$. This suggests that the elimination of the atomic variables is justified if $\kappa/\gamma_\parallel \approx \kappa/\gamma_\perp = \mathcal{O}(\epsilon)$, as γ_\parallel and γ_\perp have similar size.

Adiabatic elimination of the atomic variables

We begin by setting the time derivatives of Eqs. (2.76) to zero, to obtain

$$p_\mu = \frac{\Delta}{1 + i\Delta_\mu} \sum_{\mu'} f_{\mu-\mu'} d_{\mu'}, \quad (2.79)$$

$$d_\mu \left(1 - i\frac{\alpha_\mu}{\gamma_\parallel} \right) = \frac{\eta}{2} \frac{\Delta^2}{2C} \sum_{\mu''} (f_{-\mu''}^* p_{\mu-\mu''} + f_{\mu''}^* p_{\mu''-\mu}) + \delta_{\mu,0}. \quad (2.80)$$

Inserting (2.80) into (2.79), we get

$$d_\mu \left(1 - i\frac{\alpha_\mu}{\gamma_\parallel} \right) = \frac{\eta}{2} \frac{\Delta^3}{2C} \sum_{\mu', \mu''} \left(\frac{f_{-\mu''}^* f_{\mu-\mu'-\mu''} d_{\mu'}}{1 + i\Delta_{\mu-\mu''}} + \frac{f_{\mu''}^* f_{\mu-\mu'-\mu''} d_{-\mu'}}{1 - i\Delta_{\mu''-\mu}} \right) + \delta_{\mu,0} \quad (2.81)$$

The terms within the summation may be evaluated as

$$\sum_{\mu',\nu} \left(\frac{f_{\mu'+\nu}^* f_{\mu+\nu} d_{\mu'}}{1+i\Delta_{\mu+\mu'+\nu}} + \frac{f_{\mu'+\nu} f_{\mu+\nu}^* d_{\mu'}}{1-i\Delta_{\nu}} \right), \quad (2.82)$$

$$= \sum_{\mu',\nu} f_{\mu'+\nu}^* f_{\mu+\nu} d_{\mu'} \frac{2-i(\alpha_{\mu}+\alpha_{\mu'})/\gamma_{\perp}}{(1+i\Delta_{\mu+\mu'+\nu})(1-i\Delta_{\nu})}, \quad (2.83)$$

$$\approx \frac{2}{\Delta^2} \sum_{\mu',\nu} f_{\mu'+\nu}^* f_{\mu+\nu} d_{\mu'} \left[1 - i \frac{(\alpha_{\mu} + \alpha_{\mu'})}{2\gamma_{\perp}} \right] \quad (2.84)$$

where in the first line we have replaced μ'' with $-\mu' - \nu$ in the first term, and we have replaced μ'' with $\mu + \nu$ and μ' with $-\mu'$ in the second term. Then in the second line we have used the definition of atomic detuning (2.77) and finally we approximated $\Delta_{\mu+\mu'+\nu}, \Delta_{\nu} \approx \Delta$. We may write (2.81) as

$$d_{\mu} \left(1 - i \frac{\alpha_{\mu}}{\gamma_{\parallel}} \right) = \eta \frac{\Delta}{2C} \sum_{\mu',\nu} f_{\mu'+\nu}^* f_{\mu+\nu} d_{\mu'} \left[1 - i \frac{(\alpha_{\mu} + \alpha_{\mu'})}{2\gamma_{\perp}} \right] + \delta_{\mu,0}. \quad (2.85)$$

The leading terms of Eqs. (2.85) when $\mu = 0$ are d_0 and $\delta_{\mu,0}$ where the nonlinear term is $\mathcal{O}(\epsilon^2)$. For $n \neq 0$, the leading terms of Eqs. (2.85) are the nonlinear terms which are gain of order $\mathcal{O}(\epsilon^2)$. Hence $d_{\mu} = 0$ at order ϵ^0 , such that the solutions up to order ϵ^2 are

$$d_{\mu} = d_0^{(0)} \delta_{\mu,0} + \frac{\Delta}{2C} d_{\mu}^{(2)} + \mathcal{O}(\epsilon^4) \quad (2.86)$$

where $\Delta/2C$ is of order ϵ^2 and $d_{\mu}^{(2)} = \mathcal{O}(1)$. Inserting this solution into Eq. (2.85) we obtain

$$d_0^{(0)} \delta_{\mu,0} + \left(1 - i \frac{\alpha_{\mu}}{\gamma_{\parallel}} \right) \frac{\Delta}{2C} d_{\mu}^{(2)} = \delta_{\mu,0} + \eta \frac{\Delta}{2C} \sum_{\nu} f_{\nu}^* f_{\mu+\nu} d_0^{(0)} \left(1 - i \frac{\alpha_{\mu}}{2\gamma_{\perp}} \right). \quad (2.87)$$

For $\mu = 0$

$$d_0^{(0)} = 1, \quad d_0^{(2)} = \eta \sum_{\nu} |f_{\nu}|^2, \quad (2.88)$$

and for $\mu \neq 0$

$$d_{\mu}^{(2)} = \eta \frac{\gamma_{\parallel}}{2\gamma_{\perp}} \sum_{\nu} f_{\nu}^* f_{\mu+\nu}. \quad (2.89)$$

In the non-radiative limit $\gamma_{\parallel} = 2\gamma_{\perp}$, the second order corrections have the same form. Hence, we may write

$$d_{\mu} = \delta_{\mu,0} + \eta \frac{\Delta}{2C} \sum_{\nu} f_{\nu}^* f_{\mu+\nu}, \quad (2.90)$$

Inserting this expression into Eq. (2.79), we obtain

$$p_{\mu} = \frac{\Delta}{1+i\Delta_n} \left[f_{\mu} + \eta \frac{\Delta}{2C} \sum_{\mu',\mu''} f_{\mu-\mu'} f_{\mu''}^* f_{\mu'+\mu''} \right] \quad (2.91)$$

In Eqs. (2.76a), modal amplitudes p_μ have prefactor $2C/\Delta$ of order ϵ^{-2} . As such we evaluate Eqs. (2.91) to order ϵ^2 . We expand the prefactor of Eqs. (2.91) as

$$\frac{\Delta}{1+i\Delta_\mu} \approx \frac{\Delta}{i\Delta_\mu} = \frac{-i}{1-\alpha_\mu/(\gamma_\perp\Delta)}, \quad (2.92)$$

$$\approx -i\left(1 + \frac{\alpha_\mu}{\gamma_\perp\Delta} + \frac{\alpha_\mu^2}{\gamma_\perp^2\Delta^2}\right), \quad (2.93)$$

and keep the dominant term $-i$ of the nonlinear terms of order ϵ^2 . Hence, we rewrite Eqs. (2.91) as

$$p_\mu = -if_\mu - i\frac{\alpha_\mu}{\gamma_\perp\Delta}f_\mu - i\frac{\alpha_\mu^2}{\gamma_\perp^2\Delta^2}f_\mu - i\eta\frac{\Delta}{2C}\sum_{\mu',\mu''}f_{\mu-\mu'}f_{\mu''}^*f_{\mu'+\mu''} + \mathcal{O}(\epsilon^3) \quad (2.94)$$

such that Eqs. (2.76a) reduces to

$$\frac{df_\mu}{dt} = -\kappa\left[\left(1 + \theta - i\frac{2C}{\Delta}\frac{\alpha_\mu}{\gamma_\perp\Delta} - i\frac{2C}{\Delta}\frac{\alpha_\mu^2}{\gamma_\perp^2\Delta^2}\right)f_\mu - S\delta_{\mu,0} - i\eta\sum_{\mu',\mu''}f_{\mu-\mu'}f_{\mu''}^*f_{\mu'+\mu''}\right]. \quad (2.95)$$

We note the linear and quadratic terms of α_μ in Eq. (2.95) express the first and second order dispersion. We define the modal amplitudes

$$\bar{f}_\mu(t) = f_\mu(t)e^{-i\alpha_\mu\frac{2C}{\Delta}\frac{\kappa}{\gamma_\perp}t} \quad (2.96)$$

such that

$$\frac{d\bar{f}_\mu}{dt} = -\kappa\left[\left(1 + \theta - i\frac{2C}{\Delta}\frac{\alpha_\mu^2}{\gamma_\perp^2\Delta^2}\right)\bar{f}_\mu - S\delta_{\mu,0} - i\eta\sum_{\mu',\mu''}\bar{f}_{\mu-\mu'}\bar{f}_{\mu''}^*\bar{f}_{\mu'+\mu''}\right]. \quad (2.97)$$

The field variable $E(z, t)$ can be written in terms of \bar{f}_μ , with

$$E(z, t) = \bar{f}_\mu(t)e^{-\bar{\alpha}_\mu(t-z/v_g)} \quad (2.98)$$

where the linear dispersive term is used to define the group velocity and redefine the free spectral range

$$v_g = \tilde{c}\left(1 - \frac{2C}{\Delta^2}\frac{\kappa}{\gamma_\perp}\right), \quad \bar{\alpha} = \alpha\left(1 - \frac{2C}{\Delta^2}\frac{\kappa}{\gamma_\perp}\right). \quad (2.99)$$

We note that $v_g \approx \tilde{c}$, and $\bar{\alpha}_\mu \approx \alpha_\mu$ since $(2C/\Delta^2)(\kappa/\gamma_\perp) = \mathcal{O}(\epsilon^2)$. We now perform the usual transformation $\tau = t - z/v_g$ such that the field variable is described by purely temporal variables $F(z, t) \rightarrow F(\tau, t)$, with

$$\partial_t E(\tau, t) = \kappa\left[S - (1+i\theta)E(\tau, t) + i\eta|E(\tau, t)|^2E(\tau, t) + i\frac{2C}{\gamma_\perp^2\Delta^3}\frac{\tilde{c}^2}{v_g^2}\partial_\tau^2 E(\tau, t)\right] \quad (2.100)$$

Introducing the normalised variables

$$\bar{t} = \kappa t, \quad \bar{\tau} = \tau \sqrt{\frac{|\Delta|^3 v_g^2}{2C \bar{c}^2 \gamma_\perp^2}} \quad (2.101)$$

we arrive at the purely temporal Lugiato-Lefever equation

$$\partial_t E(\bar{\tau}, \bar{t}) = S - (1 + i\theta)E(\bar{\tau}, \bar{t}) + i\eta|E(\bar{\tau}, \bar{t})|^2 E(\bar{\tau}, \bar{t}) + i\eta\partial_{\bar{\tau}}^2 E(\bar{\tau}, \bar{t}) \quad (2.102)$$

In this work we consider normal dispersion regime, which we identify as $\eta = -1$. Hence we may write the normally dispersive LLE as

$$\partial_t E(\tau, t) = S - (1 + i\theta)E(\tau, t) + i|E(\tau, t)|^2 E(\tau, t) - i\partial_\tau^2 E(\tau, t), \quad (2.103)$$

where we have implemented the normalisation $E \rightarrow E\sqrt{\eta}$, $S \rightarrow S\sqrt{\eta}$ and dropped the bars on $\bar{t}, \bar{\tau}$ for clarity.

2.7 Stationary solutions of the Lugiato-Lefever equation with normal dispersion

The stationary solutions of the LLE can be obtained by solving the ordinary differential equation

$$0 = S - (1 + i\theta)E(\tau) + i|E(\tau)|^2 E(\tau) - i\frac{d^2}{d\tau^2} E(\tau). \quad (2.104)$$

This ordinary differential equation admits solutions that either are homogeneous or in inhomogeneous in fast time consisting of either Turing patterns and local structures (temporal cavity solitons).

2.7.1 Optical bistability of homogeneous solutions

We first consider the homogeneous stationary solutions of the LLE. These solutions are stationary in slow time ($\partial_t E = 0$) and flat in profile ($\partial_\tau^2 E = 0$) over fast time such that Eq. (2.103) may be written as

$$0 = S - (1 + i\theta)E + i|E|^2 E \quad (2.105)$$

Multiplying Eq.(2.105) with its complex conjugate, we obtain the well known cubic equation of optical bistability [as we derived earlier in Eq. (2.72)]

$$P = H^3 - 2\theta H^2 + (\theta^2 + 1)H \quad (2.106)$$

with respect to the power of the interactivity field $H = |E_0|^2$ and the input power $P = S^2$, where we assume S is real. The real, $\text{Re}(E) = U_0$, and imaginary, $\text{Im}(E) = V_0$, components of the HSSs are then

$$U_0 = \frac{S}{1 + (H - \theta)^2}, \quad V_0 = \frac{(H - \theta)S}{1 + (H - \theta)^2} \quad (2.107)$$

For $\theta < \sqrt{3}$, Eq. (2.106) is single valued and monostable. For $\theta > \sqrt{3}$, Eq. (2.106) may present one, two or three real solutions simultaneously. HSS of different power intersect at two saddle node bifurcations with locations

$$H_{\pm} = \frac{1}{3}(2\theta \pm \sqrt{\theta^2 - 1}). \quad (2.108)$$

Here, a saddle node bifurcation refers to the point in parameter space in which two stationary solutions (one stable and one unstable) collide and annihilate as a system parameter is varied. The beginning and end of optical bistability is marked by these saddle node bifurcations. Solutions of Eq. (2.106) are plotted in Fig. 2.4 for different parameter values before and after the onset of optical bistability.

To investigate the stability of the HSS, we introduce the perturbations

$$\begin{pmatrix} U(\tau, t) \\ V(\tau, t) \end{pmatrix} = \begin{pmatrix} U_0 \\ V_0 \end{pmatrix} + \epsilon \begin{pmatrix} u \\ v \end{pmatrix} e^{ik\tau + \Omega t}, \quad (2.109)$$

where Ω indicates growth rate of the perturbation of wavenumber k and $|\epsilon| \ll 1$. The corresponding eigenspectrum is then

$$\Omega(k) = \sqrt{1 - Q} \quad (2.110)$$

where

$$Q = 1 - 4H\theta + 3H^2 + \theta^2 + 2(2H - \theta)k^2 + k^4 \quad (2.111)$$

From Eq. (2.110), the instability condition $\text{Re}(\Omega) > 0$ is achieved when $Q < 0$. If one considers perturbation that are flat in profile ($k = 0$), we find that solutions satisfying $\partial P / \partial H < 0$ are unstable. Consequently, when Eq. (2.106) presents three solutions simultaneously, the middle power solution is always unstable, while the high and low power HSS are always stable.

Considering perturbation with fast time component ($k \neq 0$), we expect growth of a perturbation of wavenumber k in the normal dispersion regime for

$$k_-^2 < k^2 < k_+^2, \quad k_{\pm}^2 = \theta - 2H \pm \sqrt{H^2 - 1}. \quad (2.112)$$

From Eq. (2.112), we identify the onset of Turing instability at $H = 1$ where we expect the generation of a Turing pattern of wavenumber $k^2 = \theta - 2$. As such, for $\theta < \sqrt{3}$, the single HSS is always stable. For $\sqrt{3} < \theta < 2$, the high and low power HSSs are stable, while the middle power HSS is always unstable. For $\theta > 2$, the low power HSS becomes unstable to the formation of Turing patterns, while the middle solution is always unstable and the high power solution is always stable.

Turing patterns occupy the full fast time domain and as such we must account for the boundary conditions of the ring resonator. The number of Turing rolls over the fast time longitudinal coordinate has integer value μ , such that only patterns of discrete wavenumbers $k_{\mu}^2 = (2\pi\mu/\tau_R)^2$ may form. With the perturbation of (2.109), we consider the formation of a pattern with a single frequency component. In general, the formation of any pattern within the ring can be investigated by considering a perturbation composed

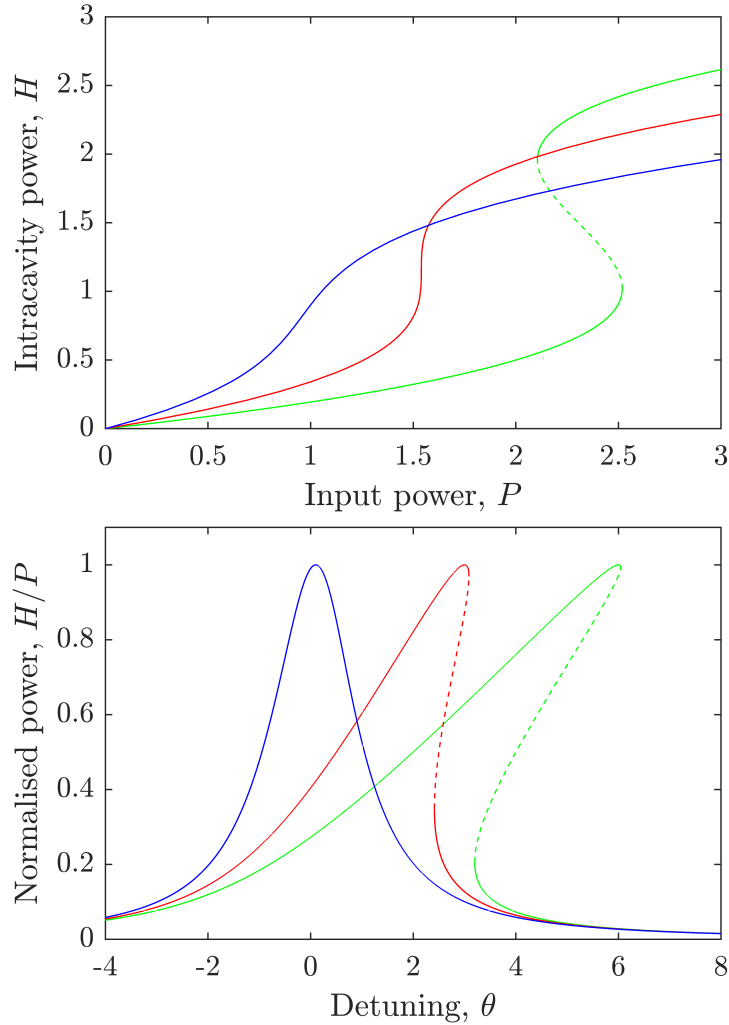


Figure 2.4: (a) The homogeneous stationary solutions of the Lugiato-Lefever equation; (blue) before the onset of optical bistability $\theta = \sqrt{3} - 1/2$, (red) at the critical value of detuning $\theta = \sqrt{3}$, (green) after the onset of optical bistability $\theta = \sqrt{3} + 1/2$. (b) A plot of the resonances for input powers (blue) $P = 0.1$, (red) $P = 3$, (green) $P = 6$. This demonstrates the increasing tilt of the peak of the resonance for increasing input power. In each case, dashed lines indicate unstable states, whereas solid lines indicate stable states.

of the superposition of the frequency components of the ring resonator, with

$$\begin{pmatrix} U(\tau, t) \\ V(\tau, t) \end{pmatrix} = \begin{pmatrix} U_0 \\ V_0 \end{pmatrix} + \epsilon \sum_{\mu} \begin{pmatrix} u_{\mu} \\ v_{\mu} \end{pmatrix} e^{ik_{\mu}\tau + \Omega t}. \quad (2.113)$$

The growth/decay rate of each frequency component is given by Eq. (2.110), such that, frequency components within the interval $k_{\mu}^- < k_{\mu}^2 < k_{\mu}^+$ [given by (2.112)] possess a positive real part of the eigenvalue $\text{Re}(\Omega(k_{\mu})) > 0$ and grow in amplitude, where the resulting pattern will be dominated by the critical mode $k_{\mu,c}$ possessing the largest eigenvalue. Consequently, resonators of longer round trip time are more susceptible to Turing pattern formation as the frequency components have narrower spacing, which are more likely or guaranteed to fall within the interval of (2.112).

2.7.2 The existence and stability of exponentially localised solutions

In this section we review the various exponentially localised stationary solutions of the LLE. Such solution approach fixed points [HSSs (2.107)] of the LLE as $\tau \rightarrow \pm\infty$. We begin by writing Eq. (2.104) as the dynamical system

$$\begin{aligned} \frac{dU}{d\tau} &= \tilde{U}, & \frac{dV}{d\tau} &= \tilde{V} \\ \frac{d\tilde{U}}{d\tau} &= U^3 + UV^2 - \theta U - V \\ \frac{d\tilde{V}}{d\tau} &= V^3 + VU^2 - \theta V + U - S \end{aligned} \quad (2.114)$$

with respect to the fast time variable. We consider the solutions of Eqs. (2.114) to evolve in fast time over the domain $-\infty < \tau < \infty$ and introduce the following terminology inspired by [35, 56, 79–84]. Spatially localised structures of Eqs. (2.114) correspond to homoclinic orbits, which refers to a trajectory that connects a fixed point of Eqs. (2.114) to itself. The fixed points of Eqs. (2.114) are obtained by setting $d\tilde{U}/d\tau = d\tilde{V}/d\tau = dU/d\tau = dV/d\tau = 0$ and correspond to the HSSs derived earlier (2.107). We also consider the heteroclinic orbits of Eqs. (2.114). These trajectories connects one fixed point to another, where due to the periodic boundary conditions of the LLEs, heteroclinic orbits present as an oppositely oriented pair over the cavity round trip. We refer to a well separated (noninteracting) pair of heteroclinic orbits as a heteroclinic cycle.

We now perform a linearisation about the fixed points of Eqs. (2.114) to obtain the corresponding Jacobian matrix

$$J = \begin{pmatrix} 0 & 0 & 1 & 0 \\ 0 & 0 & 0 & 1 \\ V^2 + 3U^2 - \theta & -1 + 2UV & 0 & 0 \\ 1 + 2UV & U^2 + 3V^2 - \theta & 0 & 0 \end{pmatrix}_{(U_0, V_0)} \quad (2.115)$$

evaluated at the fixed point U_0, V_0 . This allows us to investigate the stability of the fixed points which govern the approach of trajectories to and from the fixed points. The

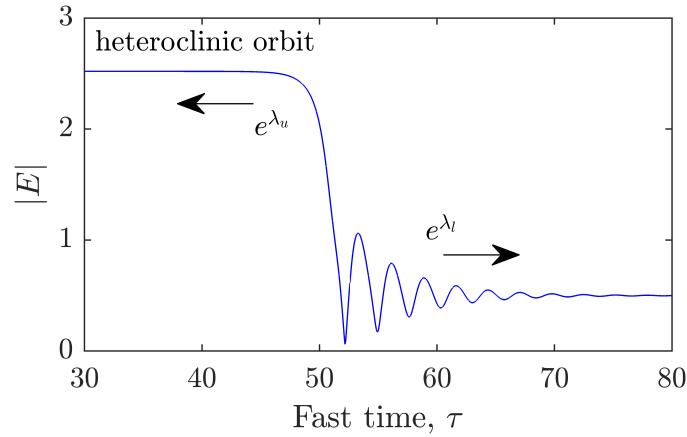


Figure 2.5: Switching front of the LLE, corresponding to a heteroclinic orbit which connect two bistable HSSs. The approach to the high HSS has smooth exponential profile, while the approach to the low power HSS presents an exponentially decaying wave train, governed by the leading eigenvalue of (2.110). Due to the periodic boundary conditions of the LLE, switching front solutions present as oppositely oriented pairs over the round trip of the cavity.

eigenspectrum of this Jacobian can be obtained by solving the characteristic equation

$$\lambda^4 - 2(2H_0 - \theta)\lambda^2 + \theta^2 + 3H_0^2 - 4\theta H_0 + 1 = 0, \quad (2.116)$$

where we obtain the eigenvalues

$$\lambda^2 = (2H - \theta) \pm \sqrt{(H^2 - 1)}. \quad (2.117)$$

The characteristic equation is quadratic in λ^2 and as such yields four eigenvalues which present in pairs of equal value with opposite sign if real, or conjugated if complex. The eigenvalues (2.117) present a complex bifurcation structure, where here we restrict ourselves to the eigenvalues which govern the solutions of our interest. The nature of the eigenvalues is primarily related to the term under the square root of Eq. (2.117). We consider regimes of $H_0 > 1$, $H_0 = 1$ and $H_0 < 1$. For $H_0 > 1$ (and the HSS is stable in slow time $\partial P/\partial H > 0$) the eigenvalues are $\lambda_{1,2} = \pm q_1, \lambda_{3,4} = \pm q_2$ if $2H - \theta > 0$, or $\lambda_{1,2} = \pm ik_1, \lambda_{3,4} = \pm ik_2$ if $2H - \theta < 0$. When $H_0 = 1$, the eigenvalues present as either a quartet of real numbers $\lambda_{1,2} = \pm q, \lambda_{3,4} = \pm q$ for $\theta < 2$ or a quartet of imaginary numbers $\lambda_{1,2} = \pm ik, \lambda_{3,4} = \pm ik$ for $\theta > 2$, and $\lambda_{1,2,3,4} = 0$ for $\theta = 0$. For $H_0 < 1$, the eigenvalues present as complex $\lambda_{1,2} = q_1 \pm ik_1, \lambda_{3,4} = q_2 \pm ik_2$.

The transition over $H_0 = 1$ when $\theta > 2$ constitutes a Hamiltonian-Hopf bifurcation of the eigenvalues [82, 85], and indicates the onset of oscillation governed by the complex eigenvalue for trajectories which approach fixed point of power $H_0 < 1$. In Fig. 2.5, we present a typical heteroclinic orbit of Eqs. (2.114) for $\theta > 2$. We can see a smooth exponential decay of the trajectory towards the high power HSS, as governed by the eigenvalue for $H > 1$. At the approach to the low power HSS, we can see exponentially decaying

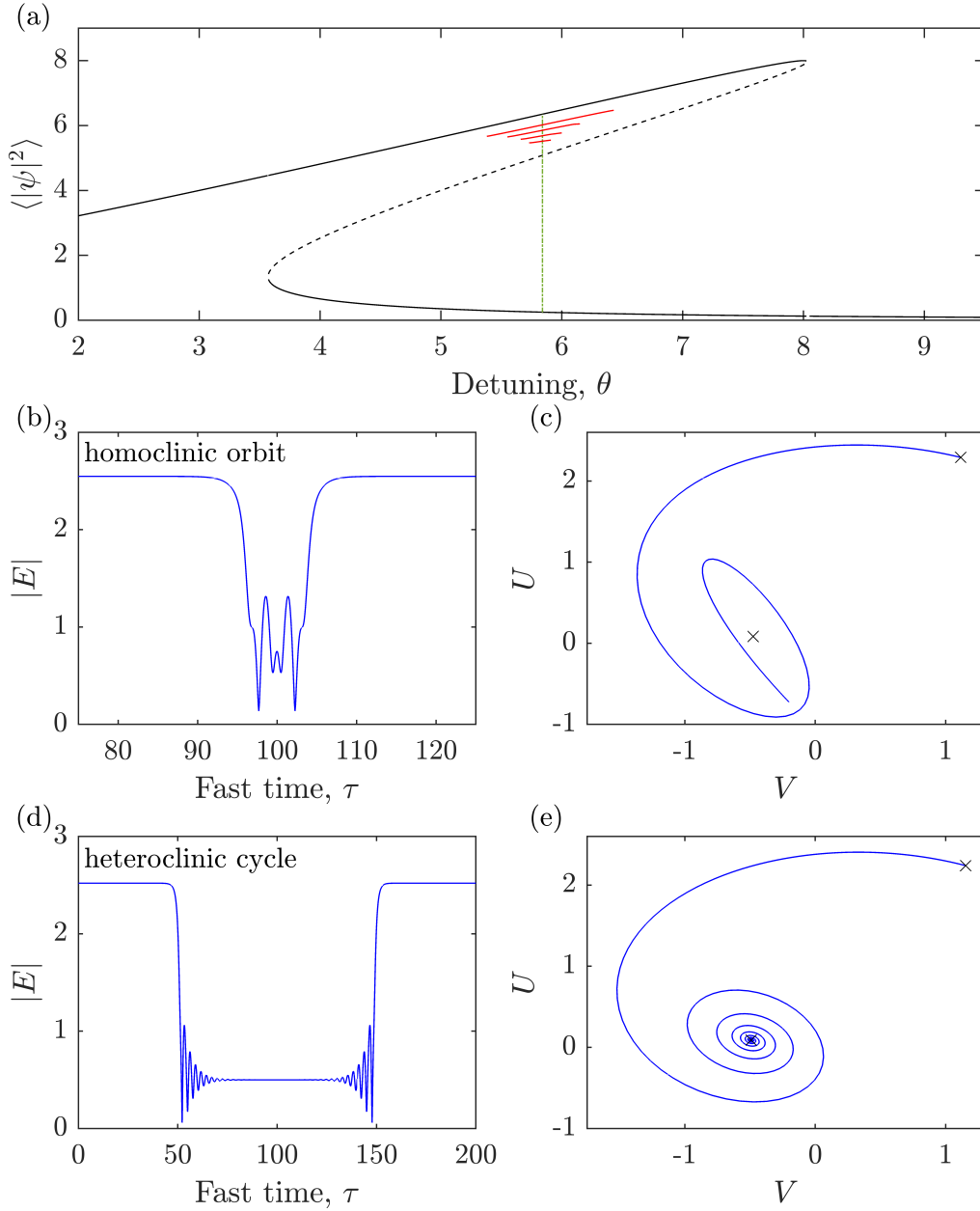


Figure 2.6: (a) Homogeneous stationary solutions (black curve), stable dark cavity solitons (red curves), and stationary heteroclinic cycles (green line, assumes noninteracting switching fronts) plotted as their average power for $S = 2\sqrt{2}$. (b)-(c) Example dark cavity soliton for $\theta = 6$ plotted over the cavity coordinate (b) and the Argand plane (c). (d)-(e) Example heteroclinic cycle at the Maxwell point $\Theta_{MP} \approx 5.83$ [green line in (a)] plotted over the cavity coordinate (d) and the Argand plane (e). High and low power HSSs are shown with x's in (c)-(e).

oscillations of the trajectory, as governed by the eigenvalue for $H > 1$. Heteroclinic orbits are commonly referred to as switching fronts (SF) due to their dynamical nature. In general, SF move with constant velocity, where SF of opposite orientation move with identical speed in opposite directions along the cavity. For a given input power, SF present a single value of detuning at which they are stationary. This parameter value is known as the Maxwell point Θ_{MP} . At this parameter value, well separated SFs form a heteroclinic cycle as shown in Fig. 2.6(d)-(e). In gradient systems the Maxwell point corresponds to the parameter value where both bistable homogeneous states have equal energy. In non-gradient system, such as the LLE, Maxwell points and hysteresis can still be possible even though an expression of the energy cannot be obtained. Although heteroclinic cycles are only present for a single parameter value in the unidirectional ring resonator, they are both prolific and robust in bidirectionally driven ring resonators (as well as unidirectional driven ring resonators with backscattering) as we will demonstrate in Chapter 4. For detuning values $\theta > \Theta_{\text{MP}}$, SFs move as to expand the domain of the low power HSS, whereas for $\theta < \Theta_{\text{MP}}$, SF move as to expand the domain of the high power HSS. As oppositely oriented switching fronts move through the cavity, they will eventually approach each other, and interact through their ‘tails’ at the connection with the HSS. When the tail of the SF exhibits a smooth exponential approach to the HSS, as can be seen in Fig. 2.5 at the connection with the high power HSS, the interaction is purely attractive. This interaction results in the annihilation of the SF pair. When the tail of the SF exhibits an exponentially decaying pattern at the approach to the HSS, as can be seen in Fig. 2.5 at the connection with the low power HSS, the interaction through these oscillation may result in the ‘locking’ of the SFs, which now form a dark cavity soliton (DCS) (homoclinic cycle). An example DCS is shown in 2.106(b)-(c). DCS solutions are distributed along a collapse snaking curve [47] in the vicinity of the Maxwell point, where distinct branches of stable DCSs can be seen in Fig. 2.106(a) (red lines) corresponding to different SF locking distances (soliton width) of the distinct cycles of the oscillatory tails. Red curves begin and end at saddle node bifurcations, which connect stable and unstable soliton branches.

The solitonic solutions shown in Fig. 2.6 were obtained through direct numerical integration of the LLE. We primarily utilised a split-step Fourier integration method as outlined in appendix C.2, and verified the validity of our results through the Crank-Nicholson integration method in appendix C.3. Through suitable perturbation of the high power bistable HSS, a stationary and stable DCS can be induced in simulation, such as is seen in Fig. 2.6(b). By slowly changing the detuning we may determine the extent of the stable DCS solution branch, as is plotted as red lines in Fig. 2.6(a). This is repeated for different sizes of initial perturbation, to yield each of the distinct stable soliton branches.

The soliton shown in Fig. 2.6(b) does not possess a singularity ($E = 0$) at their minimum, as is typical for the LLE. Hence, they may be more precisely referred to as grey solitons. Over the course of this thesis we refer to such solutions as dark solitons, as is common in the surrounding literature.

2.8 Conclusion

In this Chapter, we reviewed the physics of light matter interaction in dispersive Kerr media by deriving the nonlinear Schrödinger equation. We then gave a detailed derivation

of the celebrated Lugiato-Lefever equation, which describes the propagation of light in ring resonators. Finally, we reviews the conditions required for the existence of localised solutions (switching fronts and dark cavity soliton) of the Lugiato-Lefever equation.

Chapter 3

Symmetry Breaking in Unidirectionally Driven Ring Resonators

3.1	Introduction	42
3.2	Modelling orthogonal polarisation field components in the ring resonators	42
3.3	Spontaneous symmetry breaking of homogeneous stationary solutions	45
3.3.1	Instabilities when neglecting group-velocity dispersion	45
3.3.2	Symmetry breaking Turing patterns	46
3.4	Spontaneous symmetry breaking of vectorial dark solitons	49
3.5	Self-crystallisation of temporal cavity solitons	51
3.6	Partial self-crystallisation of temporal cavity solitons	53
3.7	Vectorial dark-bright solitons	57
3.8	Conclusion	60

3.1 Introduction

In this chapter, we consider the unidirectionally driven ring resonator as was described in Chapter 2, but here we will take into account the polarisation properties of the interaction field on the generation of frequency combs. We assume a high finesse ring resonator composed of a Kerr medium, see Fig. 1, in the normal dispersion regime. A linearly polarised driving laser is coupled into the cavity, such that the intracavity fields may be resolved into components of orthogonal polarisations. When considering polarisation components, vectorial temporal cavity solitons display features in addition to those seen for a cavity with a single field, due to the possibility of spontaneous symmetry breaking (SSB) between polarisation components [37]. The SSB of light within Kerr resonators has been demonstrated theoretically and experimentally where the intracavity field is composed of orthogonal polarised components [66–68, 86–91], but also with counterpropagating components [38, 92–97, 100–102], a combination of the two [49, 103, 104], and most recently, between two, or more, coupled resonators [105–109].

We begin in Section 3.2 by introducing the model governing the copropagation of orthogonal field components in a ring resonator, as described by Geddes et al. [36]. In Section 3.3 we review the SSB between homogeneous stationary states (HSS) of orthogonal polarisation while neglecting group-velocity dispersion, and discuss the universality of this phenomenon with respect to the systems of counterpropagating fields in ring resonators and Fabry-Pérot configurations. We then investigate the appearance of Turing instabilities of high power symmetric HSS found in the normal dispersion regime, which results in the formation of Turing patterns of alternating orthogonal polarisation field components. In Sections 3.4, we investigate the polarisation properties of vectorial dark cavity solitons (VDS) in the normal dispersion regime and its effects on the formation of frequency combs. In particular, we present a useful ‘self-crystallisation’ phenomenon in which an initially random distribution of VDSs spontaneously form a regular soliton crystal (RSC) in Section 3.5, which we first reported in [39]. Cavity soliton crystals were originally invented in [16] by using phase gradients to position them into regularly spaced structures. In the case of dispersion, the generation of RSCs has been previously demonstrated through perturbations introduced near avoided mode crossings [40–43], or an external modulation [44] of the field. Here, instead, we present a new self-organisation mechanism of long range interactions between adjacent VDSs via a SSB of Turing patterns capable to controllably generate RSC states. Finally, we characterise the formation of dark-bright vectorial solitons in Section 3.7.

3.2 Modelling orthogonal polarisation field components in the ring resonators

In the previous chapter, we have assumed that the intracavity field has preserved the polarisation properties of the input field, wherein the nonlinear polarisation reduces to the scalar form $P_{\text{NL}} = 3\epsilon_0\chi_{xxxx}^{(3)}|E|^2E$ (see Chapter 2). In general, the single mode fibres we consider contain two orthogonal polarisation modes (as is discussed in Section 2.2.3). Here, we assume that these polarisation modes are degenerate, wherein, the linearly po-

larised driving laser is coupled into the cavity, such that the intracavity field is resolved into components of orthogonal polarisations. As has been shown by Geddes et al. [36], a generalisation to mean field model (the LLE) can be made to allow for a vectorial intracavity electric field in ring and Fabry-Pérot resonators. In particular, the interaction of the two orthogonal polarisations can be described by the third order nonlinear polarisation

$$\mathbf{P}_{\text{NL}} = \varepsilon_0 \chi_{xxxx}^{(3)} (A(\mathbf{E} \cdot \mathbf{E})^* \mathbf{E} + \frac{B}{2} (\mathbf{E} \cdot \mathbf{E}) \mathbf{E}^*), \quad (3.1)$$

where $\chi_{ijkl}^{(3)}$ are the elements of the third order nonlinear susceptibility tensor with

$$A = \frac{\chi_{xxyy}^{(3)} + \chi_{xyxy}^{(3)}}{\chi_{xxxx}^{(3)}}, \quad B = \frac{2\chi_{xyyx}^{(3)}}{\chi_{xxxx}^{(3)}}, \quad (3.2)$$

and we have generalised the interactivity field into orthogonal linear polarisation components $\mathbf{E} = E_x \hat{\mathbf{x}} + E_y \hat{\mathbf{y}}$. The longitudinal LLE can then be generalised to allow for field polarisation by considering Eq. (3.1). The evolution of the electric field is given by

$$\partial_t \mathbf{E} = \mathbf{S} - (1 + i\theta) \mathbf{E} + iA(\mathbf{E} \cdot \mathbf{E}^*) \mathbf{E} + i\frac{B}{2} (\mathbf{E} \cdot \mathbf{E}) \mathbf{E}^* - i\partial_\tau^2 \mathbf{E} \quad (3.3)$$

where $\mathbf{E}(\tau, t)$ is the slowly varying envelope of the vectorial electric field, S is the amplitude of the input field, considered to be real and positive, and θ is the input pump detuning to the near nearest cavity resonance. t is the ‘slow time’ temporal variable describing the evolution over many round trips of the cavity, while τ is the ‘fast time’ longitudinal variable describing the evolution over a single round trip of the cavity in the normal dispersion case with $0 \leq \tau \leq \tau_R$, where τ_R is the resonator round trip. Here all variables and parameters are as defined identically for the LLE seen in Chapter 2.

A linear polarised field may be written as a combination of counter rotating (orthogonal) circularly polarised fields. We define fields of left and right handed circular polarisation as $E_\pm = (E_x \pm iE_y)/\sqrt{2}$ in terms of the linearly polarised fields. In doing so, we may transform Eq. (3.3) into the circularly polarised basis to obtain two coupled LLEs

$$\partial_t E_\pm = S - (1 + i\theta) E_\pm + iA|E_\pm|^2 E_\pm + i(A + B)|E_\mp|^2 E_\pm - i\partial_\tau^2 E_\pm, \quad (3.4)$$

where we have assumed that the input field is linearly polarised along the x direction as $\mathbf{S} = \sqrt{2}S\hat{\mathbf{x}}$.

Eqs. (3.4) is expressed in a general form, whereby setting the values of A and B we may model the interaction of the two field components in different nonlinear mediums [38]. For an isotropic dielectric medium with continuous wave pumping, such as the silica glass resonators we consider in our study, the coupled LLE model takes the form [24, 26, 27, 36, 38, 66, 67]

$$\partial_t E_\pm = S - (1 + i\theta) E_\pm + i|E_\pm|^2 E_\pm + 2i|E_\mp|^2 E_\pm - i\partial_\tau^2 E_\pm. \quad (3.5)$$

after a renormalisation of the amplitude S and the field intensities $|E_\pm|^2$. In this model, we have that the detuning and input field of both polarisation components are equal. As a

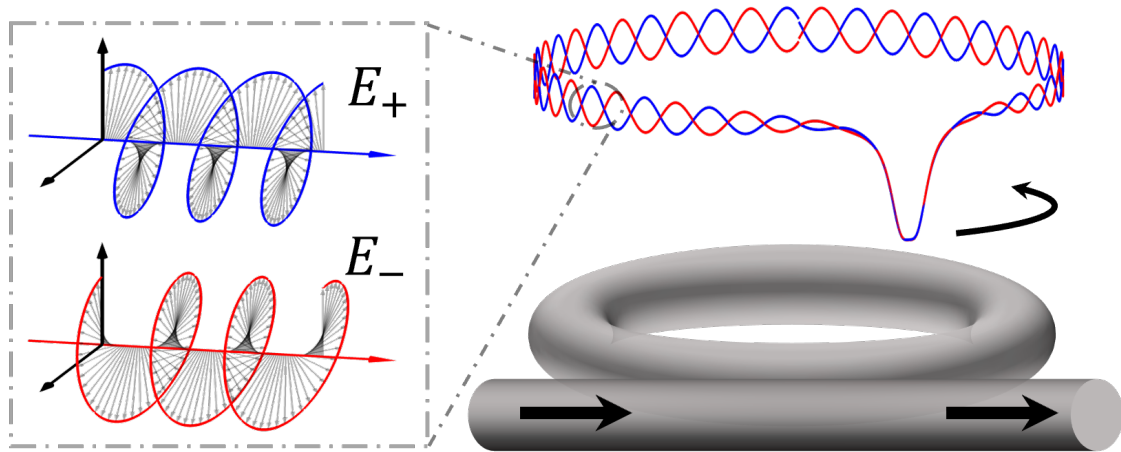


Figure 3.1: A ring resonator composed of a Kerr nonlinear medium. Linearly polarised light is coupled in and out of the resonator via a waveguide. An example intracavity power profile of a vectorial soliton is shown, presenting a Turing pattern of broken symmetry between fields of opposite circular polarisation, visible as out-of-phase oscillations in the background of the dark soliton pulse.

result, Eqs. (3.5) are invariant under the exchange of the $+$ and $-$ indices, the fundamental symmetry of this system. Hence we refer to stationary solutions satisfying $E_+ = E_-$ as symmetric and $E_+ \neq E_-$ as symmetry broken.

To support degenerate counter-rotating polarisation components, we assume that the single mode waveguide which composes the ring resonator possess a rotational symmetry on its cross section, where in general, we assume the resonator is designed to possess minimal birefringence (as discussed in Section 2.2.3). We operate in a regime in which the polarisation mode coupling is dominated by the Kerr effect, which masks the linear coupling due to birefringence. It has been experimentally demonstrated that the linear coupling between polarisation modes can be neglected by driving the two polarisation modes at different carrier frequencies [66–68, 86, 87]. The specific shift in the carrier frequency is chosen to cancel the birefringence of the waveguide, allowing for degenerate polarisation modes, as outlined in [66]. As a result, the model used in this section has been shown to be high accurate in predicting experimental outcomes [67, 86]. Spontaneous symmetry breaking between polarisation modes has so far only be observed in macroscopic resonator systems [66, 67, 86] as obtaining perfect polarisation degeneracy in micro-ring and micro-toroid resonators is extremely challenging due to intrinsic material birefringence and fabrication induced asymmetries. While true polarisation degeneracy is has yet to be achieved, such issues are under investigation with a recent observation of near-pure circularly polarised light in a whispering gallery mode microresonators [110].

Coupled LLE equations (3.5) have been demonstrated to be extremely effective in describing the interaction of orthogonal polarisation modes in fibre ring [66, 67, 86] and Fabry-Pérot [68] resonators. Although integrated optical resonators may have very different TE and TM modes, dual combs of polarised light have been realised in doped-

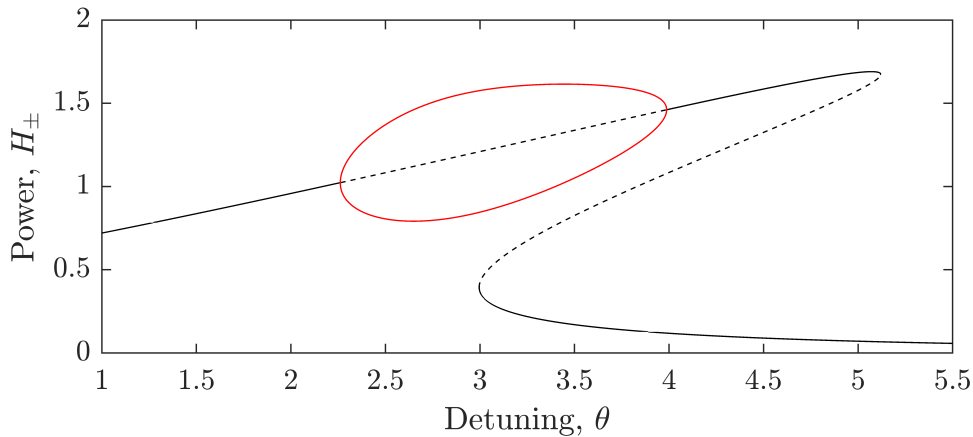


Figure 3.2: Solutions of Eqs. (3.6) corresponding to the symmetric (black curve with $H_+ = H_-$) and symmetry broken (red curve with $H_+ \neq H_-$) homogeneous stationary solutions. Dashed lines (solid lines) correspond to solutions which are unstable (stable) to perturbations neglecting fast time $k^2 = 0$.

silica-glass [111] and silicon nitride [112, 113] microresonators, and successfully described via coupled LLE in [114, 115]. Hence our analysis applies to a wide class of fibre and integrated ring resonators.

3.3 Spontaneous symmetry breaking of homogeneous stationary solutions

3.3.1 Instabilities when neglecting group-velocity dispersion

We first provide a description of the HSSs of Eqs. (3.5). These solutions are obtained from Eqs. (3.5) by setting all derivatives to zero ($\partial_t E_{\pm} = \partial_{\tau}^2 E_{\pm} = 0$) and taking the modulus square to obtain two coupled equations

$$S^2 = H_{\pm}^3 - 2(\theta - 2H_{\mp})H_{\pm}^2 + ((\theta - 2H_{\mp})^2 + 1)H_{\pm}, \quad (3.6)$$

where $H_{\pm} = |E_{0,\pm}|^2$ is the power of the HSS $E_{0,\pm} = U_{0,\pm} + iV_{0,\pm}$, and the real and imaginary components of the HSS are

$$\begin{pmatrix} U_{0,\pm} \\ V_{0,\pm} \end{pmatrix} = \begin{pmatrix} \frac{S}{1+(H_{\pm}+2H_{\mp}-\theta)^2} \\ \frac{(H_{\pm}+2H_{\mp}-\theta)S}{1+(H_{\pm}+2H_{\mp}-\theta)^2} \end{pmatrix}. \quad (3.7)$$

Eq. (3.6) admits solutions that are either linearly polarised (symmetric solutions with $H_+ = H_-$) or not linearly polarised (symmetry broken solutions with $H_+ \neq H_-$) with respect to our orthogonal linear polarisation axis \hat{x}, \hat{y} defined earlier. In Fig. 3.2 we plot example solutions of Eq. (3.6) for $S = 1.03$.

The symmetric HSS can be seen in Fig. 3.2 as the black tilted Lorentzian curve and

are the solutions to the cubic equation

$$S^2 = 9H^3 - 6\theta H^2 + (\theta^2 + 1)H, \quad (3.8)$$

This equation is of the form of the well known optical bistability curve discussed for the single LLE (see Chapter 2), where the high power and low power positive slope branches are stable while the negative slope branch is unstable to homogeneous perturbations (see then linear stability analysis in the next section) with $\lambda = \Omega(k = 0)$). The saddle node bifurcations marking the beginning and end of optical bistability are region correspond to:

$$H_{\text{SN}} = \frac{1}{9}(2\theta \pm \sqrt{\theta^2 - 3}). \quad (3.9)$$

Symmetry broken HSSs arise as a pitchfork bifurcation of the symmetric HSS, as can be seen from the red curve in Fig. 3.2. A pitchfork bifurcation refers to the splitting of a stationary state into multiple stationary states as a parameter is varied. As we move over this bifurcation point, the symmetric solutions change from stable to unstable, yielding to a symmetry broken solution of counter rotating circularly polarised field components of unequal power. We refer to this as a supercritical pitchfork bifurcation. This is an example of a polarisation induced spontaneous symmetry breaking of the linearly polarised field. The symmetry broken solutions end with a reverse pitchfork bifurcation restoring the stability of the symmetric solution. SSB pitchfork bifurcations are located at

$$H_{\text{SSB}} = \frac{1}{3}(2\theta \pm \sqrt{\theta^2 - 3}) \quad (3.10)$$

such that for the full domain between these two bifurcation, the symmetric solution is unstable. [38,96,116]

This sudden change in the stability of the linearly polarised solution as the detuning is increased is an example of a spontaneous symmetry breaking bifurcation. In general, SSB refers to a phenomenon in which two or more equal (symmetric) properties of a system suddenly become unequal (symmetry broken) for a small change in control parameter. The SSB of light within Kerr resonators has been demonstrated theoretically and experimentally where the intracavity field is composed of orthogonal polarised components [38,66–68,86–91] where Eqs. (3.5) have undergone extensive investigation in the absence of fast time effects. It is important to note the mathematical equivalence of this analysis with other systems discussed in the thesis, as these results hold true not only for orthogonal polarisations in ring resonators but also counterpropagating fields in ring resonators [38,96,117], and Fabry-Perot resonators with orthogonal polarisations [36,103]. This universality is conditional on the fact that we neglect group-velocity dispersion in these instances. SSB is possible in these system due to the nonlinearly induced nonreciprocity between the field components introduced by the self- and cross- phase modulation [38].

3.3.2 Symmetry breaking Turing patterns

In Fig. 3.3(a) we plot solutions of Eq. (3.6) for $S = 1.01, \tau_R = 150$ when scanning the detuning θ by changing the frequency of the input laser. For this value of S there are

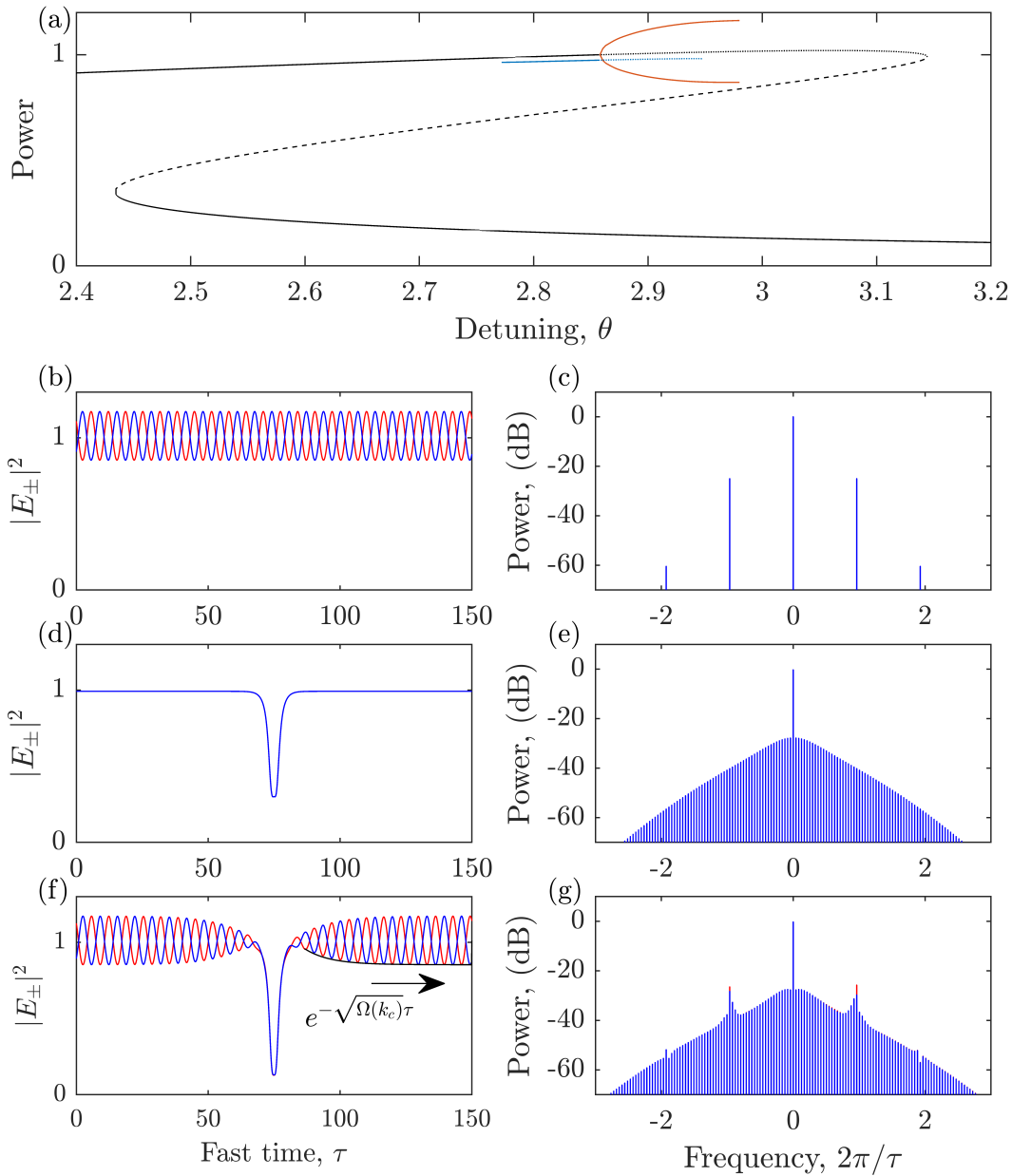


Figure 3.3: Solutions of Eqs. (3.5) for $S = 1.01$, $\tau_R = 150$. (a) Stable (solid black curves) and unstable (broken black curves) symmetric homogeneous solutions, and stable (solid blue curves) and unstable (broken blue curves) symmetric single dark soliton solutions plotted as their average power. The maximum and minimum power of a stable symmetry broken Turing pattern are also shown, in red. (b) Turing pattern of alternating polarisation for $\theta = 2.94$ and (c) the corresponding frequency comb. (d) Power profile of symmetric dark soliton solutions for $\theta = 2.8$ and (e) the corresponding frequency comb. (f) Power profile of symmetry broken dark soliton solutions for $\theta = 2.94$ and (g) the corresponding frequency comb. The black curve in (f) outlines the envelope of the Turing pattern $\propto \exp(-\sqrt{\Omega(k_c)}\tau)$ as it approaches the vectorial dark soliton.

only symmetric HSS ($H_+ = H_-$) which are plotted as the black curve. In the parameter region of our interest there are no symmetry broken HSS solutions. The symmetric HSS form a tilted Lorentzian curve, where stable solutions are plotted with solid lines and and unstable solutions as broken lines.

Of key importance is a Turing instability due to a SSB bifurcation of the high power bistable symmetric HSS typical of regimes of normal dispersion, resulting in the formation of a Turing pattern stationary states formed of alternating orthogonal polarisations. As was first described by Alan Turing in his seminal works on chemical morphogenesis [118], Turing pattern formation, in general, is characterised as the spontaneous formation of patterns from a homogeneous stationary state due to modulation instability in systems governed by partial differential equations. Here, optical Turing patterns in ring resonators is a consequence of the balancing of dispersive and nonlinear effects described previously for soliton formation. The Turing patterns of our study arise in the coupled LLEs (3.5) through the competition of the Kerr self- and cross-phase modulations through which the orthogonal field components interact, and is attributed to the normal dispersion regime. This supercritical bifurcation occurs when increasing the detuning and is plotted as a red curve depicting the maximum and minimum powers of the Turing pattern for $\tau_R = 150$ in Fig. 3.3(a). This instability is due to the field interaction through the local self- and cross-phase modulation and hence are not observed on the high power HSS of a single LLE [35, 79]. The Turing instability can be characterised by considering perturbations on the HSS $E_{\pm}(\tau, t) = E_{0,\pm} + \epsilon_{\pm}$ of the form $\epsilon_{\pm} = \epsilon a_{\pm} e^{ik_{\mu}\tau + \Omega t}$, where k_{μ} is the wavenumber of the perturbation, Ω is the slow time eigenvalue and $|\epsilon| \ll 1$. We note that the boundary conditions of the ring resonator impose discrete wavenumbers $k_{\mu} = 2\pi\mu/\tau_R$ corresponding to patterns of μ rolls along the fast time domain. Inserting this perturbation into Eqs. (3.5), we we obtain linearised equations in terms of ϵ_{\pm} ,

$$\begin{aligned} \partial_t \epsilon_{\pm} = & -(1 + i\theta - ik_{\mu}^2 - 2i|E_{0,\pm}|^2 - 2i|E_{0,\mp}|^2)\epsilon_{\pm} \\ & + iE_{0,\pm}^2 \epsilon_{\pm}^* + 2iE_{0,\pm} E_{0,\mp} \epsilon_{\mp}^* + 2iE_{0,\pm} E_{0,\mp}^* \epsilon_{\mp}. \end{aligned} \quad (3.11)$$

We may then write Eqs. (3.11) in terms of the real and imaginary components of the perturbations ϵ_{\pm} , giving

$$\begin{pmatrix} \text{Re}(\partial_t \epsilon_+) \\ \text{Im}(\partial_t \epsilon_+) \\ \text{Re}(\partial_t \epsilon_-) \\ \text{Im}(\partial_t \epsilon_-) \end{pmatrix} = \begin{pmatrix} -1 & A_1 & 0 & 0 \\ -B_1 & -1 & -C & 0 \\ 0 & 0 & -1 & A_2 \\ -C & 0 & -B_2 & -1 \end{pmatrix} \begin{pmatrix} \text{Re}(\epsilon_+) \\ \text{Im}(\epsilon_+) \\ \text{Re}(\epsilon_-) \\ \text{Im}(\epsilon_-) \end{pmatrix}. \quad (3.12)$$

Here, without loss of generality, we take the homogeneous stationary solutions to be real [96], such that, we obtain the characteristic polynomial

$$[(1 + \Omega)^2 + A_1 B_1][(1 + \Omega)^2 + A_2 B_2] - A_1 A_2 C^2 = 0, \quad (3.13)$$

where

$$\begin{aligned} A_1 &= \theta - k_\mu^2 - H_+ - 2H_-, & B_1 &= \theta - k_\mu^2 - 3H_+ - 2H_-, & C^2 &= 8H_+H_-, \\ A_2 &= \theta - k_\mu^2 - H_+ - 2H_-, & B_2 &= \theta - k_\mu^2 - 3H_+ - 2H_-. \end{aligned}$$

The growth rate of this perturbation is then

$$\Omega(k) = -1 \pm \sqrt{\frac{-A_1B_1 - A_2B_2 \pm Q}{2}}, \quad (3.14a)$$

$$Q = \sqrt{(A_1B_1 - A_2B_2)^2 + 4A_1A_2C^2}. \quad (3.14b)$$

These eigenvalues have a similar form to the linear stability analysis of [38, 96, 116] where dispersion is neglected ($k_0 = 0$), but now with the crucial dependence on k_μ^2 . From these eigenvalues we may approximate the Turing wavenumber from the critical wavenumber with largest growth, $\Omega(k_c)$. For example, we find a good agreement between the predicted $k_c \approx 0.96$ (here k_c is approximated from Eq. (3.14) by considering k a continuous variable) and measured $k \approx 1.01$ wavenumber of the Turing pattern shown in Fig. 3.3(b), despite the value of θ being well above the Turing instability threshold. The spectrum of the Turing pattern is shown in Fig. 3.3(c). We see a much larger spacing of the frequency components when compared to the VDS corresponding to the Turing pattern wavenumber.

In the normal dispersion regime, modulation instability of the high power HSS ($H_\pm > 1$) requires that perturbations on the respective polarisation components are symmetry broken, $\epsilon_+(k_\mu) \neq \epsilon_-(k_\mu)$, whereby modal amplitudes of orthogonal polarisations must, by necessity, grow out of phase. This is distinct from the decaying oscillations which form on the low power HSS ($H_\pm < 1$), upon which dark cavity solitons owe their existence. Generally, in phase oscillations present in the normal dispersion regime when $H_\pm < 1$ and may be induced by symmetric perturbations $\epsilon_+(k_\mu) = \epsilon_-(k_\mu)$, where the eigenspectrum (3.14) reduces to the single field linear stability eigenvalues (2.110), under the appropriate renormalisation. As such, Turing pattern instability for $H_\pm > 1$ is not present in single field LLE.

3.4 Spontaneous symmetry breaking of vectorial dark solitons

In the normal dispersion regime, Eqs. (3.5) exhibits VDSs [35]. These solutions are composed of localised switching fronts which connect the high and low power stable HSSs. Oppositely oriented pairs of switching fronts can ‘lock’ due to the interaction of local fast time oscillations close to the lower power HSS and become stationary. This mechanism of soliton formation was first proposed for spatial solitons composed of diffractive switching fronts [119–121], but has been demonstrated longitudinally in the ring resonator with a single field component theoretically [35] (see Chapter 2) and experimentally [19], as well as in Fabry-Pérot configurations [56] (see Chapters 5 and 6).

We first consider symmetric solitons, and note that at symmetry $E_+ = E_- = E$, Eqs. (3.5) reduce to

$$\partial_\tau E = S - (1 + i\theta)E + 3i|E|^2E - i\partial_\tau^2 E. \quad (3.15)$$

This means that under a re-normalisation of fields $E \rightarrow E/\sqrt{3}$, $S \rightarrow S/\sqrt{3}$ the stationary VDS of our system are analogous to those of the LLE discussed in Chapter 2. A branch of symmetric solutions of Eqs. (3.5) containing a single VDS is shown in 3.3(a) as the blue curve (plotted as the average power over a round trip to separate it from the HSS). At this parameter value ($S = 1.01$) symmetric VDSs are stable for values of detuning below the Turing instability, shown in Fig. 3.3(d)-3.3(e). As the detuning is increased, the VDS symmetric solution undergoes a SSB of the homogeneous background from which the soliton hangs. This SSB results in the formation of a Turing pattern of alternating polarisation components and is phenomenologically identical to the SSB of the HSS in the absence of the VDS.

The frequency comb of a symmetry broken VDS is shown in Fig. 3.3(g). It maintains a similar spectral envelope to that of the single symmetric VDS [Fig. 3.3(e)] but now it develops sidebands due to the periodic modulations at the tails. The sideband peaks are reminiscent of those generated by dispersive waves due to higher order dispersion [122]. Here they are achieved with second order dispersion only and the contribution of the Turing pattern modulation. The power and separation of these peaks correspond to the spectral lines of the frequency comb of the Turing pattern, Fig. 3.3(c).

An important property of symmetry broken VDSs is that the amplitude of the Turing pattern envelope decays as $[\exp(-\sqrt{\Omega(k_c)}\tau)]$, with $\Omega(k_c)$ given by Eq. (3.14), from the place where the VDS tails are close to the unstable symmetric HSS to a saturation value of the modulated intensity. The black line in Fig. 3.3(f) shows this exponential decay matching the Turing pattern minima at the tails of the VDS. We have verified that such agreement persists for a wide range of detunings and input pumps where symmetry broken VDS are found.

We can compare this Turing instability found on the high power HSS with that found on the low power HSS (responsible for soliton formation) by considering the fast time stability. To do so we introduce a perturbation on the longitudinal coordinate $U_{\pm} = U_0 + \epsilon u_{\pm}(\zeta)$, $V_{\pm} = V_0 + \epsilon v_{\pm}(\zeta)$ to Eqs. (3.5) about a symmetric HSS, where we use the ansatz $u_{\pm} = a_{\pm}e^{\lambda\zeta}$, $v_{\pm} = b_{\pm}e^{\lambda\zeta}$. We may replace ik with the complex λ in Eq. (3.14) and set

$$\Omega(-i\lambda) = 0 \quad (3.16)$$

to obtain the fast time eigenvalues,

$$\lambda^2 = [A + B + C \pm \sqrt{(A - B - C)^2 - 4}]/2, \quad (3.17a)$$

$$\lambda^2 = [A + B - C \pm \sqrt{(A - B + C)^2 - 4}]/2, \quad (3.17b)$$

where $A = 3H - \theta$, $B = 5H - \theta$, $C = 4H$. In Fig. 3.3(a) we see a supercritical SSB bifurcation of the high power HSS (at $\theta_c \approx 2.86$) resulting in the formation of a Turing pattern. At this bifurcation point, Eq. (3.17) gives four real $\lambda_{1,2} = \pm q_1$, $\lambda_{3,4} = \pm q_2$ and four degenerate imaginary $\lambda_{1,2} = \lambda_{3,4} = \pm ik_c$ eigenvalues. The wavenumber k_c of the imaginary eigenvalues correspond exactly with the slow time instability eigenvalue at the bifurcation. For detuning larger than the bifurcation point, $\theta > \theta_c$, Eq. 3.17 gives four real $\lambda_{1,2} = \pm q_1$, $\lambda_{3,4} = \pm q_2$ and four imaginary $\lambda_{1,2} = \pm ik_1$, $\lambda_{3,4} = \pm ik_2$ eigenvalues. Here, the imaginary eigenvalues correspond to the maximum and minimum unstable wavenumbers

of the slow time linear stability analysis. Hence they form the bounds of the range of unstable wavenumbers $k_1 < k < k_2$ for the Turing instability in the slow time. For $\theta < \theta_c$ smaller than the bifurcation point, Eq. (3.17) gives four real $\lambda_{1,2} = \pm q_1, \lambda_{3,4} = \pm q_2$ and four complex eigenvalues $\lambda_{1,2,3,4} = \pm q \pm ik$ eigenvalues. The Turing bifurcation on the high power HSS presents as a Hamiltonian-Hopf bifurcation of eigenvalues (3.17b). This bifurcation occurs with opposite direction with respect to the formation of Turing patterns that are seen on the low power HSS. Here the leading eigenvalues [Eq. (3.17b)] are purely imaginary in the domain of Turing instability, which suggests the HSS is unstable in the slow time (slow time modulation instability).

3.5 Self-crystallisation of temporal cavity solitons

We now consider solutions containing multiple VDSs along the cavity length simultaneously. After the SSB bifurcation, such solutions form Turing patterns in the intervals between VDSs. As the Turing patterns grow, adjacent VDSs are ‘pushed’ apart until an equilibrium of the pattern’s amplitude is reached on both sides of the VDS, as shown in Fig. 3.4. The formation of the symmetry broken Turing pattern is hence found to introduce long range repulsive interaction between adjacent VDSs. Note that the symmetric VDSs do not exhibit any long range interactions and the VDSs remain stationary at arbitrary separation distances (larger than the VDS size).

In Fig. 3.4(a) we start with three symmetric VDSs randomly distributed along the round trip for $S = 1.02$, $\theta = 2.94$ and $\tau_R = 150$. For these parameter values, the homogeneous background is unstable to the formation of Turing pattern of alternating polarisations. The maximum amplitude reached by the Turing patterns in the intervals separating the VDSs depends on the separation of adjacent VDSs. As the pattern amplitude grows, the VDSs are ‘pushed’ along the resonator until an equilibrium configuration of the pattern is reached on either side of each VDS. The slow time evolution of the three VDSs is shown in Fig. 3.4(c) through direct numerical integration of Eqs. (3.5). Here it can be seen that the VDSs move such as to spread out along the cavity coordinate. This evolution ends in the stationary state shown in Fig. 3.4(d) composed of VDSs located equidistantly on the round trip of the cavity and separated by Turing patterns with equal amplitude, i.e. perfectly regular soliton crystal (RSC).

The formation of such a RSC induced by SSB evolves spontaneously from the initial condition of three randomly positioned dark solitons. The organisation process corresponds to self-crystallisation from a random distribution of VDSs. The RSCs of our system are robust to a change in the number of VDS as the repulsive interaction will redistribute VDS to equidistant locations, as long as the new RSC spacing is shorter than twice the characteristic Turing patterns saturation length $\Delta\tau$, defined as the fast time distance where the pattern amplitude reaches its maximum value.

As can be seen in Fig. 3.4(e), the RSC produces a frequency comb with a smooth spectral envelope and a free spectral range three times larger than the frequency comb of the initial condition, Fig. 3.4(b). In general, a RSC composed of N VDSs produces a frequency comb equivalent to a single VDS in a cavity with round trip τ_R/N . The RSCs emulate smaller cavity sizes, such that with increasing soliton number, a frequency comb with enhanced power and greater spacing of the spectral lines is obtained. Due to

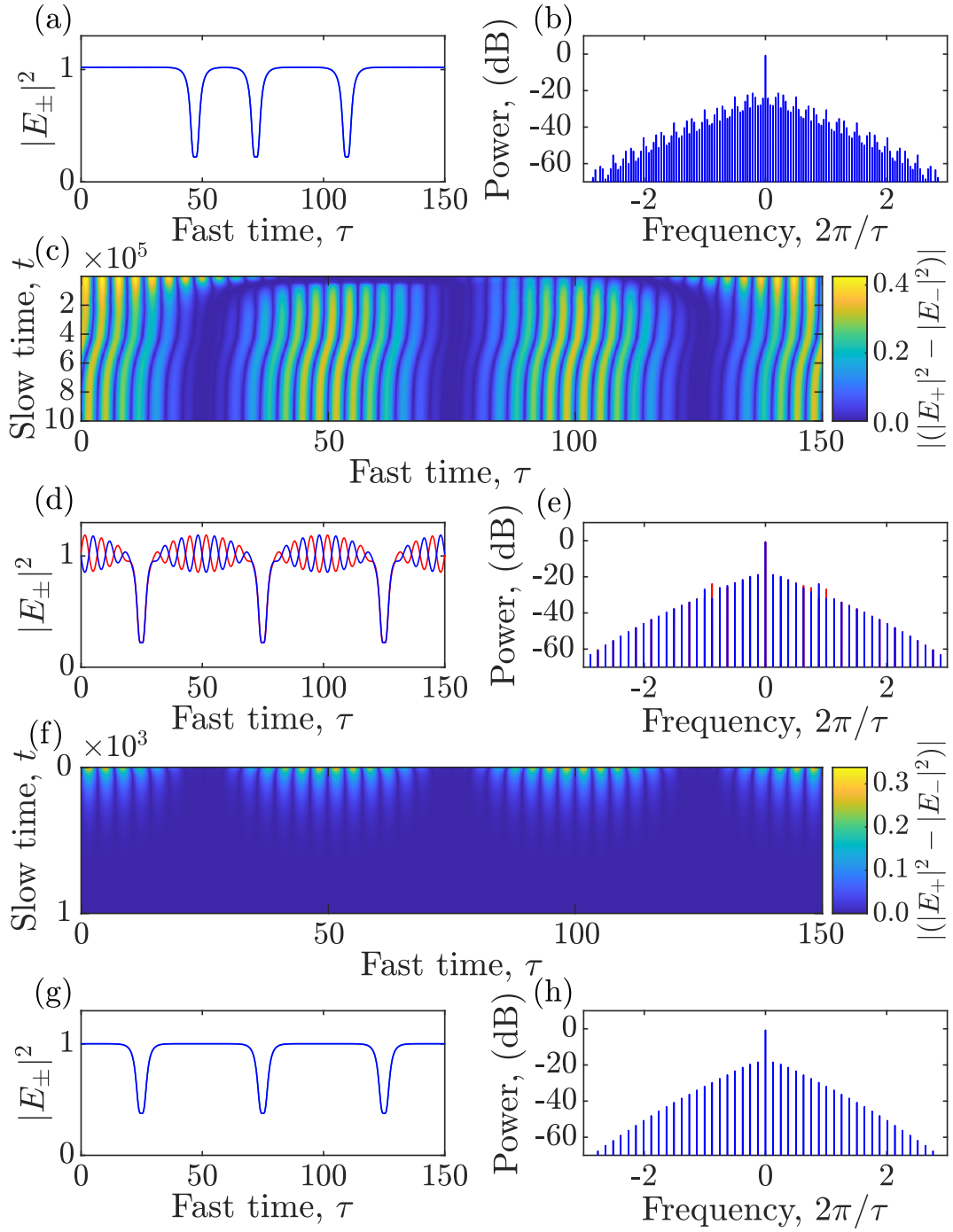


Figure 3.4: (a) Initial condition of three symmetric vectorial dark solitons and corresponding comb spectrum (b). (c) Slow time evolution of the initial condition in (a) for $S = 1.02$, $\theta = 2.91$ demonstrating the growth of SSB Turing patterns, which propel the VDSs through the cavity. (d) Final RSC stationary state and corresponding comb spectrum (e). (f) Slow time evolution after reducing the cavity detuning to $\theta = 2.81$, below the threshold for Turing patterns. (g) Final regular VDS crystal with a uniform background and corresponding comb spectrum (h).

these features, the spontaneous formation of RSC has many potential applications, such as satellite communications [123], photonic radar [124] and radio-frequency filters [125, 126]. Being a self-organised structure, the RSC of our system offer different ways to generate and control RSCs than those demonstrated in [40, 44]. As was mentioned earlier, regular peaks in the spectral envelope are due to the Turing pattern wavenumber that is required for self-crystallisation. Such peaks can be removed at will after self-crystallisation by changing the control parameters back below the SSB bifurcation, thus leaving a symmetric RSC with no pattern states between the VDS as shown for example in Fig 3.4(f) and (g).

To demonstrate generality and robustness of the self-crystallisation mechanism described above, we show in Fig. 3.5 the asymptotic results of simulations of Eqs. (3.5) for $S = 1.05, \theta = 3$ instead of $S = 1.02, \theta = 2.91$, and for one to six random VDSs in the initial condition obtained below the Turing threshold. These six configurations co-exist and can be smoothly tuned by changes in the detuning θ . A further advantage of our method with respect to other techniques of generating RCSs, is that when adding or removing one of the VDSs through an external perturbation, a crystal with an extra VDS or one less VDS smoothly nucleates via the long range interactions mediated by the Turing patterns, moving between the VDSs crystals are shown in Fig. 3.5(g), (i) and (k). On the right hand side of Fig. 3.5, we display the spectra corresponding to these asymptotic configurations. While periodic self-organised VDSs crystals are shown in (g), (i) and (k) for four, five, and six VDSs, Figs. 3.5(c) and (e) show that self-crystallisation may only happen in a section of the full cavity length as explained in the next section. We note that partial and/or full self-crystallisation has been found within the parameter ranges of $(1.01 \leq S \leq 1.06)$, $(2.86 \leq \theta \leq 3)$ and $(150 \leq \tau_R \leq 300)$ with up to six VDSs coexisting with Turing patterns. This corresponds to tens of thousands of simulations and demonstrates the robustness, the wide range of occurrence and reproduction of our mechanism of self-crystallization of temporal cavity solitons. Note that self-crystallization is also observed when changing the cross-coupling and the dispersion coefficients here kept fixed to the values of 2 and 1, respectively.

3.6 Partial self-crystallisation of temporal cavity solitons

Even in the case of a small number of VDSs in a long cavity, such as in Fig. 3.5(c) and (e), and Fig. 3.6, VDSs are found to move apart until a saturation of the Turing pattern amplitude is reached in the intervals between them. In Fig. 3.6, five VDSs have undergone SSB, and spread apart until the VDSs become stationary and produced a local RSC via self-crystallisation for $S = 1.04, \theta = 3$, (a)-(b) and for $S = 1.06, \theta = 3$, (c)-(d). The maximum range of the repulsive interaction between VDSs can be investigated using the growth rate, Eq. 3.14, of the critical wavenumber k_c of the Turing pattern away from the VDS. We are able to estimate the a maximum interaction distance $2\Delta\tau \approx -2\ln(0.01|E_{\max}|^2)/\sqrt{\Omega(k_c)}$, where we have assumed the VDS interaction disappears when the Turing amplitude reaches 1% from the maximum amplitude $|E_{\max}|^2$. This predicts a maximum lattice spacing of $2\Delta\tau \approx 37$ for $S = 1.04, \theta = 3$ and $2\Delta\tau \approx 31$ for $S = 1.06, \theta = 3$ compared to the measured values of 40, and 31 from Fig. 3.6, respectively. The interaction distance of VDSs can then be controlled by changing the parameters to alter the growth rate of the Turing patterns. A pair of VDSs will no longer interact should their separation

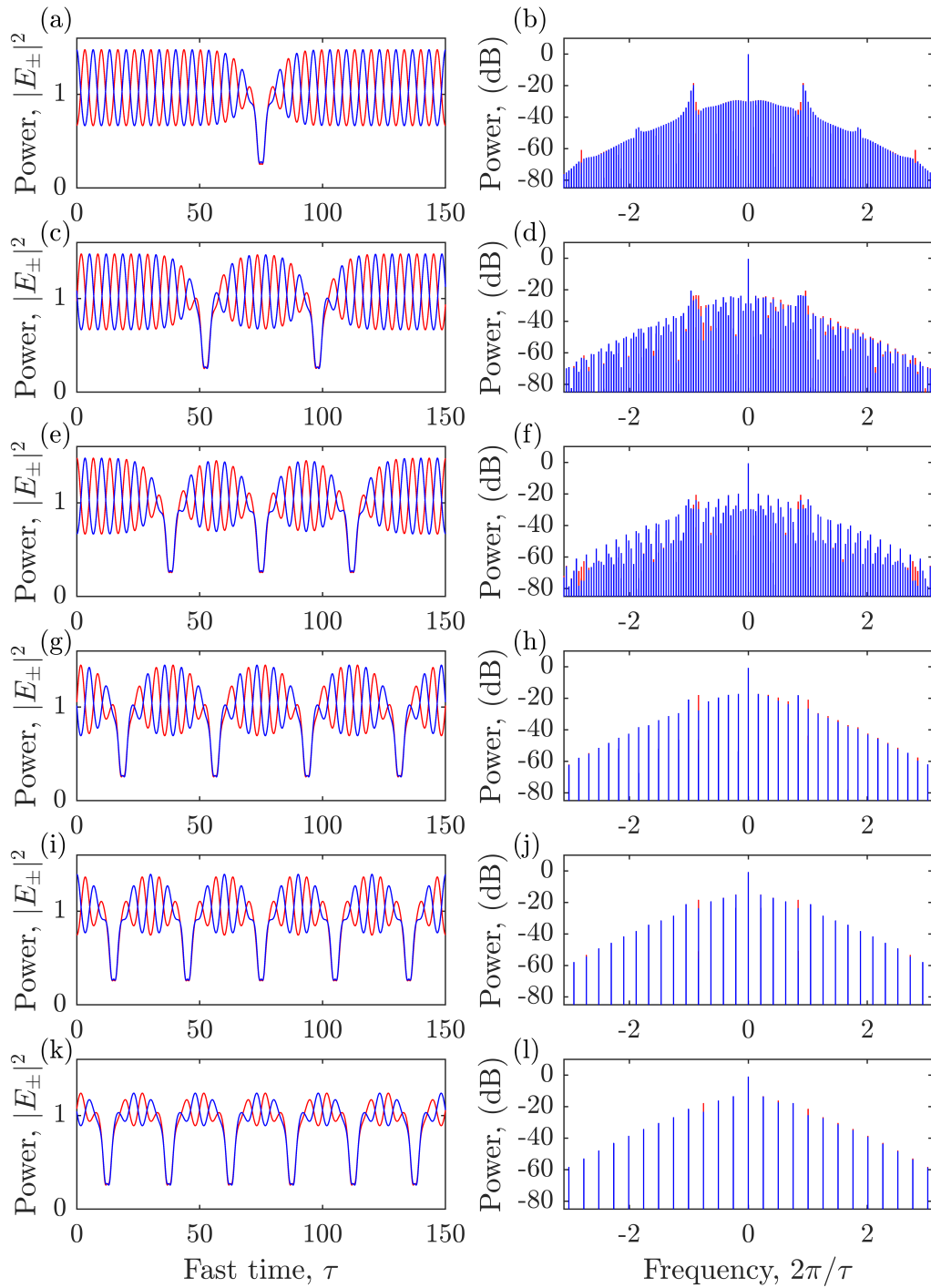


Figure 3.5: A single (a) and five crystal states (c), (e), (g), (i), (k) for $S = 1.05$, $\theta = 3.0$. The initial conditions are randomly distributed VDSs leading to partial soliton crystals with two and three VDSs in (c) and (e), and to soliton crystals of four, five, and six VDSs in (g), (i) and (k), respectively. Panels (b), (d), (f), (h), (j) and (l) show the frequency comb spectra associated with each of the asymptotic VDS states.

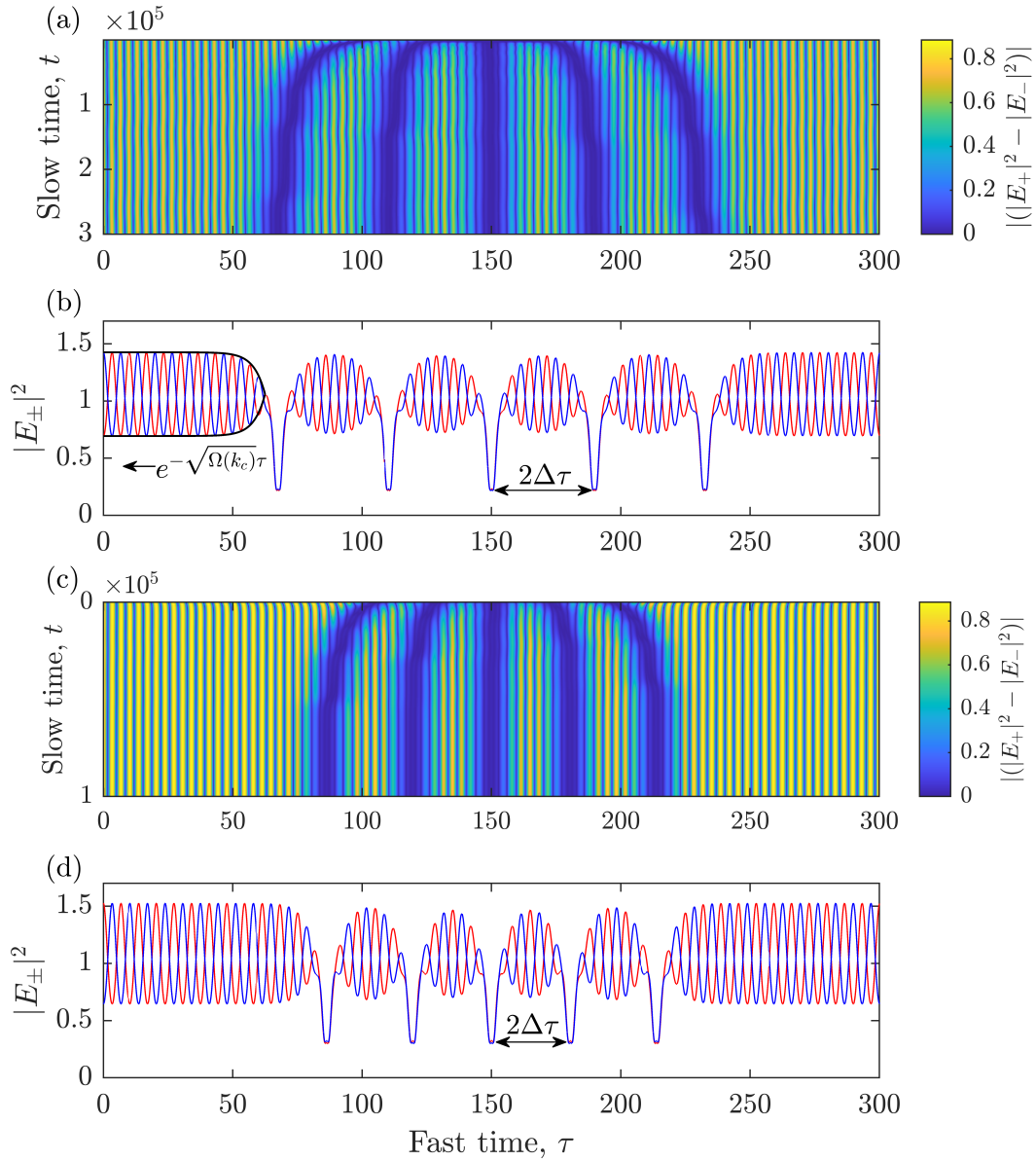


Figure 3.6: Formation (a),(c) and final partial soliton crystals (b),(d) composed of five VDSs for $S = 1.04$, $\theta = 3$ (a)-(b) and $S = 1.06$, $\theta = 3$ (c)-(d). The VDS can move no closer than $2\Delta\tau$ due to the repulsive interactions induced by the Turing pattern. $2\Delta\tau \approx 40$ for (b) and $2\Delta\tau \approx 31$ for (d). The black curve in (b) follows the Turing pattern envelope starting from full saturation towards the VDS.

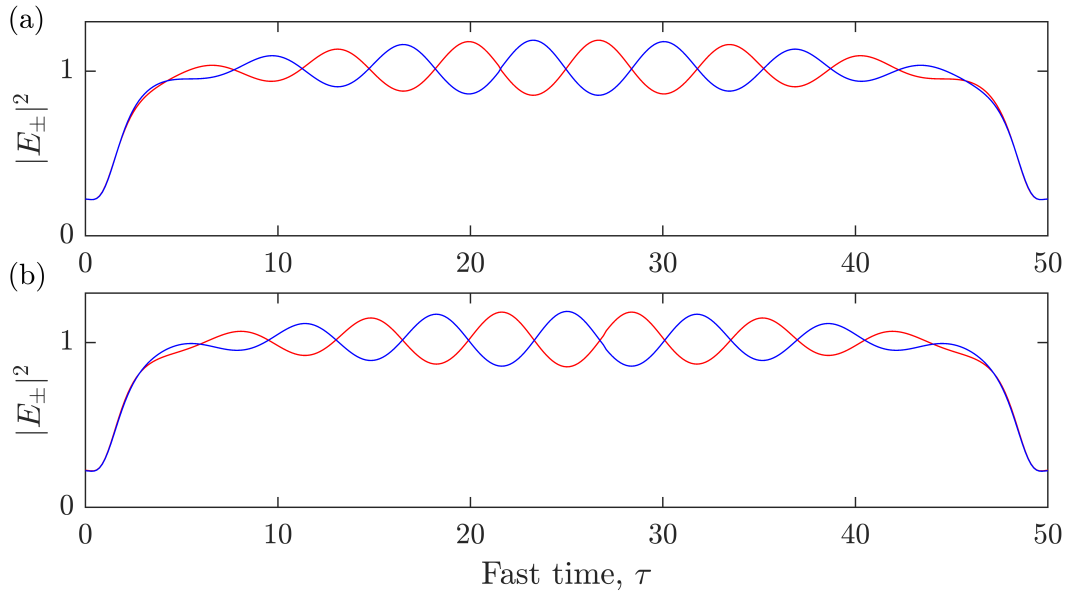


Figure 3.7: (a)-(b) Power profiles of RSC unit cells for $S = 1.02$, $\theta = 2.91$, $\tau_R = 50N$. Two additional unit cells can be obtained by exchanging the fields $E_+ \leftrightarrow E_-$ in both (a) and (b). The unit cells are related by a phase shift in the peaks of the Turing patterns of $\pi/2$.

be greater than $2\Delta\tau$ where the mediating Turing patterns reach saturation. By selecting a suitable cavity length and soliton number N such that $N > \tau_R/2\Delta\tau$ we observe the full self-crystallisation phenomenon as is shown in Fig. 3.4 and in Figs. 3.5(g),(i),(k).

RSCs are composed of a unit cell which is perfectly repeating over the cavity round trip. For example, the RSCs of Fig. 3.4(d) and Figs. 3.5(g), (k) are composed of the unit cell type shown in Fig. 3.7(a) repeated several times over the round trip. The RSCs of Fig. 3.5(i) is composed of a sequence of unit cells of the type shown in Fig. 3.7(b). These two unit cells possess the fast time symmetries $E_{\pm}(-\tau) = E_{\mp}(\tau)$ and $E_{\pm}(-\tau) = E_{\pm}(\tau)$ respectively, and two additional unit cells obtained by exchanging the fields $E_+ \leftrightarrow E_-$ in Fig. 3.7. As such, there are four possible RSCs, each related by an integer multiple phase shift of $\pi/2$ in the peaks of the Turing pattern. For Fig. 3.4, we find that all four RSCs are stable and can be reached depending on the initial condition. In general, the systems selection of one or the other type of cell strongly depends on the number of VDSs in the crystal and the ratio between the pattern wavelength and the cavity length. This can be seen in Fig. 3.5 as the crystal type alternates between unit cell type for each additional soliton.

If we return to Fig. 3.4 we see that the evolution of the three VDSs is composed of two regimes. For slow time $t < 3 \times 10^5$, the VDSs move apart due to the formation of the Turing patterns. At slow time $t \approx 3 \times 10^5$, the three VDSs approach an equal spacing in the cavity, but here the Turing pattern rolls display a non integer $\pi/2$ phase shift with respect to the stationary unit cells presented in Fig. 3.7. We now see transient dynamics in which the equidistant VDSs lattice and Turing pattern drift in fast time at different rates. This drift continues until one of the four stationary configurations is reached. We

note the possibility of forming ‘defective’ crystals composed of alternating combinations of these four unit cells, which we leave for future study.

3.7 Vectorial dark-bright solitons

In this section, we investigate cavity soliton solutions of Eqs. (3.5) in parameter regions displaying strongly symmetry broken HSS. This regime is characterised by one polarisation field component being largely suppressed by the other (e.g. $E_+ \gg E_-$). In Fig. 3.8(a), we show the HSSs for $S = 3\sqrt{2/3}$. A notable feature of the HSSs for this larger value of S , is the formation of the ‘horn’ in the symmetry broken HSSs, where one field approaches peak power and the other approaches zero amplitude. This horn forms a small region of optical bistability between symmetry broken HSSs corresponding to the red curve and the blue curves of Figs. 3.8(a)-(c). Near the peak of the symmetry broken HSS horn, and with suitable perturbation, we observe the formation vectorial dark-bright cavity solitons (VDBS). These solutions present as a pair of solitons that occupy the same domain in fast time where the dark soliton hangs from the dominant field and a bright soliton sits upon the suppressed low power field.

The formation of VDBS has seen much theoretical investigation over the last three decades [127–134] in single mode optical fibres. Such systems are governed by coupled nonlinear Schrödinger equations (NLSE), which have been shown to admit solutions of dark-bright solitons due to the cross phase modulation between field components. VDBSs of the NLSE have been observed experimentally in optical fibres between orthogonal polarised field [135], as well as matter-wave VDBS solitons, which have been demonstrated experimentally in two-species Bose-Einstein Condensates [136–138].

More recently, dark and bright bound solitons have been demonstrated experimentally in microresonators [139, 140]. In previous studies, the generation of VDBS is achieved through bichromatic input fields allowing for different dispersion coefficients for the two field components. By selecting appropriate driving frequencies, we may have one input field operate in the anomalous dispersion regime, generating a bright soliton, while the second field operates in the normal dispersion regime in which a dark soliton is supported through cross phase modulation. Dark and bright solitons are bound in the fast time and copropagate along the microresonator. Bichromatically pumped microresonators have seen much study for the generation of frequency combs [141–146] where the simultaneous generation of orthogonally polarised solitons has been demonstrated [112, 115].

Here, we present a totally different paradigm for the formation of VDBSs in a ring resonator. We generate VDBSs of Eqs. (3.5) with monochromatic pumping with both polarisation field components exhibiting identical normal dispersion. VDBSs of Eqs. (3.5) are composed of SFs which connect to four different HSSs. These four HSSs form a bistability curve which is present at the horn for both the dominant and suppressed field, as we can see in Figs. 3.8(b)-3.8(c), respectively. In Fig. 3.8(d), we show four bistable VDBS solutions of Eq. (3.5) for $S = 3\sqrt{2/3}$, $\theta = 6.194$. Each solution of increasing width, represented by a different colour, is composed of a dark soliton which hangs from the upper HSS and a bright soliton which sits on the low power HSS. In Fig. 3.8(b) we plot the dark solitons of 3.8(d) as ‘x’. In the dominant field, the switching fronts which compose the dark soliton connect to the red and blue curves of Fig. 3.8(b). Switching fronts approach the

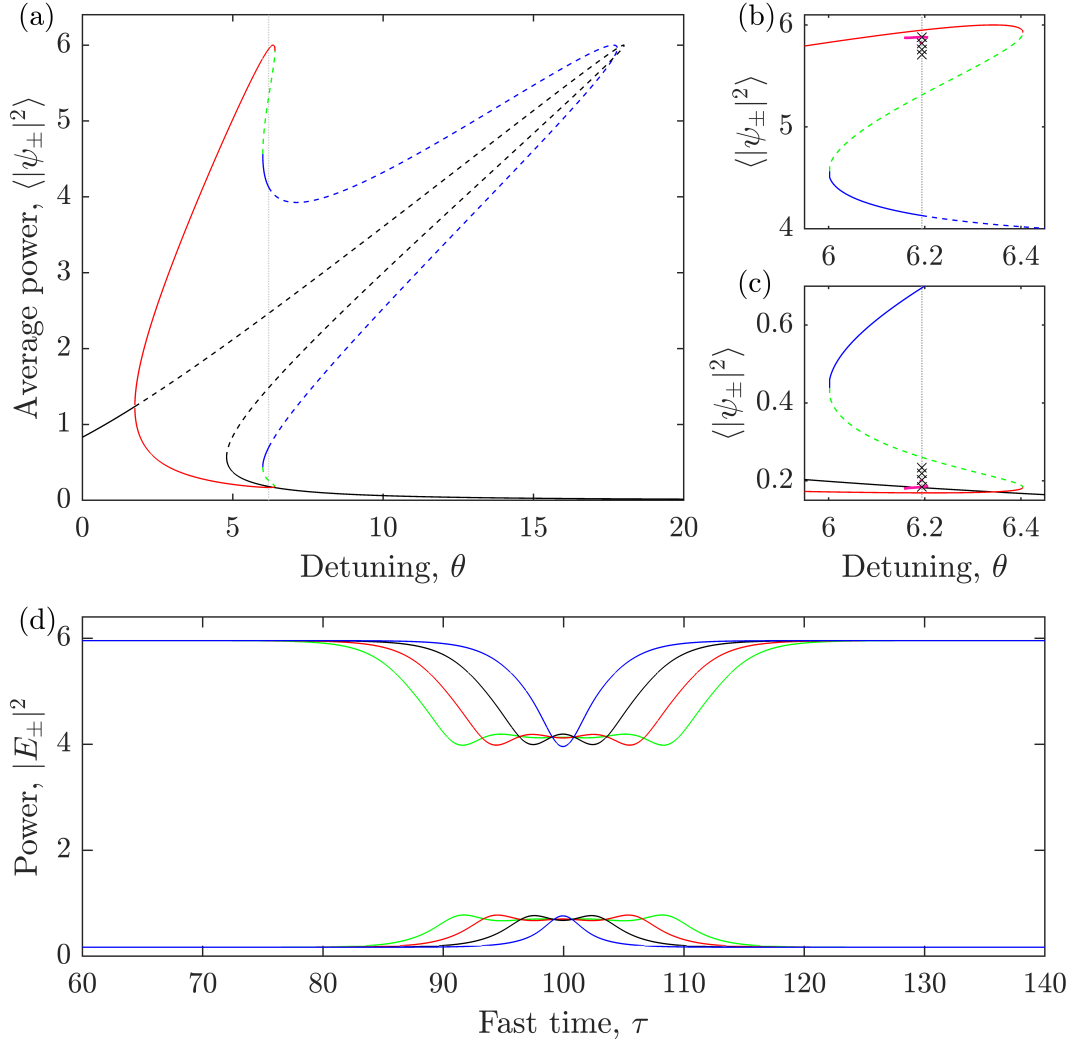


Figure 3.8: Solutions of Eqs. (3.5) for $S = 2\sqrt{2/3}$. (a) Stable (solid) and unstable (dashed) homogeneous stationary states which are symmetric (black curve) or symmetry broken (red, blue and green curves). Bistable dark-bright vector solitons for $\theta = 6.194$ are shown in (d). These solutions are composed of switching fronts that connect bistable HSS in the small region highlighted in (b) and (c), where the location of the solitons of (d) are marked with an 'x'. VDBS display collapse snaking behaviour resulting in stable solution branches, shown in pink in (b)-(c), each corresponding to distinct soliton width.

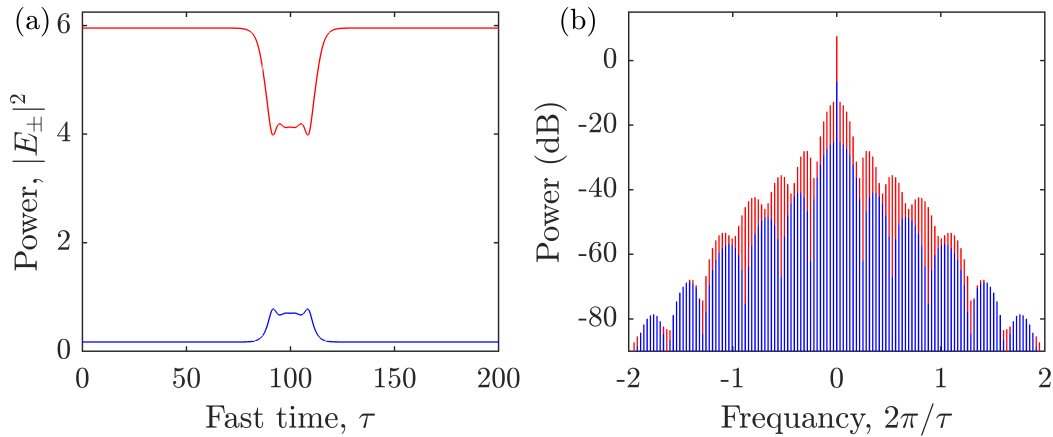


Figure 3.9: (a) Dark (red) and bright (blue) vectorial solitons for $S = 2\sqrt{2/3}$, $\theta = 6.194$, (b) and their corresponding frequency combs.

lower power (blue) HSS displaying a decaying oscillatory trajectory, whilst the approach to the higher power (red) HSS is smooth. It is the interaction of these oscillations which introduce a locking mechanism analogous to that described previously for the LLE. The corresponding bright solitons of Fig. 3.8(d) are marked with a ‘x’ in Fig. 3.8(c). Here, the switching fronts display a decaying oscillatory trajectory at the connection with the higher power (blue) HSS, and a smooth trajectory with the lower (red) HSS. The bright solitons ‘mirror’ the dark solitons in profile, exhibiting an identical size and number of peaks, due to local Kerr cross coupling. VDBSs undergo collapse snaking [35,47], displaying separate stable VDBS branches corresponding to the distinct VDBS sizes. Stable VDBS branches are shown in Fig. 6.10(a)-6.10(c) as pink curves. As VDBS solution of Eqs. (3.5) form around the symmetry broken HSS horn, they are found for much larger input power when compared to the symmetric dark-dark vectorial solitons of the previous sections.

In Fig. 3.9 we present a VDBS (a) and its corresponding frequency comb (b). VDBSs produce a duel comb [6, 7, 140, 147] at the output, where the red and blue combs corresponds to the dark and bright solitons of orthogonal polarisation, respectively. These two combs have identical spectral line spacing, corresponding to the cavity round trip time, but are symmetry broken in the spectral line power and in the spectral envelope. The difference in the power of the spectral lines is due to the much higher circulating power in the polarisation field component supporting the dark soliton when compared to the bright soliton field component. Modulations in the spectral envelope correspond to the oscillations on the peak of the bright soliton and trough of the dark soliton. These oscillations ‘mirror’ each other in the field envelope producing displaced modulations in the spectral envelope.

By slowly changing the parameters, VDBS are found to undergo a Hopf bifurcation. This results in stable breathing dynamics of the dark and bright solitons. An example dynamical VDBS is shown in Fig. 3.10 for $S = 3.2$, $\theta = 6.85$. The power profile of a VDBS at different points along the oscillatory cycle is shown in 3.10(a). These profiles correspond to the maximum and minimum of the peak (trough) of the bright (dark) soliton during

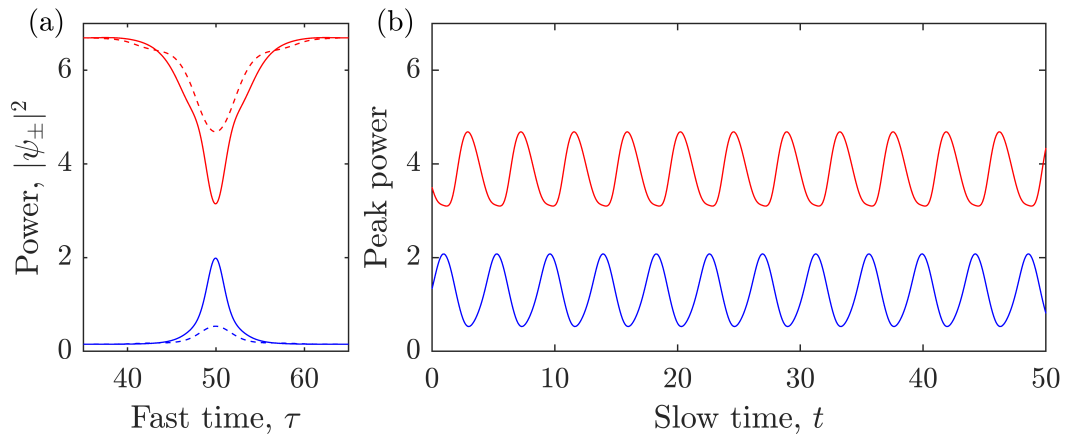


Figure 3.10: Breathing dark-bright vector soliton for $S = 3.2, \theta = 6.85$. (a) Power profile of VDBS at two points in fast time. (b) Trace of the minimum of the extrema of the dark (red) and bright (blue) soliton over slow time.

each cycle. A trace of the peak of the bright soliton (blue) and the trough of the dark soliton (red) is shown in Fig. 3.10(b). We see that the oscillations of the dark and bright solitons are perfectly synchronised.

3.8 Conclusion

In this chapter we have demonstrated the existence of Turing instabilities due to SSB of polarisation states, VDS on uniform and modulated backgrounds, long range interactions of VDS on modulated backgrounds and dark-bright cavity solitons in the same set of Eqs. (3.5) describing light with two orthogonal polarisations propagating in a ring Kerr cavity.

We demonstrated the formation of a RSC, which is achieved from a random distribution of VDSs via pattern formation with two field components of orthogonal polarisation. SSB results in the formation of Turing patterns of alternating polarisation at the tails of the VDSs. Long range interactions between VDSs are induced and mediated by Turing patterns, which increase the separation between adjacent VDSs until an equidistant equilibrium distance is reached and a regularly spaced soliton crystal is formed. Although long range interactions can also be induced by local soliton oscillations [148] and field counter-propagation [73, 117], our Turing pattern method offers new degrees of control, simple implementation, possible generalisation to other systems with two or more interacting components, smooth transitions to crystals of larger or smaller numbers of cavity solitons and even tuning of the spatial interaction length resulting in localised crystallisation. Moreover, in the regime of a Turing instability, RSCs originate spontaneously (self-crystallisation) without the need of any perturbation [40–44] and represents a new, readily implementable, method for RSC formation relevant for applications [123–126]. RSCs produce a frequency comb displaying a smooth spectral profile and increased line spacing when compared to a random distribution of cavity solitons. As such, a RSC may be used to emulate smaller cavity sizes while avoiding the experimental limitations of small

diameter ring resonators.

The same mechanism based on coexisting cavity solitons and Turing patterns can also lead to partial self-crystallisation in long cavities such as those of fibre loops, allowing one to build crystal sections with controllable numbers of cavity solitons separated by intervals of pattern solutions (or flat solutions if one moves the detuning θ back below the Turing threshold) of, again, controllable length. The frequency combs obtained at the output of these configurations cannot be obtained from single small ring resonators of lengths comparable to twice the solitons distance $2\Delta\tau$ since these are always periodic. Quasicrystals, crystals with impurities and superpositions (periodic or random) of crystals of different lengths can be realised in an optical system to simulate and investigate solid state structures of difficult realisation, i.e. photonic simulations. These come with the extra benefits of dual-mode operation and correlations. The self-crystallisation mechanism described in this work is universal in systems displaying temporal cavity solitons and Turing instabilities and has already been generalised to Fabry-Pérot configurations with two orthogonal polarisation's [103] We have also observed self-crystallisation of VDSs in configurations of ring-resonators operating away from symmetric configurations that better describe integrated microresonators as those mentioned in [111–115].

Finally, we demonstrated the possibility of VDBS. Such solutions form with suitable perturbation in regimes of highly symmetry broken HSS, in which the circulating power in one polarisation field component is much larger than the other. A dark soliton forms in the high power polarisation component which is coupled to a bright soliton forms in the low power component. In our system, VDBS are generated with equal and normal group velocity dispersion. This is at a difference with previous methods, which make use of bichromatic pumping of the resonator [140]. This results in a difference in group velocity dispersion between the field components with one laser operating in the anomalous dispersion regime, generating a bright soliton, while the second laser operates in the normal dispersion forming a dark soliton through cross-Kerr interaction with the bright soliton. In our system, the bright and dark solitons formed of switching fronts which connect to bistable symmetry broken HSS and lock due to the interaction of oscillatory tails. VDBS are shown to undergo Hopf bifurcations resulting in slow time oscillatory dynamics.

Dark-dark, and dark-bright (as well as bright-bright [67]) vectorial temporal cavity solitons are uniquely beneficial for their capacity to produce dual frequency combs, one comb for each field component. Dual comb generation has seen significant interest for application in spectroscopy by enabling greater resolution and sensitivity, when compared with single comb system [6, 7, 147]. Dual combs are typically generated by combining the outputs of two microresonators. More recently, dual comb generation has been experimentally demonstrated in a single resonator which is bichromatically driven [140]. In our single ring resonator system, we may generate a dual comb output using a single input laser.

Chapter 4

Counterpropagating Light in Bidirectionally Driven Ring Resonators

4.1	Introduction	63
4.2	Modelling the counterpropagation of light in ring resonators	64
4.3	Homogeneous steady states	70
4.4	Two switching fronts and dark soliton steady states	73
4.5	Distance of two stationary switching fronts	78
4.6	Evolution towards the two switching-front solutions	84
4.7	Oscillatory dynamics and bistability with front stationary states	87
4.8	Conclusions	91

4.1 Introduction

In this chapter, we study the interaction of two counterpropagating input fields in normally dispersive ring and micro-ring resonators, which is described by two globally coupled equations of LLE form [45, 46]. We use the term ‘global coupling’ following [47] to describe nonlinear cross terms that couple a point of the resonator to all other points in the same resonator via integrals that extend to its full length. The anomalous dispersion case has been investigated in [149] where the soliton blockade phenomenon was introduced. We characterise the formation of a novel class of robust stationary states formed by light plateaus separated by two local switching fronts in only one of two counterpropagating fields in ring resonators. Such states are due to global coupling between counterpropagating fields corresponding to the average power, and allow for frequency combs to switch from one field to the other by simply tuning the input laser frequency. Light plateau states are self-starting from noise for a wide range of detuning due to an instability of the homogeneous stationary states along the longitudinal coordinate resulting from the averaged terms. The global nature of these states display an unusual high degree of control over pulse and plateau duration in one of the fields upon changes of one of the input laser frequencies.

The primary control parameters considered here are the detunings of the two driving lasers, where one is presumed constant and the other is scanned. In practice, thermo-elastic and thermo-refractive effects due to material absorption deform the resonances of the fields [69, 70], compromising our control over the detunings of the counterpropagating fields. Microresonators composed of silica glass exhibit a positive thermal coefficients, meaning the refractive index increases with temperature, which results in a redshift of the resonance frequency. For silica microresonators, typical values of the coefficients of thermal expansion and thermal-optics are $\alpha_{\text{exp}} \approx 5.5 \times 10^{-7} K^{-1}$ and $\alpha_{\text{opt}} \approx 10^{-5} K^{-1}$, respectively, such that, the shift in the resonant frequency due to a temperature change of $\Delta T = 1^\circ\text{C}$ is [3]

$$\frac{\Delta\omega_{\text{thermo}}}{\omega_r} = (\alpha_{\text{exp}} + \alpha_{\text{opt}})\Delta T \approx 1.055 \times 10^{-5}. \quad (4.1)$$

For a high- Q ring resonator ($Q \sim 10^8$), the thermal shift in the resonance frequency is 1000 time larger than the resonance linewidth, and approximately 1000 times larger than our detuning scanning domain we present in this chapter. That said, it is generally appropriate to neglect thermal effects in our models, as we have been done throughout this thesis. The thermal shift can be incorporate into the laser detuning parameters of our models, which is appropriate for the bidirectional system as the thermal shifts of the resonances of the two directions are equal, where the thermal effects are dependant on the total power of the fields but not the propagation direction. In practice, the bidirectionally driven ring resonator exhibits a self-stabilisation effect in which the system naturally finds a balance between the thermal redshift and the detuning of the driving laser, such that, the laser remains near the resonances position. This is referred to as passive thermal locking [3].

We begin in Section 4.2 by introducing the coupled integro-partial differential equations, which governs the counterpropagation of light in the ring resonator. In Section 4.3, homogeneous steady state solutions of the globally coupled equations are investigated and

shown to undergo several bifurcations when the detunings are scanned. In Section 4.4, we characterise novel steady state solutions where one field has a homogeneous power while the other forms either a single dark temporal cavity soliton, single bright temporal cavity soliton, or power plateaus separated by sharp kinks. These solutions are unusual because in locally coupled field equations (i.e. no integral terms) fast time variations of the power of one field are reflected in the other one. It is the nature of the integro-partial-differential equations and global coupling that variations in one field are not necessarily present in the other field, leaving it in a homogeneous state. In Section 4.5, we determine the parameter ranges of the existence and stability of these hybrid solutions with sharp kinks, derive a semi-analytical expression of the distance of stationary kinks as a function of the cavity detunings, and compare it successfully with numerical simulations. In particular, we demonstrate that stationary solutions with two kinks in one of the counterpropagating fields are strongly related to similar solutions of a single normally dispersive LLE at the Maxwell point. Such stationary states have been observed with single input laser setups, where a counterpropagating field is induced by backscattering [73,74], where a connection with the Maxwell point (see Section 4.4) is also made.

Steep kinks connecting two stable homogeneous solutions in the presence of bistability have been studied extensively in diffusive systems where they are known as fronts [150], in nonlinear optics of scalar fields where they are known as switching waves [19, 54, 151], and in systems with exchange symmetry where they are known as domain walls [120, 121, 152–154]. Here, the system of interest has an exchange symmetry between the two counterpropagating fields. The hybrid solutions described in Section 4.4 display power plateaus separated by two kinks and do not reflect this exchange symmetry since one field is homogeneous and the other one is not. For this reason, we prefer to label the kinks as ‘switching fronts’ (SF) instead of ‘domain walls’ which was preferred in for example [73]. The solitonic (localised) aspect of these solutions is located in the SF and not of course in the power plateaus. For this reason we also avoid the use of the term ‘platicons’ as being an unhelpful mixing of the localised aspect of solitons with the extended character of the homogeneous solutions. In Section 4.6, we derive a semi-analytical description of zero dispersion SFs, and show that the zero dispersion SF solutions well approximate transient states with nonzero dispersion as they move towards stable two-SF states. In Section 4.7, we show the presence of nonlinear oscillations of homogeneous states in a symmetry broken and global regime similar to those predicted in symmetric regimes [96,97]. We then identify a multi-stability of slow nonlinear oscillations with SF states and continuous wave outputs offering an unprecedented variety of states for applications in high-control frequency comb generation, all optical oscillators, optical computing, time reversal symmetry breaking, and signal routing in telecommunication systems. Conclusions, connection to experiments and applications are presented in Section 4.8.

4.2 Modelling the counterpropagation of light in ring resonators

We consider the physical setting of a ring resonator driven by two bidirectional continuous wave (CW) lasers (see Fig. 4.1). Counterpropagating light within nonlinear resonators

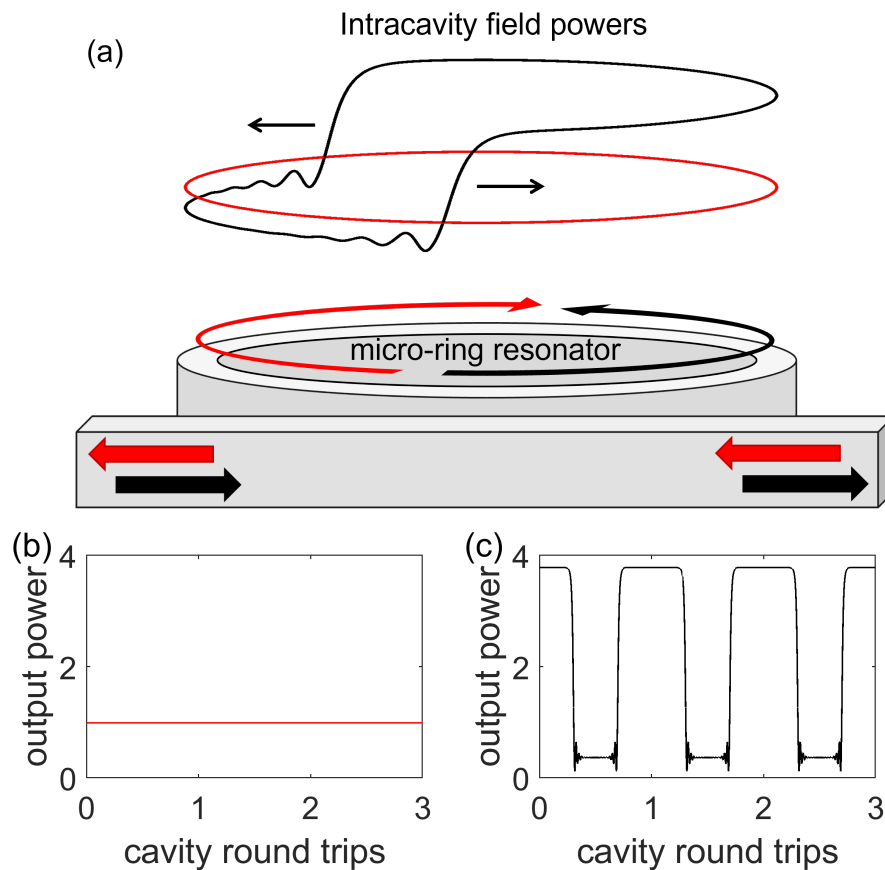


Figure 4.1: A continuous wave (CW) forward (red) and a CW backward (black) beams counterpropagate in a micro-ring resonator. For a detuning of the forward field smaller than the detuning of the backward field it is possible to obtain a power output where the forward field is still CW while the backward field displays two SFs in the intracavity power (a). This results in a switching output (c) from the backward field and CW output (b) from the forward field.

has seen much theoretical study in both ring [45, 46] and Fabry-Pérot [48] geometries. Skryabin [46] provides a detailed review of the derivation of the equations used to model this system from first principles. Here, we summarise the important considerations when modelling counterpropagating fields on timescales of the second order dispersion.

The propagation equation for the total electric field may be derived through similar means as in Section 2.4, where in this section, a notable difference is the inclusion of field components propagating on opposite directions. The electric field within the cavity can be written as a superposition of two counterpropagating fields

$$\mathcal{E}(\tau, t) \propto \bar{F}(\tau, t)e^{ik_F\tau}e^{-i\omega_F t} + \bar{B}(\tau, t)e^{-ik_B\tau}e^{-i\omega_B t} + c.c., \quad (4.2)$$

where $\bar{F}(\tau, t)$ and $\bar{B}(\tau, t)$ are normalised envelope functions of the forward and backward propagating fields, respectively, with input frequencies ω_F, ω_B and propagation constants k_F, k_B , where t is the slow time and τ is the longitudinal coordinate (fast time) along the resonator round trip time τ_R ($-\tau_R/2 \leq \tau \leq \tau_R/2$).

Coupling between forward and backward propagating fields can arise from a number of different mechanisms within a ring resonator. For example, Rayleigh scattering is ubiquitous within microresonators [71, 72], and is induced through small variations in the material composition or density, which introduces small variations in the refractive index. Rayleigh scattering manifests as a linear coupling between counterpropagating field components [45], whereby scattered light is coupled into the same mode travelling in the opposite direction, and has been utilised as a means of generating a counterpropagating field for the study of localised structures [73]. Linear coupling may also be induced via scattering at the waveguides boundary, which may be controlled through engineering of the roughness of the resonators surface [74]. In these cases, the linear coupling coefficient is considered to be smaller than cavity photon decay rate, where in general, backscattering can be suppressed through careful engineering [75]. Defects in the waveguide material may also introduce nonlinear scattering effects, such as, the Raman effect [98] (inelastic scattering of photons by vibrational modes of the medium) and Brillouin scattering [99] (arises from interaction between light and thermally induced acoustic waves). Here, we consider a bidirectional driven ring resonator in which the coupling mechanism between counterpropagating fields is dominated by the Kerr nonlinearity.

The nonlinear interaction between counterpropagating light can be characterised by the nonlinear atomic polarisation, which takes the form,

$$\mathcal{P}_{\text{NL}} \propto |\mathcal{E}|^2 \mathcal{E} = (|\bar{F}|^2 + 2|\bar{B}|^2)\bar{F}e^{ik_F\tau} + (|\bar{B}|^2 + 2|\bar{F}|^2)\bar{B}e^{-ik_B\tau} + (\text{third harmonic}). \quad (4.3)$$

Forward and backward propagating fields are coupled through self- and cross- phase modulation originating from the Kerr nonlinearity. Here, the effect of the Kerr nonlinearity is directionally dependant, with terms proportional to $\exp(\pm ik\tau)$. We may define nonlinear dielectric susceptibilities within the rotating wave approximation as,

$$\epsilon_{\text{NL}}^F \propto |\bar{F}|^2 + 2|\bar{B}|^2, \quad (4.4a)$$

$$\epsilon_{\text{NL}}^B \propto |\bar{B}|^2 + 2|\bar{F}|^2, \quad (4.4b)$$

which characterise the shift in resonance due the Kerr effect for light propagating forward

$\exp(ik_F\tau)$ and backwards $\exp(-ik_B\tau)$, respectively. As the cross-phase modulation is twice the self-phase modulation, there is a nonreciprocity of the nonlinear effect between counterpropagating fields. The difference in the shift of refractive index due to the Kerr effect results in an optical path length that is directionally dependant and has been shown to result in spontaneous symmetry breaking between the direction of circulating power [95, 155, 156] (and is mathematically similar to the polarisations of Chapter 3).

This results in the coupled equations

$$\partial_t \bar{F} + \partial_\tau \bar{F} = S_F - (1 + i\theta_F) \bar{F} + i(|\bar{F}|^2 + \nu|\bar{B}|^2) \bar{F} - i\partial_\tau^2 \bar{F}, \quad (4.5a)$$

$$\partial_t \bar{B} - \partial_\tau \bar{B} = S_B - (1 + i\theta_B) \bar{B} + i(|\bar{B}|^2 + \nu|\bar{F}|^2) \bar{B} - i\partial_\tau^2 \bar{B}. \quad (4.5b)$$

which has split our single field LLE into two coupled LLEs, one for each counterpropagating component $\exp(ik_F\tau)$ and $\exp(-ik_B\tau)$, as per the rotating wave approximation. The two fields of this system are described by mean-field equations with the self- and cross-phase modulation terms in the Kerr approximation, through which the fields interact. Eqs. (4.5) possess two distinct retarded times, one for the forward propagating field and one for the backward propagating field. As such, it is not possible to transform this set of equations into a rotating frame of reference as we have done previously for the LLE. Dynamics at the frequency of the free spectral range are prolific in Eqs. (4.5). As such, we must give careful attention to the different interaction timescales between field components.

We may express the field envelopes as the modal expansions

$$\bar{F}(\tau, t) = \sum_{\mu=-\infty}^{\infty} \bar{f}_\mu(t) e^{i\mu\bar{\alpha}\tau}, \quad \bar{B}(\tau, t) = \sum_{\mu=-\infty}^{\infty} \bar{b}_\mu(t) e^{-i\mu\bar{\alpha}\tau} \quad (4.6)$$

where $\bar{\alpha} = 2\pi/\tau_R$ is the free spectral range of the cavity and μ is the cavity mode number. To investigate the dynamical at different timescales, we define the new modal amplitudes

$$\bar{f}_\mu(t) = f_\mu(t) e^{-i\mu\bar{\alpha}t}, \quad \bar{b}_\mu(t) = b_\mu(t) e^{-i\mu\bar{\alpha}t} \quad (4.7)$$

which separates the evolution of the modal amplitudes into functions which vary on distinct timescales. Inserting the modal expansions (4.6) into Eqs. (4.5), we obtain the modal equations

$$\begin{aligned} \partial_t f_\mu = & S_F \delta_{\mu,0} - (1 + i\theta) f_\mu + (\mu\bar{\alpha})^2 f_\mu \\ & + \sum_{\mu', \mu'', \mu'''} \delta_{\mu, \mu' + \mu'' - \mu'''} \left[f_{\mu'} f_{\mu''}^* f_{\mu'''} + 2b_{\mu'''} b_{\mu''}^* f_{\mu'} e^{i\bar{\alpha}(\mu - \mu')t} \right], \end{aligned} \quad (4.8a)$$

$$\begin{aligned} \partial_t b_\mu = & S_B \delta_{\mu,0} - (1 + i\theta) b_\mu + (\mu\bar{\alpha})^2 b_\mu \\ & + \sum_{\mu', \mu'', \mu'''} \delta_{\mu, \mu' + \mu'' - \mu'''} \left[b_{\mu'} b_{\mu''}^* b_{\mu'''} + 2f_{\mu'''} f_{\mu''}^* b_{\mu'} e^{i\bar{\alpha}(\mu - \mu')t} \right], \end{aligned} \quad (4.8b)$$

where the four wave mixing momentum condition $\mu + \mu''' = \mu' + \mu''$ is implemented using the Kronecker delta $\delta_{i,j}$. Our decomposition of the modal amplitudes $\bar{f}_\mu(t), \bar{b}_\mu(t)$ yields functions which evolve over distinct time scales, where, the dynamics of the exponential term $\exp -i\mu\bar{\alpha}t$ are rapidly varying on the scale of the free spectral range $\bar{\alpha}$, whereas the

modal amplitudes $f_\mu(t), b_\mu(t)$ vary at the scale of the cavity decay time κ^{-1} . In a high fineness cavity, where the power transmission coefficient is small $T \ll 1$, these timescales are very well separated. If we perform an averaging of Eqs. (4.8) on a timescale that is longer than the round trip time but shorter than the cavity decay time, we find that each term in Eqs. (4.8) remains unchanged, except those proportional to rapidly varying exponentials. On such a timescale, the exponential terms will be non-zero only if $\mu = \mu'$. As a consequence, rapidly varying terms on the scale of $\bar{\alpha}$ can be appropriately discarded should $\mu \neq \mu'$ [45, 46, 48, 49], and the model equations (4.8) become

$$\begin{aligned} \partial_t f_\mu &= S_F \delta_{\mu,0} - (1 + i\theta) f_\mu + (\mu \bar{\alpha})^2 f_\mu \\ &+ \sum_{\mu', \mu'', \mu'''} \delta_{\mu, \mu' + \mu'' - \mu'''} f_{\mu'} f_{\mu''}^* f_{\mu'''} + 2f_\mu \sum_{\mu'} b_{\mu'} b_{\mu'}^*, \end{aligned} \quad (4.9a)$$

$$\begin{aligned} \partial_t b_\mu &= S_B \delta_{\mu,0} - (1 + i\theta) b_\mu + (\mu \bar{\alpha})^2 b_\mu \\ &+ \sum_{\mu', \mu'', \mu'''} \delta_{\mu, \mu' + \mu'' - \mu'''} b_{\mu'} b_{\mu''}^* b_{\mu'''} + 2b_\mu \sum_{\mu'} f_{\mu'} f_{\mu'}^*. \end{aligned} \quad (4.9b)$$

Defining new envelope functions

$$F(\tau, t) = \sum_{\mu=-\infty}^{\infty} f_\mu(t) e^{i\mu \bar{\alpha} \tau}, \quad B(\tau, t) = \sum_{\mu=-\infty}^{\infty} b_\mu(t) e^{-i\mu \bar{\alpha} \tau} \quad (4.10)$$

we may elucidate the effect of counterpropagation for timescales up to the second order (or higher) dispersion. Inserting the envelopes (4.10) into modal equations (4.9), the model for this system can be written in the adimensional, normalised form as a system of two integro-partial-differential equations

$$\partial_t F = S_F - (1 + i\theta_F) F + i(|F|^2 + \nu \langle |B|^2 \rangle) F - i\beta \partial_\tau^2 F \quad (4.11a)$$

$$\partial_t B = S_B - (1 + i\theta_B) B + i(|B|^2 + \nu \langle |F|^2 \rangle) B - i\beta \partial_\tau^2 B \quad (4.11b)$$

Here, we define ‘slow time’ $t = \alpha \tilde{t} / \tau_R$, which governs evolution over several round trips of the resonator with round trip time τ_R , and ‘fast time’ $\tau = \tilde{\tau} \sqrt{2\alpha/L}$ corresponding to the longitudinal cavity coordinate over the round trip time, in a frame of reference moving with the group velocity. $F = \tilde{F} \sqrt{\gamma L / \alpha}$ and $B = \tilde{B} \sqrt{\gamma L / \alpha}$ are the complex amplitudes of the forward and backward counterpropagating fields in the ring resonator of identical polarisation, with input fields $S_F = \tilde{E}_F \sqrt{\gamma L T / \alpha^3}$ and $S_B = \tilde{E}_B \sqrt{\gamma L T / \alpha^3}$ for nonlinear coefficient γ , power transmission coefficient T and total losses α . $\theta_F = \tau_R (\omega_r - \omega_F) / \alpha$ and $\theta_B = \tau_R (\omega_r - \omega_B) / \alpha$ are the laser detunings of angular frequency ω_F, ω_B from the nearest cavity resonance ω_r with round trip time τ_R . ν is the cross coupling coefficient that is in general equal to 2 for isotropic media and the last term describes normal dispersion with a positive dispersion coefficient β .

We define the power averages $\langle |F|^2 \rangle$ and $\langle |B|^2 \rangle$ as

$$\langle |F|^2 \rangle = \frac{1}{\tau_R} \int_{-\tau_R/2}^{\tau_R/2} |F(\tau, t)|^2 d\tau, \quad \langle |B|^2 \rangle = \frac{1}{\tau_R} \int_{-\tau_R/2}^{\tau_R/2} |B(\tau, t)|^2 d\tau, \quad (4.12)$$

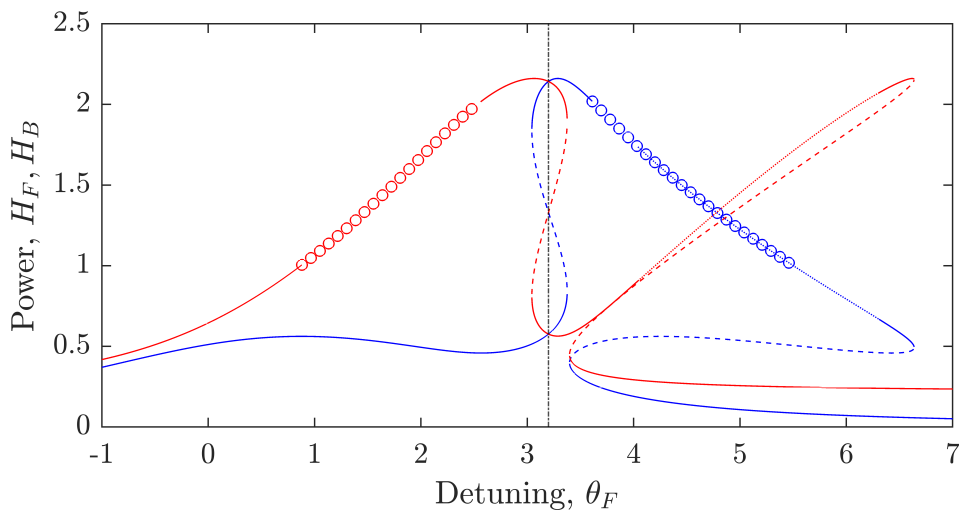


Figure 4.2: Powers H_F (red) and H_B (black) of HSS (4.13a,4.13b) when changing the detuning θ_F of the forward field for parameter values $S_F = S_B = 1.47$, $\nu = 2$, and the detuning of the backwards field kept constant at $\theta_B = 3.2$. The solid (broken) lines correspond to stable (unstable) HSS, the lines marked with the symbol ‘o’ correspond to HSS unstable to fast time perturbations, dotted lines correspond to Hopf instability of the HSS.

which were obtained from the last terms of the modal equations (4.9) following from Parseval’s theorem. The phase dynamics of the cross-coupling terms evolve with the free spectral range by the nature of counterpropagation of the two fields. This results in a large walk-off occurring between the two counter-propagating waves that see each other through an average intensity (washout effect) [45, 46]. Averaging of the Kerr cross-phase coupling term is appropriate when operating in the mean field regime. This regime is characterized by a spectral envelope which evolves on well separated temporal scales. Here, the forward and backward envelopes are defined over the fast time coordinate τ , which evolve slowly over many round trips of the resonator in the slow time coordinate t . This is achieved in practise by ensuring a high Q -factor is achieved by the resonator. The configuration and parameters used here differ from those used in [73, 74] in that we consider energy injection on both fields. It is important to note that for $S_F = S_B$ and $\theta_F = \theta_B$ the system of equations are perfectly symmetric upon the exchange of the forward and backward fields.

In our numerical investigation, we utilise split-step integration as is outlined in Appendix C.2. As the integral terms are evaluated implicitly for split-step methods, we give careful attention to the validity of our results by utilising explicit integration methods outlined in Appendix C.3. We note that, as the nonlocal Kerr coupling is applicable under the same conditions as the longitudinal LLE, there are additional constraints on the slow time step size originating from the integral (Appendix C.1).

4.3 Homogeneous steady states

The homogeneous steady-state solutions (HSS) of counterpropagating fields are identical to the two polarisation co-propagating regimes seen in Chapter 3, as cross terms may be trivially evaluated as $\langle |F|^2 \rangle = |F|^2$, $\langle |B|^2 \rangle = |B|^2$ for solutions with flat fast time profile. Eqs. (4.11) can be expressed by the coupled cubic equations

$$P_F = H_F^3 - 2(\theta_F - \nu H_B)H_F^2 + [(\theta_F - \nu H_B)^2 + 1]H_F \quad (4.13a)$$

$$P_B = H_B^3 - 2(\theta_B - \nu H_F)H_B^2 + [(\theta_B - \nu H_F)^2 + 1]H_B \quad (4.13b)$$

where $H_F = |F|^2$, $H_B = |B|^2$ (the letter H referring to the power of the HSS) while $P_F = |S_F|^2$ and $P_B = |S_B|^2$ correspond to the input powers. The real and imaginary components of the HSSs are then

$$\begin{pmatrix} U_{0,F} \\ V_{0,F} \end{pmatrix} = \begin{pmatrix} \frac{S_F}{1+(H_F+2H_B-\theta_F)^2} \\ \frac{(H_F+2H_B-\theta_F)S}{1+(H_F+2H_B-\theta_F)^2} \end{pmatrix}, \quad \begin{pmatrix} U_{0,B} \\ V_{0,B} \end{pmatrix} = \begin{pmatrix} \frac{S_B}{1+(H_B+2H_F-\theta_B)^2} \\ \frac{(H_B+2H_F-\theta_B)S}{1+(H_B+2H_F-\theta_B)^2} \end{pmatrix}. \quad (4.14)$$

Counterpropagating fields in ring resonators display spontaneous symmetry breaking of the HSS for equal detunings. This allows for optical switching between high and low power counterpropagating field, which has been observed experimentally [155, 156]. This spontaneous symmetry breaking is mathematically equivalent to the phenomenon of the previous chapter between polarisation components, conditional that we neglect dispersion, and much of that analysis is relevant for this system. For our purposes, we consider symmetry broken regimes with different detunings between for the two input field.

These algebraic equations can be solved numerically for given values of the parameters, an example of which is shown in Fig. 4.2 for equal pump powers ($P_F = P_B = 2.1609$), where one of the field detunings kept constant ($\theta_B = 3.2$) while the other (θ_F) is changed. In the vicinity of equal detunings (vertical dashed line) where the equations are symmetric upon exchange of the forward and backward fields, a bistability regime with a ‘figure 8’ shape exists. Here we expect the ‘middle’ HSS to be unstable (see dashed lines in Fig. 4.2). When increasing the forward detuning θ_F after the symmetric value 3.2, the figure of 8 ends in this case at the point where two new HSS are born in a degenerate saddle-node bifurcation, the lowermost being stable and the intermediate unstable. For values of $\theta_B < 3.2$ the saddle-node bifurcation takes place after the end of the figure of 8, while for values of $\theta_B > 3.2$ the saddle-node bifurcation takes place before the end of the figure of 8 leading to a simultaneous presence of 5 different stationary states. After the saddle-node bifurcation and the end of the figure of 8, multi-stability of homogeneous solutions is present at large values of the detuning θ_F until a reverse saddle-node bifurcation restores a single HSS at very large values of the scanned detuning.

In the asymmetric region for $\theta_F > \theta_B$ we detect Hopf bifurcations of the HSS leading to oscillations as described in Section 4.7. The two Hopf bifurcations occur on the upper branches of the HSS (see the vertical dashed lines in Fig. 4.2) and have opposite directions when increasing the detuning θ_F , with the amplitude of the oscillation growing from around $\theta_F = 4$ and decreasing to zero around $\theta_F = 6.3$. These forward and backward Hopf bifurcations are analogous in nature and stability eigenvalues to those described

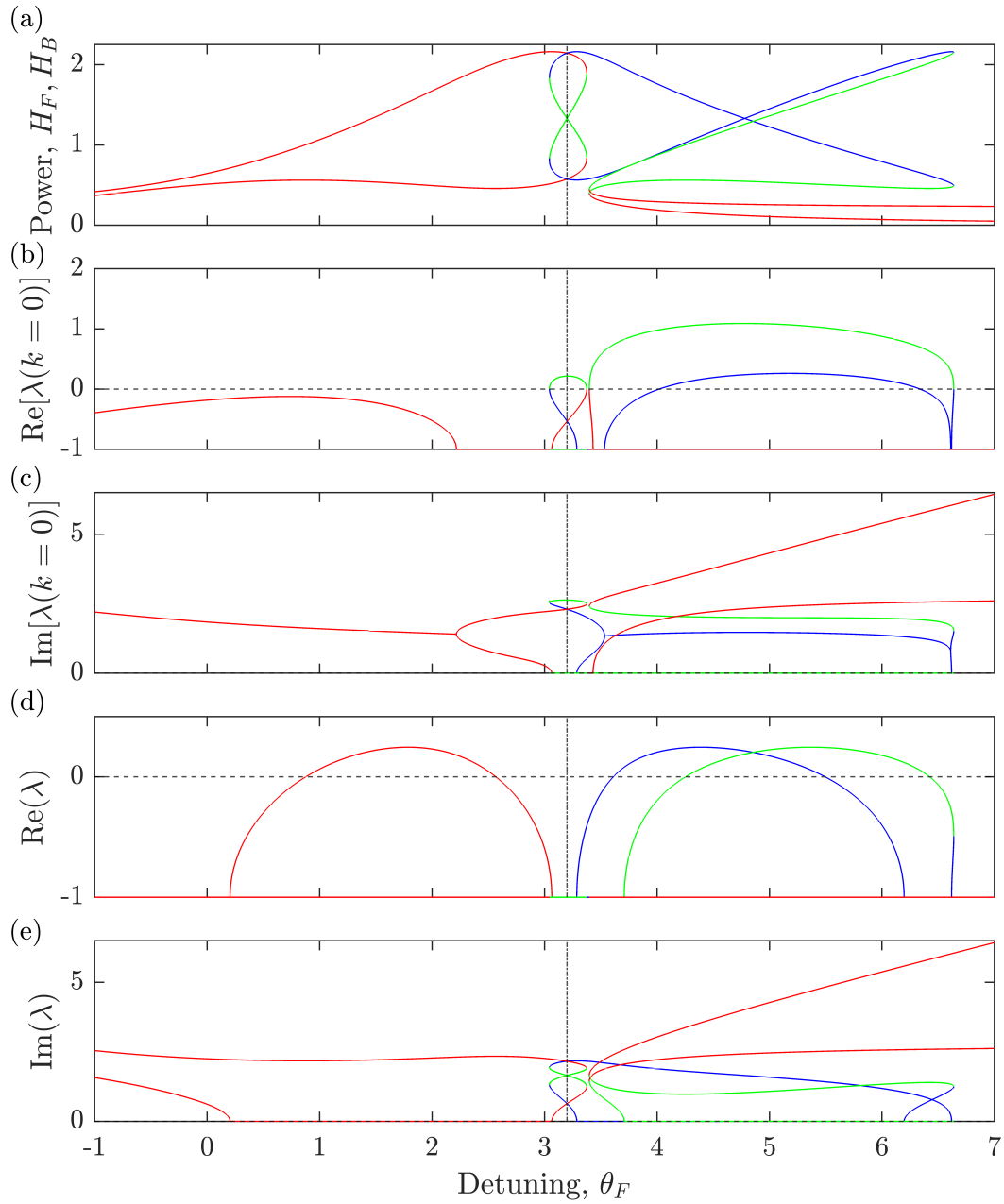


Figure 4.3: (a) Powers H_F and H_B of HSS (4.13a,4.13b) when changing the detuning θ_F of the forward field for parameter values $S_F = S_B = 1.47$, $\nu = 2$, and the detuning of the backwards field kept constant at $\theta_B = 3.2$. Curves of the same colour corresponds to distinct solutions (H_F, H_B). The corresponding eigenvalues for each solution are shown with identical colours. The real (b) and imaginary (c) components of the eigenvalues (4.16) for $k_0 = 0$ predict instability of the middle solutions (green), and a Hopf bifurcation of on high power solution (blue). The real (d) and imaginary (e) components of the eigenvalues (4.22) predict fast time instability on the left (red) and right (blue) hand side of detuning symmetry, in the field with higher circulating power.

in [38, 96] where, however, the two detunings were kept equal to each other during the scan to focus on symmetric HSS.

To investigate the stability of the HSSs, we may perform linear stability analysis on modal equations (4.9). We introduce a perturbation to the modal amplitudes

$$f_\mu = f_s \delta_{\mu,0} + \delta f_\mu, \quad b_\mu = b_s \delta_{\mu,0} + \delta b_\mu \quad (4.15)$$

about the HSSs corresponding to modes $f_s \delta_{\mu,0}, b_s \delta_{\mu,0}$. As outlined in appendix A.1, we arrive at the linear stability eigenvalues

$$\lambda(k_\mu) = -1 \pm \frac{\sqrt{-A_{1,\mu}B_{1,\mu} - A_{2,\mu}B_{2,\mu} \pm Q}}{\sqrt{2}}, \quad (4.16a)$$

$$Q = \sqrt{(A_{1,\mu}B_{1,\mu} - A_{2,\mu}B_{2,\mu})^2 + 4\delta_{\mu,0}A_{1,\mu}A_{2,\mu}C^2}, \quad (4.16b)$$

where

$$\begin{aligned} A_{1,\mu} &= k_\mu^2 - \theta_F + H_F + 2H_B, & B_{1,\mu} &= k_\mu^2 - \theta_F + 3H_F + 2H_B, & C^2 &= 16H_F H_B, \\ A_{2,\mu} &= k_\mu^2 - \theta_B + 2H_F + H_B, & B_{2,\mu} &= k_\mu^2 - \theta_B + 2H_F + 3H_B. \end{aligned}$$

with fast time wavenumber $k_\mu = 2\pi\mu/\tau_R$. Due to the presence of the Kronecker delta $\delta_{\mu,0}$ in the eigenspectrum (4.16), we must consider the cases of $\mu = 0$ and $\mu \neq 0$ separately. These two outcomes refer to perturbations that evolve in slow time with a fast time profile that is either; flat, $\mu = 0$, or exhibits a fast time component, $\mu \neq 0$. These cases are notably distinct due to the counterpropagation of fields, and can be understood by considering a linearisation of the integral terms about the HSS, which takes the form

$$\langle |\psi_s + \epsilon|^2 \rangle \sim \begin{cases} |\psi_s + \epsilon|^2, & \text{if } \epsilon \propto \exp[\lambda(k_0 = 0)t], \quad (\mu = 0), \\ |\psi_s|^2, & \text{if } \epsilon \propto \exp[\lambda(k_\mu)t + ik_\mu\tau], \quad (\mu \neq 0). \end{cases} \quad (4.17)$$

where ψ_s represents the HSS of the forward or backward field and $|\epsilon| \ll 1$. As we can see, a perturbation does not survive the integral should it contain a fast time component.

When $\mu = 0$, Eq. (4.16) reduces to eigenvalues which are mathematically identical to those seen in the absence of fast time within Kerr resonators of ring [38] and Fabry-Pérot [68] geometries, supporting two fields of orthogonal polarisation. These eigenvalues are plotted in Fig. 4.3(b)-(c) for the example HSS of Fig. 4.2 and predict the aforementioned instability of the middle HSS branches, along with the Hopf bifurcations.

When $\mu \neq 0$, eigenvalues (4.16) take the form

$$\lambda(k_\mu \neq 0) = -1 \pm \sqrt{-A_{1,\mu}B_{1,\mu}} \quad (4.18a)$$

$$\lambda(k_\mu \neq 0) = -1 \pm \sqrt{-A_{2,\mu}B_{2,\mu}}. \quad (4.18b)$$

These eigenvalues indicate the growth/decay in slow time of perturbations that are sinusoidal in fast time with wavenumber k_μ , such that, the HSSs become unstable to the formation of Turing patterns when $\text{Re}[\lambda(k_\mu \neq 0)] > 0$. By writing $-A_{1,\mu}B_{1,\mu} = 1 - c_1$ and

$-A_{2,\mu}B_{2,\mu} = 1 - c_2$ where

$$c_1 = 1 - 4H_F(\theta_F - \nu H_B) + 3H_F^2 + (\theta_F - \nu H_B)^2 + 2(2H_F^2 + \nu H_B^2 - \theta_F)k_\mu^2 + k_\mu^4, \quad (4.19a)$$

$$c_2 = 1 - 4H_B(\theta_B - \nu H_F) + 3H_B^2 + (\theta_B - \nu H_F)^2 + 2(2H_B^2 + \nu H_F^2 - \theta_B)k_\mu^2 + k_\mu^4, \quad (4.19b)$$

the instability condition corresponds to $c_{1,2} < 0$. We can expect pattern formation to occur for the unstable wavenumbers $k_{\mu,-}^2 < k_\mu^2 < k_{\mu,+}^2$ of the forward field, where

$$k_{\mu,\pm}^2 = \theta_F - 2H_F - \nu H_B \pm \sqrt{H_F^2 - 1}, \quad (4.20)$$

and in the backward field, where

$$k_{\mu,\pm}^2 = \theta_B - 2H_B - \nu H_F \pm \sqrt{H_B^2 - 1}. \quad (4.21)$$

Similar to the single field unidirectional case (LLE) these eigenvalues indicate the Turing instability starting from $H_F, H_B = 1$.

There are however further instabilities of the HSS due to the nature of the global coupling of Eqs. (4.11). In Appendix A.2, we present a linear stability analysis of the HSSs to perturbations that are inhomogeneous along the cavity round trip time at zero dispersion on the fast time scale. A new set of stability eigenvalues is found:

$$\lambda = -1 \pm \sqrt{-A_1 B_1} \quad (4.22a)$$

$$\lambda = -1 \pm \sqrt{-A_2 B_2} \quad (4.22b)$$

where $A_1 = H_F + \nu H_B - \theta_F$, $A_2 = H_B + \nu H_F - \theta_B$, $B_1 = 3H_F + \nu H_B - \theta_F$, $B_2 = 3H_B + \nu H_F - \theta_B$, with H_F and H_B being obtained from Eqs. (4.13). These new eigenvalues are entirely due to the averaged terms of this system which means that local perturbations result in changes to the unperturbed regions. The lines marked with the letter ‘o’ in Fig. 4.2 correspond to the HSS instability to inhomogeneous perturbations where the real part of at least one of the four eigenvalues (4.22) is positive. These eigenvalues predict an instability of the HSS to perturbations which are localised in fast time with nonzero contribution to the integral terms.

4.4 Two switching fronts and dark soliton steady states

In the counterpropagating system with global coupling described by Eqs. (4.11), we observe the formation of steady states made of power plateaus separated by SF in one of the two counterpropagating fields while the second field remains homogeneous, for wide ranges of the detuning values. In Fig. 4.4, we show the formation of stable SF states when starting from a narrow (a) or broad (b) perturbation of the HSS for $S_F = S_B = 1.47$, $\nu = 2$, $\theta_B = 3.2$ and $\theta_F = 2.0$. We note that the choice of input power was arbitrary, and similar solutions of stable SFs will exist for input field with similar values, such as $S_F = S_B = 1.5$ or $S_F = S_B = \sqrt{2}$. In Section 4.3, we showed that in this parameter region, HSS are unstable to inhomogeneous perturbations. In both cases of broad and narrow initial perturbations, the system evolves to the same final solution formed by a SF state

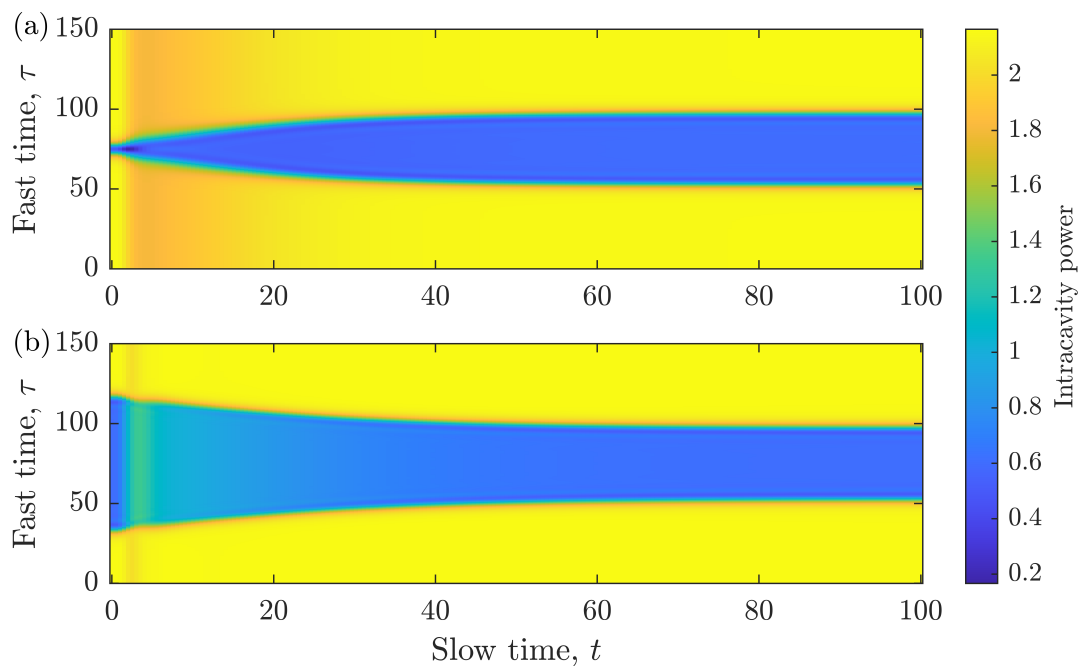


Figure 4.4: Temporal evolution of the backward power towards a stable SF state for $|S_F|^2 = |S_B|^2 = 2.1609$, $\theta_F = 2.0, \theta_B = 3.2$ from two different initial conditions with dispersion $\beta = 1$. (a) Initial condition with two kinks at narrow separation. (b) Initial condition with two kinks at wide separation.

with a well-defined separation of the two SFs. It is important to note that the SF solutions do not connect HSS of the Eqs. (4.11) and affect only one of the counterpropagating fields, the other being homogeneous. They do not correspond to symmetry exchanges of the F and B fields.

A number of stable asymptotic states are presented in Fig. 4.5 for the same values of the parameters as Fig. 4.4 but with θ_F varying from 1.2 to 4.8. In the interval $1.2 < \theta_F < 2.8$ the backward (forward) intracavity power is non-homogeneous (homogeneous), Fig. 4.5(a), while in the interval $3.4 < \theta_F < 4.8$ the forward (backward) intracavity power is non-homogeneous (homogeneous), Fig. 4.5(b). The solid lines correspond to the power profiles of the field where a dark structure is found while the dashed lines correspond to fully homogeneous solutions. When the two detunings are close to each other (for example θ_F equal to 2.8 or 3.4 in Fig. 4.5) the inhomogeneous field has the shape of a localised dark soliton. In the interval of $2.8 < \theta_F < 3.4$, there are no inhomogeneous stable solutions and the system relaxes to the HSS seen in Fig. 4.2. This instability of the dark soliton solution is affected by the dispersion of the field and dark solitons can persist in larger detuning ranges for $\beta < 1$. For the present choice of parameter values there is no bistability between the two SF states close to detuning symmetry. We will see in Section 4.5 that for $P_F = P_B = 3$, for example, an overlap region where both SF states are stable, exists. In this overlap region, bistability of SF states is observed where SFs are present in either the forward or the backward field with the other field homogeneous for the same parameter values.

For detunings $\theta_F < \theta_B$ below symmetry, there is a wide region of parameter space where SFs separated by light plateaus are the only stable solutions of the system. Here, light plateaus within two SFs are self-starting states and there is no need of any perturbation to the system to drive the dynamics towards them.

For $\theta_F < \theta_B$ there are small regions of bistability between HSS and light plateaus within two SFs. For $\theta_F > \theta_B$ there is a wide region of bistability between low intensity HSS and light plateaus within two SFs and even tristability with the addition of oscillating HSS. In all the regions of multi-stability we have found that input pulses made of a square wave of around twice the background input power, of duration $\tilde{\tau}$ and applied for a transient time \tilde{t} to the field where the light plateaus will appear, results in the formation of stationary light plateaus within two SFs if the input pump pulse duration $\tilde{\tau}/\tau_R$ is of the order of $(1 - \Delta)$ where Δ is the final separation of the SFs (see Section 4.5).

When the two detunings are very different from each other, the inhomogeneous field can take the shape of a localised bright soliton while the other field remains homogeneous. Bright solitons are in general not stable in the normally dispersive unidirectional system (LLE) and annihilate each other as the fronts collide. Bright solitons formed by two SFs are instead stable in counterpropagation due to the robustness introduced by global coupling but the SFs will still annihilate if they are brought too close to each other. Such states have been observed in single laser setups [74]. In the limit of zero dispersion, bright structures can be made arbitrarily narrow when changing the detuning. The dispersion affects the steepness of SFs and for a given θ_F , it will determine whether we have a bright structure of two non interacting SFs or a bright soliton or an annihilation of the two SFs. For given values of the detunings, bright structures with a minimum full width at half maximum (FWHM) can be found and their dependence from the dispersion coefficient β

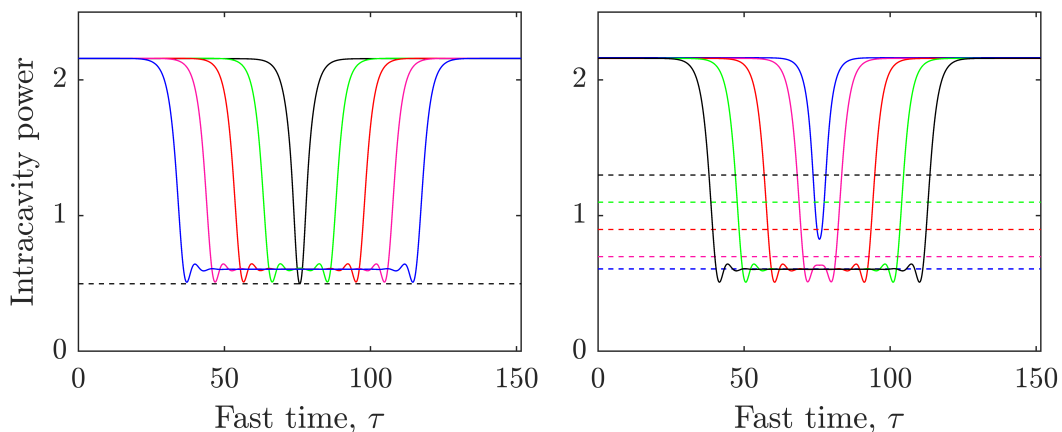


Figure 4.5: Various SF states for $S_F = S_B = 1.47$, $\nu = 2$, $\beta = 1$, $\theta_B = 3.2$. (a) Backward (forward) field power of steady state solutions, solid lines (dashed lines), for five values with decreasing distance between SFs $\theta_F = 1.2$ (blue), $\theta_F = 1.6$ (magenta), $\theta_F = 2.0$ (red), $\theta_F = 2.4$ (green), $\theta_F = 2.8$ (black). (b) Forward (backward) field power of steady state solutions, solid lines (dashed lines) for five values with increasing distance between SFs $\theta_F = 3.4$ (blue), $\theta_F = 3.6$ (magenta), $\theta_F = 4.0$ (red), $\theta_F = 4.4$ (green), $\theta_F = 4.8$ (black).

can be established in numerical simulations as shown in Fig. 4.6.

Stable SF states and stable dark solitons are present due to the global coupling of the two counterpropagating fields. The phase independent interaction of counterpropagating fields introduced a shift in the detuning of the fields. To this end we define effective detunings

$$\tilde{\theta}_F = \theta_F - \nu \langle |B|^2 \rangle \quad (4.23a)$$

$$\tilde{\theta}_B = \theta_B - \nu \langle |F|^2 \rangle \quad (4.23b)$$

that reduce the counterpropagating Eq. (4.11) to a pair of LLEs coupled via their effective detunings:

$$\partial_t F = S_F - (1 + i\tilde{\theta}_F)F + i|F|^2 F - i\beta \partial_\tau^2 F \quad (4.24a)$$

$$\partial_t B = S_B - (1 + i\tilde{\theta}_B)B + i|B|^2 B - i\beta \partial_\tau^2 B. \quad (4.24b)$$

Taken separately when ignoring the coupling through the effective detunings, each of these LLEs displays a Maxwell point for normal dispersion corresponding to a set of parameter values where solutions made of power plateaus well separated by SFs are stable. For any other parameter value close to the Maxwell point, SFs are observed to move close or away from each other. At the Maxwell point and at the Maxwell point only, the LLE displays a multi-stability of power plateaus solutions with two stationary SFs at arbitrary separations. In gradient systems the Maxwell point corresponds to the parameter value where both bistable homogeneous states have equal energy. In non-gradient system, such

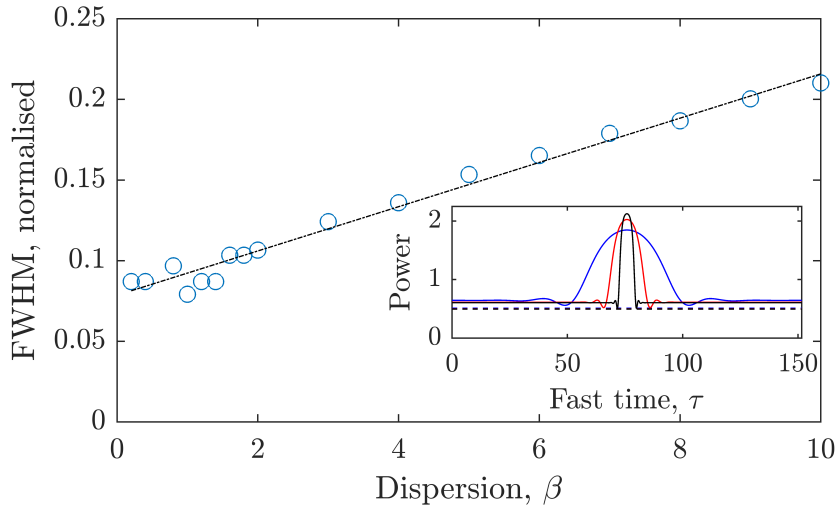


Figure 4.6: Minimum possible FWHM size of bright solitons for different values of the dispersion coefficient β at parameter values $P_F = P_B = 2.1609$, $\theta_B = 3.2$ where θ_F is chosen to provide the narrowest soliton for each value of β . Circles represent the FWHM values from simulations while the dashed line is a linear fit of the data. Inset: Power distribution of three bright solitons of minimum FWHM in the backward field while the forward power remains constant (dashed line) for dispersion values $\beta = 0.1$ (black line), $\beta = 1$ (red line) and $\beta = 10$ (blue line) with increasing FWHM.

as the LLE, Maxwell points and hysteresis can still be possible even though an expression of the energy cannot be obtained.

There are very important differences between our SF states and dark solitons due to global coupling and structures of similar shape in the single LLE with normal dispersion (at the Maxwell point or close to the Maxwell point) studied theoretically in [35, 54] and experimentally in [19–21]. For example, the power of the homogeneous field and the power values of the plateaus before and after the two SFs in the inhomogeneous field are not the values of the HSS studied in Section 4.3. When the values of the two field detunings are well separated, stable SF states are not due to locking mechanisms of the tails of the SFs as for example observed in optical parametric oscillators [120, 121]. However, when the detunings of the two fields are quite close to each other, dark solitons owe their stability to the local oscillations in the lower part of the SF as shown in Fig. 4.5 for $\theta_B = 3.2$ and $\theta_F = 2.8$, 3.4 and 3.6.

When increasing the detuning θ_F while keeping the detuning θ_B fixed, one observes first a decreasing separation between the two stable SFs in the backward field, Fig. 4.5(a) and then, after the symmetric state $\theta_F = \theta_B$, an increasing distance between the two stable SFs in the forward field as seen in Fig. 4.5(b). In the latter case, the power of the homogeneous backward field changes substantially upon variations of $\theta_F > \theta_B$ while the power of the homogeneous forward field changes only a little upon variations of $\theta_F < \theta_B$ (see Fig. 4.5a). This effect is a direct result of the effective detunings that contain the integrals (4.12).

One very interesting feature when scanning one of the detunings (say θ_F) while keeping the other one fixed by changing the input frequency of one of the two pumps, is that upon crossing the symmetric state $\theta_F = \theta_B$, stable SFs and dark solitons switch from one propagation direction (the backward for $\theta_F < \theta_B$) to the other (the forward for $\theta_F > \theta_B$). This provides the operator of this device to select at will the direction, in which the solitary structures and, consequently, an optical frequency comb occurs.

In general $2N$ SFs may coexist within a long cavity. Two examples of stationary states with four SFs are shown in Fig. 4.7(b)-(c). At stationary state, the upper and lower power plateaus connected by the 4 SFs have identical power to the plateaus of the two SF stationary state shown in Fig. 4.7(a). The average power of a $2N$ SF stationary state is also identical to the two SF stationary state. This is due to the Maxwell point condition on the effective detuning. As such the total proportion of the upper and lower plateaus for all $2N$ SF stationary states are identical. This means that the distance between SFs of each pair $\Delta_1, \dots, \Delta_N$ of $2N$ SFs sums up to the SF distance Δ of the two SF stationary state, $\Delta = \sum_{n=1}^N \Delta_n$. In regions of the fast time instability of the HSS, different SF structures may form. Fig. 4.7(d)-(e) shows the spontaneous formation of many SFs from an unstable HSS under the action of noise. The location and separations of SFs of the stationary state [Fig. 4.7(d)] are random, showing plateaus and dark soliton structures coexisting in the cavity, and yet satisfying the constraint on the sum of Δ_n being Δ .

4.5 Distance of two stationary switching fronts

From numerical simulations we obtain stationary solutions with two stable SFs separated by a distance Δ . We aim here to obtain an analytical expression of the the distance Δ when using θ_F as a control parameter.

We start from the case of two SFs in the backward field for a given value of θ_B when changing $\theta_F < \theta_B$ (see Fig. 4.5a). In this case the forward field power $|F|^2$ is homogeneous and appears to be independent of the detuning θ_F . Note that this homogeneous value of the forward power is not the HSS value H_F discussed in Section 4.3. For the stationary solutions we can write:

$$S_F = (1 + i\tilde{\theta}_F)F - i|F|^2F \quad (4.25a)$$

$$S_B = (1 + i\tilde{\theta}_B)B - i|B|^2B + i\beta\partial_z^2 B \quad (4.25b)$$

where we have used Eqs. (4.23a) and (4.23b). Each solution of the backward field equation (4.25b) when changing θ_F has a one to one correspondence with one of the multi-stable stationary solutions of a single Lugiato-Lefever equation (LLE) at the Maxwell point given by

$$S_B = (1 + i\Theta_{\text{MP}})B - i|B|^2B + i\beta\partial_z^2 B \quad (4.26)$$

where Θ_{MP} is the cavity detuning at Maxwell point which depends on the input power P_B . The functional dependence of Θ_{MP} from P_B can be obtained by asymptotic methods close to the critical detuning value $\sqrt{3}$ for $P_B \approx 8\sqrt{3}/9$ and by variational methods for $P_B > 10$ [73]. Neither of these approximations is satisfactory in the range $2 < P_B < 7$ of values used here (see Fig. 4.8). By computing the Maxwell points numerically (see blue

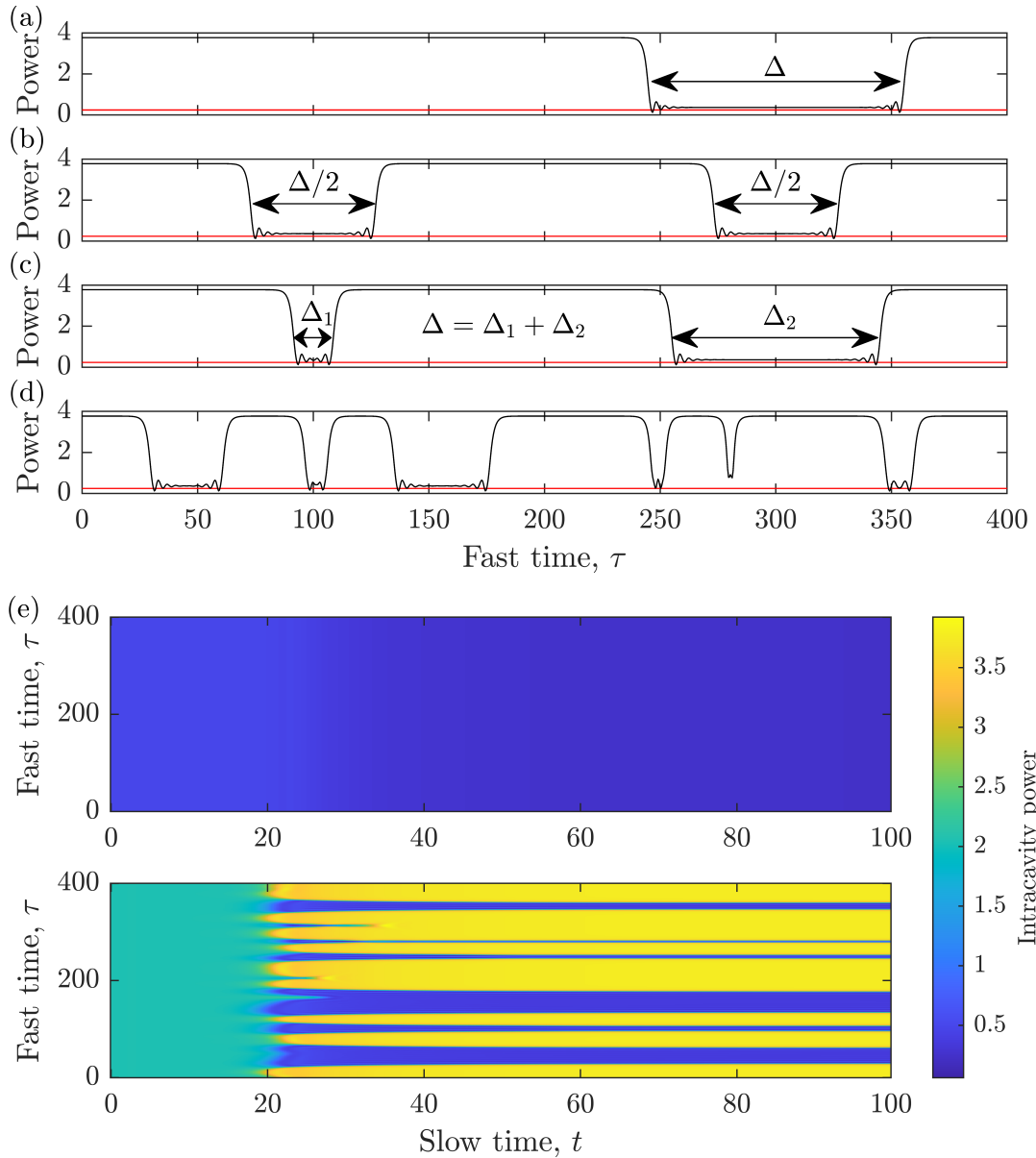


Figure 4.7: (a)-(d). Light plateaus stationary solutions obtained from different perturbations of the HSS, displaying either 2 SFs (a), or 4 SFs (b)-(c), or dark solitons and SFs (d) for $P_F = P_B = 4, \theta_B = 4$ and $\theta_F = 1.9$ ($\Delta \approx 0.3$). A single wide perturbation gives a 2 SF stationary state (a), two perturbations of equal (b) or unequal width (c) give 4 SF stationary states. (d) A stationary state resulting from the spontaneous formation of SFs and dark structures due to small amplitude initial noise. In each case (a)-(d) the average power of the field, and the plateau powers, are identical. (e) Evolution to a stationary state with SFs and dark solitons in the backward field (lower) with flat forward field (upper) due to noise. The final stationary state is shown in (d).

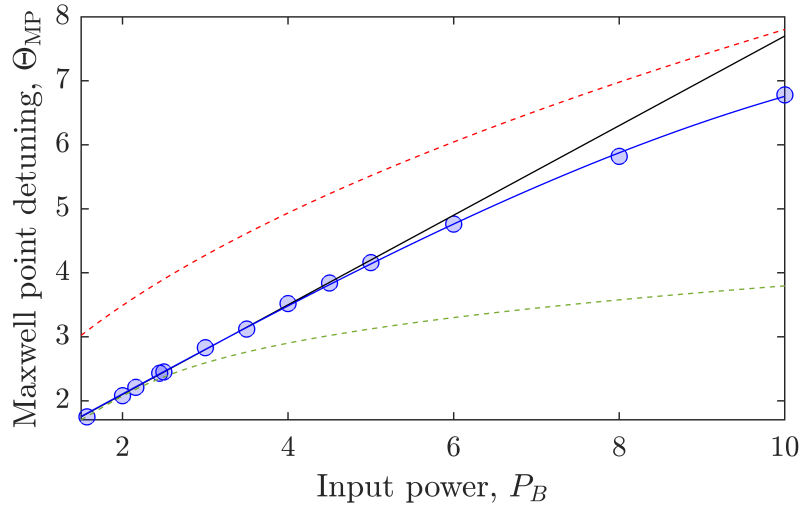


Figure 4.8: The detuning Θ_{MP} of a single LLE (4.26) at the Maxwell point as a function of $P_B = S_B^2$. The circles are numerically evaluated points from which we obtain the linear (Eq. 4.27 in black) and cubic (Eq. 4.28 in blue) fitted curves for the Maxwell point distribution. The dashed green and dashed red curves correspond to the asymptotic and variational methods of [73], respectively.

line in Fig. 4.8) we find that a simple linear dependence of Θ_{MP} from P_B

$$\Theta_{MP} \approx \eta(1 + P_B) \quad (4.27)$$

with $\eta = 0.7$ approximates the numerical values much better in the interval of interest (see black line in Fig. 4.8). Additional terms can be included in the approximation to extend the range of validity to $P_B = 10$

$$\Theta_{MP} \approx \eta(-0.001997P_B^3 + 0.006503P_B^2 + P_B + 1) \quad (4.28)$$

By using the equivalence between (4.25b) and (4.26) as well as the definition of $\tilde{\theta}_B$ in (4.23b) we obtain the value of the power of the homogeneous forward field for the SF state in the backward field:

$$\langle |F|^2 \rangle = |F|^2 = \frac{1}{\nu}[\theta_B - \Theta_{MP}] \approx \frac{1}{\nu}[\theta_B - \eta(1 + P_B)] \quad (4.29)$$

As shown in the numerical simulations of the two SFs for $\theta_F < \theta_B = 3.2$ in Fig. 4.5(a), $|F|^2$ is independent of the control parameter θ_F and its value is just below 0.5 for the case of $P_B = 2.1609$, in agreement with (4.29). The power $Y_B = |B|^2$ of the homogeneous states of (4.26) satisfies

$$Y_B^3 - 2\Theta_{MP}Y_B^2 + (1 + \Theta_{MP}^2)Y_B - P_B = 0 \quad (4.30)$$

from which it is possible to obtain the values of the plateau powers Y_B^+ and Y_B^- where the

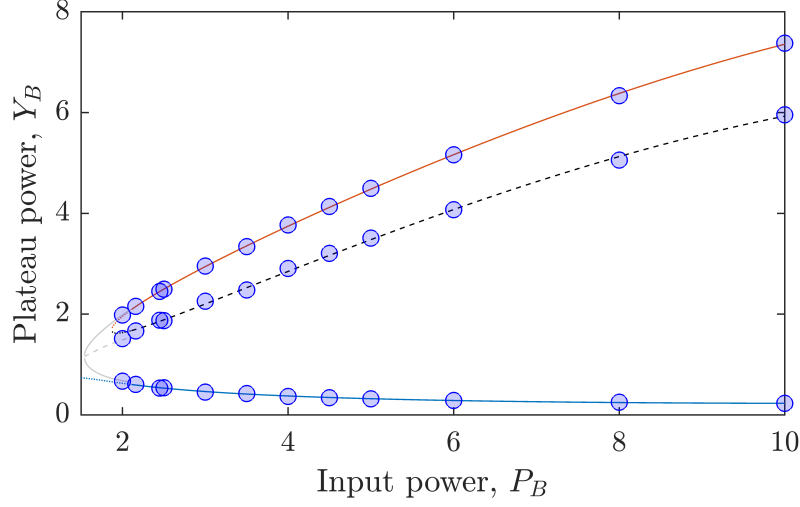


Figure 4.9: Power Y_B of the homogeneous solutions before and after a SF for a single LLE at Maxwell point (4.30). SFs are possible after the onset of bistability at critical pump power $P_B \approx 8\sqrt{3}/9$ where the higher Y_B^+ (red) and the lower Y_B^- (blue) branches are stable but the dashed middle solution is unstable. The Maxwell point detunings Θ_{MP} are approximated by (4.28) for $P > 2.1$ and by an asymptotic approach for $P < 2.1$. The blue circles are homogeneous solutions before and after a SF from the simulation of (4.11a)-(4.11b).

SFs start and end. Note that since Θ_{MP} does not depend on θ_F , Y_B^+ and Y_B^- also do not depend on θ_F as shown in Fig. 4.5 for the SF states. Comparison of Y_B^+ and Y_B^- obtained from (4.30) with the numerical evaluation of Θ_{MP} and with the approximate expression (4.28) are shown in Fig. 4.9 in the interval of interest for P_B between 2 and 10.

It is now possible to obtain an expression for the stationary distance Δ of the two SFs. In the zero dispersion case $\beta = 0$, the SFs are vertical lines between Y_B^+ and Y_B^- so that

$$\begin{aligned} \langle |B|^2 \rangle &= \Delta Y_B^- + (1 - \Delta) Y_B^+ \\ \Delta &= \frac{Y_B^+ - \langle |B|^2 \rangle}{Y_B^+ - Y_B^-} \end{aligned} \quad (4.31)$$

However from (4.25a) one obtains:

$$\langle |B|^2 \rangle = \frac{1}{\nu} \left[\theta_F - |F|^2 \pm \sqrt{\frac{P_F}{|F|^2} - 1} \right] \quad (4.32)$$

where P_F is the forward input power S_F^2 and $|F|^2$ is given by Eq. (4.29). Hence the combinations of Eq. (4.30) and Eq. (4.32) provide an expression of the distance Δ between the two SFs at zero dispersion via Eq. (4.31) in terms of parameters θ_F , θ_B , P_F , P_B (see the black line in Fig. 4.10 for $P_F = P_B = 2.1609$, $\theta_F = 1.4$, $\theta_B = 3.2$). For dispersion different from zero, the distance Δ remains unchanged as shown in Fig. 4.10 for $\beta = 5$

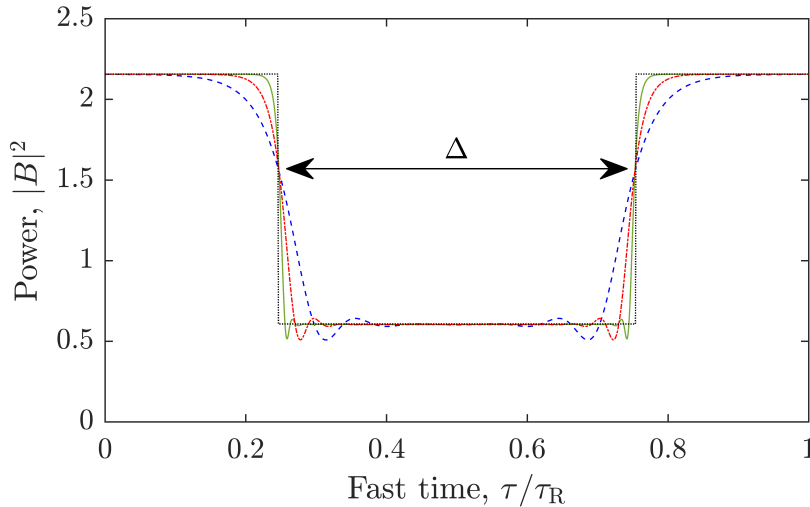


Figure 4.10: Power distribution of an inhomogeneous B field exhibiting two non-interacting SFs with separation Δ for parameter values $P_F = P_B = 2.1609$, $\theta_F = 1.4$, $\theta_B = 3.2$ and dispersion coefficient $\beta = 5$ (blue dashed line), $\beta = 1$ (red dashed dotted line), $\beta = 0.1$ (green line), and $\beta = 0$ (black dotted line). Here the fast time (x axis) is normalised to the round trip time.

(blue line), $\beta = 1$ (red line), $\beta = 0.1$ (green line). This means the second order dispersion β affects the steepness of SFs but does not change the pulse duration (SF distance) of the output for non-interacting SFs.

When using θ_F as a control parameter, expression (4.31) works very well when compared with the distance of two stationary SFs obtained from the simulations of Eqs. (4.11) done with $\beta = 1$, see left hand side of Figs. 4.11(a)-(b). In particular we note that Δ is a function of θ_F only through $\langle |B|^2 \rangle$ as expressed in Eq. (4.32). This means that the distance Δ decreases linearly with θ_F with a slope given by $[\nu(Y_B^+ - Y_B^-)]^2$. Once the detuning $\theta_F < \theta_B$ and the input powers P_B and P_F are chosen, it is possible to obtain accurately the distance of the two SFs from Eq. (4.31) even in the regime of small distances and locked SFs (dark solitons) as shown in Fig. 4.11.

The conditions of validity of Eqs. (4.29) and (4.32) predict that two stable SFs can be found in the interval $\eta(1 + P_B) < \theta_B < \nu P_F + \eta(1 + P_B)$, given that $0 < \Delta < 1$. This allows us to determine regions in parameter space where vertical SF form as shown in 4.11(c)-(d). It is interesting to see that for values of $P_B > 2.145$ where stable SFs in the backward field are observed even for $\theta_F > \theta_B$, the predictions of Eq. (4.31) remain in good agreement with the numerical results (see red lines on the left of Fig. 4.11 (a)-(b) for $P_B = P_F = 3$).

Eqs. (4.29) and (4.31) suggest that precise control over the pulse duration (SF distance) of the output field is possible by simply changing the laser detuning. This allows for control over the frequency comb generation efficiency by laser parameters in contrast with conventional microresonator dark solitons, where the pulse duration is determined by the dispersion.

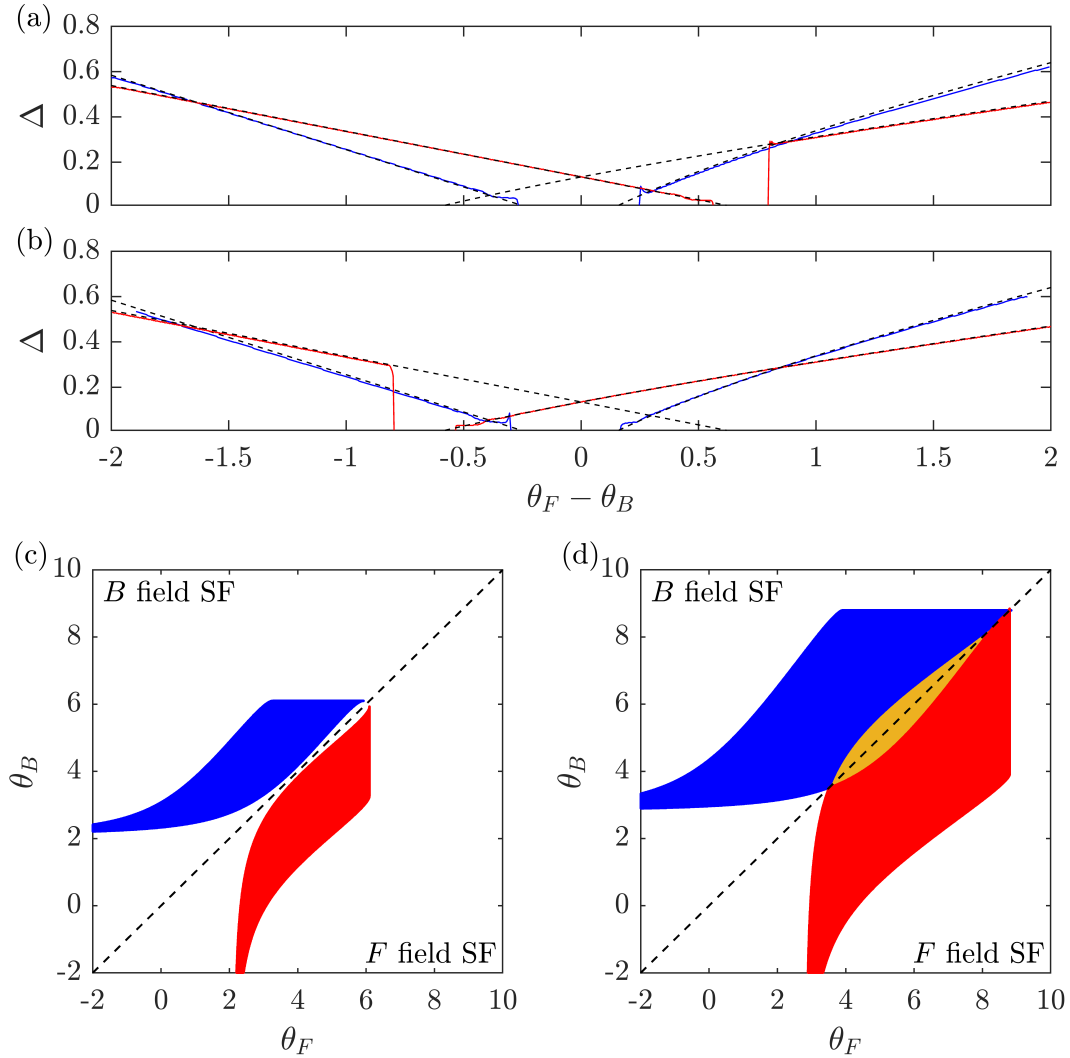


Figure 4.11: (a)-(b) SF separation Δ when changing the detuning θ_F for fixed pump powers $P_F = P_B$ and detuning θ_B . Solid black (solid red) lines correspond to simulation results from (4.11a)-(4.11b) with $\beta = 1$ and for $P_F = P_B = 2.1609$, $\theta_B = 3.2$ ($P_F = P_B = 3$, $\theta_B = 5$). (a) is a forward scan and (b) is a backwards scan. The blue dashed lines are the analytical results of Eqs. (4.31) and (4.36). (c)-(d) Range of detuning values where SF solutions exist and are stable for the B field (blue region) and for the F field (red region) or both fields (orange region), (c) $P_F = P_B = 2$ and (d) $P_F = P_B = 3$.

We now move to the case $\theta_F > \theta_B$. In this case it is the backward field B that is homogeneous and the two stable SFs are found in the forward field F . In this case the role of Eqs. (4.25a)-(4.25b) is exchanged:

$$S_F = (1 + i\tilde{\theta}_F)F - i|F|^2F + i\beta\partial_\tau^2 F \quad (4.33a)$$

$$S_B = (1 + i\tilde{\theta}_B)B - i|B|^2B \quad (4.33b)$$

and one obtains $\Theta'_{\text{MP}} \approx \eta(1 + P_F)$ as well as:

$$\langle |B|^2 \rangle = |B|^2 = \frac{1}{\nu}[\theta_F - \Theta'_{\text{MP}}] \approx \frac{1}{\nu}[\theta_F - \eta(1 + P_F)] \quad (4.34)$$

In the case of $\theta_F > \theta_B$, the homogeneous power of the backward field grows linearly with θ_F , which agrees with the simulation in Fig. 4.5(b). The form of the equation for the power $Y_F = |F|^2$, however, remains basically unchanged from Eq. (4.30),

$$Y_F^3 - 2\Theta'_{\text{MP}}Y_F^2 + (1 + (\Theta'_{\text{MP}})^2)Y_F - P_F = 0 \quad (4.35)$$

so that the homogeneous powers Y_F^+ and Y_F^- before and after the SFs are still independent from θ_F and, in the case of $P_F = P_B$, they have the same values of Y_B^+ and Y_B^- found for $\theta_F < \theta_B$ since $\Theta'_{\text{MP}} = \Theta_{\text{MP}}$. Finally,

$$\begin{aligned} \langle |F|^2 \rangle &= \Delta Y_F^- + (1 - \Delta)Y_F^+ \\ \Delta &= \frac{Y_F^+ - \langle |F|^2 \rangle}{Y_F^+ - Y_F^-} \end{aligned} \quad (4.36)$$

and

$$\langle |F|^2 \rangle = \frac{1}{\nu} \left[\theta_B - |B|^2 \pm \sqrt{\frac{P_B}{|B|^2} - 1} \right] \quad (4.37)$$

The distance Δ depends on θ_F through $\langle |F|^2 \rangle$ and then through $|B|^2$ given in Eq. (4.34) and (4.37). At difference from the case $\theta_F < \theta_B$ this dependence is nonlinear, the slope of the curve is reversed and the distance Δ now grows with the detuning θ_F . The agreement of Eq. (4.36) with the numerical simulations as shown in the right hand part of Fig. 4.11 is again excellent. Similar to the B field case, the conditions of existence of vertical SFs for the F field is $\eta(1 + P_F) < \theta_F < \nu P_F + \eta(1 + P_F)$ given that $0 < \Delta < 1$ [see Fig. 4.11(c)-(d)].

4.6 Evolution towards the two switching-front solutions

Despite the one to one correspondence of the SF solutions of the counterpropagating system and those of the LLE at Maxwell point, the dynamics of front solutions in the counterpropagating system are different from those seen in the LLE. Here we describe first the transient evolutions of a two SF solution in the counterpropagating system as the SFs move towards the unique stationary separation of the fronts.

In Fig. 4.4, we have seen that when the HSS of the counterpropagating system are

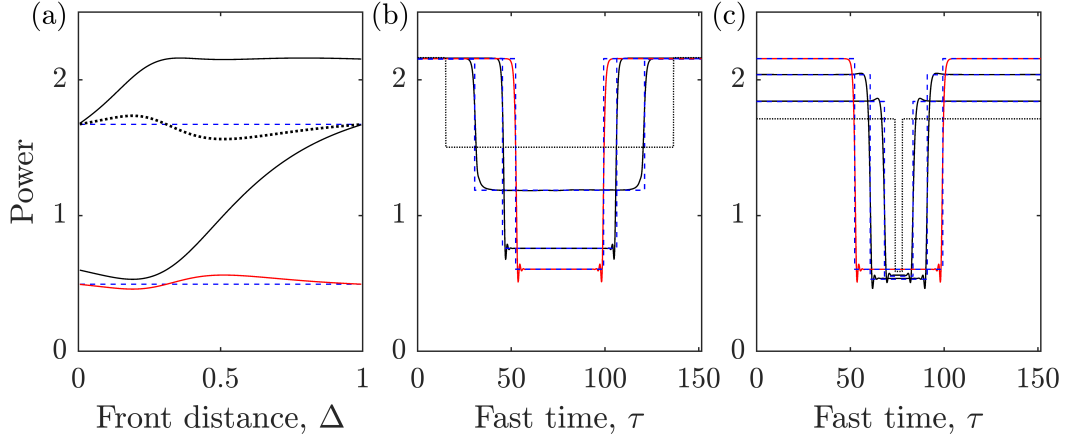


Figure 4.12: (a) Power of the homogeneous states Y_B^\pm connected by the SFs (solid black line), homogeneous field power H_F (solid red line), and average power of the field displaying SFs (dotted black line) versus the front separation is changed. The HSS in the absence of SFs is given by the dashed blue lines. (b)-(c) Comparison between the zero dispersion two front solutions using Eqs. (4.38)-(4.39) (dashed blue lines) and evolving two front solutions from the numerical integration of Eqs. (4.25a)-(4.25b) with $\beta = 0.1$ (solid lines) for shrinking front distance (b) and expanding front distance (c). The dotted black lines are the initial conditions. Parameter values are $P_F = P_B = 2.1609$, $\theta_F = 2.0$, and $\theta_B = 3.2$. The final and stationary front separation (thick red line) is $\Delta = 0.31$ in both (b)-(c).

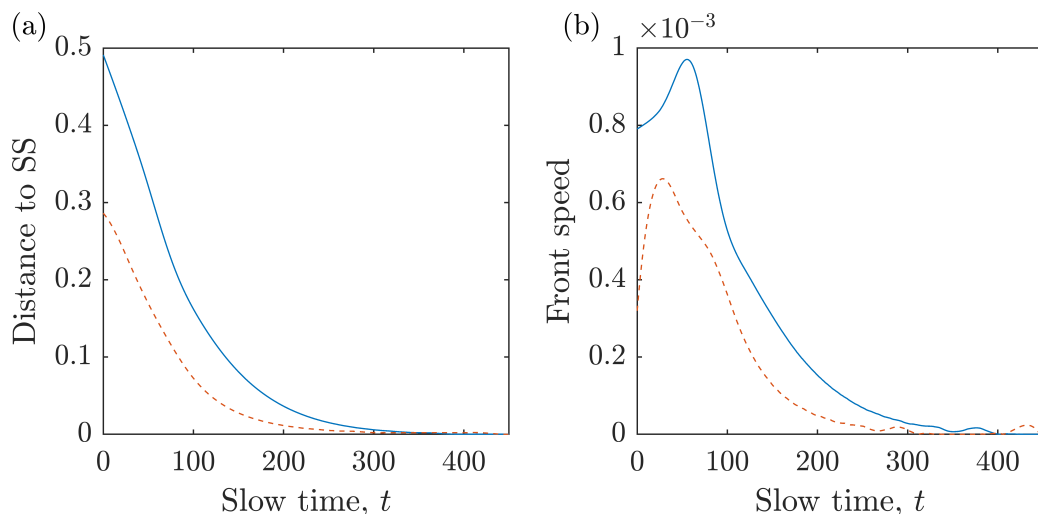


Figure 4.13: Front separation (a) and front velocity (b) vs slow time while approaching a SF solution. From the data from Fig. 4.4, we track the front separation relative to the separation of the final SF solution in (a), use the dimensionless slope of (a) to determine the front speed in (b). Solid blue line represents the wide initial condition, red dashed line the narrow initial condition.

unstable to inhomogeneous perturbations, the system relaxes to a SF solution. We consider here initial conditions made of two SFs between two homogeneous states in one field (the backward one for $\theta_F < \theta_B$) while the other field is homogeneous across the resonator. When the front separation is not at the stationary value, the values of the homogeneous states at the beginning and at the end of each front in the counterpropagating system depend on the average power of the fields. This means that these values are different from those at the final front separation at the stationary value. The values of the homogeneous power before and after a front for arbitrary separations can be calculated by considering states of the zero dispersion case of Eqs. (4.11), where the second order derivative with respect to the fast time and the first derivative with respect to the slow time are neglected. For a two front solution in the B field, the upper and lower homogeneous solutions separating the SFs can be determined by solving the coupled equations

$$P_B = Y_B^3 - (\theta_B - \nu Y_F) Y_B^2 + [(\theta_F - \nu Y_F)^2 + 1] Y_B \quad (4.38)$$

$$P_F = Y_F^3 - (\theta_F - \nu[\Delta Y_B^- + (1 - \Delta) Y_B^+]) Y_F^2 + [(\theta_F - \nu[\Delta Y_B^- + (1 - \Delta) Y_B^+])^2 + 1] Y_F \quad (4.39)$$

where Y_B^+, Y_B^- are the upper and lower homogeneous solutions of the zero dispersion SF solution present in the B field (solutions of Eq. (4.39) in a bistable state) with average power $\langle |B|^2 \rangle = \Delta Y_B^-(\Delta) + (1 - \Delta) Y_B^+(\Delta)$ and Δ is the front separation. Note that the expressions for the average powers of front solutions are independent of dispersion. These solutions are plotted in Fig. 4.12a.

Fig. 4.12(b) and (c) show that two-front profiles that use the solutions of Eqs. (4.38)-

(4.39) with a given separation Δ provide excellent approximations to the numerical solutions of Eqs. (4.25a) and (4.25b) with $\beta = 1$ during the transients to the the final SF solution for both cases of shrinking and expanding front separation. The SFs are moving with opposite velocities and with a well defined distance $\Delta(t)$. For each value of the slow time t and distance $\Delta(t)$, the dynamical solution is well approximated by two SFs between homogeneous states provided by Eqs. (4.39) given a separation distance Δ . Since for each value of θ_F there is only one stationary value of Δ , generic separations of the two SFs separated by homogeneous power from Eqs. (4.39) evolve in time but maintain their shape with a changing separation leading to different homogeneous powers. As such the front separation determines the power of homogeneous solutions, which in turn determines the velocity of the SFs, which in turns changes the front separation. This leads to a front velocity that depends on the front separation.

Although the shape of the transient solutions are well approximated by two vertical SFs at every moment in time, the front separation and the front velocity are non-trivial functions of time as shown in Fig. 4.13. The instantaneous velocity of the SF can be considered equivalent to the velocity of a SF of an LLE with identical input field, S , and and effective detuning, θ_{eff} , and cavity round trip τ_R .

4.7 Oscillatory dynamics and bistability with front stationary states

Dynamical regimes in ring resonators have been previously studied for homogeneous counterpropagating fields with symmetrical input fields and detunings [96,97]. It was seen that under the correct conditions, a pair of oppositely directed Hopf bifurcations can occur when changing the detuning $\theta_F = \theta_B$, allowing for sustained homogeneous oscillations that could exhibit period doubling bifurcations, chaos and crisis events. In Section 4.3 we saw oppositely directed Hopf bifurcation for the HSS occurring when changing θ_F in an asymmetric regime of different detunings between the two counterpropagating waves since θ_B is kept fixed (which can be seen in Fig. 4.2 as the dotted line in the interval $4.02 < \theta_F < 6.33$). These Hopf bifurcations affect the highest power HSS resulting in oscillations which are bistable with the lowest power HSS. An example of large homogeneous oscillations in the power of the two fields is displayed in Fig. 4.14(a) from simulations of Eqs. (4.11).

In the parameter region of Fig. 4.14, the HSS of large powers are unstable not only to homogeneous oscillations but also to local perturbations on the fast time scale (see the line marked with ‘o’ in the interval $3.35 < \theta_F < 6.47$ in Fig. 4.2). We find that depending on the initial condition, the system can evolve to either the homogeneous oscillations of Fig. 4.14(a) or to a SF solution in the forward field with a homogeneous backward field [see Fig. 4.14(b)] or to a HSS corresponding to low powers. To display the richness of possible asymptotic states of Eqs. (4.11), we show in Fig. 4.15 the asymptotic trajectories of oscillating homogeneous fields, the asymptotic trajectories of the SF state and the asymptotic points of the HSS of low powers in the phase (Argand) plane for the same parameters of Fig. 4.14. Depending on the initial condition, the micro-ring device can evolve to any of these three final states generating either large amplitude slow oscillations

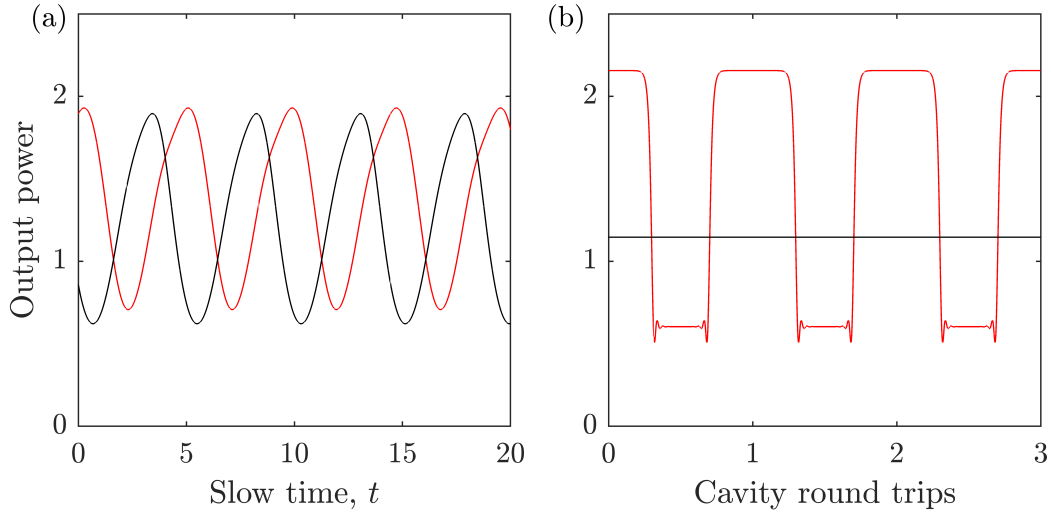


Figure 4.14: Bistability of slow and fast oscillations for parameter values $\beta = 1$, $P_F = P_B = 2.1609$, $\theta_F = 4.5$, and $\theta_B = 3.2$. (a) Periodic oscillations of the homogeneous powers of both counterpropagating fields over the slow time. (b) Output power of a SF solution in the forward field (red line) and homogeneous steady state for the backward field (black line) over three cavity round trip times.

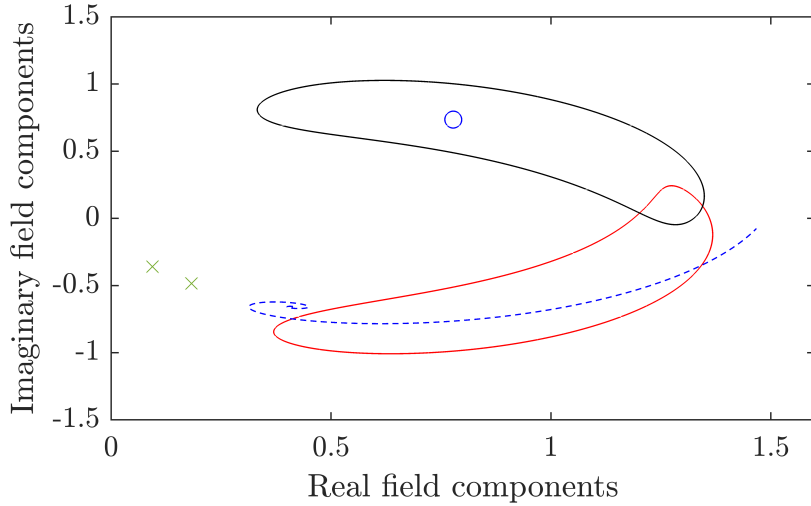


Figure 4.15: Possible asymptotic states for $\beta = 1$, $P_F = P_B = 2.1609$, $\theta_F = 4.5$, and $\theta_B = 3.2$ in the phase (Argand) plane. Stable limit cycle trajectories of the homogeneous forward (red solid line) and backward (black solid line) fields; stable SF solution of the forward field (blue dashed line) and its homogeneous backward field (blue circle); stable HSS of low powers (green Xs for forward and backward fields).

in both fields, or large amplitude fast oscillations in just one field (the forward one) or no output oscillations at all. This provides the operator with a remarkable number of output waveforms with possible selection of each one by suitable perturbation of the input fields (in their amplitude or phase). It is possible to generate light plateau states using a transient pulsing input field containing sudden step to provide perturbations to the HSS.

When scanning the forward detuning for the parameter values studied here, we do not observe period doubling bifurcations or deterministic chaos at difference with typical simulations at parameter symmetry [38, 96, 97]. We observe however sudden crises when the stable trajectory of the limit cycle can intersect the unstable HSS in the regions of multiple stationary states. This results in sudden instabilities of the oscillations, which collapse to the lower stable HSS. In Fig. 4.16 we show simulations of counterpropagating fields when scanning the detuning θ_F forwards and backwards. Forward and backward Hopf bifurcations can be clearly seen in the forward scan at $P_F = P_B = 1.95$ in Fig. 4.16(a) where the dotted lines represent the maxima and minima of the oscillating powers of the homogeneous fields over slow time variations. When increasing the input power, attractor crises are observed both in the forward (at $\theta_F \approx 5.05$) and in the backward (at $\theta_F \approx 5.62$) scans [see Fig. 4.16(b)-(c)] leading to transfers to the low power HSS. Note however that depending on the initial condition of the backward scan, there is the possibility of observing no oscillations and no crises as displayed in Fig. 4.16(d).

Fig. 4.16 focuses on homogeneous oscillations and HSS of low powers. The situation is further complicated by the presence of SF states in the forward field with a homogeneous backward field. When changing θ_F there is a further temporal instability of the SF solutions which causes the homogeneous states connecting the SFs to start to oscillate resulting in the entire inhomogeneous structure to oscillate, along with homogeneous oscillations of the backward field. For $\theta_F < 5.35$ these oscillations are damped allowing for stable SF states, but for $5.35 < \theta_F < 6.25$ such oscillations grow, destroying fast time structures and the system moves to the HSS corresponding to low powers as shown in Fig. 4.17.

The linear stability of SF solutions can be determined at zero dispersion using the expressions for the average field powers derived earlier in this section. Considering a SF solution in the backward field with a homogeneous forward field, their average powers are given by Eqs. (4.32) and (4.35), respectively. As calculated in Appendix A.3 the stability of the homogeneous states before and after the SFs to fast time (fast time) perturbation are given by the eigenvalues

$$\lambda_B^+ = -1 \pm \sqrt{(\Theta_{\text{MP}} - Y_B^+)(3Y_B^+ - \Theta_{\text{MP}})} \quad (4.40a)$$

$$\lambda_B^- = -1 \pm \sqrt{(\Theta_{\text{MP}} - Y_B^-)(3Y_B^- - \Theta_{\text{MP}})}. \quad (4.40b)$$

These eigenvalues depend on the pump power only. When changing the detuning θ_F , the corresponding SF solution maps into one of the multi-stable two SF solutions of an LLE at Maxwell point. The homogeneous forward field eigenvalues are

$$\lambda_F = -1 \pm \sqrt{(\tilde{\theta}_F - Y_F)(3Y_F - \tilde{\theta}_F)} \quad (4.41)$$

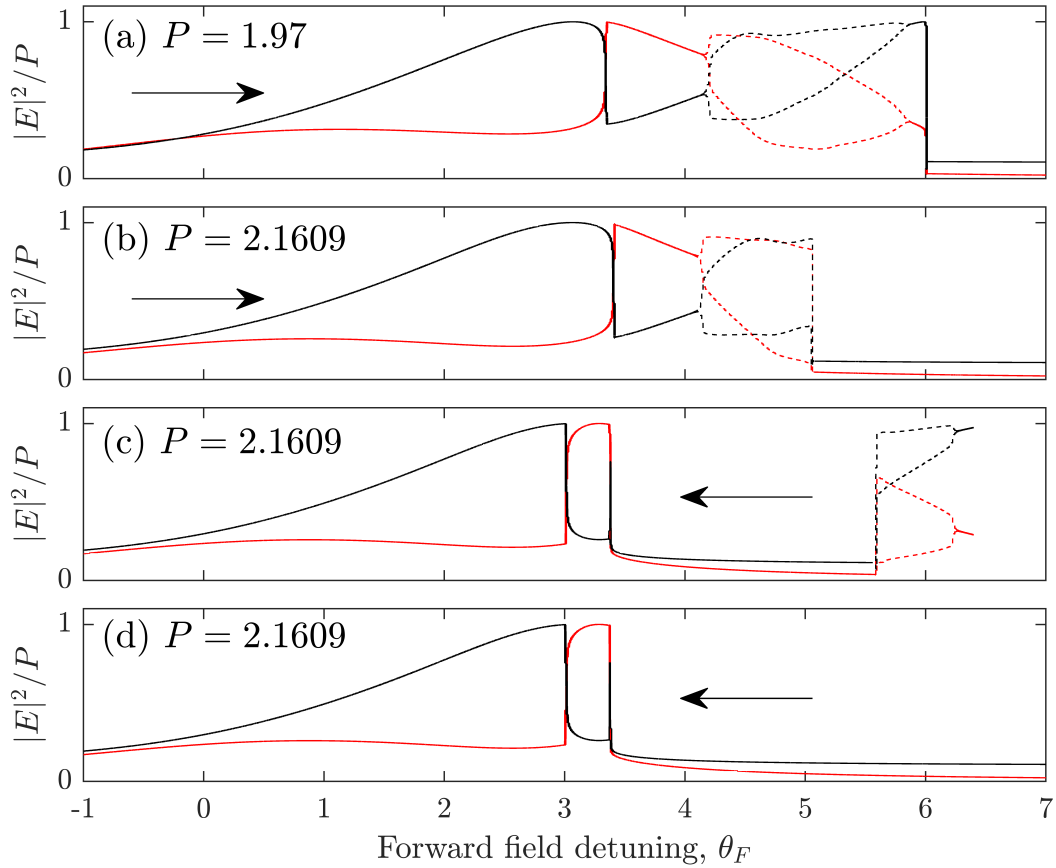


Figure 4.16: Homogeneous field powers (black line backward field, red line forward field) when scanning the detuning θ_F for fixed detuning $\theta_B = 3.2$ and fixed equal pump powers $P = P_F = P_B$. Dashed lines correspond to the power extrema during oscillation. (a) Forward scan for $P = 1.95$. Limit cycle oscillations are present in the detuning range $4.2 < \theta_F < 5.9$. (b) Forward scan for $P = 2.1609$. Limit cycle oscillations are present in the detuning range $4.1 < \theta_F < 5.1$. (c) Backward scan for $P = 2.1609$ starting at $\theta_F = 6.4$. Limit cycle oscillations are present in the detuning range $5.5 < \theta_F < 6.2$. (d) Backward scan for $P = 2.1609$ starting at $\theta_F = 7.0$. No oscillations observed.

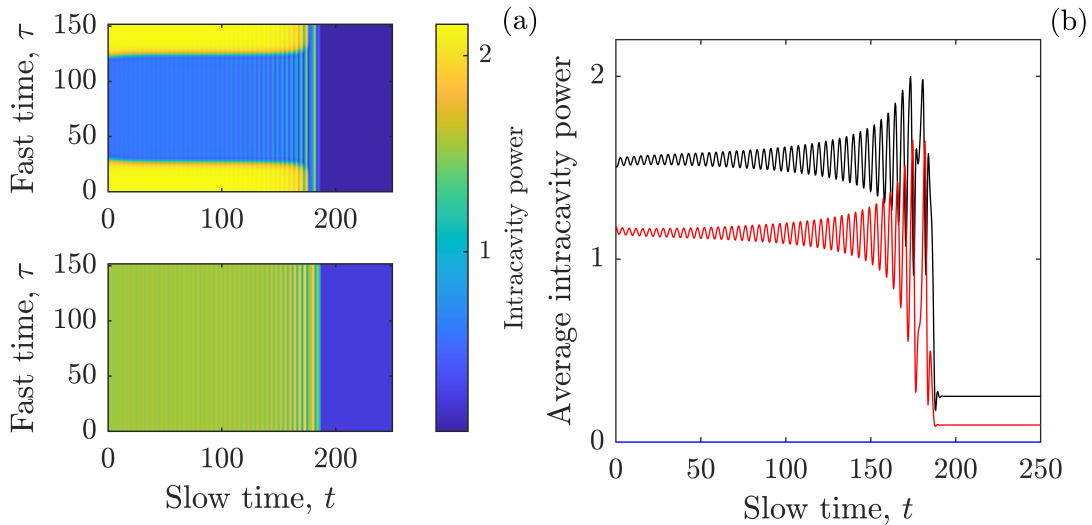


Figure 4.17: Dynamical evolution from an initial condition of a two SF solution in the forward field and a homogeneous solution in the backward field for $P_F = P_B = 2.1609$, $\theta_F = 5.3$, $\theta_B = 3.2$. Oscillations grow until both fields reach the stable HSS of low powers. (a) Intracavity power of the forward (upper) and backward (lower) fields over slow time. (b) Average interactivity power of the forward (red) and backward (black) over slow time.

where $\tilde{\theta}_F = \theta_F - \nu \langle |B_s|^2 \rangle$ is the effective detuning, and depend on θ_B implicitly through the integrated power $\langle |B|^2 \rangle$.

By using the stability eigenvalues λ_B^\pm and λ_F it is possible to determine instabilities of the SF solutions when the real part of one of these eigenvalues goes from negative to positive. For example plateau solutions separated by SF are susceptible to Hopf bifurcations and oscillations of the homogeneous states that are connected to the SFs. This instability is introduced by perturbations to the SF states that change the average power of the field as seen in Appendix A.3. For the parameter values used in this work $P_F = P_B = 2.1609$, $\theta_B = 3.2$, these oscillations grow in the region $5.35 < \theta_F < 6.25$ resulting in the collapse of local structures to the HSS.

4.8 Conclusions

We have investigated the effects of global average coupling induced by the interaction of two input beams counterpropagating in a ring resonator with normal dispersion. In particular, we find novel stationary states of light plateaus that are separated by two switching fronts. By controlling the input laser frequency detuning, the propagation direction of the light plateau states can be switched between clockwise and counterclockwise. We have derived semi-analytical expressions of the distance between stable switching fronts and the powers of the plateaus as a function of the detunings. These expressions rely on the knowledge of the Maxwell point location in the parameter space of the LLE. By using a numerical fit from LLE simulations, we found excellent agreement between the obtained formulas and the numerical simulations. Maxwell point locations can also be determined

by asymptotic or variational approaches [73] but at the detriment of the agreement with numerical simulations. Apart from being present in only one of the two counterpropagating fields, light plateaus in our global system are unusual in that they have power values different from the homogeneous steady states of the system. Global average coupling introduces a balancing of areas associated with the two plateau powers resulting in a controllable distance of two stationary SFs by the detunings which in turn can be tuned by changing the frequency of the input fields. Robust SF solutions are present for large ranges of detuning allowing great control over the distance of the two SFs through the laser parameters. This allows the user to precisely control the pulse duration of the output field, and hence the frequency comb generation efficiency by changing the input fields detuning. The second order dispersion determines the steepness of SFs with no effect on the pulse duration when well separated. This is different from conventional microresonator dark and bright solitons, whose width is determined by second order dispersion. In addition we find that changing the laser detuning across the symmetric state results in the SF solutions to disappear from one field and then to reappear in the other field. This results in the SFs switching direction in the microresonator while scanning a single detuning parameter thus allowing for a corresponding switch of the beam where a frequency comb is generated.

The analytic description of SF and plateaus extends to transient states, allowing us to describe the changes of plateau power and SFs separation as they move towards the final stationary state corresponding to a given SF separation.

We have also investigated oscillations in symmetry broken ($\theta_F \neq \theta_B$) counterpropagation. We have identified stable limit cycle oscillations in detuning symmetry broken regimes, and observed sudden crisis in which the oscillations become unstable due to a collision with an unstable HSS. Stable oscillatory dynamics coexist with SF solutions for large ranges of parameter values. We have even identified a multi-stability of oscillations with SF solutions and the lowest power homogeneous stationary state. Depending on the initial condition, the micro-ring device can evolve to any of these three final states generating either large amplitude slow oscillations in both fields, or large amplitude fast oscillations in just one field or no output oscillations at all. This provides the operator with a remarkable number of output waveforms with possible selection of each one by suitable perturbation of the input fields (in their amplitude or phase).

Microresonator systems have undergone much study in recent years. All our predictions have been obtained for realistic parameters with possible experimental verification in a variety of ring resonator setups, from micro-ring to fibre loops. Frequency comb generation has also been demonstrated using two lasers for bichromatic pumping of a micro-ring resonator for the generation of dark bright solitons [140]. A modification to this setup to incorporate bidirectional pumping should allow for the generation of counterpropagating SF states. Single input laser setups in the presence of back scattering have indeed predicted and observed Maxwell point front solutions in micro-ring resonators [73, 74]. Back scattering of the pump laser results in a counterpropagating field, allowing for a single laser setup to produce plateaus that can be the result of extending our model to these configurations.

Configurations of alternating SF and light plateaus in only one field are not just interesting for their fundamental features being related to global coupling of two waves and integro-partial-differential equations. The robust, highly configurable, and controllable

SFs solutions of counterpropagating light can be useful in many real world applications such as all optical oscillators, optical computing, time reversal symmetry breaking, and signal routing in telecommunication systems. Future considerations for this system include a pulse driving configuration in one or both of the input fields. The results presented in this chapter can be further enhanced by polarisation considerations of the counterpropagating fields. This would introduce additional spontaneous symmetry breaking between polarisation modes similar to those observed in [66, 68, 157].

Chapter 5

Dark Solitons in Fabry-Pérot Resonators

5.1	Introduction	95
5.2	Fundamentals of Fabry-Pérot resonators	96
5.2.1	The Fabry-Pérot cavity	96
5.2.2	Resonance enhancement	98
5.2.3	Coupling efficiency	99
5.2.4	Cavity finesse and quality factor	99
5.3	The Fabry-Pérot model	100
5.4	Homogeneous solutions and fast time dynamics	104
5.4.1	Homogeneous stationary solutions	105
5.4.2	Plateau solutions	105
5.5	Linear stability analysis of plateau solutions in slow time	107
5.5.1	Turing pattern instability	107
5.5.2	Homogeneous instability of plateaus	108
5.6	Localised solutions	109
5.6.1	Switching fronts and their dynamics	110
5.6.2	Dark cavity solitons	114
5.7	Oscillatory dynamics of dark solitons	117
5.8	Conclusions	119

5.1 Introduction

We continue our discussion of dissipative cavity solitons in this chapter, but at a difference to the ring resonator system described in the previous chapters, here we consider the Fabry-Pérot (FP) resonator. The FP resonator was originally conceived in 1899 by Charles Fabry and Alfred Pérot [161] to study fine details in the spectrum of light for application in high-resolution spectroscopy. They used two parallel and highly reflective mirrors, forming an optical cavity. Light within the cavity undergoes multiple reflections, back and forth between the mirrors, where a fraction of the light is transmitted through the mirrors upon each reflection. The phase sensitive interactions of the forward and backward propagating interactivity fields result in standing wave resonant modes. This creates sharp interference fringes that can be analysed to determine spectral components with high precision. When temporally coherent light is coupled into the cavity, the electric field between the mirrors may present a resonance enhancement of the optical power due to constructive interference between the driving field and circulating field. By enclosing a nonlinear medium between the mirrors, nonlinear optical phenomenon (such as the Kerr effect) may be enhanced at lower driving powers [162, 163].

The generation of temporal cavity solitons (TCS) within FP resonators has seen a flurry of interest, where in recent years the regime of anomalous group velocity dispersion has been investigated, first analytically [48, 49] and then experimentally demonstrated for continuous wave [29, 50] and pulsed [52, 53] driving. The generation of frequency combs produced by modulation instabilities and Turing patterns have also been demonstrated in FP resonators [51]. We note that dark and bright solitons as well as plateau solutions have also been discussed in compound resonator systems such as the time-delayed Gires-Tournois interferometers formed by a FP cavity and external mirrors [158, 159]. This has resulted in increasing interest in geometrically linear resonators for the generation of TCS as the FP cavity can offer additional engineering possibilities when compared to a ring resonator for tailoring dispersion and allowing for greater control over the bandwidth and temporal duration of cavity soliton pulses. Such possibilities include the engineering of the core-cladding index [160], analogous to the engineering of ring resonator geometry, or the design of the mirror dispersion [29].

This chapter proceeds as follows: In Section 5.2, we introduce the FP resonator, discussing generally the physics and operation of the cavity for the purpose of enhancing nonlinear optical effects. This culminates in Section 5.3, where we derive the equation of the a FP resonator (as first derived in [48]) filled with a Kerr nonlinear medium and investigate the inherent counterpropagation of light under normal dispersion conditions. We review the existence and stability of the homogeneous stationary states (HSS) of the FP configuration in Section 5.4, then investigate the conditions required for the existence of local structures (switching fronts [SF] and dark cavity solitons [DCS]) in Section 5.5. We first characterise the bistable homogeneous states (plateaus) from which local structures hang, and analyse their stability in the fast time, in Section 5.5.1, and in the slow time, in Section 5.5.2. Solutions containing moving fronts exist and are described in Section 5.6.1, where we discuss how the FP configuration results in many unstable stationary solutions, which are instead stable in the equivalent ring resonator seen in Chapter 4. Nonetheless, we describe the DCS stationary solutions of the FP resonator in Section 5.6,

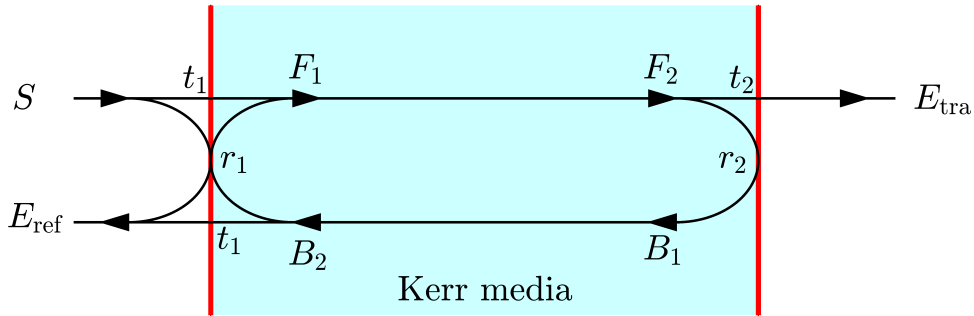


Figure 5.1: A schematic representation of a Fabry-Pérot resonator composed of two mirrors (red lines) filled with a Kerr nonlinear media, and operating at steady state. The incident field S is coupled into the resonator via one of the mirrors, with reflection and transmission coefficients r_1, t_1 . Incident light injected or reflected by the mirror takes contributions from the circulating field with $F_1 = t_1 S - r_1 B_2$ and $E_{\text{ref}} = r_1 S + t_1 B_2$, respectively. The intracavity field is decomposed into forward and backward propagating components F, B , which accumulate phase θ as they travel between the mirrors $F_2 = a \exp(i\theta) F_1, B_2 = a \exp(i\theta) B_1$, where a accounts for propagation losses. At the feedback mirror, light may be reflected back into the cavity $B_1 = -r_2 F_2$, or transmitted out of the cavity $E_{\text{tra}} = t_2 F_2$ with reflection and transmission coefficients r_2, t_2 .

which are found to be detuning shifted with respect to those in a ring resonator by the average power of the field over a round trip of the cavity, and are described by a modified LLE. This is a result of an additional nonlocal coupling term exhibited by the FP model originating from counterpropagation of the intracavity fields. To properly elucidate the effects of the shift in detuning, stationary solutions of the FP model and their stability are compared with those of ring resonators with normal dispersion [35, 54], those of FP with anomalous dispersion [48] and those of counterpropagating light in ring resonators with normal dispersion [117]. Finally we investigate in Section 5.7 oscillatory DCS solutions in a FP cavity and discuss the effects of the nonlocal coupling on the oscillating solitons, homogeneous background, and the interaction of two oscillating DCSs. In particular, the long range interaction between DCSs is capable of synchronising their oscillations.

Since a single pulse of these local structures can exist within the cavity it is preferential to label these as cavity solitons even in regimes when they may form trains of pulses. This is in agreement with the laser case [164].

5.2 Fundamentals of Fabry-Pérot resonators

5.2.1 The Fabry-Pérot cavity

A schematic representation of a FP cavity is shown in Fig. 5.1. It is composed of two mirrors characterised by reflection and transmission coefficients r_1, t_1 and r_2, t_2 , respectively, and filled with a Kerr nonlinear media. A continuous wave incident electric field

S is coupled into the cavity through one of the mirrors, which circulates for many round trips, and can be decomposed into forward F and backward B propagating components. Assuming steady state operation, the electric field at different points of the FP system can be related through the following equations [162], (as discussed further in Fig. 5.1),

$$\begin{aligned} F_1 &= t_1 S - r_1 B_2, & B_1 &= -r_2 F_2, & E_{\text{tra}} &= t_2 F_2, \\ F_2 &= a e^{i\theta} F_1, & B_2 &= a e^{i\theta} B_1, & E_{\text{ref}} &= r_1 S + t_1 B_2, \end{aligned}$$

where propagation losses are accounted for by the introduction of parameter a and we have implemented Stokes relations. As light propagates the length of the cavity, through the nonlinear media, it accumulates phase $\theta = \tau_R \omega$ with frequency ω and cavity round trip time τ_R , and may be interpreted as a normalised cavity detuning. Phase may also take contributions from the reflections at the mirrors, which may also be incorporated into θ [29].

The electric field coupling out of the cavity at each mirror may be quantified in terms of the injected field. By accounting for the contributions from each consecutive reflection as light circulates the cavity, we define an effective reflectivity coefficient as,

$$\tilde{r} = r_1 - t_1^2 r_2 a^2 e^{i2\theta} \sum_{m=1}^{\infty} (r_1 r_2 a^2 e^{i2\theta})^{m-1} = \frac{r_1 - r_2 a^2 e^{i2\theta}}{1 - r_1 r_2 a^2 e^{i2\theta}}, \quad (5.1)$$

and effective transmissivity coefficient,

$$\tilde{t} = t_1 t_2 a e^{i\theta} \sum_{m=1}^{\infty} (r_1 r_2 a^2 e^{i2\theta})^{m-1} = \frac{t_1 t_2 a e^{i\theta}}{1 - r_1 r_2 a^2 e^{i2\theta}}. \quad (5.2)$$

Here, we have made use of the geometric series $\sum_{m=1}^{\infty} x^{m-1} = (1-x)^{-1}$, for $x < 1$, to evaluate consecutive reflections. These coefficients are complex valued, obeying the relation $|\tilde{r}|^2 + |\tilde{t}|^2 = 1$ assuming lossless interaction with the cavity mirrors, and are used to relate the incident field with the two output fields as,

$$E_{\text{ref}} = \tilde{r} S, \quad E_{\text{tra}} = \tilde{t} S. \quad (5.3)$$

We may then obtain the power transmission and reflections as

$$\frac{|E_{\text{ref}}|^2}{|S|^2} = \frac{(\sqrt{R_1} - a^2 \sqrt{R_2})^2 + 4a^2 \sqrt{R_1 R_2} \sin^2(\theta)}{(1 - a^2 \sqrt{R_1 R_2})^2 + 4a^2 \sqrt{R_1 R_2} \sin^2(\theta)}, \quad (5.4)$$

$$\frac{|E_{\text{tra}}|^2}{|S|^2} = \frac{a^2 (1 - R_1)(1 - R_2)}{(1 - a^2 \sqrt{R_1 R_2})^2 + 4a^2 \sqrt{R_1 R_2} \sin^2(\theta)}, \quad (5.5)$$

where $R_{1,2} = r_{1,2}^2$, $T_{1,2} = t_{1,2}^2$ and $T_{1,2} + R_{1,2} = 1$. In Fig. 5.2(a), we plot the reflection and transmission coefficient with respect to the normalised cavity detuning 2θ . Here we can see that for $2\theta = 2\pi m$, where m is an integer, the transmission coefficient is $|\tilde{t}|^2 = 1$. This represents the resonance condition, where the total power coupled out of the resonator occurs at the feedback mirror. When operating far from resonance, much of the light is reflected away from the cavity by the coupling mirror $|\tilde{t}|^2 \ll |\tilde{r}|^2$.

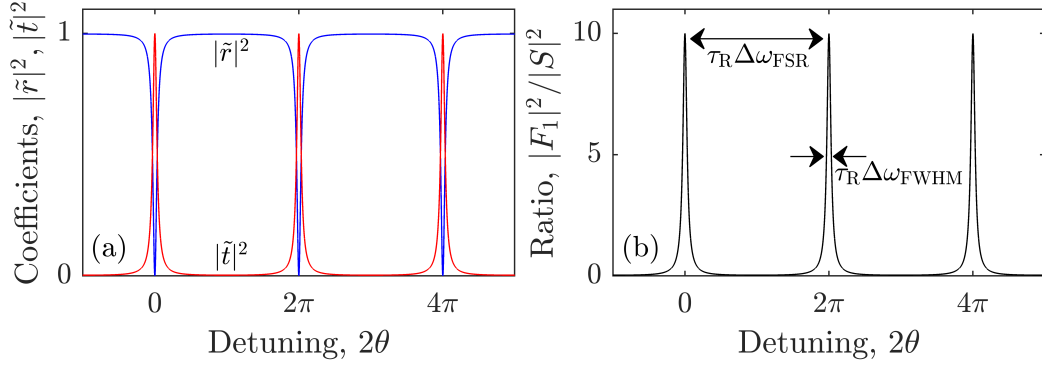


Figure 5.2: (a) Effective coefficients of reflection \tilde{r} (blue) and transmission \tilde{t} (red) for the output fields E_{ref} and E_{tra} of a Fabry-Pérot resonator. (b) Corresponding ratio of circulating field power $|F_1|^2$ and incident field power $|S|^2$. In both figures, the reflection coefficients are $R_1 = R_2 = 0.9$. These figures demonstrate the resonance enhancement within the Fabry-Pérot resonator, with resonance condition $2\theta = 2\pi m$, where m is an integer.

5.2.2 Resonance enhancement

When driven by a temporally coherent plane wave electric field, the interaction between forward and backward propagating fields between the mirrors is phase sensitive. As opposed to the ring resonator system, light within the FP cavity exists as standing waves due to interference of forward and backward propagating fields, innate to the FP boundary conditions. The total circulating power within the cavity consists of the sum of multiple reflections as light circulates the cavity, such that, the intracavity power is maximized when all the fields propagate in phase and constructively interfere. This allows the electric field within the resonator to have significantly greater power than the incident light. We may characterise the resonance enhancement of the circulating field through the ratio of the incident field S and circulating field F_1 , where

$$F_1 = t_1 S + r_1 r_2 a^2 e^{i2\theta} F_1 \implies \frac{F_1}{S} = \frac{t_1}{1 - r_1 r_2 a^2 e^{i2\theta}}, \quad (5.6)$$

and the intracavity power can be expressed as

$$\frac{|F_1|^2}{|S|^2} = \frac{1 - R_1}{(1 - a^2 \sqrt{R_1 R_2})^2 + 4a^2 \sqrt{R_1 R_2} \sin^2(\theta)}. \quad (5.7)$$

Resonance enhancement of the intracavity field is achieved at the resonance condition $2\theta = 2\pi m$ where m is an integer. As can be seen in Fig. 5.2(b), the resonances appear as peaks separated by integer multiples of 2π where the free spectral range of the cavity is defined $\Delta\omega_{\text{FSR}} = 2\pi/\tau_R$. For a reflectively coefficient of $R_1 = R_2 = 0.9$, the maximum power of the intracavity field is 10 times the incident field. This is the mechanism by which the FP resonator may be used to enhance nonlinear optical effects at lower input power. At resonance with equal reflectivities $R_1 \approx R_2 = R$ and negligible losses $a \approx 1$,

the resonance enhancement reduces to $|F_1|^2/|S|^2 = (1 - R)^{-1}$. From this, it is apparent from this expression that resonance enhancement increase as $R \rightarrow 1$.

5.2.3 Coupling efficiency

To determine the efficiency in which incident light is coupled into the cavity, we introduce the coupling coefficient $0 < \eta < 1$. We define this coefficient as the ratio of power coupled into the resonator through the coupling mirror $\kappa_1 \approx T_1/\tau_R$ and the power lost on each round trip, with [29]

$$\eta = \frac{T_1}{\tau_R \alpha_i + T_1 + T_2}, \quad (5.8)$$

where the output coupling rate of the feedback mirror is $\kappa_2 \approx T_2/\tau_R$ and α_i represents propagation losses per unit of fast time. The critical coupling condition for a FP cavity is achieved when the power output rate at the coupling mirror is equal all other losses. This corresponds to the optimal coupling efficiency in practice, occurring at $\eta = 1/2$, where the mirror transmissivity coefficients are related as $T_1 = T_2 + \tau_R \alpha_i$. Should the out coupling rates of the two mirrors be identical $T_1 \approx T_2 = T$, the coupling coefficient reduces to $\eta = T/(2T + \tau_R \alpha_i) < 1/2$. In this case, critically coupling can only be achieved asymptotically in the limit of low propagation losses ($T \gg \tau_R \alpha_i$).

5.2.4 Cavity finesse and quality factor

In Section 2.3.4, we provide definitions for the cavity finesse (\mathcal{F}) and quality factor (Q -factor) for the ring resonator system. The fundamental definitions and physical meanings of these quantities remain the same and can be evaluated for FP resonator.

The cavity finesse is defined as the ratio of the free spectral range and the linewidth. We may obtain the linewidth of the FP cavity by setting the transmitted power (5.5) to one half the resonance peak, $|E_{\text{tra}}(\theta_{\text{FWHM}})|^2 = |E_{\text{tra}}(\theta = 0)|^2/2$, whereby assuming a narrow resonance, $\sin(\theta) \approx \theta$, the linewidth becomes,

$$\Delta\omega_{\text{FWHM}} = \frac{1}{\tau_R} \theta_{\text{FWHM}} = \frac{1 - a^2(R_1 R_2)^{1/2}}{2\tau_R a(R_1 R_2)^{1/4}}. \quad (5.9)$$

The cavity finesse is then

$$\mathcal{F} = \frac{\Delta\omega_{\text{FSR}}}{\Delta\omega_{\text{FWHM}}} = \frac{\pi a(R_1 R_2)^{1/4}}{1 - a^2(R_1 R_2)^{1/2}}. \quad (5.10)$$

In the context of optical resonators, the Q -factor at frequency ω can be defined in the limit of high- Q in terms of the finesse as,

$$Q = \frac{\omega_r}{\Delta\omega_{\text{FWHM}}} = \mathcal{F} \frac{\omega}{\Delta\omega_{\text{FSR}}} = \frac{\omega\tau_R}{2} \frac{a(R_1 R_2)^{1/4}}{1 - a^2(R_1 R_2)^{1/2}}. \quad (5.11)$$

The Q -factor and finesse are two key parameters that quantify the performance of a FP resonator in practice. In this these, we assume light may circulate the cavity many times before being lost. This corresponds to the high- Q limit ($R_1, R_2 \rightarrow 1$), which has been

demonstrated experimentally in FP microresonators for the generation bright temporal cavity solitons [29] where a Q -factor of $Q \approx 4 \times 10^6$ was achieved.

5.3 The Fabry-Pérot model

We consider a high finesse FP resonator composed of highly reflective mirrors and filled with a Kerr medium, see Fig. 5.3. The resonator is driven by linearly polarised light, which is coupled through one of the cavity mirrors into the resonator and the intracavity field is coupled out upon each reflection. The coefficient of transmissivity of the mirrors is taken to be small $T \ll 1$ (high finesse), in line with experimental realisations [29]. The formation of TCS in the FP system has undergone extensive theoretical investigation in the anomalous dispersion regime in [48] where the so called Lugiato-Lefever equation for the Fabry-Pérot was first derived. Here, we study the normal dispersion regime of the FP. This model is of integro-partial differential equation form, and was obtained in [48] by uniting the forward and backward counterpropagating field envelopes into a single envelope, defined over the full round trip time of the cavity. This travelling wave formalism of the FP cavity allows for direct comparison with the ring resonator described by the Lugiato-Lefever equation. In this section, we provide a derivation of this FP model, outlining the motivations and regimes of validity.

The propagation of the electric field through the Kerr nonlinear media enclosed by the mirrors may be treated similarly to Section 2.4, with a key distinction that the total electric field is composed of fields propagating in opposite directions. We may express the total electric field between the mirrors as

$$\mathcal{E}(\tau, t) \propto F(\tau, t)e^{ik\tau} + B(\tau, t)e^{-ik\tau}, \quad (5.12)$$

where F and B are the slowly varying amplitudes of the forward and backward propagating field components, respectively. Much like the ring resonator case, we consider $\mathcal{E}(\tau, t)$ to be spectrally narrow so that the evolution of the transverse modal distribution may be neglected, and we restrict our attention to the evolution of the longitudinal field components. The interaction between counterpropagating fields may be characterised by the nonlinear atomic polarisation

$$\mathcal{P}_{\text{NL}} \propto |\mathcal{E}|^2 \mathcal{E} = (|F|^2 + 2|B|^2)e^{ik\tau} + (|B|^2 + 2|F|^2)e^{-ik\tau} + (\text{third harmonic}), \quad (5.13)$$

where we assume the interaction of counterpropagating fields is dominated by the Kerr effect. Forward and backward propagating fields are coupled through self- and cross-phase modulation via the Kerr nonlinearity, where it can be seen that the Kerr effect is directionally dependant, varying with exponential terms $\exp(\pm ik\tau)$ within the rotating wave approximation. The evolution of the electric field within the FP cavity may be written as [48]

$$\partial_t F + \partial_\tau F = S - (1 + i\theta)F + i(|F| + 2|B|^2)F - i\partial_\tau^2 F, \quad (5.14a)$$

$$\partial_t B - \partial_\tau B = S - (1 + i\theta)B + i(|B| + 2|F|^2)B - i\partial_\tau^2 B, \quad (5.14b)$$

where the equation of the total electric field is split into two coupled partial differential

equations, one for each counterpropagating component $\exp(ik\tau)$ and $\exp(-ik\tau)$, defined over the interval between the mirrors $0 \leq \tau \leq \tau_R/2$. Eqs. (5.14) obey boundary conditions

$$F(0, t) = B(0, t), \quad F(\tau_R/2, t) = B(\tau_R/2, t) \quad (5.15)$$

corresponding to reflections at the two mirrors located at $\tau = 0$ and $\tau = \tau_R/2$. The evolution of the counterpropagating fields of this system are described by Eq. (5.14) in the mean field (high- Q) limit and interact through self- and cross- phase modulation terms in the Kerr approximation. Here, τ_R is the resonator round trip time, S is the amplitude of the normalised input field, which is considered to be real and positive, and θ is the normalised detuning of the input to the near nearest cavity resonance (normalisation given in Section 2.6). We define t as the ‘slow time’ temporal variable describing the evolution over many round trips of the cavity whilst τ is the ‘fast time’ longitudinal variable describing the evolution over a single round trip of the linear cavity.

Eqs. (5.14) possess two distinct retarded times, one for the forward propagating field and one for the backward propagating field. As such, it is not possible to transform this set of equations into a rotating frame of reference, as we have done previously for the ring resonator. This has significant implications for numerical simulation, as to complete a single round trip of the cavity one must; integrate Eq. (5.14a) over the cavity length, implement the first boundary condition (5.15), then integrate Eq. (5.14b) backwards over the cavity length, implementing the second boundary condition. In the limit of high- Q , this will require a significant number of round trips of the resonator to reach the long timescale at which the mean field amplitudes evolve. This issue is resolved by implementing a travelling wave formalism to the FP, which allows us to unite the Eqs. (5.14a) and (5.14a) into a single equation with periodic boundary conditions [48]. This mean field model allows for temporal steps which encompass multiple round trips of the cavity, significantly increasing computational speed.

We begin by performing modal expansions of the field envelopes, with,

$$F(\tau, t) = \sum_{\mu=-\infty}^{\infty} \bar{f}_{\mu}(t) e^{i\mu\alpha\tau}, \quad B(\tau, t) = \sum_{\mu=-\infty}^{\infty} \bar{f}_{\mu}(t) e^{-i\mu\alpha\tau}, \quad (5.16)$$

where $\alpha = 2\pi/\tau_R$ the the free spectral range of the cavity and $\bar{f}_{\mu}(t)$ is the modal amplitude with mode number μ . Using these modal definitions, it is possible to expand the domain of the field envelopes $F(\tau, t), B(\tau, t)$ over the full round trip of the cavity $-\tau_R/2 \leq \tau \leq \tau_R/2$, which amounts to defining,

$$F(\tau, t) = B(-\tau, t), \quad B(\tau, t) = F(-\tau, t). \quad (5.17)$$

Consulting the boundary conditions (5.15), we see that the field envelopes now obey periodic boundary conditions. We note that despite similar equations between the counterpropagating ring (4.5) and FP (5.14) resonators, we do not observe symmetry breaking phenomena between counterpropagating field of the FP cavity. This is due to the aforementioned boundary conditions (5.15) of the mean field FP. To investigate the dynamics

of the fields, we decompose the modal amplitude as

$$\bar{f}_\mu(t) = f_\mu(t)e^{-i\mu\alpha t}, \quad (5.18)$$

into functions which evolve of distinct timescales. The modal amplitude $f_\mu(t)$ evolves on the timescale of photon decay within the cavity $\kappa^{-1} = \tau_R/T$, where T is the mirror transmission coefficient. On the other hand, the exponential term $\exp(-i\mu\alpha t)$ evolves at the timescale of the repetition rate of the cavity $\alpha = 2\pi/\tau_R$. In the limit of a high- Q resonator, we have that $T \ll 1$, and the evolutionary timescales of these two functions are well separated. Inserting the modal expansions (5.16) into Eqs. (5.14a), we obtain the modal equations,

$$\begin{aligned} \partial_t f_\mu = & S\delta_{\mu,0} - (1 + i\theta)f_\mu + (\mu\alpha)^2 f_\mu, \\ & + \sum_{\mu', \mu'', \mu'''} \delta_{\mu, \mu' + \mu'' - \mu'''} \left[f_{\mu'} f_{\mu''}^* f_{\mu'''} + 2f_{\mu'''} f_{\mu''}^* f_{\mu'} e^{i\bar{\alpha}(\mu - \mu')t} \right]. \end{aligned} \quad (5.19)$$

Here, it can be seen that the rapidly varying exponentials appear only in the final term, corresponding to the cross-phase modulation. Should we perform an average of Eq. (5.19) on a timescale greater than the round trip time, but lesser than the photon decay time, we find that all terms remain unaffected, except those possessing the exponential terms. For $\mu \neq \mu'$, exponential terms vanish under the averaging. Hence, setting $\mu = \mu'$ for the term containing the exponential function, we obtain

$$\begin{aligned} \partial_t f_\mu = & S\delta_{\mu,0} - (1 + i\theta)f_\mu + (\mu\alpha)^2 f_\mu \\ & + \sum_{\mu', \mu'', \mu'''} \delta_{\mu, \mu' + \mu'' - \mu'''} f_{\mu'} f_{\mu''}^* f_{\mu'''} + 2f_\mu \sum_{\mu'} f_{\mu'} f_{\mu'}^*. \end{aligned} \quad (5.20)$$

This amounts to neglecting terms which do not conserve energy, where we note that the modal Eqs. (5.20) are in agreement to those used [53]. Introducing the new envelope

$$\psi(\tau, t) = \sum_{\mu=-\infty}^{\infty} f_\mu(t) e^{i\mu\alpha\tau}, \quad (5.21)$$

we obtain the integro-partial differential equation,

$$\partial_t \psi = S - (1 + i\theta)\psi + i(|\psi|^2 + 2\langle |\psi|^2 \rangle)\psi - i\partial_\tau^2 \psi. \quad (5.22)$$

An identical equation is obtained by inserting the modal expansions (5.16) into Eq. (5.14b). In this formalism, the intracavity field is modelled as a travelling wave of slowly varying amplitude $\psi(\tau, t)$ defined over the domain $-\tau_R/2 \leq \tau \leq \tau_R/2$ with periodic boundary conditions. The field of Eq. (5.22) is related to the slowly varying envelopes of the forward, $F(\tau, t)$, and backward, $B(\tau, t)$, counterpropagating fields via

$$F(\tau, t) = \sum_{\mu=-\infty}^{\infty} f_\mu(t) e^{-i\mu\alpha(t-\tau)}, \quad B(\tau, t) = \sum_{\mu=-\infty}^{\infty} f_\mu(t) e^{-i\mu\alpha(t+\tau)} \quad (5.23)$$

over the domain $0 \leq \tau \leq \tau_R/2$, where the modal coefficients, f_μ , are defined as

$$f_\mu(t) = \frac{1}{\tau_R} \int_{-\tau_R/2}^{\tau_R/2} d\tau e^{-i\mu\alpha\tau} \psi(\tau, t). \quad (5.24)$$

Eq. (5.22) was obtained under the conditions of a large material detuning, a high- Q cavity, negligible higher-order dispersion, slowly varying amplitude and Kerr-cubic approximations (see Section 2.6). We note that the chromatic dispersion in a FP resonator is not limited to the material dispersion and can take significant contributions from the mirrors. In particular, the generation of bright temporal cavity solitons demonstrated experimentally in an integrated FP microresonator observed a chromatic dispersion dominated by the photonic crystal reflectors [29]. When operating in the mean field limit, the effects of dispersion of different origin may be aggregated into β_2 owing to their negligible effect on the pulse over a single trip of the cavity, and incorporated into the normalisation, as is done in our model.

The term notated with angled brackets in Eq. (5.22) represents the integral

$$\langle |\psi|^2 \rangle = \frac{1}{\tau_R} \int_{-\tau_R/2}^{\tau_R/2} |\psi|^2 d\tau \quad (5.25)$$

corresponding to the average power of the intracavity field over a round trip of the resonator. Integral terms of this kind are also present in bidirectionally pumped ring resonators [45, 46, 117], as we have discussed at length in Chapter 4, and arises due to the rapid phase dynamics of cross-coupling terms of the counterpropagating fields, such that counterpropagating fields see each other through their average intensity. It is appropriate to resolve the counterpropagating field into the single equation with integral cross-phase modulation in the limit of a high- Q factor. FP microresonators have been experimental shown to possess high Q -factors, where in particular, bright temporal cavity solitons have been experimentally observed in FP microresonators with $Q = 4 \times 10^6$ [29].

This formulation of the FP system allows us to clearly compare the FP solutions with those of a ring resonator system with a single circulating field. The FP model differs from the ring by an additional phase shift term (integral cross-phase modulation term) which may be compensated by a redefinition of the detuning. The connection between the FP and ring resonator geometries can be understood by writing Eq. (5.22) as the LLE

$$\partial_t \psi = S - (1 + i\theta_{\text{eff}})\psi + i|\psi|^2\psi - i\partial_\tau^2 \psi. \quad (5.26)$$

We can see that the stationary solutions ($\partial_t \psi = 0$) of the FP [Eq. (5.22)] are also stationary solutions of the LLE [Eq. (5.26)] with an identical input field S and an effective detuning,

$$\theta_{\text{eff}} = \theta - 2\langle |\psi|^2 \rangle, \quad (5.27)$$

that is shifted by twice the average power of the intracavity field. The role of effective detuning in the bidirectionally driven ring resonator was investigated in Chapter 4. The innate counterpropagation within the FP system results in many of the characteristic features of counterpropagating TCSs discussed in the previous chapter, but with distinct

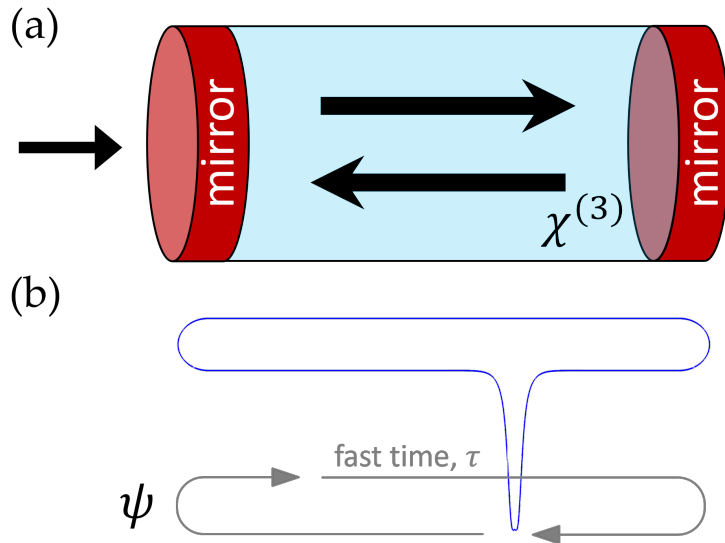


Figure 5.3: Setup: (a) A Fabry Pérot resonator filled with a Kerr medium. A linearly polarised input field enters the cavity on one side and circulates the cavity for many round trips, where part of the field is coupled out upon each reflection at the mirrors. (b) An example field power displaying a DCS is shown.

differences which we discuss in this chapter.

5.4 Homogeneous solutions and fast time dynamics

We now investigate the conditions under which local structures, such as switching fronts and dark solutions, arise in the FP. We begin by writing Eq. (5.22) as

$$\begin{aligned}
 \partial_\tau U &= \tilde{V}, & \partial_\tau V &= \tilde{U}, \\
 \partial_\tau \tilde{U} &= -(\theta - \langle U^2 + V^2 \rangle)U - V + UV^2 + U^3 \\
 \partial_\tau \tilde{V} &= -(\theta - \langle U^2 + V^2 \rangle)V + U + VU^2 + V^3 - S
 \end{aligned} \tag{5.28}$$

where we have set $\partial_t \psi = 0$ and U, V are the real and imaginary components of ψ . We consider the system of Eqs. (5.28) to evolve in fast time τ over a round trip of the cavity, where we implement a similar formulation to describe local structures as was seen for the ring resonator in Chapter 2, adopting terminology of [35, 56, 80–84]. Under this construction, the fixed points U_0, V_0 of Eq. (5.28) correspond to $\partial_\tau U = \partial_\tau V = \partial_\tau \tilde{U} = \partial_\tau \tilde{V} = 0$. The exponentially localised structures we consider approach these fixed point as $\tau \rightarrow \pm\infty$. Due to the presence of the nonlocal terms, the fixed points of Eq. (5.28) depend on the round trip average power of the field and require the full evolution over the round trip of the resonator for their determination.

5.4.1 Homogeneous stationary solutions

If we first consider solutions with flat profile over the round trip of the resonator, such that $\langle |\psi_0|^2 \rangle = |\psi_0|^2$, we obtain the HSSs of the FP cavity. Setting $\partial_\tau U = \partial_\tau V = \partial_\tau \tilde{U} = \partial_\tau \tilde{V} = 0$ in Eqs. (5.28) with $\langle |\psi_0|^2 \rangle = |\psi_0|^2$ we obtain the HSSs

$$\begin{pmatrix} U_0 \\ V_0 \end{pmatrix} = \begin{pmatrix} \frac{S}{1+(3H-\theta)^2} \\ \frac{(3H-\theta)S}{1+(3H-\theta)^2} \end{pmatrix}, \quad (5.29)$$

where the power of the HSS ($H = |\psi_0|^2$) is obtained by solving

$$H^3 - 2(\theta - 2H)H^2 + \{(\theta - 2H)^2 + 1\}H = S^2. \quad (5.30)$$

These stationary solutions are discussed in detail in [48], and briefly discussed in Appendix B.1, where a more general discussion on the instabilities of the FP resonators is given in [165].

The HSSs are fixed points of Eq. (5.28) only when the average power over the round trip is equal to the fixed points power. It is not possible for a solution to start and return to a fixed point, and have an average power that is equal to that fixed points power (such as with front and DCS solutions, see Sections 5.6.1 and 5.6.2). As such, local solutions cannot hang from the HSS since the presence of a nonlocal fast time inhomogeneity changes the average power of the field, such that the condition required for the HSS fixed point is not satisfied $\langle |\psi_0|^2 \rangle = |\psi_0|^2$. Hence the HSS of the FP model are a subset of fixed points, which do not support exponentially localised solutions.

5.4.2 Plateau solutions

The fixed points of Eq. (5.28) relevant to the formation of local structures belong to solutions composed of flat increments over the round trip of the cavity. To aid our investigation, we approximate these solutions as two fixed points, of Eq. (5.28), occupying distinct domains of fast time which are connected by step functions. We refer to these fixed points as plateaus to distinguish them from the HSSs, as we have done previously in the ring resonator. These plateau states have uniform powers Y_u and Y_l different from the HSSs, existing over a domain of finite sizes $1 - \Delta$ and Δ , respectively, where Δ is a fast time duration $0 \leq \Delta \leq 1$ parametrising the separation of the step functions and normalised with respect to the round trip time. The round trip average power is then given by $\langle |\psi|^2 \rangle = \Delta Y_l + (1 - \Delta)Y_u$. The real and imaginary parts of the plateau solutions are

$$\begin{pmatrix} U_{u,l} \\ V_{u,l} \end{pmatrix} = \begin{pmatrix} \frac{S}{1+(Y_{u,l}-\theta+2\Delta Y_l+2(1-\Delta)Y_u)^2} \\ \frac{(Y_{u,l}-\theta+2\Delta Y_l+2(1-\Delta)Y_u)S}{1+(Y_{u,l}-\theta+2\Delta Y_l+2(1-\Delta)Y_u)^2} \end{pmatrix}, \quad (5.31)$$

where the plateau powers are the solutions of the coupled equations

$$\begin{aligned} Y_{u,l}^3 - 2(\theta - 2\Delta Y_l - 2(1 - \Delta)Y_u)Y_{u,l}^2 \\ + \{(\theta - 2\Delta Y_l - 2(1 - \Delta)Y_u)^2 + 1\}Y_{u,l} = S^2. \end{aligned} \quad (5.32)$$

When solving Eq. (5.32), there are up to nine possible solutions for each value of the plateau duration Δ . There exists at most one correct pair of upper and lower plateaus which may be selected by restricting the plateaus to real solutions that satisfy $Y_u > Y_l$, where at most three pairs of (Y_u, Y_l) solutions remain. For each of these pairs, one can evaluate the effective detuning, Eq. (5.27), where only one pair of plateaus will correspond to the upper and lower HSS of the corresponding LLE, if a solution exists. In this way, one obtains two plateau powers for each value of Δ unless the effective detuning is outside the bistability region of the corresponding LLE. We have used this approximation to great effectiveness in Chapter 4 to describe and predict stable plateau solutions connected by switching fronts in bidirectionally pumped ring resonators [117]. In the FP system, we find that this approximation is also very effective, but as we will see in Section 5.6.1, solutions of plateaus connected by switching fronts are dynamical for the FP model for condition where we expect to find large ranges of stability in bidirectional ring resonators.

To study the stability of the plateaus in fast time, we introduce the linear perturbation $U = U_0 + \epsilon u, V = V_0 + \epsilon v$ to the fixed point U_0, V_0 , where we continue with our assumption of plateaus that exist on discrete intervals in fast time connected by step functions. To investigate the fast time stability of each plateau, we must appropriately evaluate the effect of the perturbation on the integral term. In what follows we assume that the perturbation on the plateau has negligible effect on the average power of the full solution $\langle (U_0 + \epsilon u)^2 + (V_0 + \epsilon v)^2 \rangle = \langle U_0^2 + V_0^2 \rangle$. We find that this is a suitable assumption for this perturbation due to the robustness of the integral term to local inhomogeneity. Hence, the fast time stability of the plateau states can be understood by considering the Jacobian matrix

$$J = \begin{pmatrix} 0 & 0 & 1 & 0 \\ 0 & 0 & 0 & 1 \\ V^2 + 3U^2 - \theta_{\text{eff}} & -1 + 2UV & 0 & 0 \\ 1 + 2UV & U^2 + 3V^2 - \theta_{\text{eff}} & 0 & 0 \end{pmatrix}_{(U_0, V_0, \theta_{\text{eff}})} \quad (5.33)$$

where J is evaluated at a single fixed point of Eqs. (5.28) and θ_{eff} is the effective detuning of the full round trip stationary solution (composed of two fixed points connected by step functions). This Jacobian provides eigenvalues of the form

$$\lambda = \pm \sqrt{(2Y - \theta_{\text{eff}}) \pm \sqrt{(Y^2 - 1)}} \quad (5.34)$$

where $Y = U_0^2 + V_0^2$ is the plateau power of the perturbed stationary state. The Jacobian (5.33) has a similar form to the fast time analysis performed for a LLE [35], where θ replaces the effective detuning and the plateaus correspond to the HSS. The eigenvalues of Eq. (5.34) rule the escape from and the approach to plateau states Y_{\pm} along the stable and unstable manifolds. Of key relevance is the transition that occurs at plateau power $Y = 1$, below which the eigenvalues of Eq. (5.34) become complex. The lower power plateau typically exist beneath the threshold, $Y_- < 1$, displaying fast time oscillation. This allows for the structurally stable intersection of stable and unstable manifolds of the plateau corresponding to the formation of dark cavity solitons [166]. These eigenvalues are essential in the determination of the presence of local oscillations responsible for the existence and stability of dark cavity solitons in Section 5.6.2. We note that the higher

power plateau always has power $Y_+ > 1$ and yields four real eigenvalues for the parameters that we have considered.

5.5 Linear stability analysis of plateau solutions in slow time

We continue our investigation of the plateau solutions here, but now consider linear perturbations which evolve in slow time. As in the previous section, we assume solutions formed by two plateaus of higher $\psi_u(\tau, t)$ and lower $\psi_l(\tau, t)$ power coexisting on a round trip $\psi = \psi_u + \psi_l$ and joined by two step functions separated by the normalised duration Δ in fast time. Inserting this solution into Eq. (5.22), we see that the plateaus $\psi_{u,l}$ interact only through the average power over the round trip of the cavity $\langle |\psi|^2 \rangle = \Delta \langle |\psi_l|^2 \rangle + (1 - \Delta) \langle |\psi_u|^2 \rangle$ due to our assumption of steep SFs (step functions). As such, we may rewrite Eq. (5.22) as the two coupled equations,

$$\partial_t \psi_{u,l} = S - (1 + i\theta) \psi_{u,l} + i(|\psi_{u,l}|^2 + 2[\Delta \langle |\psi_l|^2 \rangle + (1 - \Delta) \langle |\psi_u|^2 \rangle]) \psi_{u,l} - i \partial_\tau^2 \psi_{u,l}, \quad (5.35)$$

on distinct domains $-1/2 \leq \tau/\tau_R \leq (\Delta - 1/2)$ and $(\Delta - 1/2) \leq \tau/\tau_R \leq 1/2$ which govern the lower and upper plateaus respectively. Integral terms on each plateau are evaluated as

$$\langle |\psi_l|^2 \rangle = \int_{-\tau_R/2}^{\tau_R(\Delta-1/2)} |\psi_l(\tau, t)|^2 d\tau, \quad \langle |\psi_u|^2 \rangle = \int_{\tau_R(\Delta-1/2)}^{\tau_R/2} |\psi_u(\tau, t)|^2 d\tau. \quad (5.36)$$

Eqs. (5.35) represent an approximate system, whereby introducing a linear perturbation to the plateaus $\psi_{u,l}$, we may investigate their slow time stability and the conditions required for the formation of dark solitons which hang from them. In the following sections, our analysis outlines the conditions required for plateaus to coexist stably, and characterises the decaying Turing oscillations on the low power plateau required for the formation of dark solitons in the FP resonator.

5.5.1 Turing pattern instability

First, we investigate the linear stability of the upper and lower plateaus to the growth/decay of Turing patterns of wavenumbers k_u and k_l , and slow time growth rates Ω_u and Ω_l , respectively. We introduce perturbations of the form

$$\psi_{u,l} = \psi_{u,l}^s + \epsilon a_{u,l} e^{ik_{u,l}\tau + \Omega_{u,l}t}, \quad (5.37)$$

where $\epsilon \ll 1$. In the case where the wavenumbers on each respective plateau are periodic, $k_l \Delta \tau_R = 2\pi n_l$ and $k_u(1 - \Delta)\tau_R = 2\pi n_u$ for integers $n_{u,l} \neq 0$, the effect of the perturbations on the round trip average becomes $\langle |\psi_{u,l}|^2 \rangle = \langle |\psi_{u,l}^s|^2 \rangle = |\psi_{u,l}^s|^2$, and we find that the growth rates $\Omega_{u,l}$ of the perturbations on the higher power and lower power plateaus are respectively (as derived in Appendix B.2)

$$\Omega_{u,l} = -1 \pm \sqrt{4Y_{u,l}\theta_{\text{eff}} - 3Y_{u,l}^2 - \theta_{\text{eff}}^2 - 2(2Y_{u,l} - \theta_{\text{eff}})k_{u,l}^2 - k_{u,l}^4} \quad (5.38)$$

The effective detuning is now given by $\theta_{\text{eff}} = \theta - 2\Delta(U_l^2 + V_l^2) - 2(1 - \Delta)(U_u^2 + V_u^2)$. Since the coupling between plateaus through the integral terms is independent of their phases, the stability of the upper and lower plateaus are independent of their phases. We may use this fact to assume without loss of generality that the plateau solutions are purely real, such that, an appropriate Jacobian of perturbation (5.39) is

$$J' = \begin{pmatrix} -1 & \tilde{A}_u & 0 & 0 \\ -\tilde{B}_u & -1 & \Delta C & 0 \\ 0 & 0 & -1 & \tilde{A}_l \\ (1 - \Delta)C & 0 & -\tilde{B}_l & -1 \end{pmatrix}, \quad (5.41)$$

where

$$\begin{aligned} \tilde{A}_u &= \theta_{\text{eff}} - Y_u, & \tilde{B}_u &= \theta_{\text{eff}} - (7 - 4\Delta)Y_u, & C &= 4\sqrt{Y_u Y_l}, \\ \tilde{A}_l &= \theta_{\text{eff}} - Y_l, & \tilde{B}_l &= \theta_{\text{eff}} - (3 - 4\Delta)Y_l, \end{aligned}$$

and $\theta_{\text{eff}} = \theta - 2\Delta Y_l - 2(1 - \Delta)Y_u$. This is obtained from matrix (5.40) by setting $V_{u,l} = 0$, and possess the identical eigenspectrum

$$\lambda = -1 \pm \sqrt{\frac{-\tilde{A}_u \tilde{B}_u - \tilde{A}_l \tilde{B}_l \pm Q}{2}}, \quad (5.42)$$

$$Q = \sqrt{(\tilde{A}_u \tilde{B}_u - \tilde{A}_l \tilde{B}_l)^2 + 4\Delta(1 - \Delta)\tilde{A}_u \tilde{A}_l C^2}. \quad (5.43)$$

These eigenvalues indicate the relative stability of a pair of plateaus coexisting along the round trip to perturbation which change the average power of the solution. By evaluating these eigenvalues, we obtain Fig. 5.4, where the stability of plateau states to perturbations on the average power is presented in the parameter space (θ_{eff}, S) , where the lower power plateau has size $\Delta = 0.2$. This allows for a direct comparison with the solutions of bistable HSSs, as seen for a ring resonator [35]. We find that near the onset of optical bistability, plateau solutions in the FP configuration are unstable, as depicted by the yellow zone of Fig. 5.4. The green zone shows stable plateaus, and the blue zone indicates an absence of plateau stationary states (solutions of stable HSS). The transition from the green to the yellow zone corresponds to a transition of the real part of the relevant eigenvalues of Eq. (5.43) from negative to positive and the plateaus collapsing to the low power HSS. Hence, we find parameter regimes in which there is a bistability of the HSSs of the FP model but there are no stable solutions of coexisting plateaus. In regions where plateau solutions are unstable, the system cannot support exponentially localised structures which approach them, such as the switching fronts discussed in the next section, and indeed we do not observe the formation of stable DCSs in these regimes.

5.6 Localised solutions

In the previous sections, we have studied the existence and stability of plateau solutions connected with a step function. These solutions serve as an approximation to exponen-

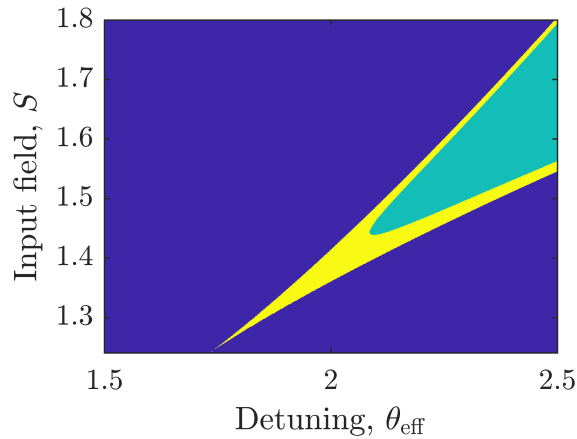


Figure 5.4: Stability of coexisting plateaus in the parameter space of shifted detuning, θ_{eff} , and input field, S , for a fixed duration of the lower power plateau $\Delta = 0.2$. The blue region corresponds to stable HSSs of the FP model, whereas the green region corresponds to two stable plateaus coexisting on the round trip of the resonator, and the yellow region to two unstable plateau solutions.

tially localised solutions of Eqs. (5.28), that approach flat solutions (fixed points) along the fast time variable τ . There are two kinds of such solutions: heteroclinic orbits, which are trajectories that connect two separate fixed points of Eq. (5.28), and homoclinic orbits, corresponding to a trajectory that leaves and returns to the same fixed point of Eq. (5.28). The former corresponds to a switching front (SF) solution, while the latter are here associated with cavity solitons: bright (dark) cavity solitons when the fixed point corresponds to the high (low) power plateau. As the boundary conditions of a FP resonator are periodic, SF solutions exist as a pair with opposite orientation in the cavity. Taken together, and when well separated, they form a heteroclinic cycle. The DCS solutions described in later sections are themselves composed of oppositely oriented SFs which interact and lock with each other through local oscillations close to the lower power fixed point, as was first proposed for spatial solitons composed of diffractive switching fronts [119–121]. An example of a single SF (heteroclinic orbit) and a DCS (homoclinic orbit) in the (U, V) plane are presented in Fig. 5.5. These trajectories are anchored to the plateau solutions discussed in Section 5.4 for a given value of the distance Δ . The blue solid lines in Fig. 5.5 correspond to the family of plateau solutions when changing Δ while the circles mark the positions of the HSS.

5.6.1 Switching fronts and their dynamics

To understand the SF stationary states (heteroclinic orbit) and their dynamics within the FP cavity, we make comparison with similar solutions found in ring resonators, discussed in Chapter 2. This is done due to the mathematical equivalence of the stationary solutions or the receptive models, up to a shift in detuning. The HSSs of the FP model are plotted in Fig. 5.6(a) as blue curves. The HSSs of an equivalent ring resonator model are plotted as green curves. When comparing these tilted Lorentzian curves, it is very clear that the effect

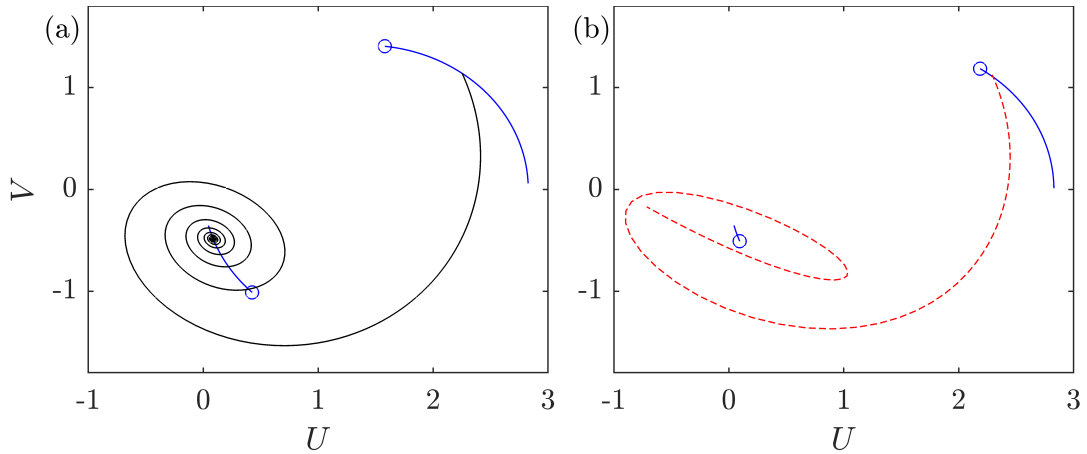


Figure 5.5: Examples of (a) SF heteroclinic (black line) and (b) DCS homoclinic (red dashed line) trajectories of Eqs. (5.28) in the Argand plane where U and V are the real and imaginary parts of the intracavity field, respectively. Solid blue lines correspond to upper and lower plateaus when scanning Δ . Circles correspond to HSSs.

of the shift in the detuning is most prominent for high power solutions, resulting in a large shift at the peak of the resonance. SFs within the FP cavity occur as oppositely oriented pairs, are generally dynamical, and move with identical speed but opposite directions. The velocity of SF solutions depend on of the average power of the field which may be expressed in terms of their separation Δ . A key characteristic of the SF dynamics is the presence of a turning point, where the velocities of both SFs change sign. An example of the slow time evolution is shown in Fig. 5.7 for fixed parameters, and an initial condition near a velocity turning point at $\Delta \approx 0.5$. In Fig. 5.7(a) [Fig. 5.7(b)] the SF initial condition has separation slightly narrower (wider) than at the velocity turning point. We can see that the SF solutions either move towards each other until they annihilate [Fig. 5.7(a)], or move away from each other until the effective detuning is shifted beyond the bistability region of the equivalent LLE [Fig. 5.7(b)], and collapses to the HSS.

The velocity turning points of a SF within a FP resonator are plotted in Fig. 5.6(a) as a solid black line. Each point along the line corresponds to a specific value of Δ (average power), at which the effective detuning correspond to the Maxwell point of the LLE (plotted as the dash-dot black line in Fig. 5.6(a)). The Maxwell point of the LLE is, by definition, the unique value of detuning Θ_{MP} (for the chosen driving power) where the velocity of a non-interacting SF is exactly zero [35, 54]. This then constitutes a stationary state of the FP model at a unique value of Δ , in which effective detuning that is equal to Θ_{MP} . Hence, the black line of Fig. 5.6(a) corresponds to a projection of the dash-dot black line via the effective detuning relationship (5.27). Due to the dependence of the effective detuning on the average power of the field, there exist for each value of detuning a single separation (Δ) of SFs that corresponds to a turning point. The turning point can be then located semi-analytically given that we know Θ_{MP} , as shown for example in a bidirectionally pumped ring resonator [117] discussed in Chapter 4. The direction of the SF motion is then determined by the effective detuning being greater than Θ_{MP}

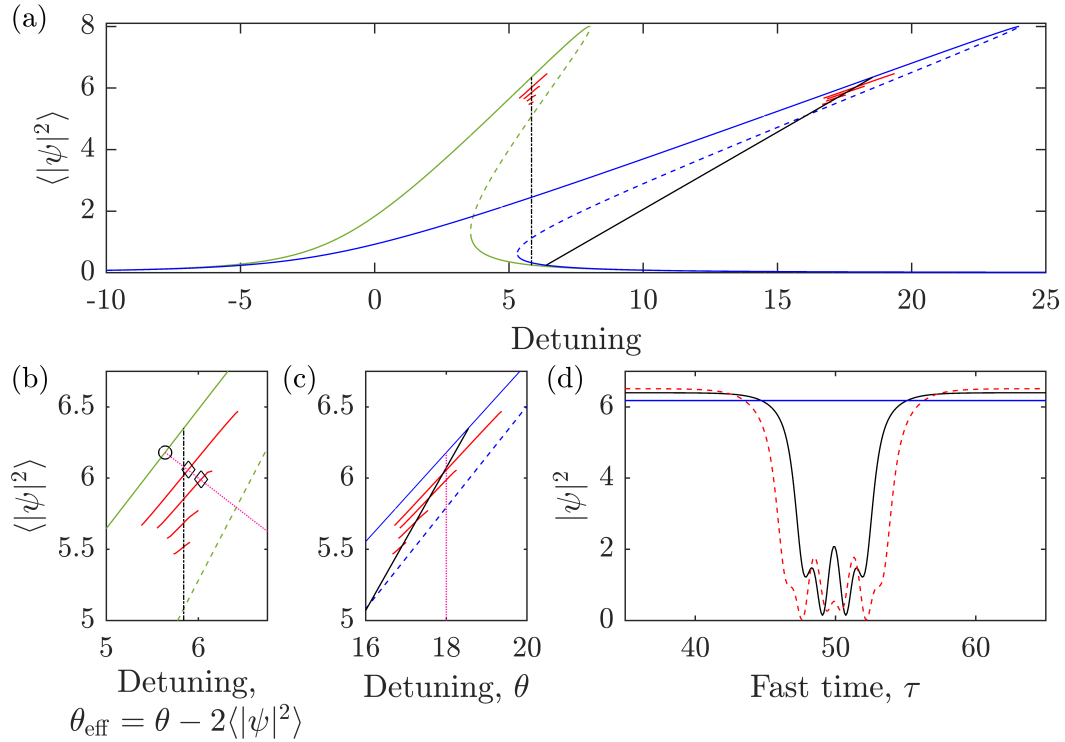


Figure 5.6: (a) Solutions of the FP model and equivalent ring resonator model for input field $S = 2\sqrt{2}$ with round trip time $\tau_R = 100$. HSSs of the FP (ring resonator) model correspond to blue (green) lines. Dashed curves correspond to unstable HSSs. Stationary SF solutions are plotted by using their round trip average power for the FP model (black line) and for the ring resonator model (black dot-dashed line). Stable dark solitons solutions of different sizes correspond to the red lines and form branches of distinct width. (b) Solutions of the ring resonator model (LLE) plotted with respect to the detuning θ_{eff} , which are related to the FP solutions through the effective detuning relationship, Eq. (5.27). (c) Solutions of the FP model plotted with respect to the detuning and correspond to a zoomed in window of (a). (d) Power profile of bistable stationary dark solitons for parameters $S = 2\sqrt{2}$, $\theta = 18$, $\tau_R = 100$ and correspond to the two diamonds in (b). The solid blue line in (d) corresponds to the highest power HSS, marked with a circle in (b).

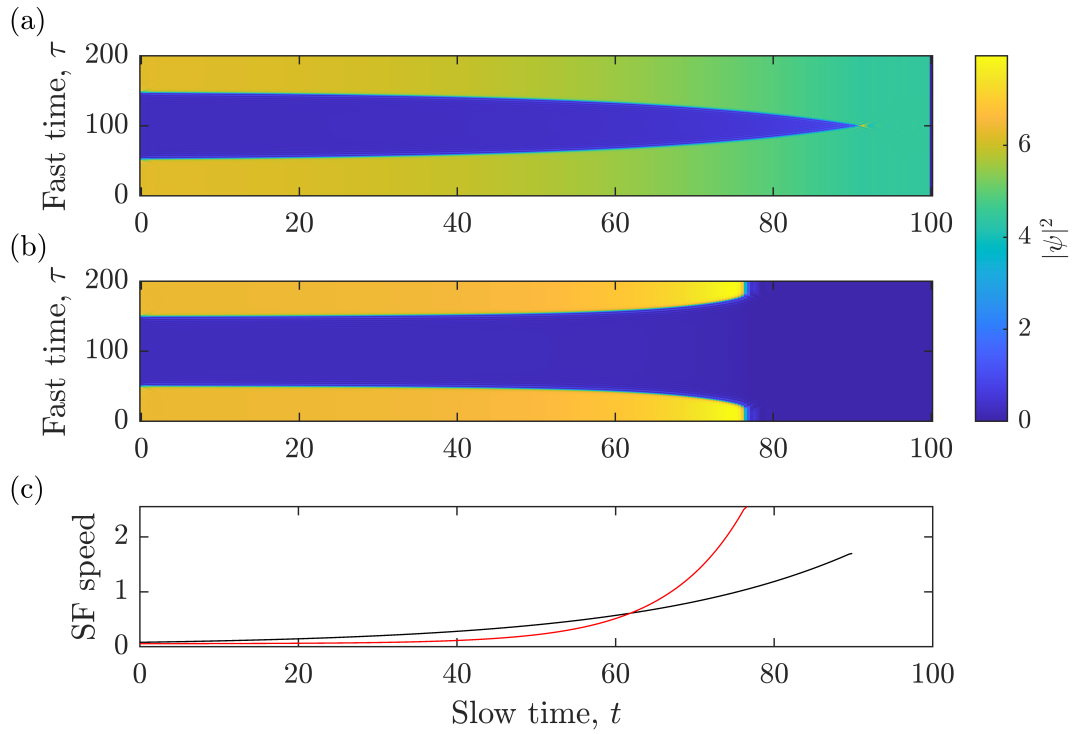


Figure 5.7: (a)-(b) SFs dynamics over slow time, with initial condition near the velocity turning point of the SF, at separation of $\Delta \approx 0.5$, for parameters $S = 2\sqrt{2}$, $\theta = 12.5$. (a) shows the evolution of two SFs from a square wave initial condition with slightly smaller SF distance than the turning point, whereas, (b) shows the evolution from an initial condition with slightly larger SF distance than the turning point. In both cases the SFs move away from the starting location and eventually collapse to one of the bistable HSSs. (c) SF velocities corresponding to panels (a) and (b) with black and red curves, respectively.

[Fig. 5.7(a)] or lesser than Θ_{MP} [Fig. 5.7(b)], or equivalently if the SF separation is greater than or lesser than the unique value of Δ .

In Chapter 4 it was shown, for counterpropagating light in ring resonators, that there exists an abundance of stable and robust light plateau stationary states composed of non-interacting SFs that form in one field, while the profile of the counterpropagating field is flat. The ring resonator system is described by two equations with similar form to Eq. (5.22), one equation for the forward field and one for the backward field, and coupled through nonlocal cross-Kerr interaction. It is interesting to note that, for counterpropagation in a ring resonator, SFs of a given initial separation move towards (instead of away from) the velocity turning point [117]. The difference in the direction of the SF motion when compared with the FP model is due to distinct backward and forward field profiles present within the ring resonators, that induce nonreciprocal shift in detuning of the two field components. As such, the motion of the SFs does not explicitly depend on its own average power, but instead depends on the power of the field with flat profile. However, the stability of SF solutions in a FP configuration depends critically on its own average power, inducing a shift in detuning which diverges from the Maxwell point with SF motion, resulting in SFs solutions that always move away from the turning point (see Fig. 5.7). This explains why we do not observe the rich phenomenology of stable SFs solutions of the counterpropagation in ring resonators [117] and why only DCS are achieved through the locking mechanism originating from the interaction of SF through their oscillating tails, as described in the next section.

Finally, we note that although SF (heteroclinic) solutions are not stationary in an FP configuration, the calculations of the plateau solutions in Section 5.4 are still worth mentioning. During the motion displayed in Fig. 5.7, the solution progresses through the plateaus corresponding to different sizes of Δ , instant by instant, until the two SF interact with each other. During the SF motion, the cusp point of the heteroclinic trajectory of Fig. 5.5(a) moves along the blue curves, that are the plateau solutions of Eq. (5.32). If the initial Δ is larger than that corresponding to the velocity turning point, the cusp of the heteroclinic trajectory moves leftward along the blue solid line until it reaches the HSS marked by the circle. If the initial Δ is smaller than the velocity turning point, the cusp of the heteroclinic trajectory moves rightward along the blue solid line until the SF collide and annihilate, and the system collapses to the lower HSS (circle closer to the origin of the axes).

5.6.2 Dark cavity solitons

For a FP resonator in the normal dispersion regime, we observe the formation of DCS steady states. Such states are composed of two SFs that lock with each other due of the interaction of fast time oscillations present close to the lower plateau, as shown for single field ring resonators in [35] and in optical parametric oscillators [120, 121]. Bistable DCS stationary solutions of Eq. (5.22) are shown in Fig. 5.6(d) for parameter values $S = 2\sqrt{2}$, $\theta = 18$, $\tau_R = 100$. The two dark soliton solutions have different widths corresponding to distinct cycles of the oscillations which form on the low power plateau. Such solitons can be obtained by a perturbation of the HSS of suitable width. The results of this thesis were obtained first through direct numerical integration of Eq. (5.22) via the Fourier split

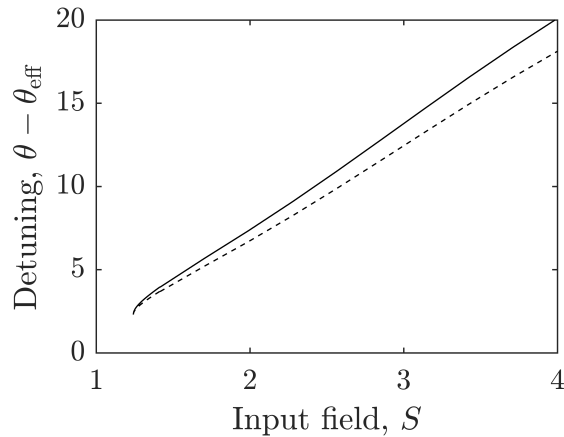


Figure 5.8: Approximate difference in detuning between dark soliton solutions of the FP resonator and equivalent ring resonator models, with respect to the common input field. The black line corresponds to the SF turning point of the FP model when $\Delta = 0$. The dashed line corresponds to the SF turning point when $\Delta = 0.1$.

step method (Appendix C.2) and then verified using lattice relaxation methods.

It can be seen that the plateau power is different from the high power HSS (blue line in Fig. 5.6(d)), and different for DCSs of different widths. As was discussed in section 5.4, the plateau power of an exponentially localised state depends on the average power of the field over the round trip of the cavity, such that, solitons of different width display different plateau power due to their different average power. The DCSs of Fig. 5.6(d) correspond to the diamonds in Fig. 5.6(b), where the plateau solutions from which the DCSs hang correspond to the points on the solid blue curve of Fig. 5.5(b). Note that the bistable DCSs and the HSSs of the FP model are distributed along the line $\langle |\psi|^2 \rangle = -\theta_{\text{eff}}/2 + \theta/2$ as shown in Figs. 5.6(b) and 5.6(c) as a pink dotted line, respectively. In agreement with the linear stability analysis of Section 5.4, we note that there are no oscillations close to the higher power plateaus and that the oscillations close to the lower power regions corresponds to wavenumbers $k \approx 2.7 \pm 0.1$. This is far from the Turing wavenumber of the HSS, with $k_H = 5.99$, as expected, but reasonably close to the predicted $k_Y = 3.3$. The latter discrepancy is due to the fact that the waveform resulting from the interaction of the SFs leads to local deformations of the sinusoidal profiles assumed in the perturbations of Eq. (5.37). From the predicted value of $k_Y = 3.3$, we can estimate the size of the two DCS of Fig. 5.6(d) to be around $\Delta' \approx 5.7$ and $\Delta' \approx 7.6$, respectively, which is expressed in the units used in the figure. These estimates compare reasonably well with the measured values of $\Delta' \approx 6.7$ and $\Delta' \approx 8.5$.

DCS solutions are much further detuned than the DCSs of an equivalent ring resonator. To see this, we plot in Fig. 5.8 the locations of DCSs for a given input power S with respect to the difference in detuning between the FP resonator θ and an equivalent ring resonator model θ_{eff} . The location of a DCS can be approximated using the SF turning point line, represented as a solid black line in Fig. 5.6(a), whereby selecting a point along this line, we may obtain an estimate for a DCS of width Δ . In Fig. 5.8, we plot the DCS solutions

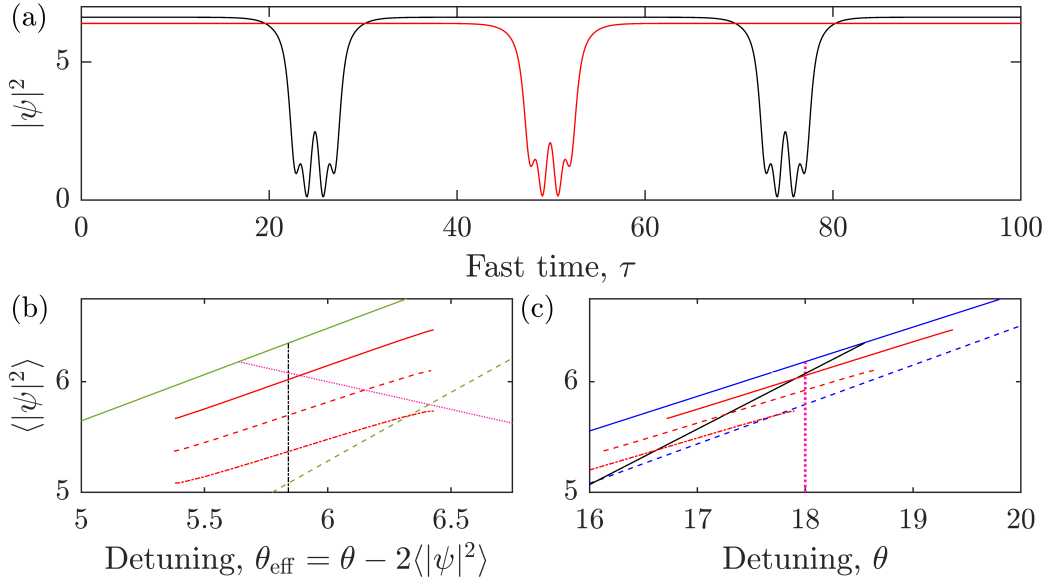


Figure 5.9: (a) Soliton states containing a single soliton, red line, and two solitons simultaneously, black line, for $S = 2\sqrt{2}, \theta = 18$. (b)-(c) FP solutions plotted over detuning (or shifted detuning) with respect to their average power. HSS are plotted as blue, (b), green (c), where the black curves corresponds to the SF turning point, and stable dark solitons are plotted as red curves of one soliton, solid line, two solitons, dashed line, and three solitons, dot-dashed line, present in the cavity. The pink dotted line correspond to the solutions with $\theta = 18$.

of duration $\Delta = 0$ as a black curve (corresponding to the intersection of the turning point line and the high power HSS). The dashed black line in Fig. 5.8 shows solutions in which SFs are stationary with separation $\Delta = 0.1$, the approximate size of the DCS of Fig. 5.6(d). These lines were calculated using the numerical fit of the Maxwell point of the ring resonator model from [117] [Eq. (4.27) of Chapter 4]. We see that as the input power is increased the shift becomes larger. Furthermore, the range of detunings where DCS exist is much larger for the FP model when compared to an equivalent ring resonator system. For example, the longest DCS solution branch for an FP resonator spans $16.75 < \theta < 19.37$, see Fig. 5.6(c), whilst DCS in the equivalent ring resonator system are present only in the range $5.38 < \theta_{\text{eff}} < 6.43$, approximately 2.5 times smaller.

We also note that due to the large average power of DCS solutions, there is a much larger shift in detuning when compared with the bright solitons, which sit upon the low power HSS. This means the bright cavity soliton stationary states of the anomalous dispersion regime, as described in [48], are far more similar to the ring case, occurring within a similar parameter interval as $\theta - \theta_{\text{eff}}$ is smaller, when compared to the DCSs presented here for the normal dispersion regime.

The average power of the field is also affected by the number of solitons present in the cavity, such that, the existence and stability of the solitons depend also on the number of solitons in the cavity. Fig. 5.9(a) shows two bistable solutions for $S = 2\sqrt{2}, \theta = 18$

corresponding to two simultaneous DCSs and a single DCS in the cavity. We see that the presence of an additional soliton modifies the low power oscillations and the plateau power. In Figs. 5.9(b) and 5.9(c) we plot the DCS solutions as red curves with one soliton, solid, two solitons, dashed, and three solitons, dot-dashed, present in the cavity with an identical number of fast-time oscillations. With each additional soliton in the cavity, the average power of the field decreases. As such, solution branches containing a large number of solitons appear at lower values of the detuning. For detuning $\theta = 18$, input field $S = 2\sqrt{2}$ and $\tau_R = 100$, we find that states of one and two solitons are possible, but that further perturbations of the system will not allow the formation of additional solitons, leading instead to the destruction of pre-existing solitons. This is due to the tilting of the collapse snaking DCS solutions due to the presence of the integral term [47].

5.7 Oscillatory dynamics of dark solitons

We now investigate the dynamics of DCSs above a temporal instability of Eq. (5.22). For the case of a ring resonator, Hopf bifurcations are shown to introduce dynamical instabilities of DCS solutions, resulting in local oscillations of the soliton [35]. In what follows we demonstrate the effects of the nonlocal coupling of Eq. (5.22) on the dynamics of oscillatory soliton solutions.

In Fig. 5.10(a) we show an example of an oscillatory solution of the FP model, with input field $S = 2\sqrt{2}$ and detuning $\theta = 18$. We can see that the temporal dynamics of the system are not confined to the soliton but extends to an oscillation of the background plateau. As the soliton moves through its limit cycle oscillation, there is a change in the average power of the field. Hence, due to the nonlocal self-interaction term, regions of the cavity far from the soliton exhibit oscillatory dynamics with identical period to that of the soliton. These oscillations are small due to the small change in average power originating from the oscillation of the soliton. A trace of the minimum power of the oscillating soliton is plotted in Fig. 5.11(a), showing stable limit cycle oscillations. In Fig. 5.10(b) we introduce an oscillating dark soliton to an initial stationary solution containing a stable stationary dark soliton shown in Fig. 5.6(d). The presence of the oscillating soliton induces small temporal oscillations in the plateau power and tiny oscillations in the peaks of the pre-existing DCS. The trace of the minimum power is plotted in Fig. 5.11(b) as a black curve for the oscillating soliton, and a red curve for the stable soliton. We note that the oscillation period has decreased from that of Fig. 5.10(a). In Fig. 5.10(c), we show the evolution of two synchronised breathing solitons. Here we see a larger oscillation amplitude of the plateau power when compared to the single soliton case, due to the larger change in the average power of the field resulting from the second oscillating soliton. In Fig. 5.11(c), we plot the trace of the minimum power of the two oscillating solitons, seen in Fig. 5.10(c), starting from an unsynchronised initial condition. As the system evolves over the slow time the soliton phases begin to overlap, resulting in full synchronisation. The resulting dynamics has now experienced a period doubling with respect to the single oscillating soliton. In Fig. 5.11(d), we plot the evolution of a single soliton with half the cavity length, $\tau_R = 50$, of the previous examples. We see that the dynamics of a single soliton with $\tau_R = 50$ is identical to the synchronised dynamics of the two solitons with $\tau_R = 100$ of Fig. 5.10(c) and 5.11(c). In general we find that the dynamics of N well separated

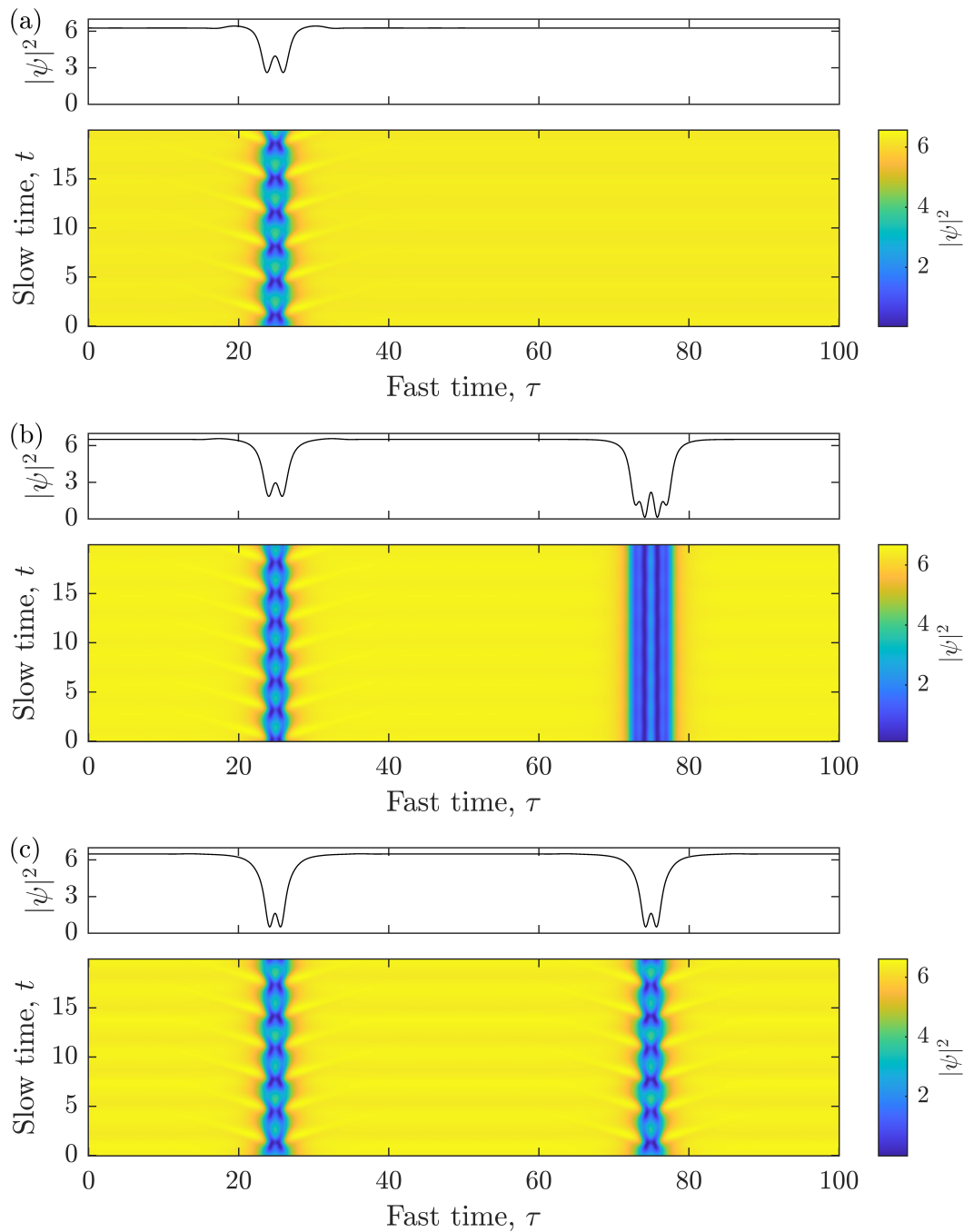


Figure 5.10: (a) The limit cycle of a single oscillating soliton. (b) The limit cycle of a single oscillating soliton and a single ‘stationary’ soliton. (c) The limit cycle oscillations of two synchronised solitons. Each plot is obtained for identical parameters $\theta = 18$, $S = 2\sqrt{2}$. The upper panels correspond to the power profile at $t = 20$, and the lower panels display the slow time evolution.

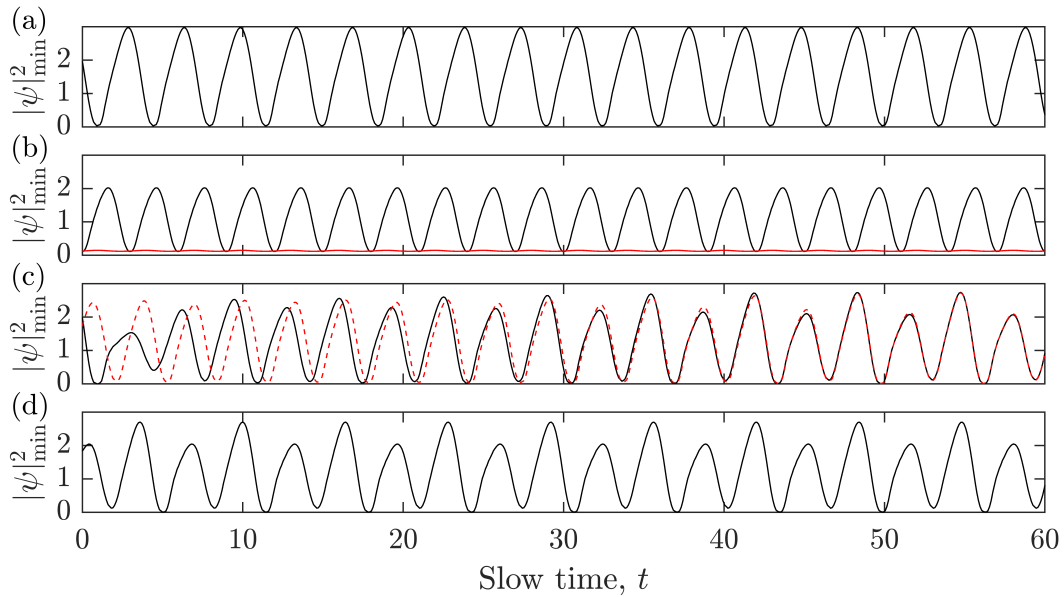


Figure 5.11: Oscillating solutions of the FP resonator with (a) one oscillating soliton in a FP cavity of length $\tau_R = 100$, (b) one oscillating soliton and one ‘stationary’ soliton in a FP cavity of length $\tau_R = 100$, (c) two oscillating solitons in a FP cavity of length $\tau_R = 100$, (d) one oscillating soliton in a FP cavity of length $\tau_R = 50$, Each plot is obtained for identical parameters $\theta = 18$, $S = 2\sqrt{2}$.

solitons in a cavity of round trip τ_R synchronises towards the dynamics of a single soliton in a cavity of round trip τ_R/N .

We find that well separated solitons, located such that they do not interact through the local dynamics at the tails, experience oscillation-phase dependent interaction through the nonlocal coupling. We note that oscillating solitons of the normally dispersive LLE interact locally through their tails and as such do not exhibit synchronisation when well separated in a long cavity [35]. In the FP model, the change in average power of the field during an oscillation of a single oscillating soliton is small, and as such the change in the power of the background plateau is also small. By increasing the length of the FP cavity, we can reduce the effects of soliton oscillation on the average power, such that, we can approach the LLE dynamics of independent solutions. The dynamics of the FP model is most distinct from the ring resonator LLE when the cavity length is small or the number of oscillating solitons is large, where long range interactions are strongest, leading to synchronisation.

5.8 Conclusions

In this chapter, we have presented the dynamics and stationary states of the Fabry-Pérot cavity in the normal dispersion regime, characterising solutions of; plateaus, switching fronts and dark cavity solitons. Through the definition of an effective detuning, we demonstrated analogies and differences of these solutions with the stationary states of the ring

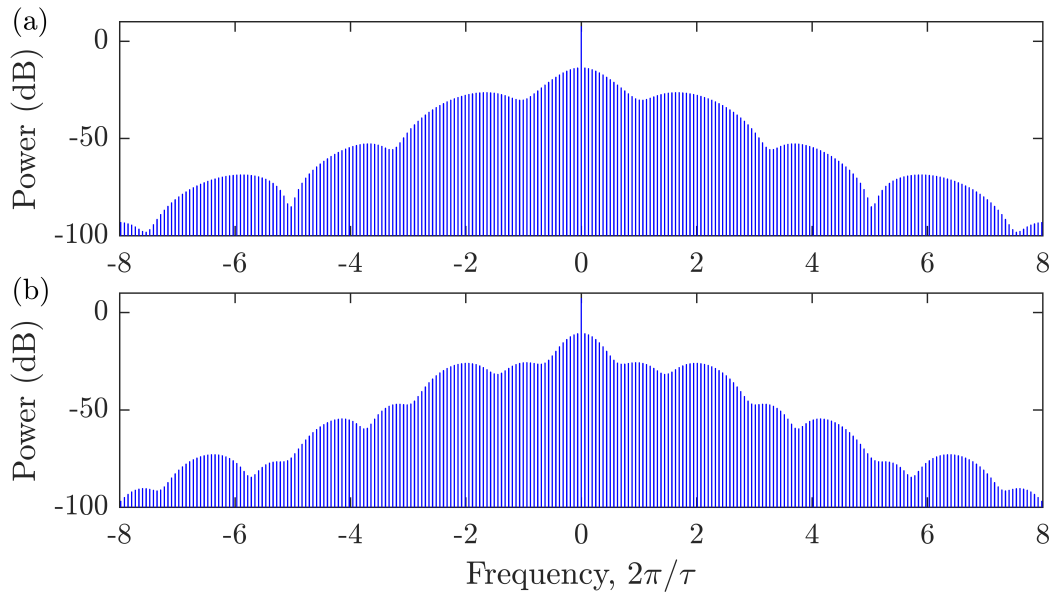


Figure 5.12: Bistable frequency combs for parameter $S = 2\sqrt{2}$, $\theta = 18$, $2L = 100$. These spectra correspond to the dark solitons shown in Fig. 5.6(d) with lesser (a) and greater (b) width.

resonator case. This is due to the mathematical equivalence of the stationary states of the Fabry-Pérot model and a Lugiato-Lefever equation with identical driving field and a detuning that is shifted by the average power of the intracavity field over a single round trip.

We began by discussing the physics Fabry-Pérot system, where we give a derivation of the integro-partial differential equation which governs the dynamics of the intracavity field. We then characterise the homogeneous solutions, outlining the conditions required for exponentially localised solutions to exist, such as switching fronts and dark cavity solitons. A peculiar feature of the Fabry-Pérot resonator is that the homogenous stationary solutions cannot support localised structures (as they do in the ring resonator model) but instead, dark cavity solitons and switching fronts hang from plateau solutions, which are dependent on the average power of the solution over the round trip time of the cavity. This is due to nonlocal self-interactions, which induce a shift in the detuning proportional to twice the average power.

Through an investigation of approximate solutions, formed by two homogeneous plateaus connected by step functions, we identified a region of plateau instability, near the onset of optical bistability of the homogeneous stationary states. Hence, local solutions are unstable for such parameter intervals. This instability is a direct consequence of the nonlocal self-interaction, and has no analogy in the case of purely local coupling.

Linear stability analysis, with respect to fast time inhomogeneous perturbations, is shown to predict Turing instabilities on the low power plateaus. This was used to characterise the wavenumber of decaying oscillations of switching fronts on approach to the plateau, where it was found that the wavenumber is much smaller than those correspond-

ing to Turing instabilities of the homogeneous stationary state. It is this wavenumber that rules the local oscillations close to the lower plateau when two switching fronts lock to form a stable dark soliton.

When compared with counterpropagating light in a ring resonator [117], it turns out that ‘light plateau’ solutions in a Fabry-Pérot cavity with normal dispersion are generally unstable. This is due to the motion of switching fronts, which move away from light plateau stationary states due to the divergence of the effective detuning from the Maxwell point with switch front motion.

The average power of the field, and hence the shift in detuning, is comparatively large for the dark solitons of the normal dispersion regime, when compared with the bright solitons of the anomalous dispersion regime. The large shift results in dark soliton solution branches that are elongated, occupying a larger domain of detuning values than an equivalent ring resonator configuration, and found in strongly detuned regimes.

Finally, we investigated the effects of nonlocal coupling on dynamics of oscillatory solitons. We find that nonlocal self-interaction induces temporal oscillations on the homogeneous background power. In the presence of two oscillating solitons, we observe oscillation-phase dependent interaction, resulting in modification and synchronisation of their oscillation periods. In general, it was found that the dynamics of N solitons in a cavity with round trip time τ_R , synchronised to the dynamics of a single soliton with cavity round trip time τ_R/N . Furthermore, the dynamics of the system approached that of an equivalent ring resonator in the limits of a long cavity and small soliton number (small change in average power).

All of the results presented in this chapter were obtained for parameter values that are realistically feasible in existing experimental realisations [29]. When these systems operate at normal dispersion, we expect to see the formation of dark solitons steady states in experimental verifications. The Fabry-Pérot system allows for additional design consideration of the cavity properties allowing for control over frequency comb generation. Example frequency combs of the Fabry-Pérot resonator are shown in Fig. 5.12 which correspond to the dark solitons of Fig. 5.6(d) and show distinct modulations on the combs, corresponding to the number of low intensity fast time oscillations of the dark soliton [23]. The engineering of frequency combs can be useful in applications in precision spectroscopy, LIDAR, and channel generation for telecom systems [3].

Chapter 6

Spontaneous Symmetry Breaking in Fabry-Pérot Resonators

6.1	Introduction	123
6.2	Modelling the Fabry-Pérot resonator with polarisation consideration	124
6.2.1	Derivation of the Fabry-Pérot model with vectorial electric field	124
6.2.2	Equation of the Fabry-Pérot with a single field component	131
6.3	Homogeneous stationary states	131
6.3.1	Linear stability of the homogeneous stationary states	132
6.3.2	Spontaneous symmetry breaking codimension-2 bifurcation	134
6.4	Spontaneous symmetry breaking of vectorial dark solitons	139
6.4.1	Codimension-2 bifurcation of vectorial dark solitons	139
6.4.2	Linear stability analysis of the plateau for Turing pattern formation	141
6.4.3	Spontaneous symmetry breaking in the presence of nonlocal coupling	143
6.5	Self-crystallisation of vectorial dark solitons	144
6.6	Partial crystal formation	147
6.7	Vectorial dark-bright solitons	150
6.7.1	Vectorial dark-bright solitons in Fabry-Pérot resonators	150
6.7.2	Nonlocal coupling of oscillating vectorial dark-bright solitons	153
6.8	Vectorial cavity soliton distribution in parameter space	158
6.9	Conclusion	159

6.1 Introduction

In this chapter, we continue our investigation on the formation of temporal cavity solitons within the Fabry-Pérot (FP) resonator, but at a difference to the previous chapter, we model intracavity fields of orthogonal polarisations. The system under study is outlined generally in Sections 5.2 and 5.3, and is composed of highly reflective mirrors which encloses a Kerr nonlinear medium operating within the regime of normal group velocity dispersion. Previously we made the assumption that the intracavity field preserved the polarisation properties of the driving field, taken to be linearly polarised, thus restricting the intracavity solutions to the linearly polarised case. Here, we relax this assumption by considering polarisation mode degeneracy of the waveguide and mirrors, such that, the cavity may support counter-rotating orthogonal polarisation components. By introducing polarisation considerations to the FP cavity, the now vectorial (two component [37]) temporal cavity solitons display features in addition to those seen for the single field FP resonator [48, 56] in Chapter 5. This is due to the possibility of spontaneous symmetry breaking (SSB) between orthogonal polarisation components, where the SSB of light within the FP resonator has been demonstrated experimentally when neglecting dispersion [68]. More generally, SSB has been demonstrated theoretically and experimentally in Kerr resonators (of ring and FP geometry) where the intracavity field is composed of orthogonal polarised components [66–68, 86–91], counterpropagating components [38, 92–97, 100–102], a combination of the two [49, 103, 104], and most recently, between two, or more, coupled resonators [105–109].

The design considerations required of the waveguide to obtain degenerate orthogonal polarisation modes has been discussed previously in Section 2.2.3, where we outline the importance of negligible birefringence (which manifests as a linear coupling between polarisation modes). In our model, we assume that the input field is linearly polarised, and may be decomposed within the resonator into counter-rotating circular polarisation components. This introduces additional constraints, as the waveguide cross-section is required to possess circular symmetry to support degenerate modes of circular polarisation. Another source of birefringence, particular to the FP resonator, is a consequence of imperfections on the high reflectivity mirrors, which form the cavity. For example, the thin-film deposition process commonly used for fibre FP cavities [68] may lead to stresses or anisotropic structures, causing the coating layers to exhibit different refractive indices for different polarisation states. In practice, birefringence originating from mirror imperfections, and geometric asymmetry of the waveguide, are always present and must be accounted for. SSB between counter-rotating fields in a FP resonator has been demonstrated experimentally in [68], where SSB was shown to occur if the linear resonance splitting due to birefringence was below 5% of the cavity linewidth. We assume in this chapter that the Kerr effect is dominant over the linear coupling of birefringent interaction, and the latter can therefore be neglected.

We begin this chapter by deriving our model for the FP resonator (Section 6.2), presenting an intracavity field composed of two forward and two backward counterpropagating fields of orthogonal counter-rotating polarisations [49]. Our model takes inspiration from the methods of Cole et al. [48], where we combine forward and backward propagating field equations of common polarisation to obtain a pair of mean field integro-partial differen-

tial equations, describing fields of counter-rotating circular polarisation over the round trip of the cavity. Here, the interaction between counterpropagating and counter-rotating field components is assumed to be dominated by the Kerr effect and modelled following from Pitois et al. [55]. In Section 6.3 we present the homogeneous stationary states (HSS) of this system, where we note a mathematical equivalence with the HSSs of the ring resonator (seen in Chapter 3 and Chapter 4). Nonetheless, the FP resonator presents distinct features, where in particular, our linear stability analysis predicts a codimension-2 SSB bifurcation of the high power bistable HSS. This bifurcation represents a collision between two SSB bifurcations; a reverse supercritical pitchfork bifurcation resulting in symmetry broken HSSs, and a forward supercritical pitchfork bifurcation resulting in the formation of Turing patterns of alternating polarisation components, found innately in the normal dispersion regime. This bifurcation structure is found to extend to symmetric vectorial dark solitons (VDS) in Section 6.4, resulting in a multitude of different symmetry broken VDS stationary states. Of particular interest is the Turing instability resulting in the formation of patterns of alternating polarisation on the homogeneous background power (plateau) from which the VDS hangs. This SSB phenomenon has been previously demonstrated in the ring resonator (Chapter 3), and was shown to introduce long range interactions between adjacent VDSs. These long range interactions induce a spontaneous self-organisation of VDSs, which move from a random distribution over the round trip, to a regular soliton crystal (RSC) composed of equidistant VDSs over the round trip. In Sections 6.5 and 6.6, we generalise this ‘self-crystallisation’ phenomenon to the FP resonator and discuss the differences between ring and FP configurations. Finally, we characterise the formation of dark-bright vectorial solitons in Section 6.7. Example dark-bright vectorial solitons are obtained with field components of identical normal group velocity dispersion, and are shown to undergo a Hopf bifurcation, resulting in non trivial breathing dynamics.

6.2 Modelling the Fabry-Pérot resonator with polarisation consideration

6.2.1 Derivation of the Fabry-Pérot model with vectorial electric field

Here, we present the derivation of our model for the polarisation degenerate FP resonator, as first communicated in [49] (and previously for the single field case in [48]). This derivation takes inspiration from the linearly polarised case [56], where we generalise the single field FP model by resolving the linearly polarised forward and backward propagating fields within the cavity into counter-rotating circularly polarised field components. We then combine the forward F_{\pm} and backward B_{\pm} counterpropagating fields of common polarisation ‘+’ or ‘-’, such that, the system of four fields and four equations is reduced to two coupled generalised Lugiato-Lefever equations (LLE), describing the evolution of two fields ψ_{\pm} over the full round trip of the resonator, as seen in Fig. 6.1.

The total electric field within the cavity can be expressed in terms of linear polarisation components,

$$\mathcal{E}(\tau, t) \propto \hat{x}\mathcal{E}_x(\tau, t) + \hat{y}\mathcal{E}_y(\tau, t) \quad (6.1)$$

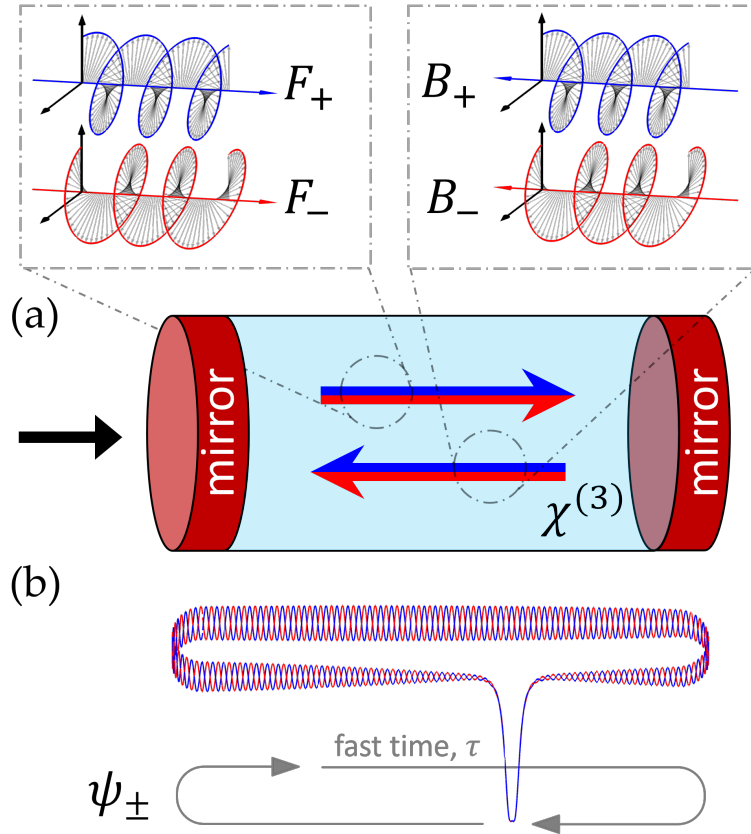


Figure 6.1: (a) A Fabry-Pérot resonator composed of two highly reflective mirrors filled with a Kerr, $\chi^{(3)}$, nonlinear medium. A linearly polarised input field is coupled into the resonator, where the forward, $F_{\pm}(\tau, t)$, and backward, $B_{\pm}(\tau, t)$, counterpropagating fields defined on the domain $0 \leq \tau \leq \tau_R/2$ are resolved into counter-rotating circular polarisation components ‘+’, ‘-’. (b) An example vectorial dark soliton solution is presented in terms of the field envelopes $\psi_{\pm}(\tau, t)$, defined over the extended domain $-\tau_R/2 \leq \tau \leq \tau_R/2$, where τ_R is the cavity round trip time.

where

$$\mathcal{E}_x(\tau, t) = E_x(\tau, t) + c.c., \quad \mathcal{E}_y(\tau, t) = E_y(\tau, t) + c.c.. \quad (6.2)$$

Here, $E_x(\tau, t)$ and $E_y(\tau, t)$ are the slowly varying envelopes of the electric field polarised along the x and y orthogonal directions, respectively. As has been shown by Pitois et al. [55], the interaction of two electric fields counterpropagating in an isomorphic dielectric medium with Kerr nonlinearity can be described by the third order nonlinear atomic polarisation along $\hat{\mathbf{x}}$ and $\hat{\mathbf{y}}$ orthogonal directions, with,

$$\begin{aligned} P_{x,y} = & (\chi_{xxyy} + \chi_{xyxy} + \chi_{xyxy})|E_{x,y}|^2 E_{x,y} \\ & + (\chi_{xyxy} + \chi_{xyyx})|E_{y,x}|^2 E_{x,y} + \chi_{xyyx} E_{y,x}^2 E_{x,y}^* \end{aligned} \quad (6.3)$$

In the case of silica fibres, components of the third order nonlinear susceptibility χ_{ijkl} are related as $\chi_{xxyy} = \chi_{xyxy} = \chi_{xyyx} = \chi_{xxxx}/3$, such that, Eq. (6.3) reduces to

$$P_{x,y} = \chi_{xxxx}(|E_{x,y}|^2 E_{x,y} + \frac{2}{3}|E_{y,x}|^2 E_{x,y} + \frac{1}{3}E_{y,x}^2 E_{x,y}^*). \quad (6.4)$$

Within the FP cavity, fields of orthogonal polarisation contain forward and backward propagating components, such that, we may write the electric field envelope as,

$$E_{x,y}(\tau, t) = F_{x,y}(\tau, t)e^{ik\tau} + B_{x,y}(\tau, t)e^{-ik\tau}, \quad (6.5)$$

where $F_{x,y}(\tau, t)$ and $B_{x,y}(\tau, t)$ are slowly varying amplitudes of the forward and backward counterpropagating fields polarised along the x and y directions and k is a propagation constant. By performing the transformation

$$F_{\pm}(\tau, t) = \frac{1}{\sqrt{2}}[F_x(\tau, t) \pm iF_y(\tau, t)], \quad B_{\pm}(\tau, t) = \frac{1}{\sqrt{2}}[B_x(\tau, t) \pm iB_y(\tau, t)], \quad (6.6)$$

we may express the forward and backward field envelopes as counter-rotating circularly polarised fields. Inserting Eqs. (6.6) into the nonlinear atomic polarisation (6.4), the interaction of the four fields within the cavity F_+, F_-, B_+, B_- due to the Kerr effect may be quantified with the nonlinear atomic polarisation,

$$P_{\pm} = \chi_{xxxx} \frac{2}{3} \left\{ |F_{\pm}|^2 F_{\pm} + 2|B_{\pm}|^2 F_{\pm} + 2|F_{\mp}|^2 F_{\pm} + 2|B_{\mp}|^2 F_{\pm} + 2B_{\pm} B_{\mp}^* F_{\mp} \right\} e^{ik\tau} \quad (6.7a)$$

$$+ \frac{2}{3} \left\{ |B_{\pm}|^2 B_{\pm} + 2|F_{\pm}|^2 B_{\pm} + 2|B_{\mp}|^2 B_{\pm} + 2|F_{\mp}|^2 B_{\pm} + 2F_{\pm} F_{\mp}^* B_{\mp} \right\} e^{-ik\tau} \quad (6.7b)$$

+ (third harmonic terms).

Eq. (6.7) suggests a nonreciprocal Kerr response with respect to fields of different propagation direction [$\propto \exp(\pm ik\tau)$] and polarisations (' \pm '), which may be separated into four expressions. We obtain the governing coupled equations through the identical procedure performed many times in thesis, whereby the nonlinear atomic polarisation is inserted into Maxwell's equations, where under the assumption that the spectrum of $\mathcal{E}(\tau, t)$ is sufficiently narrow so we may neglect dispersive changes in the transverse components of the electric field. Terms proportional to $\exp(ik\tau)$ and $\exp(-ik\tau)$ may be separated into

distinct equations as per the rotating wave approximation, and again split into equations of counter-rotating polarisations, such that, incorporating the effects of the pump, losses, dispersion, and detuning, we arrive at

$$\partial_t F_+ + \partial_\tau F_+ = S - (1 + i\theta)F_+ - i\partial_\tau^2 F_+ \quad (6.8a)$$

$$+ i\frac{2}{3}\left\{|F_+|^2 F_+ + 2|B_+|^2 F_+ + 2|F_-|^2 F_+ + 2|B_-|^2 F_+ + 2B_+ B_-^* F_-\right\},$$

$$\partial_t B_+ - \partial_\tau B_+ = S - (1 + i\theta)B_+ - i\partial_\tau^2 B_+ \quad (6.8b)$$

$$+ i\frac{2}{3}\left\{|B_+|^2 B_+ + 2|F_+|^2 B_+ + 2|B_-|^2 B_+ + 2|F_-|^2 B_+ + 2F_+ F_-^* B_-\right\},$$

$$\partial_t F_- + \partial_\tau F_- = S - i(1 + i\theta)F_- - i\partial_\tau^2 F_- \quad (6.8c)$$

$$+ i\frac{2}{3}\left\{|F_-|^2 F_- + 2|B_-|^2 F_- + 2|F_+|^2 F_- + 2|B_+|^2 F_- + 2B_- B_+^* F_+\right\},$$

$$\partial_t B_- - \partial_\tau B_- = S - (1 + i\theta)B_- - i\partial_\tau^2 B_- \quad (6.8d)$$

$$+ i\frac{2}{3}\left\{|B_-|^2 B_- + 2|F_-|^2 B_- + 2|B_+|^2 B_- + 2|F_+|^2 B_- + 2F_- F_+^* B_+\right\},$$

These four equations are of the form of coupled generalised LLE's (normalisation given in Section 2.6), which describe field components which propagate forward, F , and backward, B , in the cavity with right handed, '+', and left handed, '-' circular polarisations within the usual slowly varying field amplitude approximation. The resonator is driven by a single linearly polarised input field assumed to be polarised along the x direction as $\mathbf{S} = \sqrt{2}S\hat{x}$, with detuning to the nearest cavity resonance θ . As usual, t is the 'slow time' temporal variable describing the evolution over many round trips of the cavity, while τ is the 'fast time' longitudinal variable describing the evolution of the four fields over a single round trip of the cavity. Eqs. (6.8) obey the boundary conditions

$$F_\pm(0, t) = B_\pm(0, t), \quad F_\pm(\tau_R/2, t) = B_\pm(\tau_R/2, t), \quad (6.9)$$

upon reflection at the mirrors, located at $\tau = 0$ and $\tau_R/2$, where τ_R is the cavity round trip time. These fields are defined in the interval between the mirrors ($0 \leq \tau \leq \tau_R/2$). In Eqs. (6.8), the nonlinear interaction terms are enclosed in curly brackets. The first nonlinear term of each equation corresponds to self-phase modulation. The second, third and fourth terms correspond to cross-phase modulation between each of the four fields, respectively. The final term of each equation corresponds to an exchange of energy between fields that are counter-rotating and counterpropagating. This term describes a four wave mixing phenomenon whose effect appears explicitly in the presence of four field interactions between counterpropagating and orthogonally polarised fields.

As with the single field FP cavity, it is not possible for us to perform the typical transformation into a moving frame of reference to eliminate terms which evolve on the scale of the group velocity ($\partial_\tau F_\pm$ and $\partial_\tau B_\pm$), as done for the ring resonator. This is due to the existence of two distinct retarded times, between the forward propagation [Eqs. (6.8a) and (6.8c)] and the backwards propagation [Eqs. (6.8b) and (6.8d)] of equations the FP cavity.

We now aim to coalesce equations of forward and backward propagating fields of com-

mon polarisation, following the procedure of [48]. This begins by introducing appropriate model expansions for the four intracavity fields, with [33]

$$F_{\pm}(\tau, t) = \sum_{\mu=-\infty}^{\infty} \bar{f}_{\mu}^{\pm}(t) e^{i\mu\alpha\tau}, \quad B_{\pm}(\tau, t) = \sum_{\mu=-\infty}^{\infty} \bar{f}_{\mu}^{\pm}(t) e^{-i\mu\alpha\tau}, \quad (6.10)$$

where $\alpha = 2\pi/\tau_R$ is the free spectral range of the cavity with round trip time τ_R and $\bar{f}_{\mu}^{\pm}(t)$ is the modal amplitude of mode number μ . The expansions (6.10) suggest that the envelopes $F_{\pm}(\tau, t)$, $B_{\pm}(\tau, t)$ may now be defined over an extended interval encompassing the full round trip of the cavity $-\tau_R/2 \leq \tau \leq \tau_R/2$. This amounts to defining the field variables as

$$F_{\pm}(\tau, t) = F_{\pm}(-\tau, t), \quad B_{\pm}(\tau, t) = B_{\pm}(-\tau, t), \quad (6.11)$$

over the extended interval. Comparing our original boundary conditions (6.9) with (6.11), we see that the field variables obey periodic boundary conditions over this extended domain. Due to the periodic boundary, it is now possible to express the dynamics of this system in terms of travelling waves (similar to the ring resonator system) as opposed to the standing waves characteristic of the FP resonator. We note that the modal amplitudes can be obtained through the field amplitudes as,

$$\bar{f}_{\mu}^{\pm}(t) = \int_{-\tau_R/2}^{\tau_R/2} d\tau e^{i\mu\alpha\tau} F_{\pm}(\tau, t) = \int_{-\tau_R/2}^{\tau_R/2} d\tau e^{-i\mu\alpha\tau} B_{\pm}(\tau, t). \quad (6.12)$$

Focusing on Eq. (6.8a) for now, we insert modal expansions (6.10) into Eq. (6.8a) to obtain the modal of equation,

$$\begin{aligned} \partial_t \bar{f}_{\mu}^+ &= S\delta_{\mu,0} - i\mu\alpha \bar{f}_{\mu}^+ - (1 + i\theta) \bar{f}_{\mu}^+ + i(\mu\alpha)^2 \bar{f}_{\mu}^+ \\ &+ \frac{2i}{3} \sum_{\mu', \mu'', \mu'''} \delta_{\mu, \mu' + \mu'' - \mu'''} \left\{ \bar{f}_{\mu'}^+ \bar{f}_{\mu''}^+ (\bar{f}_{\mu'''}^+)^* + 2\bar{f}_{\mu'}^+ \bar{f}_{\mu''}^+ (\bar{f}_{\mu'''}^+)^* \right. \\ &\quad + 2\bar{f}_{\mu'}^+ \bar{f}_{\mu''}^- (\bar{f}_{\mu'''}^-)^* + 2\bar{f}_{\mu'}^- \bar{f}_{\mu''}^+ (\bar{f}_{\mu'''}^-)^* \\ &\quad \left. + 2\bar{f}_{\mu'''}^+ (\bar{f}_{\mu''}^-)^* \bar{f}_{\mu'}^- \right\}, \end{aligned} \quad (6.13)$$

were we have implemented the four wave momentum matching condition $\mu + \mu''' = \mu' + \mu''$ through the Kronecker delta $\delta_{i,j}$, which takes the values 1 when $i = j$ and 0 otherwise. In addition, the continuous wave driving field corresponds to $\mu = 0$, and is notated as $S\delta_{\mu,0}$. We proceed from here by splitting the mode amplitudes into two functions that evolve on distinct time scales

$$\bar{f}_{\mu}^{\pm}(t) = f_{\mu}^{\pm}(t) e^{-i\mu\alpha t} \quad (6.14)$$

such that the set of modal equations (6.13) become

$$\begin{aligned}
 \partial_t f_\mu^+ = & S\delta_{\mu,0} - (1 + i\theta)f_\mu^+ + i(\mu\alpha)^2 f_\mu^+ \\
 & + \frac{2i}{3} \sum_{\mu', \mu'', \mu'''} \delta_{\mu, \mu' + \mu'' - \mu'''} \left\{ f_{\mu'}^+ f_{\mu''}^+ (f_{\mu'''}^+)^* + 2f_{\mu'}^+ f_{\mu''}^+ (f_{\mu'''}^+)^* e^{i2\alpha(\mu - \mu')t} \right. \\
 & \qquad \qquad \qquad + 2f_{\mu'}^+ f_{\mu''}^- (f_{\mu'''}^-)^* + 2f_{\mu'}^- f_{\mu''}^+ (f_{\mu'''}^-)^* e^{i2\alpha(\mu - \mu')t} \\
 & \qquad \qquad \qquad \left. + 2f_{\mu'''}^+ (f_{\mu''}^-)^* f_{\mu'}^- e^{i2\alpha(\mu - \mu')t} \right\}. \tag{6.15}
 \end{aligned}$$

The exponential function $\exp(-i\mu\alpha t)$, resulting from decomposition of the modal amplitude (6.14), displays rapid dynamics varying on a timescale of the cavity repetition rate $\alpha = 2\pi/\tau_R$. Conversely, the modal amplitudes $f_\mu(t)$ evolve on the timescale of the photon lifetime of the cavity $\kappa^{-1} = \tau_R/T$. For the high fineness cavities we consider here, the power transmission coefficient is small $T \ll 1$, and as such, these functions vary on well separated timescales. In Eqs. (6.15), we can see that rapid dynamics at the timescale of the free spectral range are prolific, originating from exponential functions which appear only in terms of cross-phase modulation. In particular, these dynamical terms are a consequence of the interaction of counterpropagating fields, and appear in the relevant cross-phase interactions.

For our purposes, we consider dynamics on the time scale of second order (or higher) dispersion. Should we perform an averaging of Eqs. (6.15) on a timescale that is much longer than the round trip time but shorter than the cavity photon lifetime, we find that all terms remain unchanged with the exception of those proportional to the exponential terms $\exp[i2\alpha(\mu - \mu')t]$. Exponential terms satisfying $\mu \neq \mu'$ vanish under the average. Hence, to characterise the dynamics on the timescale of the dispersive effect, we retain only exponential terms which satisfy $\mu = \mu'$ (and equally $\mu'' = \mu'''$ due to the momentum matching condition). This condition can be understood as removing terms which do not conserve energy, and are appropriately discarded [45, 46, 48, 49]. Under these considerations, Eqs. (6.15) reduce to

$$\begin{aligned}
 \partial_t f_\mu^+ = & S\delta_{\mu,0} - (1 + i\theta)f_\mu^+ + i(\mu\alpha)^2 f_\mu^+ \\
 & + \frac{2i}{3} \sum_{\mu', \mu'', \mu'''} \delta_{\mu, \mu' + \mu'' - \mu'''} f_{\mu'}^+ f_{\mu''}^+ (f_{\mu'''}^+)^* + \frac{4i}{3} f_\mu^+ \sum_{\mu'} (f_{\mu'}^+)^* f_{\mu'}^+ \\
 & + \frac{4i}{3} \sum_{\mu', \mu'', \mu'''} \delta_{\mu, \mu' + \mu'' - \mu'''} f_{\mu'}^+ f_{\mu''}^- (f_{\mu'''}^-)^* + \frac{4i}{3} f_\mu^+ \sum_{\mu'} f_{\mu'}^- (f_{\mu'}^-)^* \\
 & + \frac{4i}{3} f_\mu^- \sum_{\mu'} (f_{\mu'}^-)^* f_{\mu'}^+. \tag{6.16}
 \end{aligned}$$

Finally, we define the new field variables

$$\psi_\pm(\tau, t) = \sum_{\mu=-\infty}^{\infty} f_\mu^\pm(t) e^{i\mu\alpha\tau}, \tag{6.17}$$

such that we may collapse the modal equations (6.16) into

$$\begin{aligned}
 \partial_t \psi_+ &= S - (1 + i\theta)\psi_+ - i\partial_\tau^2 \psi_+ \\
 &+ i\frac{2}{3} \left\{ |\psi_+|^2 \psi_+ + 2\psi_+ \frac{1}{\tau_R} \int_{-\tau_R/2}^{\tau_R/2} |\psi_+|^2 d\tau \right. \\
 &\quad + 2|\psi_-|^2 \psi_+ + 2\psi_+ \frac{1}{\tau_R} \int_{-\tau_R/2}^{\tau_R/2} |\psi_-|^2 d\tau \\
 &\quad \left. + 2\psi_- \frac{1}{\tau_R} \int_{-\tau_R/2}^{\tau_R/2} \psi_+ \psi_-^* d\tau \right\}, \tag{6.18}
 \end{aligned}$$

where the integral terms follow from Parseval's theorem

$$\sum_{\mu'=-\infty}^{\infty} f_{\mu'}^a (f_{\mu'}^b)^* = \frac{1}{\tau_R} \int_{-\tau_R/2}^{\tau_R/2} d\tau \psi_a \psi_b^*, \tag{6.19}$$

where a, b correspond to either '+' or '-' polarisation. An identical result is obtained when starting from Eq. (6.8b), whereby Eqs. (6.8a) and (6.8b) are now described by a single integro-partial differential equation (6.18). By following the same steps, but starting from Eqs. (6.8c) or (6.8d), we obtain identical equation to (6.18) with an exchange of the polarisation labels $+ \leftrightarrow -$. Hence our model of the FP resonator with orthogonal polarisation field components is

$$\begin{aligned}
 \partial_t \psi_\pm &= S - (1 + i\theta)\psi_\pm - i\partial_\tau^2 \psi_\pm \tag{6.20} \\
 &+ i\frac{2}{3} \left\{ |\psi_\pm|^2 \psi_\pm + 2|\psi_\mp|^2 \psi_\pm + 2\langle |\psi_\pm|^2 \rangle \psi_\pm + 2\langle |\psi_\mp|^2 \rangle \psi_\pm + 2\langle \psi_\pm \psi_\mp^* \rangle \psi_\mp \right\}.
 \end{aligned}$$

As we first derived in [49], this system is described by two coupled integro-partial differential equations, which can be understood as two coupled generalised LLEs [24]. They describe the evolution of fields $\psi_\pm(\tau, t)$ of slowly varying amplitudes and orthogonal polarisation over the extended domain $-\tau_R/2 \leq \tau \leq \tau_R/2$ with periodic boundary conditions, where τ_R is the resonator round trip. The terms of Eqs. (6.20) enclosed in angled brackets represent integrals in fast time over a single round trip of the cavity

$$\langle |\psi_\pm|^2 \rangle = \frac{1}{\tau_R} \int_{-\tau_R/2}^{\tau_R/2} |\psi_\pm|^2 d\tau, \tag{6.21}$$

$$\langle \psi_\pm \psi_\mp^* \rangle = \frac{1}{\tau_R} \int_{-\tau_R/2}^{\tau_R/2} \psi_\pm \psi_\mp^* d\tau. \tag{6.22}$$

Integral terms arise due to counterpropagation of intracavity fields innately present in the FP configuration and are the result of rapid phase dynamics of cross-coupling terms between counterpropagating fields, such that they see each other through an average. The integral of Eq. (6.21) corresponds to the average intracavity power of the field over a round trip of the cavity. Nonlocal coupling of this kind is also present in bidirectionally pumped ring resonators [45, 46, 117], (Chapter 4), as well as the single field FP [48, 56] (Chapter

5). Of particular importance here is the term given in (6.22), which is not explicitly present in the aforementioned systems. This term corresponds to an energy exchange between circular components of the fields and is only present for four field interactions of orthogonal polarisations and counterpropagation [55].

The fields $\psi_{\pm}(\tau, t)$ are related to the four slowly varying intracavity field envelopes of forward propagation $F_{\pm}(\tau, t)$ and backward propagation $B_{\pm}(\tau, t)$ via the modal expansions

$$F_{\pm}(\tau, t) = \sum_{\mu=-\infty}^{+\infty} f_{\mu}^{\pm}(t) e^{-i\mu\alpha(t-\tau)}, \quad (6.23)$$

$$B_{\pm}(\tau, t) = \sum_{\mu=-\infty}^{+\infty} f_{\mu}^{\pm}(t) e^{-i\mu\alpha(t+\tau)}, \quad (6.24)$$

which defined over the domain over the domain $0 \leq \tau \leq \tau_R$, where the modal coefficients are evaluated as

$$f_{\mu}^{\pm}(t) = \frac{1}{\tau_R} \int_{-\tau_R/2}^{\tau_R/2} d\tau e^{-i\mu\alpha\tau} \psi_{\pm}(\tau, t). \quad (6.25)$$

6.2.2 Equation of the Fabry-Pérot with a single field component

Eqs. (6.20) of the FP are invariant under the exchange of the indices $+$ and $-$, representing a fundamental symmetry of the system. Setting $\psi_+ = \psi_- = \psi$, the coupled Eqs. (6.20) reduce to the single equation,

$$\partial_t \psi = S - (1 + i\theta)\psi + 2i(|\psi|^2 + 2\langle|\psi|^2\rangle)\psi - \partial_{\tau}^2 \psi. \quad (6.26)$$

Performing the renormalisations; $\psi \rightarrow \psi/\sqrt{2}$, $S \rightarrow S/\sqrt{2}$, we obtain the equation of the FP resonator with a single linearly polarised intracavity field, Eq. (5.22), discussed in Chapter 5. As a consequence, the symmetric stationary solutions of Eqs. (6.20) are also stationary solutions Eq. (5.22), up to a renormalisation, and have been described at length the previous chapter. This similarity does not necessarily extend to the stability of such solutions, with the possibility of spontaneous symmetry breaking of the now vectorial dark solitons, which we will discuss in the following sections.

6.3 Homogeneous stationary states

The HSSs of the polarisation degenerate FP cavity can be obtained from Eqs. (6.20) by setting all derivatives to zero ($\partial_t \psi_{\pm} = 0$, $\partial_{\tau}^2 \psi_{\pm} = 0$). This results in the coupled equations

$$S^2 = 4H_{\pm}^3 - 4(\theta - 4H_{\mp})H_{\pm}^2 + ((\theta - 4H_{\mp})^2 + 1)H_{\pm}, \quad (6.27)$$

where $H_{\pm} = |\psi_{\pm}|^2$, and the real and imaginary parts of the HSSs are

$$\begin{pmatrix} U_{0,\pm} \\ V_{0,\pm} \end{pmatrix} = \begin{pmatrix} \frac{S}{1+(2H_{\pm}+4H_{\mp}-\theta)^2} \\ \frac{(2H_{\pm}+4H_{\mp}-\theta)S}{1+(2H_{\pm}+4H_{\mp}-\theta)^2} \end{pmatrix}. \quad (6.28)$$

These solutions are obtained by recognising that the integral terms can be trivially evaluated as $\langle |\psi_{\pm}|^2 \rangle = |\psi_{\pm}|^2$, $\langle \psi_{\pm} \psi_{\mp}^* \rangle = \psi_{\pm} \psi_{\mp}^*$ for solutions with flat profile. Eqs. (6.27) admit solutions that are either linearly polarised (symmetric $H_+ = H_-$) or not linearly polarised (symmetry broken $H_+ \neq H_-$), and allow for the SSB of light within the FP resonator. This has been demonstrated experimentally within a FP cavity when neglecting fast time effects [68], where within this regime, the set of equations (6.27) are mathematically equivalent to those discussed in Chapter 3 for the ring resonator with two orthogonal polarisation field components [38, 66], or two counterpropagating intracavity fields [38, 96, 117] discussed in Chapter 4, under the renormalisation $H_{\pm} \rightarrow H_{\pm}/2$, $S^2 \rightarrow S^2/2$. Despite the apparent universality of HSSs between ring and FP resonators, this analogy does not necessarily extend to the stability of these stationary solutions. In the following sections, we characterise the stability of the HSSs, outlining the different aspects of the SSB bifurcation structure of the HSSs when compared to the ring resonator, with particular focus on the formation of Turing patterns phenomenologically similar to those described for ring resonators in Chapter 3.

6.3.1 Linear stability of the homogeneous stationary states

To investigate the linear stability of the HSSs, we perform a linearisation of the modal amplitudes, whose evolution is governed by the modal equations (6.16), which rewrite here to include both polarisation equations,

$$\begin{aligned} \partial_t f_{\mu}^{\pm} &= S\delta_{\mu,0} - (1+i\theta)f_{\mu}^{\pm} + ik_{\mu}^2 f_{\mu}^{\pm} \\ &+ \frac{2i}{3} \sum_{\mu',\mu'',\mu'''} \delta_{\mu,\mu'+\mu''-\mu'''} f_{\mu'}^{\pm} f_{\mu''}^{\pm} (f_{\mu'''}^{\pm})^* + \frac{4i}{3} f_{\mu}^{\pm} \sum_{\mu'} (f_{\mu'}^{\pm})^* f_{\mu'}^{\pm} \\ &+ \frac{4i}{3} \sum_{\mu',\mu'',\mu'''} \delta_{\mu,\mu'+\mu''-\mu'''} f_{\mu'}^{\pm} f_{\mu''}^{\mp} (f_{\mu'''}^{\mp})^* + \frac{4i}{3} f_{\mu}^{\pm} \sum_{\mu'} f_{\mu'}^{\mp} (f_{\mu'}^{\mp})^* \\ &+ \frac{4i}{3} f_{\mu}^{\mp} \sum_{\mu'} (f_{\mu'}^{\mp})^* f_{\mu'}^{\pm}, \end{aligned} \quad (6.29)$$

where $f_{\mu}(t)$ is the modal amplitude with cavity mode number μ and fast time wavenumber $k_{\mu}^2 = (2\pi\mu/\tau_R)^2$. The HSSs of Eqs. (6.20) correspond to the modal coefficients

$$f_{\mu,s}^{\pm} = \psi_s^{\pm} \delta_{\mu,0} \quad (6.30)$$

where $\delta_{\mu,0}$ is the Kronecker delta. We introduce a linear perturbation to the counter-rotating polarisation components of the form

$$f_{\mu}^{\pm} = \psi_s^{\pm} \delta_{\mu,0} + \delta f_{\mu}^{\pm}, \quad (6.31)$$

which is inserted into Eqs. (6.29), yielding the linearised set of equations

$$\begin{aligned} \partial_t \delta f_\mu^\pm &= -(1 + i\theta) \delta f_\mu^\pm + ik_\mu^2 \delta f_\mu^\pm & (6.32) \\ &+ \frac{2i}{3} \{ (4|\psi_s^\pm|^2 + 4|\psi_s^\mp|^2) \delta f_\mu^\pm + 4\psi_s^\pm (\psi_s^\mp)^* \delta f_\mu^\mp + (\psi_s^\pm)^2 (\delta f_{-\mu}^\pm)^* + 2\psi_s^\pm \psi_s^\mp (\delta f_{-\mu}^\mp)^* \} \\ &+ \frac{4i}{3} \delta_{\mu,0} \{ (|\psi_s^\pm|^2 + |\psi_s^\mp|^2) \delta f_0^\pm + \psi_s^\pm (\psi_s^\mp)^* \delta f_0^\mp + (\psi_s^\pm)^2 (\delta f_0^\pm)^* + 2\psi_s^\pm \psi_s^\mp (\delta f_0^\mp)^* \}. \end{aligned}$$

Without the loss of generality, we may assume that the homogeneous stationary solutions are real. Hence we may express the real and imaginary components of the perturbations as

$$\begin{pmatrix} \partial_t \operatorname{Re}(\delta f_\mu^+) \\ \partial_t \operatorname{Im}(\delta f_\mu^+) \\ \partial_t \operatorname{Re}(\delta f_\mu^-) \\ \partial_t \operatorname{Im}(\delta f_\mu^-) \end{pmatrix} = \begin{pmatrix} -1 & -A_+ & 0 & -\frac{1}{6}(1 - \delta_{\mu,0})C \\ B_+ & -1 & \frac{1}{2}C & 0 \\ 0 & -\frac{1}{6}(1 - \delta_{\mu,0})C & -1 & -A_- \\ \frac{1}{2}C & 0 & B_- & -1 \end{pmatrix} \begin{pmatrix} \operatorname{Re}(\delta f_\mu^+) \\ \operatorname{Im}(\delta f_\mu^+) \\ \operatorname{Re}(\delta f_\mu^-) \\ \operatorname{Im}(\delta f_\mu^-) \end{pmatrix}, \quad (6.33)$$

where

$$A_\pm = -\theta + k_\mu^2 + 2\psi_\pm^2 + \frac{4}{3}(2 + \delta_{\mu,0})\psi_\mp^2, \quad (6.34)$$

$$B_\pm = -\theta + k_\mu^2 + \frac{2}{3}(5 + 4\delta_{\mu,0})\psi_\pm^2 + \frac{4}{3}(2 + \delta_{\mu,0})\psi_\mp^2, \quad (6.35)$$

$$C^2 = 64(1 + 3\delta_{\mu,0})\psi_+^2 \psi_-^2. \quad (6.36)$$

The Jacobian matrix of Eq. (6.33) yields the characteristic equation,

$$\begin{aligned} 0 &= (\lambda + 1)^4 + \left[A_+ B_+ + A_- B_- + \frac{1}{6}(1 - \delta_{\mu,0})C^2 \right] (\lambda + 1)^2 \\ &+ A_+ A_- B_+ B_- - \frac{1}{4} A_+ A_- C^2 - \frac{1}{36}(1 - \delta_{\mu,0})C^2 \left[B_+ B_- + \frac{1}{4}C^2 \right], \end{aligned} \quad (6.37)$$

wherefrom, we obtain the the eigenvalues [49]

$$\lambda(k_\mu) = -1 \pm \frac{\sqrt{-A_+ B_+ - A_- B_- - \frac{1}{6}(1 - \delta_{\mu,0})C^2 \pm Q}}{\sqrt{2}}, \quad (6.38)$$

with

$$Q = \sqrt{(A_+ B_+ - A_- B_-)^2 + A_+ A_- C^2 + (1 - \delta_{\mu,0}) \frac{C^2}{9} (3A_+ B_+ + B_+ B_- + 3A_- B_-)}. \quad (6.39)$$

Due to the presence of the Kronecker delta $\delta_{\mu,0}$ in the eigenspectrum (6.38), it is apparent that we must consider separately the cases of $\mu = 0$ and $\mu \neq 0$. These two outcomes refer to the scenario in which the perturbation evolving in slow time has a flat profile, $\mu = 0$, or exhibits a sinusoidal fast time component $\mu \neq 0$, and are made notably distinct from each other due to the inherent counterpropagation of fields within the FP resonator. This

distinction is made most clear when expressed in terms of the field envelopes, where, these two cases refer to whether or not the the perturbation $|\epsilon| \ll 1$ of wavenumber k_μ survives under the integral terms, with

$$\langle (\psi_s^a + \epsilon^a)(\psi_s^b + \epsilon^b)^* \rangle \sim \begin{cases} (\psi_s^a + \epsilon^a)(\psi_s^b + \epsilon^b)^*, & \text{if } \epsilon \propto \exp[\lambda(k_0 = 0)t], (\mu = 0), \\ \psi_s^a(\psi_s^b)^*, & \text{if } \epsilon \propto \exp[\lambda(k_\mu)t + ik_\mu\tau], (\mu \neq 0). \end{cases} \quad (6.40)$$

where we indicate polarisations with $a, b = \pm$. A perturbation will not survive the averaging imposed by the integral terms (originating from counterpropagation) should it contain a sinusoidal fast time component, and hence, integral terms will not contribute to the dynamics of the linear perturbation.

In Fig. 6.2(a), we plot example HSSs of Eqs. (6.27) for $S = 1.2425$, and their corresponding eigenvalues in Fig. 6.2(b)-(c). The eigenvalues of Eq. (6.38) are evaluated for $\mu = 0$ ($k_0^2 = 0$) and $k_\mu^2 = 4.83$, respectively. Here, we have selected the value of k_μ^2 to be the first wavenumber with unstable eigenvalue, where at least one eigenvalue (6.38) has positive real part, on the high power symmetric HSS when increasing the detuning. This yields a total of eight eigenvalues, whose real and imaginary parts are plotted in Figs. 6.2(b)-(c), respectively.

When $\mu = 0$, Eq. (6.38) reduces to eigenvalues which, under the appropriate renormalisation, are mathematically identical to those seen when neglecting fast time effects in the ring resonator system with two orthogonally polarised field components (Chapter 3), or two counterpropagating field components (Chapter 4) [38], and are discussed in detail for the polarisation degenerate FP in [68] when neglecting dispersion. As such, eigenvalues (6.38) predict the typical stability when $\mu = 0$, where the middle branch of the tilted Lorentzian curve (symmetric HSSs) is unstable, while the lower branch is stable, and the high power HSS is unstable between the SSB pitchfork bifurcations located at

$$H_{\text{SSB}} = \frac{1}{6}(2\theta \pm \sqrt{\theta^2 - 3}), \quad (6.41)$$

within which, symmetric HSSs move towards symmetry broken HSSs, where the bifurcations (6.41) mark the beginning and the end of the symmetry broken HSS ‘bubble’. We also see a region of Hopf instability ($5.15 < \theta < 7.32$), for which the symmetry broken HSSs are unstable to slow time oscillation. This phenomenon has seen much investigation within the literature for ring resonator systems (possessing mathematically equivalent HSS and eigenvalues), where further details are outlined in [38].

When $\mu \neq 0$, the eigenvalues indicate the growth/decay in slow time of perturbations that are sinusoidal in the fast time with wavenumber k_μ . Most notably, these eigenvalues indicate the appearance of an instability on the high power HSSs, near the peak of the Lorentzian curve in Fig. 6.2. As we will discuss in the following sections, this instability may be utilised to predict the onset of SSB Turing patterns of alternating polarisations.

6.3.2 Spontaneous symmetry breaking codimension-2 bifurcation

Here, we restrict our attention to the SSB phenomenon of the high power HSS, where, the SSB bifurcations of the high power symmetric HSS are shown in Figs. 6.3(a)-(c)

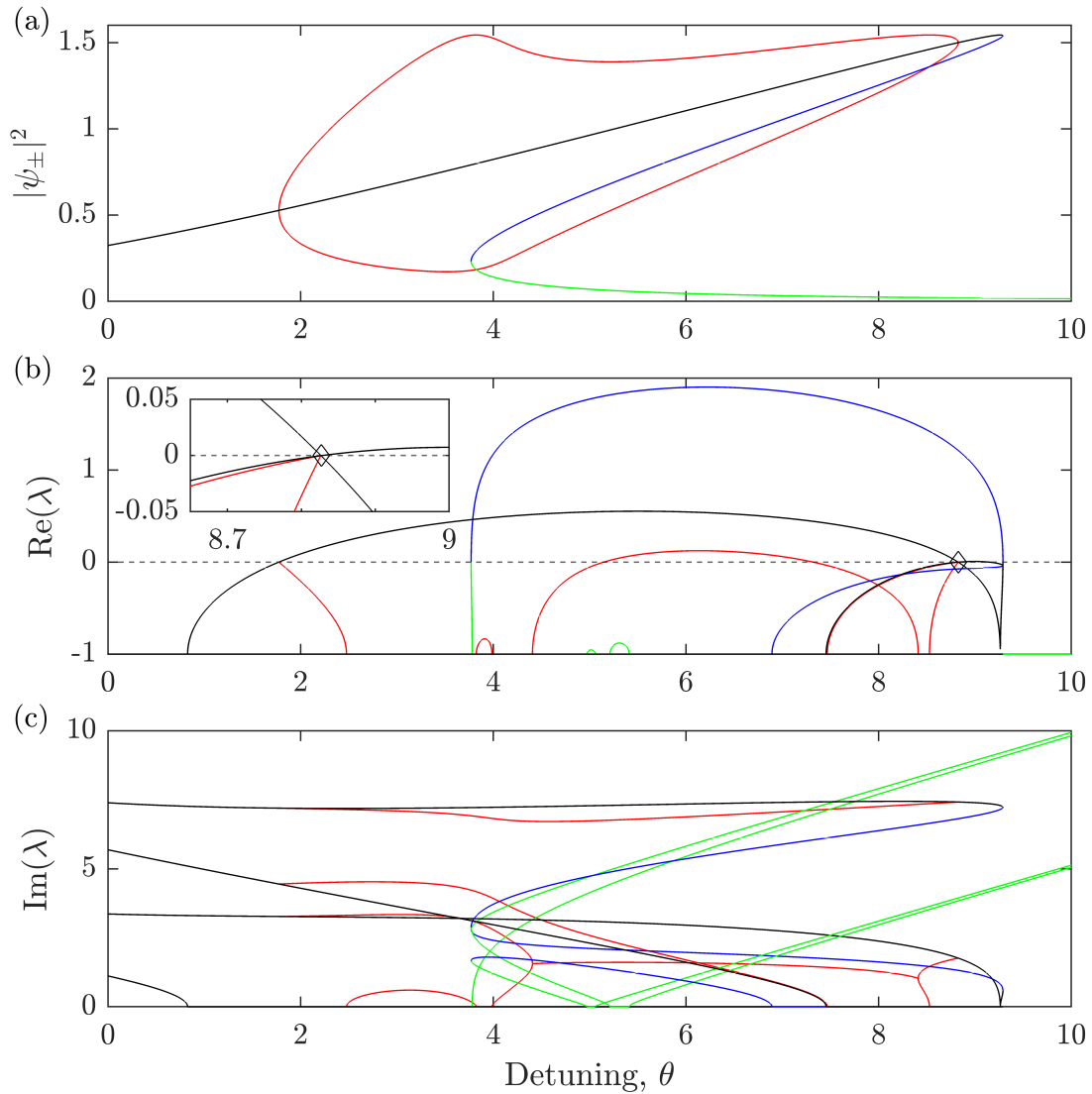


Figure 6.2: (a) HSSs of Eqs. (6.27) with the corresponding real (b) and imaginary (c) parts of the linear stability eigenvalues (6.38), where $S = 1.2425$. Eigenvalues (6.38) are evaluated for $k_0^2 = 0$ and $k_\mu^2 = 4.83$, yielding a total of 8 eigenvalues, and plotted above the axes of symmetry $\text{Re}(\lambda) = -1$, $\text{Im}(\lambda) = 0$. Black, blue, and green curves correspond to the high, middle, and low power symmetric HSSs, respectively. The red curve corresponds to the symmetry broken HSSs. The zoomed in window in (b) shows the codimension-2 bifurcation point $(S, \theta)_{\text{codim-2}} \approx (1.2425, 8.827)$ on the high power HSS (black curves) where the real part of the relevant $\mu = 0$ and a $\mu \neq 0$ eigenvalues are simultaneously zero, which is indicated with a black diamond.

for different values of the input field S . In each of these cases, the HSSs [Eqs. (6.27)] are plotted near the peak of the symmetric Lorentzian curve, where the high power HSS branch is shown as a black curve, and the symmetry broken HSS as the red curves. We indicate the stability of the HSSs using the linear stability eigenvalues of the previous section, Eq. (6.38), and indicate regions of stable and unstable HSSs by solid and dashed lines, respectively.

Fig. 6.3(a) depicts a region of stable symmetric HSSs (solid black line) flanked by two oppositely oriented supercritical pitchfork bifurcations, both of which result in the SSB of the symmetric HSS. For lower values of the detuning, we see a reverse pitchfork bifurcation in which the high power symmetric HSS become unstable to symmetry broken HSSs (red curve). This is predicted by the linear stability analysis ($\mu = 0$), where the higher power symmetric HSS is unstable between two SSB pitchfork bifurcations (6.41), as discussed previously. Of particular interest is the appearance of a bifurcation of the symmetric HSS distinctly associated with the normal dispersion regime. This bifurcation occurs when increasing the detuning, where the symmetric HSS suddenly becomes unstable to perturbations of nonzero wavenumber ($\mu \neq 0$). This results in the formation of a Turing pattern stationary state composed of alternating field components of orthogonal polarisation, an example of which can be seen in Fig. 6.4(ii). The maximum and minimum power of the resulting Turing pattern stationary state is shown in Fig. 6.3(a) as the blue curve. This instability originates with the self- and cross-phase modulation terms of Eqs. (6.20) that are local in fast time, where generally SSB also requires a nonreciprocal Kerr response between orthogonal polarisation components. Previously, we characterized a Turing pattern instability found between orthogonal polarisation components within the unidirectionally driven ring resonator, in Chapter 3 (Section 3.3.2). The Turing instability of the FP cavity is analogous to the ring resonator case, where both system possess analogous mechanisms (nonreciprocal and local Kerr interaction between field components) allowing for the formation of symmetry broken Turing patterns in the normal dispersion regime. Despite the mathematically equivalent HSSs, this instability is not observed between the counterpropagating fields of the bidirectionally driven ring resonator (Chapter 4) due to nonlocal cross-interaction, and consequently, a lack of local cross-interaction, originating from the counterpropagation of the fields.

We note that the Turing patterns observed here are of travelling wave character. This is distinct from typical standing wave Turing patterns of the FP cavity, due to phase sensitive interactions between forward and backward propagating fields. The travelling wave formalism of the dynamical variables implemented in this chapter allow us to describe Turing patterns (and temporal cavity solitons) of the FP resonator that are phenomenology similar to the temporal structures of the ring resonator. In addition, only symmetry broken perturbations will result in a Turing pattern instability. This is due to the distinct stability of the single field FP cavity, which do not present Turing instabilities for $H > 1$. Hence, symmetric perturbations of nonzero wavenumber return to the symmetric HSS, with stability indicated in Appendix B.1.

By increasing the power of the driving field, we observe a decrease in the separation between the two oppositely oriented pitchfork bifurcations until they collide. For this critical parameter value, of input field $S \approx 1.2425$ and detuning $\theta \approx 8.827$, the appearance of the Turing instability ($\mu \neq 0$) perfectly coincides with the reverse pitchfork SSB bifur-

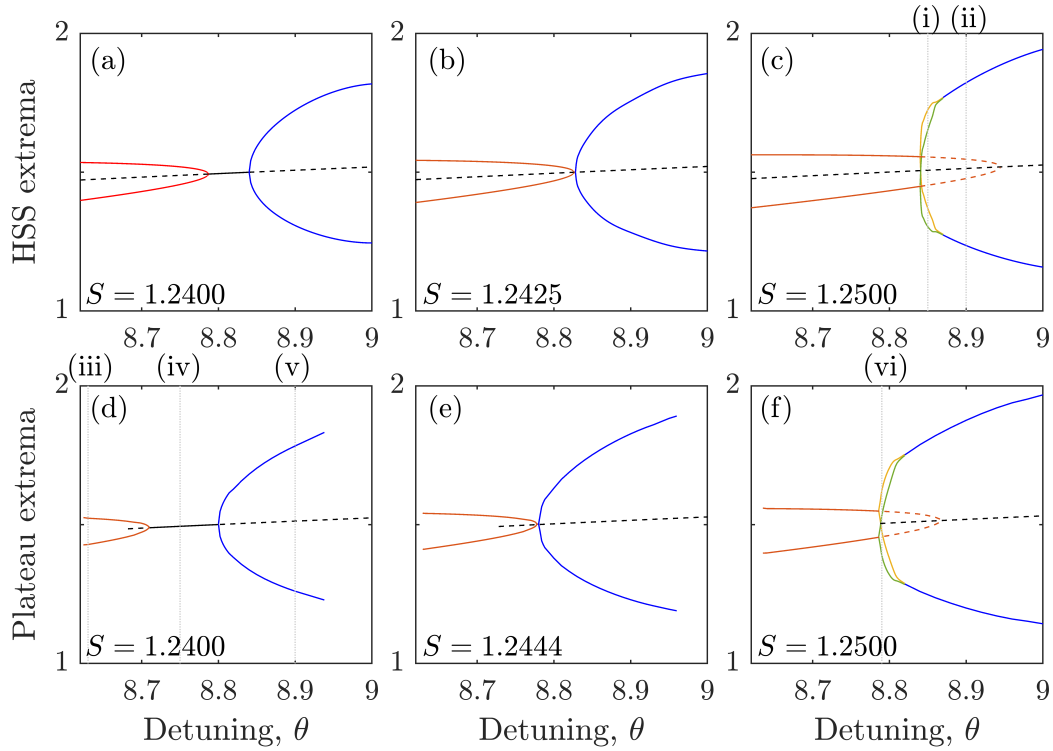


Figure 6.3: Spontaneous symmetry bifurcations of the HSSs (a)-(c) and vectorial dark solitons (d)-(f) for $\tau_R = 500$. Black curves correspond to the high power symmetric HSS (a)-(c) or high power plateau (d)-(f). Red curves correspond to the power of symmetry broken HSSs (a)-(c) or symmetry broken plateaus (d)-(f). Blue, green and orange curves correspond to the maximum/minimum power of Turing patterns of alternating orthogonal polarisations which bifurcated from the HSSs (a)-(c) or plateaus (d)-(f). (b) and (e) shows a codimension-2 bifurcation at $\theta \approx 8.827$ and $\theta \approx 8.779$, respectively. (a) and (d) show the bifurcation structure for a driving power less than the codimension-2 value, $S = 1.24$, whereas, (c) and (f) show the bifurcation structure for driving power greater than the codimension-2 value, $S = 1.25$. Example solutions (i)-(vi) are plotted in Fig. 6.4.

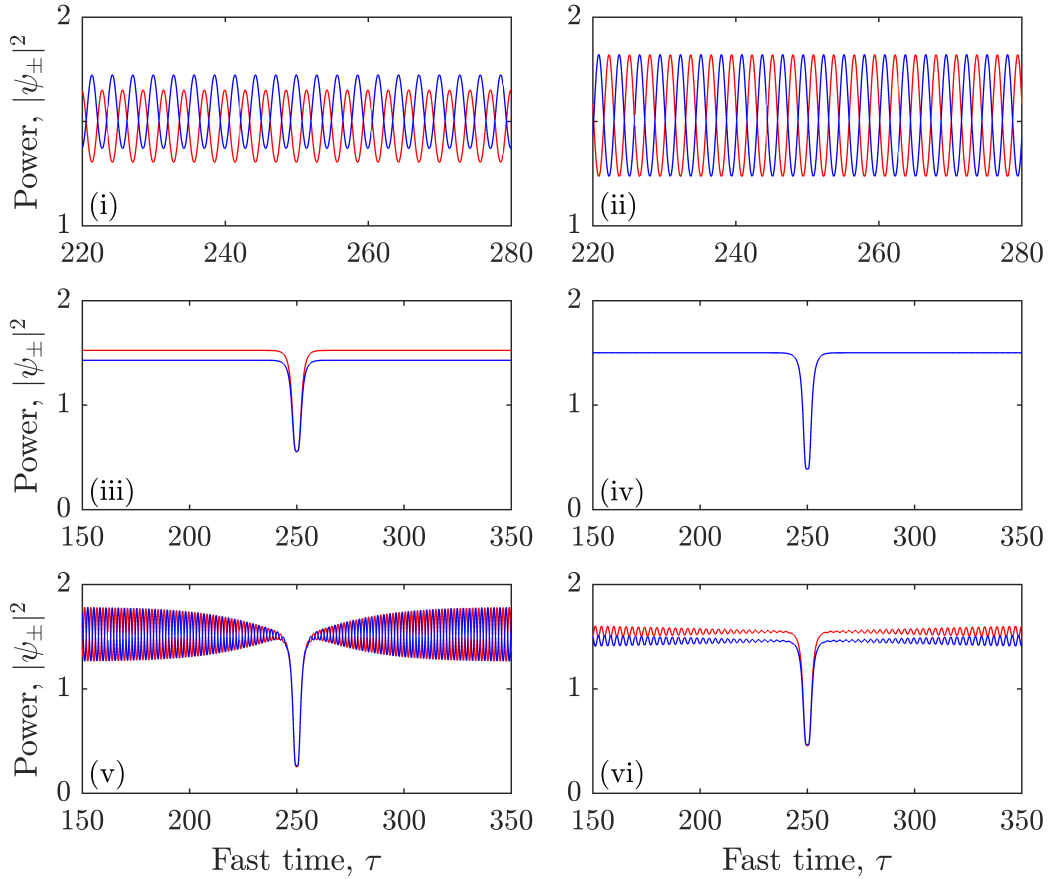


Figure 6.4: Example symmetry broken Turing patterns (i)-(ii) and vectorial dark solitons (iii)-(vi) for $\tau_R = 500$. (i) Turing pattern with unequal amplitudes $(S, \theta) = (1.25, 8.85)$. (ii) Turing pattern with equal amplitudes $(S, \theta) = (1.25, 8.9)$. (iii) Symmetry broken vectorial dark soliton with split plateaus of flat profile $(S, \theta) = (1.24, 8.63)$. (iv) Symmetric vectorial dark soliton with plateau of flat profile $(S, \theta) = (1.24, 8.75)$. (v) Symmetry broken vectorial dark soliton with symmetry broken Turing patterns on the plateau $(S, \theta) = (1.24, 8.9)$. (vi) Symmetry broken vectorial dark soliton with plateaus of split power and Turing pattern modulation $(S, \theta) = (1.25, 8.79)$.

cation ($\mu = 0$) of the symmetry broken HSSs, as can be seen in Fig. 6.3(b). This point is shown as a diamond in Fig. 6.2(b) where it can be seen that the real part of the relevant $\text{Re}[\lambda(k_0 = 0)]$ eigenvalue transitions from positive (unstable) to negative (stable), and the relevant $\text{Re}[\lambda(k_\mu \neq 0)]$ eigenvalue transitions from negative (stable) to positive (unstable), simultaneously, as the detuning is increased. This is an example of a codimension-2 bifurcation point, where in our case, both bifurcations correspond to a SSB event of the symmetric HSS.

Although there exists a mathematical equivalence between the symmetric and symmetry broken HSSs of the ring and FP resonators, the ring resonator system does not present a codimension-2 bifurcation. This is attributed to the integral term, which introduces a large divergence in eigenspectrum between ring and FP models for perturbations with $\mu \neq 0$, despite the mathematically equivalent eigenspectrum when $\mu = 0$.

When further increasing the input field to $S = 1.25$, we see that the two bifurcations have a cross over, introducing a region of symmetry broken HSSs that are unstable to the formation of Turing patterns, as can be seen in Fig. 6.3(c). This results in a small interval of detuning in which the Turing pattern of one field is dominant (orange curve) while the other one is suppressed (green curve), an example of which can be seen in Fig. 6.4(i).

6.4 Spontaneous symmetry breaking of vectorial dark solitons

6.4.1 Codimension-2 bifurcation of vectorial dark solitons

Here, we investigate the SSB of symmetric ($\psi_+ = \psi_- = \psi$) vectorial dark solitons (VDS) within the FP cavity. As discussed earlier in Section 6.2.2, at symmetry, Eqs. (6.20) reduce to the single field FP model under the appropriate renormalisation [48, 56]. As a result, the symmetric stationary solutions of Eqs. (6.20) are equivalent to the stationary solutions of the FP with a single field component, and are discussed at length in Chapter 5. In the numerical simulation of Eqs. (6.20), we observe the formation of VDS stationary solutions, in which, a dark soliton presents in both field components of orthogonal polarisation, occupying the same domain in fast time. Much like the dark solitons of the single field FP model, VDSs are composed of oppositely oriented switching fronts (SFs) that connect two homogeneous solutions (plateaus). SFs become stationary due to a locking mechanism induced by the interaction of local fast time oscillations on the lower power plateau, as was first proposed for spatial solitons composed of diffractive switching fronts [119–121], and demonstrated for temporal cavity solitons in the single field FP [56] in Chapter 5, and the ring resonator [35] in Chapters 2, 3 and 4. We have previously demonstrated that exponentially localised solutions (such as dark cavity solitons) within the FP cavity do not hang from the HSSs, but instead, hang from a plateau solution whose existence and stability is dependent on the average power of the intracavity field over a round trip of the cavity. This is a typical feature of the integro-partial differential equations prolific in this thesis, where nonlocal Kerr interaction is introduced due to the counterpropagation of intracavity fields found innately within the FP cavity, and also demonstrated for bidirectionally driven ring resonators [117].

At symmetry, the plateau solutions can be found by solving the coupled equations

$$\begin{aligned} 4Y_{u,l}^3 &- 4(\theta - 4\Delta Y_l - 4(1 - \Delta)Y_u)Y_{u,l}^2 \\ &+ \{(\theta - 4\Delta Y_l - 4(1 - \Delta)Y_u)^2 + 1\}Y_{u,l} = S^2, \end{aligned} \quad (6.42)$$

where the intracavity field is assumed to be composed of plateaus ψ_l, ψ_u connected by step functions with $\psi = \psi_l + \psi_u$, such that, $Y_l = |\psi_l|^2$ is the power of the lower plateau, $Y_u = |\psi_u|^2$ is power of the upper plateau, and the average power over the round trip time can be expressed as $\langle |\psi|^2 \rangle = \Delta Y_l + (1 - \Delta)Y_u$. Here, Δ is the duration of the lower plateau normalised to the cavity round trip time $0 < \Delta < 1$. This assumption has been used with great effectiveness to predict the stationary solutions in similar systems, such as in Chapters 4 and 5.

In Figs. 6.3(d)-(f), we show the SSB bifurcations of the high power plateau when a single VDS is present in the cavity. VDS solutions were obtained through direct numerical integration when scanning the detuning θ for different values of the input field S , or methods of lattice relaxation. The plateau of the symmetric VDS displays SSB phenomenon analogous to the HSSs discussed earlier, but now is effected by additional contributions from the VDS to the nonlocal coupling terms.

In Fig. 6.3(d), we show the plateau power of symmetric VDSs, plotted as a black curve, where an example stable symmetric VDS is shown in Fig. 6.4(iv). We indicated regions of stable and unstable VDSs as solid and dashed lines, respectively. Similar to the corresponding HSS bifurcation diagram [Fig. 6.3(a)], stable symmetric VDSs are flanked by two oppositely oriented pitchfork bifurcations, both of which correspond to a SSB event. When decreasing the detuning, we encounter the reverse pitchfork bifurcation at $\theta \approx 8.71$. This results in a splitting of the plateau power between polarisation components, such that, one field becomes dominant, and the other suppressed, while continuing to support the VDS, as shown in Fig. 6.4(iii). The power of the dominant and suppressed plateaus are plotted as red curves in Fig. 6.3(d) and are associated with the reverse pitchfork bifurcation of the HSSs. We see that the bifurcation point of the plateau is displaced with respect to the HSS, occurring for a different value of detuning. This is a consequence of a shift in detuning $\theta_{\text{eff}} = \theta - 4\langle |\psi|^2 \rangle$ induced by counterpropagation, where due to the presence of the VDS, the average power within the cavity is smaller [48, 49, 56, 117, 149]. In the limit of a large round trip time of the cavity, we have that $\langle |\psi|^2 \rangle \rightarrow H$. As a result, the bifurcation point of the plateau approaches the bifurcation point of the HSS in this limit.

For larger values of detuning, we encounter the forward pitchfork bifurcation of the VDS ($\theta \approx 8.8$). This results in the formation of a fast time Turing pattern on the background plateau, composed of alternating fields of orthogonal polarisations. For detuning values greater than the bifurcation point, the symmetric VDS branch becomes unstable to symmetry broken solutions displaying rapid fast time oscillations of increasing amplitude with greater distance from the VDS, until a saturation amplitude is reached. An example of which is shown in Fig. 6.4(v). The maximum and minimum power of the stationary Turing pattern is shown as a blue curve in Fig. 6.3(d). The formation of symmetry broken Turing patterns can be similarly understood as originating from the interaction of the local self- and cross-Kerr modulation of Eqs. (6.20), as was demonstrated earlier for the

HSS, where again, we note that the Turing pattern bifurcation point has been displaced with respect to the equivalent instability of the HSSs.

In Fig. 6.3(e) we show the SSB bifurcations of the symmetric VDS for $S = 1.2444$. At the parameter value $(S, \theta)_{\text{codim-2}} \approx (1.2444, 8.78)$, we see a codimension-2 bifurcation of the VDS. Here, the reverse pitchfork bifurcation of the plateau perfectly coincides with the forward pitchfork bifurcation corresponding to the formation of Turing patterns. This codimension-2 point occurs for different parameter values when compared to the HSSs due to the shift detuning introduced by the presence of the VDS in the cavity. In general, the location and existence of these two SSB bifurcations depend on the average power of the symmetric VDS solution (size and number of VDSs within the cavity). This means that, while the codimension-2 point of the HSSs occurs at a unique parameter value, the codimension-2 point of a symmetric VDS occurs at parameter values that is dependant on the particular symmetric VDS solution.

Further increasing the input field to $S = 1.25$, we see in Fig. 6.3(f) that the pitchfork bifurcations have crossed over. This has resulted in an interval of detuning in which one field component presents a dominant plateau with Turing pattern oscillations, while the other is suppressed. An example of which is shown in Fig. 6.4(vi).

6.4.2 Linear stability analysis of the plateau for Turing pattern formation

We may investigate the formation of Turing patterns on symmetric VDS solutions by approximating the VDSs as two plateaus occupying distinct domains of fast time connected by step functions $\psi^s = \psi_u^s + \psi_l^s$. We introduce a linear perturbation to each plateau $\psi_{\pm,u}(\tau, t) = \psi_u^s + \epsilon_{\pm,u}(\tau, t)$, $\psi_{\pm,l}(\tau, t) = \psi_l^s + \epsilon_{\pm,l}(\tau, t)$ of the form

$$\psi_{\pm,u}(\tau, t) = \psi_u^s + \epsilon a_{\pm,u} e^{ik_u \tau + \Omega_u t} \quad (6.43)$$

$$\psi_{\pm,l}(\tau, t) = \psi_l^s + \epsilon a_{\pm,l} e^{ik_l \tau + \Omega_l t} \quad (6.44)$$

where $\psi_{u,l}^s$ are the plateau solutions of higher u and lower l power, $k_{u,l}$ and $\Omega_{u,l}$ are the wavenumbers and growth rates of the perturbation on the respective plateaus, and $|\epsilon| \ll 1$. Inspired by the linear stability analysis previously performed for the HSSs we assume that the perturbation does not survive the integral terms, such that perturbations (6.43) and (6.44) obey

$$\langle (\psi_i^s + \epsilon_i)(\psi_j^s + \epsilon_j)^* \rangle = \langle |\psi^s|^2 \rangle = \Delta |\psi_l^s|^2 + (1 - \Delta) |\psi_u^s|^2. \quad (6.45)$$

where $i, j = \pm$ indicate the polarisation. This is akin to assuming that the wavenumbers are periodic on their respective plateau, $k_u = 2\pi n_u / \tau_R (1 - \Delta)$, $k_l = 2\pi n_l / \tau_R \Delta$ with mode numbers $n_{u,l} \neq 0$. Inserting the step function approximation into Eqs. (6.20), we obtain

separate partial differential equations for each plateau, with

$$\partial_t \psi_{\pm,u} = S - (1 - i\theta)\psi_{\pm,u} - i\partial_\tau^2 \psi_{\pm,u} \quad (6.46)$$

$$+ i\frac{2}{3} \left\{ |\psi_{\pm,u}|^2 \psi_{\pm,u} + 2|\psi_{\mp,u}|^2 \psi_{\pm,u} + 2[\Delta|\psi_{\pm,l}|^2 + (1 - \Delta)|\psi_{\pm,u}|^2] \psi_{\pm,u} \right. \\ \left. + 2[\Delta|\psi_{\mp,l}|^2 + (1 - \Delta)|\psi_{\mp,u}|^2] \psi_{\pm,u} + 2[\Delta\psi_{\pm,l}\psi_{\mp,l}^* + (1 - \Delta)\psi_{\pm,u}\psi_{\mp,u}^*] \psi_{\mp,u} \right\},$$

$$\partial_t \psi_{\pm,l} = S - (1 - i\theta)\psi_{\pm,l} - i\partial_\tau^2 \psi_{\pm,l} \quad (6.47)$$

$$+ i\frac{2}{3} \left\{ |\psi_{\pm,l}|^2 \psi_{\pm,l} + 2|\psi_{\mp,l}|^2 \psi_{\pm,l} + 2[\Delta|\psi_{\pm,l}|^2 + (1 - \Delta)|\psi_{\pm,u}|^2] \psi_{\pm,l} \right. \\ \left. + 2[\Delta|\psi_{\mp,l}|^2 + (1 - \Delta)|\psi_{\mp,u}|^2] \psi_{\pm,l} + 2[\Delta\psi_{\pm,l}\psi_{\mp,l}^* + (1 - \Delta)\psi_{\pm,u}\psi_{\mp,u}^*] \psi_{\mp,l} \right\}.$$

As the perturbations do not survive the nonlocal coupling terms, coupling of the perturbations on the upper and lower plateaus are not phase sensitive. Hence, without loss of generality, we may consider the higher and lower power plateaus to be real. Inserting the perturbations (6.43), (6.44), into 6.46, we arrive at the linearised equations

$$\partial_t \epsilon_{\pm,u} = -(1 + i\theta)\epsilon_{\pm,u} + ik_u^2 \epsilon_{\pm,u} \quad (6.48)$$

$$+ i\frac{2}{3} \left\{ 4[(\psi_u^s)^2 + \langle |\psi^s|^2 \rangle] \epsilon_{\pm,u} + 2[(\psi_u^s)^2 + \langle |\psi^s|^2 \rangle] \epsilon_{\mp,u} + (\psi_u^s)^2 \epsilon_{\pm,u}^* + 2(\psi_u^s)^2 \epsilon_{\mp,u}^* \right\},$$

$$\partial_t \epsilon_{\pm,l} = -(1 + i\theta)\epsilon_{\pm,l} + ik_l^2 \epsilon_{\pm,l} \quad (6.49)$$

$$+ i\frac{2}{3} \left\{ 4[(\psi_l^s)^2 + \langle |\psi^s|^2 \rangle] \epsilon_{\pm,l} + 2[(\psi_l^s)^2 + \langle |\psi^s|^2 \rangle] \epsilon_{\mp,l} + (\psi_l^s)^2 \epsilon_{\pm,l}^* + 2(\psi_l^s)^2 \epsilon_{\mp,l}^* \right\},$$

which may be expressed as

$$\begin{pmatrix} \partial_t u_u^+ \\ \partial_t v_u^+ \\ \partial_t u_u^- \\ \partial_t v_u^- \\ \partial_t u_l^+ \\ \partial_t v_l^+ \\ \partial_t u_l^- \\ \partial_t v_l^- \end{pmatrix} = \begin{pmatrix} -1 & A_u & 0 & C & 0 & 0 & 0 & 0 \\ -B_u & -1 & -C_u & 0 & 0 & 0 & 0 & 0 \\ 0 & C & -1 & A_u & 0 & 0 & 0 & 0 \\ -C_u & 0 & -B_u & -1 & 0 & 0 & 0 & 0 \\ 0 & 0 & 0 & 0 & -1 & A_l & 0 & C \\ 0 & 0 & 0 & 0 & -B_l & -1 & -C_l & 0 \\ 0 & 0 & 0 & 0 & 0 & C & -1 & A_l \\ 0 & 0 & 0 & 0 & -C_l & 0 & -B_l & -1 \end{pmatrix} \begin{pmatrix} u_u^+ \\ v_u^+ \\ u_u^- \\ v_u^- \\ u_l^+ \\ v_l^+ \\ u_l^- \\ v_l^- \end{pmatrix} \quad (6.50)$$

in terms of the real and imaginary parts of the perturbations $\epsilon_{\pm,u} = u_{\pm,u}^{\pm} + iv_{\pm,u}^{\pm}$, $\epsilon_{\pm,l} = u_{\pm,l}^{\pm} + iv_{\pm,l}^{\pm}$, and we have

$$A_u = \theta - k_u^2 - 2(\psi_u^s)^2 - 8/3\langle |\psi^s|^2 \rangle, \quad A_l = \theta - k_l^2 - 2(\psi_l^s)^2 - 8/3\langle |\psi^s|^2 \rangle, \\ B_u = \theta - k_u^2 - \frac{10}{3}(\psi_u^s)^2 - 8/3\langle |\psi^s|^2 \rangle, \quad B_l = \theta - k_l^2 - \frac{10}{3}(\psi_l^s)^2 - 8/3\langle |\psi^s|^2 \rangle,$$

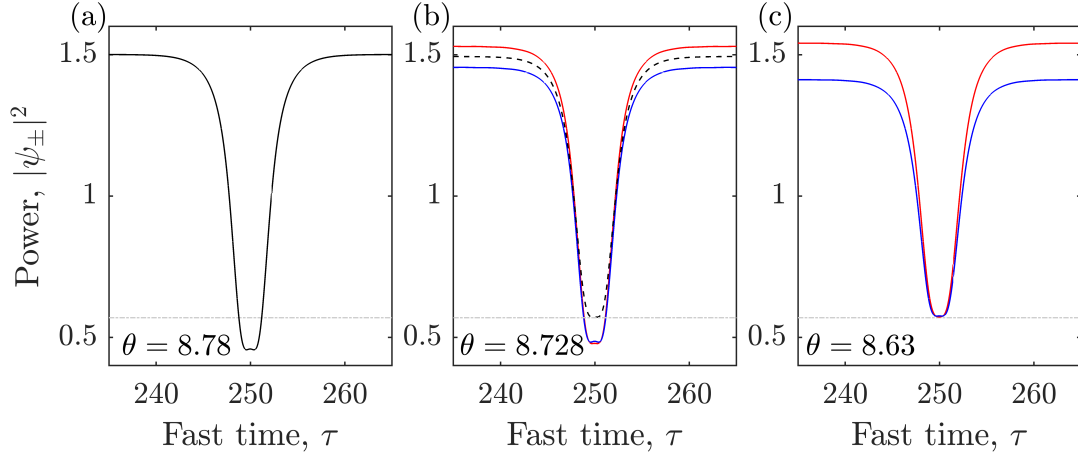


Figure 6.5: (a) Shows a VDS solution (black curve) at the codimension-2 point $(S, \theta)_{\text{codim-2}} \approx (1.2444, 8.78)$. By decreasing the detuning, we observe SSB of the VDS, where the symmetric solution becomes unstable (dashed black curve) to the symmetry broken VDS (red and blue curves). (b) corresponds to the saddle node bifurcation marking the end of the symmetric VDS solution branch. Further decreasing the detuning, we see the unstable symmetric VDS stationary state has vanished, such that, only the symmetry broken VDS remains until the saddle node bifurcation at (c).

$$C = -4/3 \langle |\psi^s|^2 \rangle, \quad C_u = C - \frac{8}{3} (\psi_u^s)^2, \quad C_l = C - \frac{8}{3} (\psi_l^s)^2.$$

This analysis yields eigenvalues

$$\Omega_{u,l}(k_{u,l}) = -1 \pm \sqrt{-A_{u,l}B_{u,l} - CC_{u,l} \pm (A_{u,l}C_{u,l} + B_{u,l}C)}, \quad (6.51)$$

where $(\psi_{u,l}^s)^2$ are the powers of the higher and lower power plateaus, and $\langle |\psi^s|^2 \rangle$ is the average power of the intracavity field over a single round trip of the cavity. This method of linear stability analysis has been utilised previously to good effectiveness [56, 117] in the presence of integral terms, and we find the linear stability analysis performed here accurately predicts the onset of pattern instability for symmetric VDSs. We note that the eigenvalues of Eqs. (6.51) reduce to the eigenvalues of symmetric HSS in the limit $\langle |\psi^s|^2 \rangle \rightarrow |\psi^s|^2$, further cementing the connection with the HSSs.

6.4.3 Spontaneous symmetry breaking in the presence of nonlocal coupling

In the bifurcation diagrams of Fig. 6.3(d)-(f), it can be seen that, when decreasing the detuning, the symmetry broken VDS branches (red curves) exist in an interval that extends far beyond the end of the symmetric soliton branch. This is phenomenologically atypical of a SSB pitchfork bifurcation, where the symmetric solution usually persist over the full domain of the symmetry broken solutions and is unstable, as seen for the symmetry broken HSSs of Fig. 6.2. In Fig. 6.5(a) we plot the a single VDS at the codimension-2 point

$(S, \theta)_{\text{codim-2}} \approx (1.2444, 8.78)$. When decreasing the detuning, the VDS moves toward the symmetry broken VDSs stationary state. If we instead follow the unstable symmetric VDS, we see the VDS trough increase in power as the detuning is scanned until we reach a saddle node bifurcation, marking the end of the symmetric VDS solution branch. The final symmetric VDS is shown with a dashed line in Fig. 6.5(b). The interaction of the oscillatory tails to which the dark solitons owe their existence is highly dependent on the power of the lower plateau (the power of the trough), and is highly relevant in the determination of the decay rate and wavenumber of these oscillations. Beyond this value of detuning, the interaction of the oscillatory tails is insufficient to induce the locking mechanism due to the increasing power of the trough. As can be seen in Fig. 6.5(b), the stable symmetry broken VDS has diverged from the symmetric solutions and is able to survive due to the lower value of trough power. By further decreasing the detuning, the power of the trough of the symmetry broken VDSs rises until the locking mechanism fails, shown in Fig. 6.5(c), at a similar trough power to the symmetric VDS. This failure of the locking mechanism is delayed for the symmetry broken solutions due to the slower rate of increase in the trough power of the VDSs. This phenomenon is a result of the nonlocal coupling, whose contributions differ between symmetric and symmetry broken solutions, and acts to displace the existence of the symmetry broken solutions beyond the range of the symmetric solution branch from which they bifurcate. This results in an extended range of parameter values where there exists only symmetry broken VDSs, despite having parameter symmetry between the two field equations (6.20).

6.5 Self-crystallisation of vectorial dark solitons

We now consider a FP resonator containing multiple VDSs simultaneously along the round trip of the cavity. These solutions undergo SSB bifurcations similar to those discussed earlier for a single VDS. Above the SSB bifurcation point, Turing patterns are observed to form in the intervals between adjacent VDSs. The growth of Turing patterns induces motion in the VDSs, wherein adjacent VDSs are ‘pushed’ apart until an equilibrium of the pattern’s amplitude is reached on both sides of each VDS. Hence, this SSB phenomenon introduces long range repulsive interaction between adjacent VDSs, which are mediated by the formation of the symmetry broken Turing patterns. In the absence of Turing patterns, the symmetric VDSs do not exhibit long range repulsive interactions and the VDSs remain stationary at arbitrary separations along the cavity round trip. This dynamical process is analogous to the ‘self-crystallisation’ phenomenon described for the ring resonator with vectorial intracavity field in Sections 3.5 and 3.6. Due to the absence of counterpropagating fields within the ring resonator, nonlocal coupling is not the primary source of the long range interaction between solitons in this case, but instead, VDSs interact locally through the Turing patterns. Here, we demonstrate that the ‘self-crystallisation’ mechanism may be generalised to FP resonators with orthogonal polarisations components [103], and as such, is universal in systems displaying temporal cavity solitons and Turing instabilities under local self- and cross-phase modulation. We discuss the differences in self-crystallisation in ring and FP resonators and the effects originating from nonlocal coupling.

The self-crystallisation process of VDSs within the FP resonator unfolds as follows. In

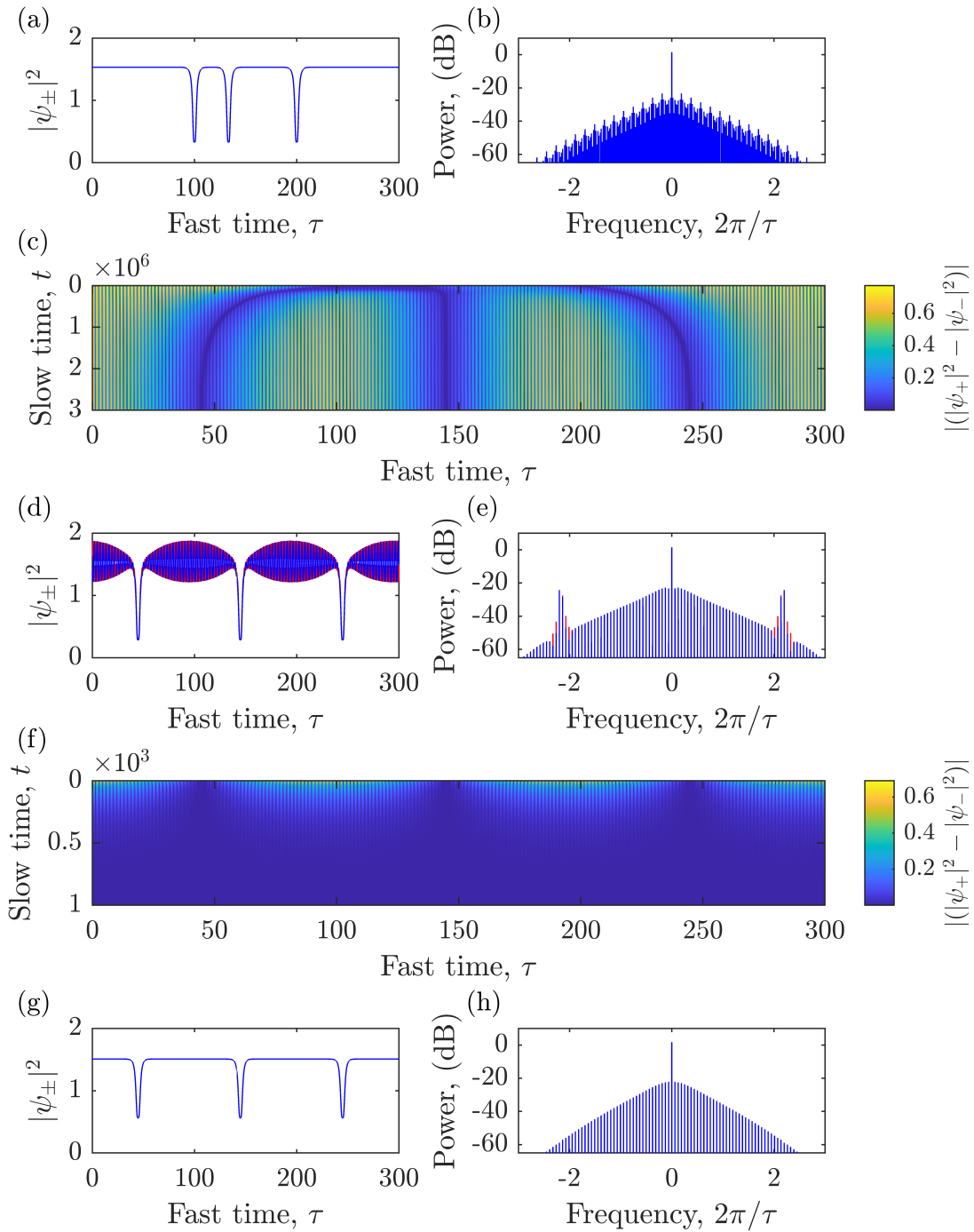


Figure 6.6: (a) Initial condition of three symmetric vectorial dark solitons and corresponding comb spectrum (b). (c) Slow time evolution of the initial condition (a), for $S = 1.25$, $\theta = 8.8$, demonstrating the growth of SSB Turing patterns, which propel the VDSs through the cavity. (d) Final RSC stationary state and corresponding comb spectrum (e). (f) Slow time evolution after reducing the cavity detuning to $\theta = 8.63$, below the threshold for Turing patterns. (g) Final regular VDS crystal with a uniform background and corresponding comb spectrum (h).

Fig. 6.6(a), we introduce three randomly distributed symmetric VDSs along the cavity round trip time. For the parameter values $S = 1.25$, $\theta = 8.8$, $\tau_R = 300$, the background plateau from which the three VDSs hang is unstable to the formation of a symmetry broken Turing pattern. As the pattern amplitude grows, the VDSs are ‘pushed’ along the resonator, where the maximum amplitude reached by the Turing patterns in the intervals between the VDSs depend on the separation of adjacent VDSs. In Fig. 6.6(c), we show the slow time evolution of the VDSs, where it can be seen that they move so as to spread out along the cavity coordinate, until an equilibrium configuration of the Turing patterns is reached on both sides of each VDS. This results in the stable stationary state shown in Fig. 6.6(d). This stationary solution is composed of VDSs located equidistantly on the round trip of the cavity, separated by Turing patterns of equal amplitude, forming a perfectly regular soliton crystal (RSC).

The formation of a RSC from an initial condition of three VDSs randomly positioned along the cavity coordinate is spontaneous, induced by SSB of the VDSs. The self-crystallisation process in the FP resonator unfolds in a similar manner to that of the ring resonator, wherein the spontaneous self-organisation of VDSs is induced by long range interactions originating from SSB Turing patterns, and does not rely on perturbations introduced to the LLE model, such as those induced near avoided mode crossings [40], or through an external modulation of the field [44]. Furthermore, by scanning the detuning back over the Turing instability bifurcation point, Turing pattern modulations in the intervals between VDSs vanish, as shown in Fig. 6.6(f). This evolution results in the formation of a symmetric RSC, as shown in Fig. 6.6(g). While the long range interaction resulting from the nonlocal (global) coupling is always present in the FP resonator, ‘self-crystallisation relies on the long range (local) interactions of VDSs, mediated by Turing patterns, and as such, VDSs will not display the self-crystallisation phenomenon below the SSB Turing pattern bifurcation.

The RSC created by the self-organisation of VDSs produces a frequency comb [Fig. 6.6(e)] with a smooth spectral envelope and a free spectral range three times larger than the frequency comb of the initial condition [Fig. 6.6(b)]. Regularly occupying peaks (sidebands) appear in the spectral envelope, due to the contributions from the Turing pattern wavenumber on the frequency domain, and is required for self-crystallisation. Such peaks can be removed at will after self-crystallisation by scanning the control parameters below the SSB bifurcation of the Turing patterns, as shown in 6.6(f), thus eliminating the contributions from the Turing pattern wavenumber on the frequency domain. In general, a RSC composed of N VDSs produces a frequency comb equivalent to a single VDS in a cavity with round trip time τ_R/N . An important property of RSCs is their capacity to emulate smaller cavity sizes, such that, with increasing soliton number, a frequency comb with enhanced power and greater spacing of the spectral lines is obtained. As such, the formation of RSCs has many potential applications, such as satellite communications [123], photonic radar [124] and radio-frequency filters [125, 126], where the universality of this mechanism in ring and FP resonators creates different practical methods for the generation and control RSCs, distinct from previously demonstrated methods [40, 44].

6.6 Partial crystal formation

Adjacent VDSs experience repulsive interactions due to the growth of Turing patterns over slow time. The VDSs will remain dynamical until the Turing patterns on both sides of each VDS reaches a saturation of their amplitudes and becomes stationary. In Fig. 6.7(a), we show the evolution of two VDSs in a long cavity. This results in the formation of the partial crystal stationary state shown in Fig. 6.7(b). In general, a partial crystal may be composed of two or more equidistant VDSs in a local region of the cavity, with the remainder of the cavity occupied by a Turing pattern of constant amplitude. They are formed when the Turing pattern amplitude reaches saturation before a RSC is formed. In Fig. 6.7(b), we annotate the VDS spacing of the partial crystal $2\Delta\tau$, which is defined as twice the distance in fast time over which the amplitude of the pattern reaches its maximum value, and hence an equilibrium is achieved on both sides of the VDSs. We may use this characteristic length to determine the conditions required for self-crystallisation, whereby should the VDS number N be sufficient large that $2N\Delta\tau > \tau_R$, the system will evolve towards a RSC, as seen in Fig. 6.7(c) and (d).

In Fig. 6.7(c), we show the evolution of five tightly packed VDSs in a FP resonator resulting in the formation of a RSC, Fig. 6.7(d). This evolution is split into two stages. For $t < 2 \times 10^5$, the Turing pattern amplitudes between the tightly packed VDSs is small (near symmetry) due to the long pattern saturation distance $\Delta\tau$. This results in relatively slow dynamics of the VDSs. The slow dynamics continue until the VDS are sufficiently far apart to support larger amplitude Turing patterns, at around $t \approx 2 \times 10^5$. At this time, VDS dynamics become significantly faster.

To compare the RSC solutions of the ring and FP resonator, we have selected mathematically equivalent symmetric solitons as an initial condition, with comparable parameter values $S_{\text{FP}} = 1.05\sqrt{3/2} = S_{\text{ring}}\sqrt{3/2}$, which makes use of the renormalisation factor between the symmetric case of the two models. This allows us to appropriately compare the RSC and partial crystals of Figs. 3.5 and 3.6 of the ring resonator model with the FP model, shown in Fig. 6.7. If we compare with the analogous long range interactions of the ring resonator, we find that the pattern saturation distance, with respect to the round trip time, is larger in the FP cavity. As such, the FP system is more prone to the slow dynamics of Fig. 6.7(c). Conversely, the greater value of $2\Delta\tau$ suggest that the FP resonator is more congruent to the formation of RSCs, with greater robustness to changes in soliton number, as repulsive interactions will redistribute VDSs to equidistant locations. This is conditional on the Turing patterns saturation length $2\Delta\tau$, which must be less than the lattice spacing of the RSC. We also note that the Turing pattern wavenumber within the FP resonator is larger, at around two times greater than the ring resonator. Similarly, the partial crystal spacing in the FP resonator is approximately two times greater than the comparable ring resonator.

The RSCs within a FP cavity, such as in Figs. 6.6 and 6.7, are composed of unit cells which are perfectly repeating over the round trip of the cavity. There are four possible unit cells, each related by a $\pi/2$ shift in the phase of the Turing pattern. In Fig. 6.8 we present example unit cells for $S = 1.25, \theta = 8.8$. The unit cells possess fast time symmetries associated with fast time parity with (a) $\psi_{\pm}(-\tau) = \psi_{\mp}(\tau)$ and (b) $\psi_{\pm}(-\tau) = \psi_{\pm}(\tau)$. Two additional unit cells are obtained by exchanging the fields $\psi_+ \leftrightarrow \psi_-$ in Fig. 6.8.

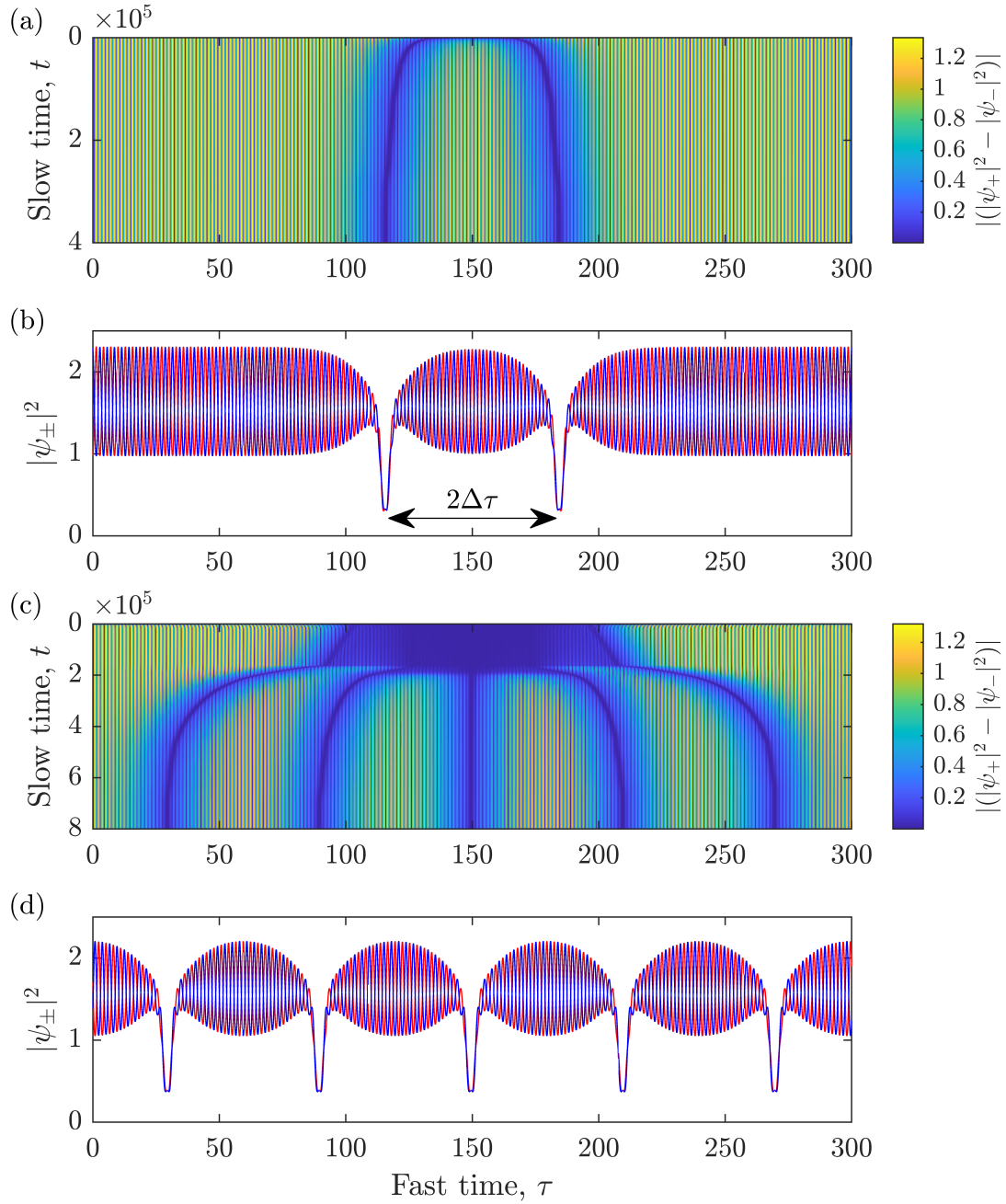


Figure 6.7: (a) Slow time evolution of two VDSs resulting in the formation of the partial soliton crystal, with power profile (b) and Turing pattern saturation distance $\Delta\tau$, for $S = 1.05\sqrt{3/2}, \theta = 9.1$. (c) Slow time evolution of five VDSs form a tightly packed initial condition, for $S = 1.05\sqrt{3/2}, \theta = 8.9$. This evolution results in the RSC stationary state (d).

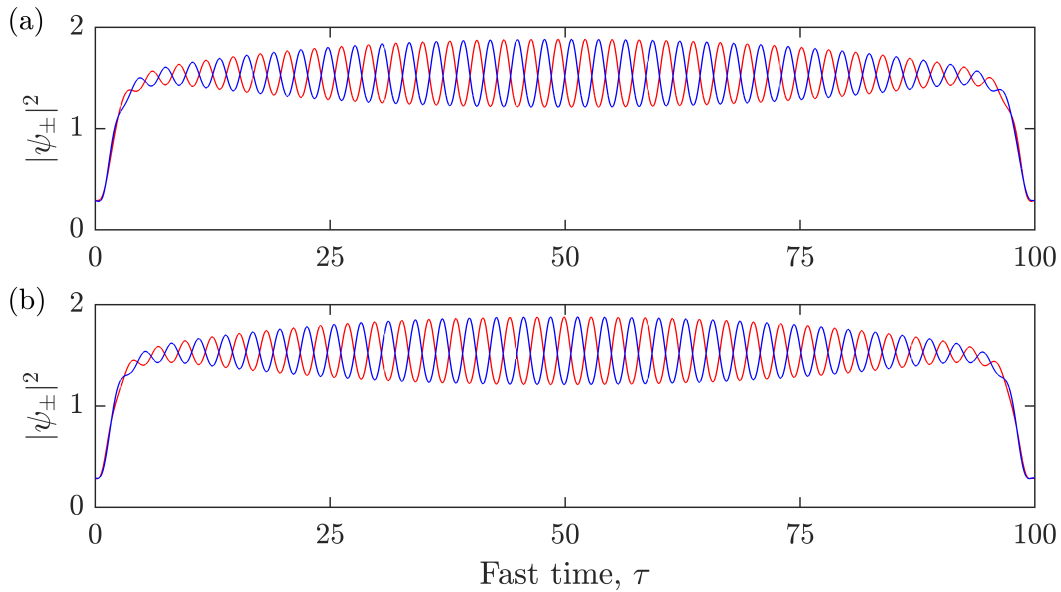


Figure 6.8: (a)-(b) Power profiles of RSC unit cells for $S = 1.25$, $\theta = 8.8$, $\tau_R = 100N$, and soliton number N . Two additional unit cells can be obtained by exchanging the fields $\psi_+ \leftrightarrow \psi_-$ in both (a) and (b). The four unit cells are related by a phase shift in the peaks of the Turing patterns of $\pi/2$.

As we have previously shown for the single field FP resonator in Chapter 5, the non-local coupling terms present in systems of counterpropagating light introduce long range interactions between well separated solitons within the cavity, such that, the existence and stability of the solitons is dependent on the soliton number [56, 117]. The symmetric VDSs of the two component FP model [Eqs. (6.20)] display identical long range interactions, as shown in Fig 5.9, which modify the self-crystallisation process. In Fig. 6.9, we plot the SSB bifurcation diagram of a plateau supporting three VDSs simultaneously within the cavity for $S = 1.24$, $\tau_R = 500$. We see that the symmetric solution undergoes a SSB at $\theta \approx 8.75$ resulting in the growth of symmetry broken Turing patterns and the formation of a RSC. Here, the maximum and minimum power of the stationary Turing pattern is plotted as the blue curve. For these parameter values, solutions containing three VDSs may exist as either a symmetry broken RSC, for $\theta > 8.75$, or as a symmetric distribution along the cavity coordinate, $\theta < 8.75$, (whereby a soliton crystal may be formed from the random distribution of VDSs by scanning the detuning over $\theta \approx 8.75$ to induce SSB of the plateau, leading to the self-crystallisation of the VDSs). Here, solutions containing three VDSs do not possess the reverse pitchfork bifurcation, as was seen for the single VDS solutions, which we plot in Fig. 6.9 as grey curves. The location and existence of the SSB bifurcation required for self-crystallisation is dependent on the soliton number and size, which shifts the location and stability of stationary solutions, and has become more prominent due to the increased number of solitons.

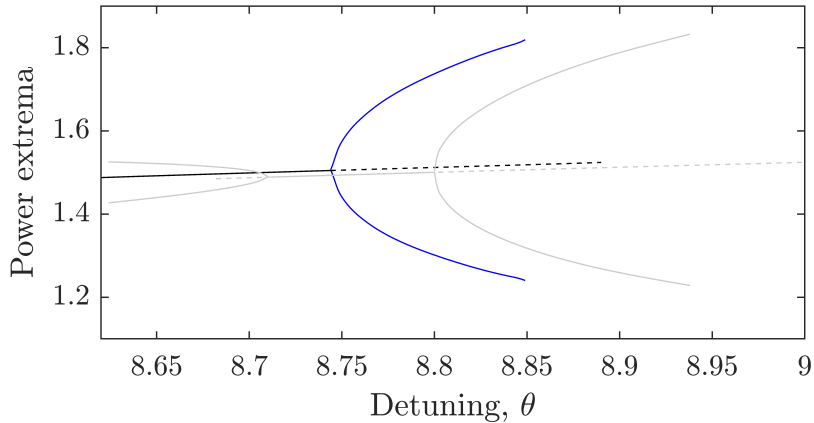


Figure 6.9: Spontaneous symmetry breaking bifurcations for $S = 1.24$, $\tau_R = 500$ in the presence of three VDSs simultaneously within the cavity. The plateau power of the VDSs is plotted as a black curve. The blue curve shows the maximum and minimum amplitude of the symmetry broken Turing patterns of alternating polarisation which form in between equidistant VDSs. The gray curves show the single VDS bifurcations of Fig. 6.3(a). In both cases, stable and unstable solutions are depicted with solid and dashed lines, respectively. This demonstrates a non-insignificant displacement of the locations of the bifurcations when increasing the number of solitons, where in particular, we notice the absence of the reverse pitchfork bifurcation for the three soliton case.

6.7 Vectorial dark-bright solitons

6.7.1 Vectorial dark-bright solitons in Fabry-Pérot resonators

We now change the focus of our investigation to vectorial soliton solutions of Eqs. (6.20) which exist in parameter regions displaying strongly symmetry broken HSSs. In Fig. 6.10(a), we show the HSSs for $S = 3$. A notable feature of the HSSs for this value of S is the formation of a ‘horn’ in the symmetry broken HSSs, where one polarisation component is largely dominant, approaching the peak power, and the other is largely suppressed, approaching zero power (e.g. $\psi_+ \gg \psi_-$). This horn forms a small region of optical bistability between symmetry broken HSSs corresponding to the red and blue curves of Fig. 6.10(a)-(c). Near the peak of the symmetry broken HSS horn, and with suitable perturbation, we observe the formation of vectorial dark-bright cavity solitons (VDBS). These solutions present as a pair of coupled solitons occupying the same domain in fast time, where the dark soliton hangs from the dominant field and a bright soliton sits upon the suppressed low power field, as is shown in Fig. 6.10(d).

VDBS solutions have been demonstrated in a large variety of physical systems, such as in single mode optical fibres [127–135], as well as two-species Bose-Einstein Condensates [136–138]. The formation of the VDBSs in each case is reliant on the nonlinear cross-phase modulation between the two respective field components, where despite the significantly different physics, these systems are mathematically analogous and governed by coupled nonlinear Schrödinger equations. In microresonator systems, the generation of VDBSs can

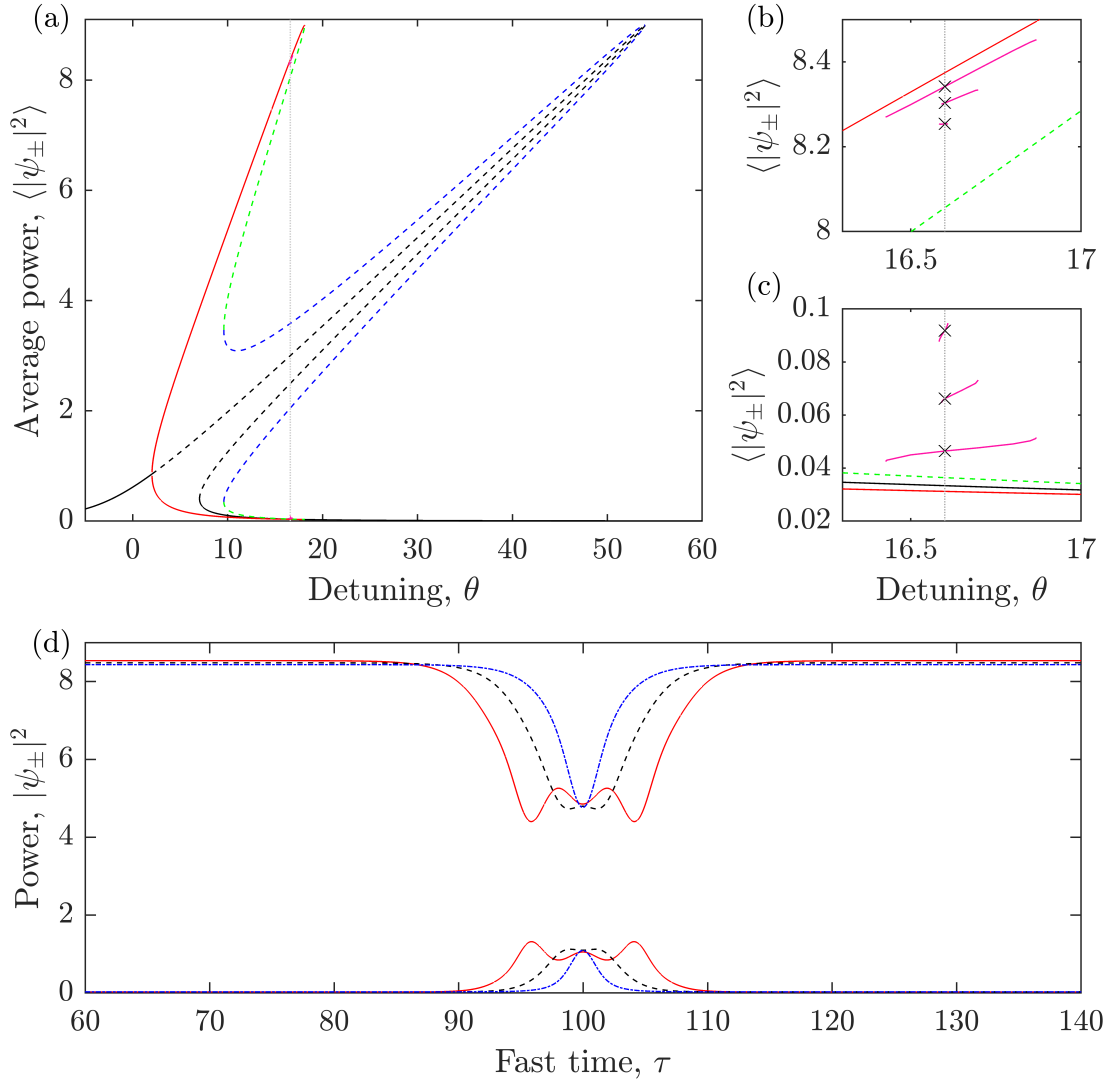


Figure 6.10: (a) Solutions of the FP cavity for $S = 3$, $\tau_R = 200$ are plotted as their average power over the round trip. The symmetric and symmetry broken HSSs are plotted as the black and red curves respectively. In the vicinity of $\theta = 16.6$, we plot stable branches of vectorial dark-bright solitons. This collapse snaking behaviour can be seen near the dominant symmetry broken HSS (b), corresponding to the dark soliton, and near the suppressed symmetry broken HSS (c), corresponding to the bright soliton. (d) Bistable vectorial dark-bright solitons for parameters $S = 3$, $\theta = 16.6$, $\tau_R = 200$. Three solutions are shown, each for identical parameters, presenting different locking distances corresponding to one trough (dot dashed blue line), two troughs (dashed black), and three troughs (solid red line), and are indicated in (b) and (c) as x's.

be achieved through bichromatic input fields. In particular, the generation of frequency combs via bichromatically driven microresonators has been widely demonstrated to produce bright-bright soliton pairs [141–146], where in addition, the simultaneous generation of frequency combs between fields of orthogonal polarisations has been demonstrated [112, 115]. Recently, vectorial dark-bright solitons have been experimentally demonstrated in microresonators [139, 140]. This was achieved by appropriately selecting the two driving frequencies, such that, one of the intracavity fields operates within the regime of anomalous group velocity dispersion, generating a bright soliton, while the second field operates in the normal group velocity dispersion regime, which supports a dark soliton through cross-phase modulation with the bright soliton. Dark and bright solitons are bound in the fast time due to Kerr interaction and copropagate along the microresonator. In chapter 3, we discussed the possibility of VDBSs which form between the orthogonally polarised field components of the ring resonator. This represented a new paradigm for the formation of VDBSs, as the two field components experience identical normal group velocity dispersion with identical driving amplitude and detuning to the nearest cavity resonance. In this section, we consider the formation of VDBSs of orthogonally polarised field components within a FP resonator described by Eqs. (6.20), where we outline the distinct characteristic of the FP system.

In Fig. 6.10(d), we show three bistable VDBS for $S = 3, \theta = 18.6$. The dark and bright soliton of the VDBS are each composed of SFs that connect the two high power plateaus and two low power plateaus, respectively, within a regime of optical bistability. In the dominant field, SFs which compose the dark soliton (shown as an ‘x’ in 6.10(b)) connect to plateaus near the red and blue curves of Fig. 6.10(b). The SF approaches the lower power plateau displaying a decaying oscillatory trajectory, whilst the approach to the higher power plateau is smooth. It is the interactions of these oscillations on the low power plateau which introduce a locking mechanism analogous to that described previously for vectorial dark-dark solitons. The corresponding bright solitons of Fig. 6.10(d) are marked with an ‘x’ in Fig. 6.10(c). Here, the switching fronts display a decaying oscillatory trajectory at the connection with the higher power plateau near the blue curve, and a smooth trajectory on approach to the lower power plateau near the red curve. The bright solitons ‘mirror’ the dark solitons in profile, exhibiting an identical size and number of peaks, due to local cross-phase modulation. The three VDBSs of Fig. 6.10(d) display different locking distances (soliton widths) corresponding to the distinct cycles of the oscillatory tails, with three (red solid), two (black dashed), and one (blue dash-dot) peaks (troughs) in the bright (dark) soliton. Typical of systems of counterpropagating field components, VDBSs do not sit upon the HSSs of this system, but instead hang from plateaus whose existence and stability is dependent on the size and number of VDBS. It can be seen that the powers of the plateaus of the three bistable VDBSs are different. This is attributed to the difference in nonlocal coupling of fields with different soliton widths.

VDBS solutions are distributions along a collapse snaking curve, where we show stable VDBS solution branches corresponding to the distinct VDBS sizes in Fig. 6.10(b)-(c) as pink curves. Due to the presence of nonlocal terms, we expect the collapse snaking of the VDBS solutions to be tilted in parameter space [47, 56, 117], but due to the counteracting contributions of the dark and bright solitons to the averaging terms, this effect is small. As the VDBS solutions of Eqs. (6.20) form around the symmetry broken HSS horn, they are

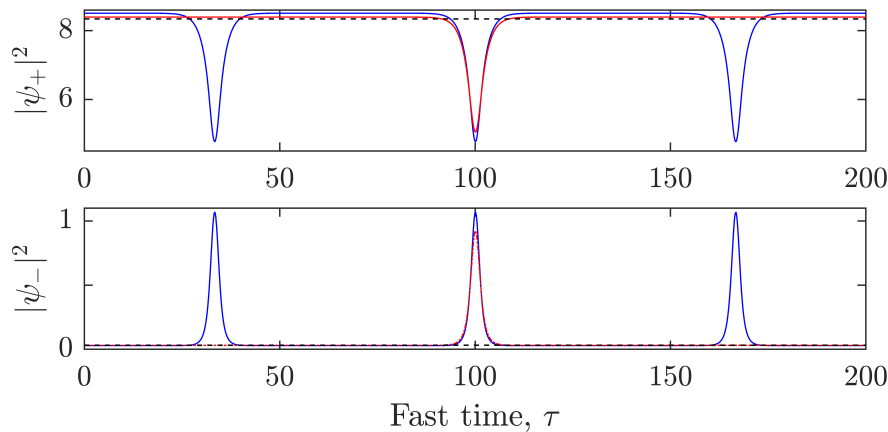


Figure 6.11: Dark bright soliton for $S = 3, \theta = 16.5, \tau_R = 200$. Upper panel. One (red) and three (blue) dark solitons and the HSS (black) of the ψ_+ field. Lower panel. One (red) and three (blue) bright solitons and the HSS (black) of the corresponding ψ_- field.

found for much larger input power when compared to the symmetric dark-dark vectorial solitons of the previous sections.

VDBS solutions of the FP are phenomenologically similar to the VDBSs seen within the ring resonator, as presented in Section 3.7. We note that it is not possible to project the solutions of the polarisation degenerate FP resonator onto the solutions of the polarisation degenerate ring resonator, through the definition of an effective detuning, as we had done in the previous chapter between the solutions of the single field FP model and single field ring model. This is due to the four wave mixing integral term Eq. (6.22) [presenting in the last term of Eqs. (6.20)], which introduces a complex valued integral with linear cross-coupling between polarisation components. This prevents us from defining a useful effective detuning. As a consequence, the VDBS stationary solutions of Eq. (6.20) do not have a one to one correspondence to those seen in Section 3.7 for the ring resonator. One benefit of the FP resonator for the generation of VDBSs, when compared with the ring resonator, is that the VDBS branches exist over a much larger range of detuning. For comparable inputs $S_{\text{ring}}\sqrt{3/2} = S_{\text{FP}} = 3$, the solution branch of the FP cavity is approximately 8.82 times larger.

6.7.2 Nonlocal coupling of oscillating vectorial dark-bright solitons

When slowly changing the control parameters, the VDBS are found to undergo a Hopf bifurcation, resulting in breathing dynamics of the dark and bright solitons. In the ring resonator system (Section 3.7), a similar temporal instability is present and results in stable local dynamics confined to the dark-bright soliton pair. Within the FP cavity, nonlocal coupling introduces long range interactions between VDBSs, whose effects we characterise in this section.

The power profile of a single oscillating VDBS is shown in Fig. 6.12(a) at different points along its dynamical cycle, corresponding to the maximum and minimum power of the peak (trough) of the bright (dark) soliton. As the dark and bright solitons move

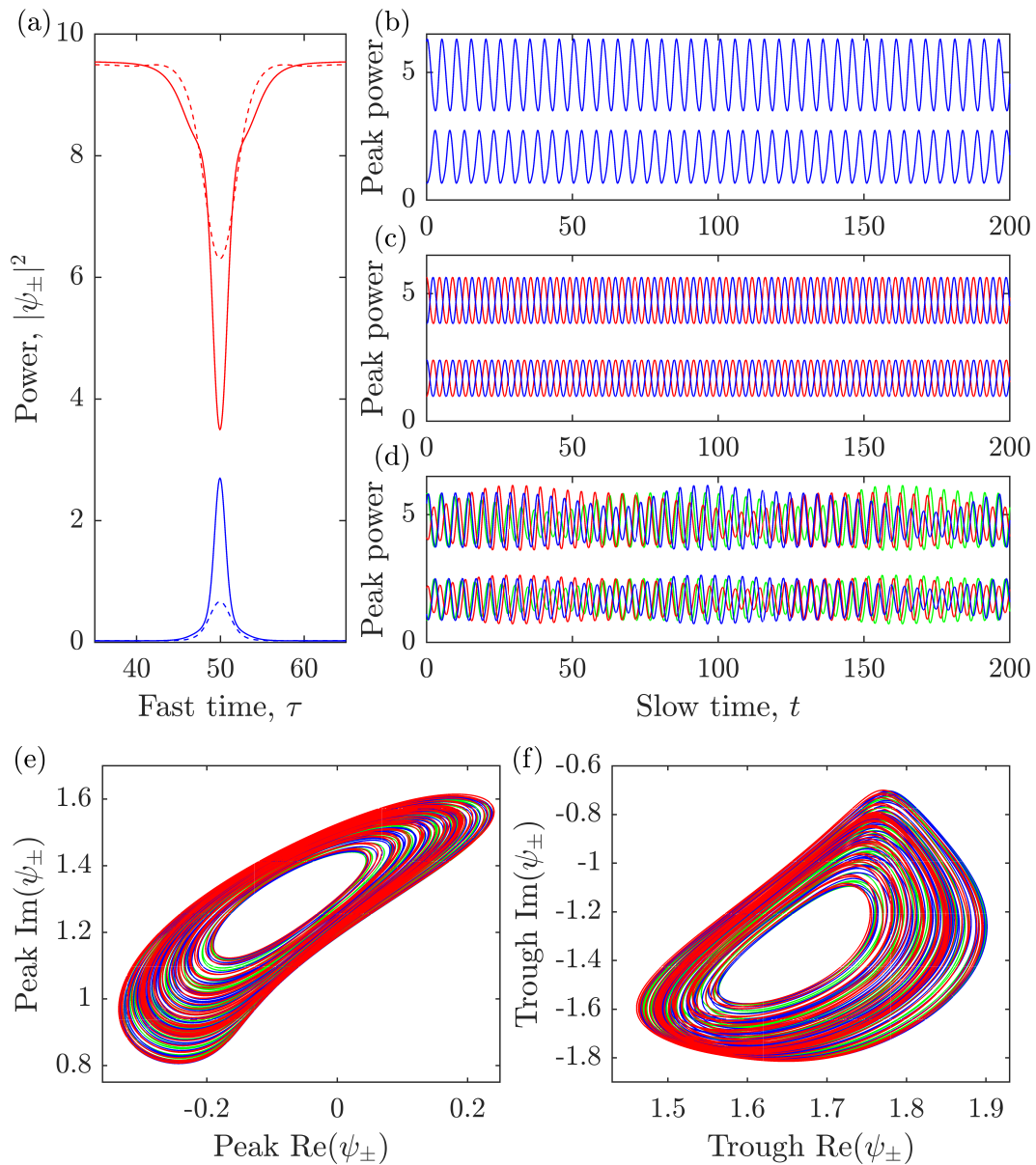


Figure 6.12: Dynamical solitons for $S = 3.2, \theta = 18.6$. (a) Power profile of a single oscillating VDBS at two different points in its limit cycle, shown as solid and dashed lines. (b) Trace of the peak (trough) of the bright (dark) soliton of a single VDBS for $\tau_R = 100$. (c) Trace of the bright and dark solitons of two VDBS, where different VDBSs are distinguished by different coloured curves for $\tau_R = 200$. Nonlocal interactions between VDBS results in out of phase oscillation. (d) Trace of the bright and dark solitons of three VDBS, distinguished by different coloured curves for $\tau_R = 300$. (e) Trajectory of bright soliton peaks in the Argand plane corresponding to (d). (f) Trajectory of dark soliton troughs in the Argand plane corresponding to (d). In both cases, the red, blue and green VDBS follow nontrivial limit torus trajectories.

through their limit cycle, the dynamics induce a small change in the nonlocal (averaging) terms of Eqs. (6.20). As a consequence, the temporal dynamics of this system are not confined to the VDBS but extends to an oscillation over the background plateaus, where generally, regions of the cavity far from the VDBS exhibit oscillatory dynamics induced by the Hopf instability associated with the VDBS. Oscillations of the background power have significantly smaller amplitude when compared to the VDBS peak, as the contribution of the VDBS dynamics to the nonlinear terms is small. In Fig. 6.12(b) we trace the maximum and minimum power of the bright and dark soliton respectively, where it can be seen that the dark and bright solitons are perfectly synchronised in their dynamics.

In Fig. 6.12, example dynamical VDBS solutions are shown for a cavity containing one (b), two (c) and three (d) oscillating VDBSs simultaneously within the cavity of round trip times $\tau_R = 100$, $\tau_R = 200$ and $\tau_R = 300$, respectively. Here, we increase the cavity round trip time for cavities containing a larger number of simultaneous solitons. This is done to preserve the value of the nonlocal terms of Eqs. (6.20) at stationary state, so as to elucidate the effects of the nonlocal coupling on the soliton dynamics without effecting the existence and stability of the VDBS stationary solutions with increasing soliton number. The interaction of stationary VDBSs is demonstrated in Fig. 6.11, where we show bistable solutions of the HSS, a single VDBS and three VDBS. It can be seen that the homogeneous background, along with the extrema of the VDBS, have different powers depending on the number of VDBS within the cavity, should the round trip time not be adjusted.

In Fig. 6.12(c), we consider two VDBSs well separated within a FP cavity with double the round trip time ($\tau_R = 200$). The traces of the maximum and minimum power of the bright and dark soliton, respectively, are plotted for both VDBSs with red curves for the ‘right’ VDBS and blue for the ‘left’ VDBS. The two VDBSs interact through the nonlocal terms resulting in stable anti-synchronous dynamics, where the two bright solitons (and two dark soliton) oscillate exactly π out of phase. In Section 5.7, we investigated the dynamics of dark solitons of the single field FP, where we found that, in general, the dynamics of N well separated solitons in a cavity of round trip τ_R synchronised towards the dynamics of a single soliton in a cavity of round trip τ_R/N . This is not the case for VDBSs of the two component FP. This can be further demonstrated if we consider three VDBS well separated within a FP cavity with round trip time $\tau_R = 300$. As before, we plot the trace of the extrema of three VDBSs in Fig. 6.12(d), distinguished by different colours. We see that the dynamics of the three oscillating VDBS have become nontrivial. Plotting the trajectory of the maxima of each bright soliton and the minima of each dark soliton in the Argand plane, in Figs. 6.12(e) and (f), respectively, we can see that the VDBSs evolve as overlapping limit torus trajectories.

If instead, we consider the trajectories of two VDBSs for different values of the round trip time, we can characterise the contribution of the integral terms to the dynamics. Generally, the strength of the interaction between nonlocally coupled VDBSs is dependent on the number density of VDBSs over the round trip time. The interaction strength of two VDBSs is weighted by the size of τ_R with weaker interaction in the limit of large τ_R . In Fig. 6.12(c), VDBS display anti-synchronous limit cycle oscillations. When increasing the round trip time, limit cycle oscillation are found to give way to stable limit torus oscillations, wherein VDBSs oscillate along overlapping trajectories with small periodic variations in their phase and amplitude over slow time. This overlap of trajectories

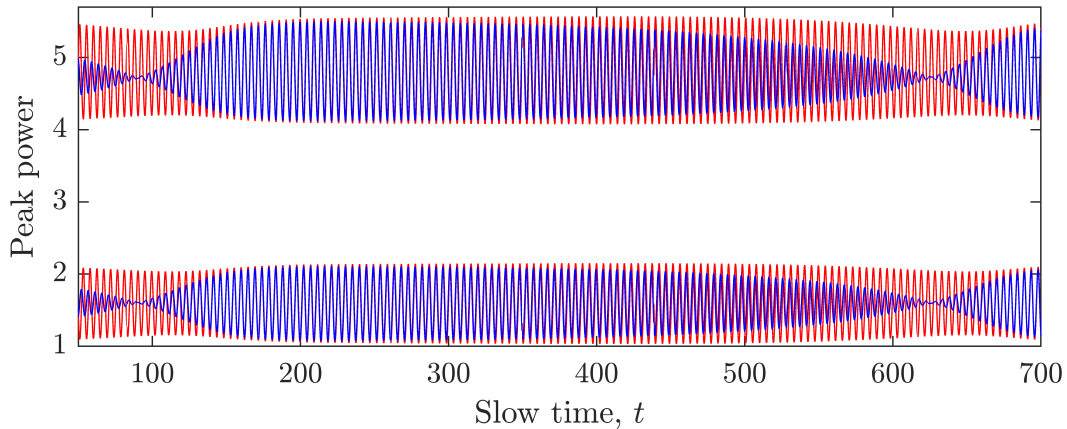


Figure 6.13: A pair of dynamical vectorial dark-bright solitons (VDBS) for $S = 3.2$, $\theta = 18.6$, $\tau_R = 400$. Trace of the bright and dark solitons of two VDBS, where different VDBS are distinguished by different coloured curves. Nonlocal interactions between VDBS results in desynchronisation of oscillations, resulting in a decreasing amplitude in one of the VDBSs. As the amplitude approaches zero, the dynamics suddenly return to near symmetric oscillations.

eventually gives way to VDBSs which evolve along distinct trajectories, as can be seen in Fig. 6.13 for the round trip time $\tau_R = 400$. Here, one of the VDBSs display dominant dynamics (red curve), oscillating with near constant amplitude, while the second VDBS exhibits oscillations growing and dying in amplitude (blue curve). We see that the amplitude of the submissive VDBS is dependent on the mismatch of oscillation phase between the two VDBSs, where the blue VDBS oscillates with large amplitude when in phase with the red VDBS. As the VDBSs evolve, their oscillations move progressively out of phase, such that, the amplitude of oscillation approaches zero, at which point the system rapidly moves back to equal amplitude synchronised oscillation, and the dynamics repeat. These dynamics should allow for the possibility of periodic switching of the death of oscillation between the two VDBSs. For even larger cavities round trip times, the dynamics of the VDBSs return to stable limit cycle oscillation. In such regimes, the two VDBS oscillate with constant amplitudes of different size and identical frequency, with constant phase offset. These limit cycle oscillations approach symmetry (identical limit cycle trajectories) in the limit of large τ_R . This suggests that VDBSs favour synchronisation in the limit of large cavity round trip times, anti-synchronous dynamics for short cavity round trip time, and nontrivial limit torus dynamics for intermediary values.

The distinct dynamical regimes found when increasing τ_R can be explained by considering the change in the relative sizes of the real valued nonlocal terms [Eq. (6.21)] and complex valued nonlocal term [Eq. (6.22)] over slow time. As has been shown in Section 5.7 for the single field FP model [56], real valued nonlocal terms are associated with synchronous dynamics, regardless of cavity size. As such, we may attribute anti-synchronous dynamics to the unique feature of Eqs. (6.20), namely the complex valued nonlocal term. Oscillations of the dark and bright solitons give opposite contributions to

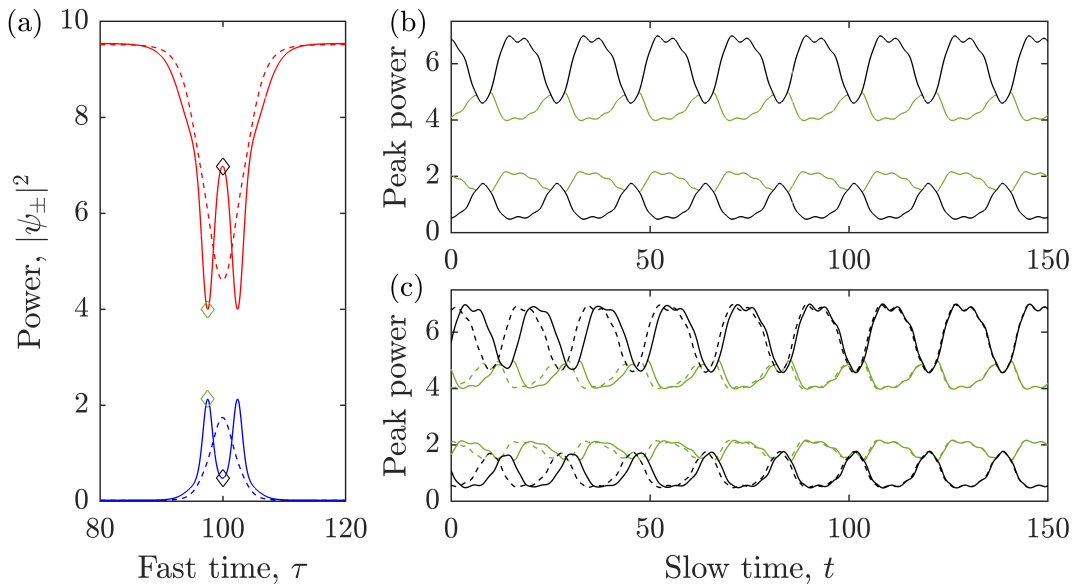


Figure 6.14: Dynamical vectorial dark-bright solitons (VDBS) for $S = 3.2, \theta = 18.6$. (a) Power profiles at two instances in slow time along the VDBS oscillation cycle corresponding to profiles of one and two peaks. (b) Trace of the off centre trough/peak (green line) and central trough/peak (black line) of a single VDBS for $\tau_R = 200$. (b) Trace of the off centre trough/peak (red) and central trough/peak (blue) of two VDBS for $\tau_R = 400$. The solid curve is the first VDBS pair and the dashed curve is the second VDBS. The two VDBSs oscillate out of phase initially, but synchronise over time due to nonlocal coupling. The tracking points of the trace are indicated with diamonds in (a).

the average power and hence result in relatively small changes in the real valued integral terms. For small cavity sizes, the dynamics are dominated by the complex valued nonlocal term (6.22), but as the cavity size increases, the change in (6.22) decreases until the contribution of the real valued integrals become dominant and synchronous dynamics are achieved.

This can be further demonstrated by considering the dynamics of a VDBS of larger width. In Fig. 6.14(a), we present the power profile of a VDBS at two points in its dynamics cycle, as it oscillates between two peaks/troughs and one peak/trough. This dynamical VDBS is found for identical parameter values of the asynchronous VDBSs of Fig. 6.12(c), which are hence bistable. The trace of the central peak/trough and the two side peaks/troughs are plotted in Fig. 6.14(b) as black and green curves, respectively, and show the stable limit cycle oscillation of the VDBS. If we introduce an additional VDBS into the cavity for $\tau_R = 400$, we find that the VDBSs move towards synchronous dynamics, as can be seen in Fig. 6.14(c). Comparing the dynamics of Figs. 6.12 and 6.14, we see that the particular profile of the oscillating VDBSs contributes to whether the long range interactions result in synchronous or anti-synchronous dynamics. In particular, we note that the dynamics of Fig. 6.14(c) induces a significantly larger change in the real valued integral terms, when compared with the single peak VDBSs. This is due to the more

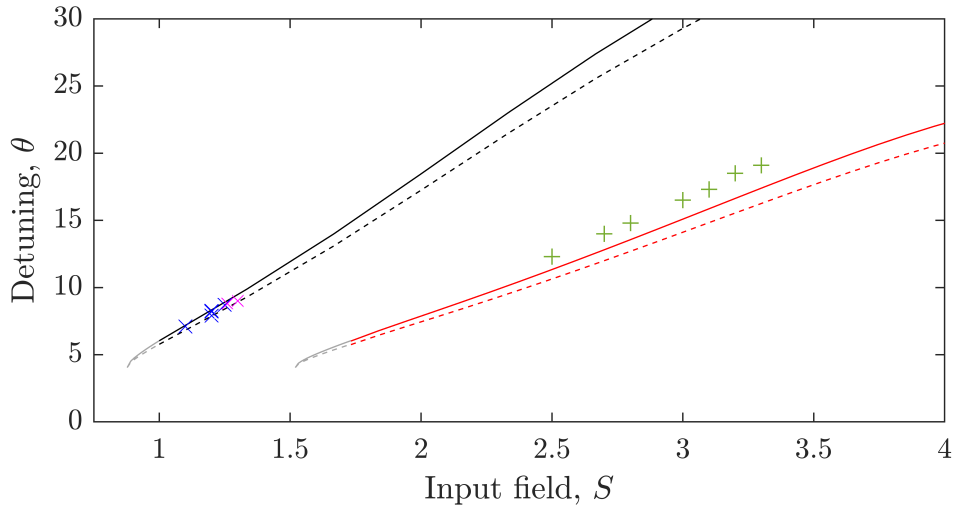


Figure 6.15: Vectorial dark-dark and dark-bright soliton distribution in parameter space. Example symmetric vectorial dark-dark solitons are plotted as x's and vectorial dark-bright solitons as +'s. Semi-analytical Maxwell point solitons at zero dispersion are shown at symmetry for $\Delta = 0$ (black line), $\Delta = 0.1$ (black dashed line). For a single field equation (6.52) the semi-analytical Maxwell point solitons are shown for the high power field, with $\Delta = 0$ (red line), $\Delta = 0.1$ (red dashed line).

complicated oscillation, resulting in larger variation in the soliton width (pulse duration), associated with moving between one and two peaks. As such, the synchronous dynamics are dominant for VDBSs of this profile for much smaller τ_R .

We note that, although oscillating VDBSs are present in the ring resonator system, as discussed in Section 3.7, they do not interact when well separated due to the absence of global coupling, and hence oscillate independently.

6.8 Vectorial cavity soliton distribution in parameter space

As is phenomenologically analogous to the local structures of Chapter 4 and Chapter 5, the soliton solutions of this system are related to the so called Maxwell point of the LLE [56, 117], which allows us to predict the location of VDSs and VDBSs of Eqs. (6.20). For the LLE, the Maxwell point corresponds to a line in the parameter space (S, θ) at which SF solutions have zero velocity. This results in a multitude of stationary solutions composed of noninteracting SFs with arbitrary separations [35, 117]. Due to nonlocal coupling of field within a FP resonator, the Maxwell point solutions are tilted in parameter space [47, 56, 117], such that, for each value of the detuning, there exists a single SF separation at which they have zero velocity. The Maxwell point of the FP model represents a line in the parameter space (S, θ, Δ) corresponding to a turning point in the SF velocity, which occurs when two SFs have separation Δ . In order to predict the formation of VDSs, we plot the Maxwell points for SF separations with a typical soliton sizes $\Delta = 0$ (black solid curve) and $\Delta = 0.1$ (black broken curve), in Fig. 6.15. These lines were

calculated numerically assuming step function solutions, where the detuning is given by $\theta = \Theta_{\text{MP}} + 2\Delta Y_l + 2(1 - \Delta)Y_u$, where we have used the Maxwell point relationship [Eq. (4.27)] between S and Θ_{MP} (determined in Chapter 4). Example symmetric VDS solutions obtained by direct numerical integration of Eqs. (6.20) are shown in Fig. 6.15 as x's and demonstrating good agreement with the predicted locations.

Conversely, VDBSs present as highly symmetry broken solutions in which one field is largely suppressed ($\psi_+ \ll \psi_-$ or $\psi_- \ll \psi_+$). This is most prominent with the background plateau of the bright soliton, as can be seen in Fig. 6.10(d), which approaches zero power. Due to the large disparity in the power of the fields containing dark and bright solitons, we can make the assumption that the bright soliton field acts perturbatively on the field supporting the dark soliton. If we presume that the bright soliton field approaches zero $|\psi_-|^2 \rightarrow 0$ at all points in the cavity, we may approximate the equation governing the field supporting the dark soliton as

$$\partial_t \psi_+ = S - (1 + i\theta)\psi_+ + i\frac{2}{3}\{|\psi_+|^2 + 2\langle|\psi_+|^2\rangle\}\psi_+ - i\partial_\tau^2 \psi_+. \quad (6.52)$$

This equation is identical to the single field FP model under renormalisation. Eq. (6.52) is only an approximation to the field ψ_+ of Eqs. (6.20), but nonetheless, if we plot the corresponding Maxwell points of Eq. (6.52) in Fig. 6.15 (red curve), we may predict the distribution of VDBSs in parameter space. Example VDBS solutions obtained via direct numerical integration are indicated with +'s, and can be seen to follow the predictive curve. +'s appear slightly above this curve due to our approximation $|\psi_-|^2 \rightarrow 0$.

6.9 Conclusion

In this chapter we modelled the propagation of light composed of counter-rotating circular polarisation components within a FP cavity filled with a Kerr nonlinear medium. Taking inspiration from the methods of [48], we derived two coupled integro-partial differential equations, describing the intracavity fields of orthogonal polarisation, which interact through self- and cross-phase modulation.

Linear stability analysis of our model yielded a bifurcation structure of competing SSB bifurcations. We presented the SSB bifurcations of the homogeneous stationary states within the FP cavity, where we characterise a codimension-2 bifurcation point of the symmetric HSSs unique to the normal dispersion regime. The codimension-2 bifurcation represents a point in parameter space in which the reverse pitchfork bifurcation of the symmetry broken HSSs and a forward pitchfork bifurcation of a Turing instability collide, and the real part of the corresponding eigenvalues are simultaneously zero. The SSB of the HSS associated with the reverse pitchfork bifurcation has been previously demonstrated experimentally when neglecting dispersion [68]. Here, we characterised the forward pitchfork bifurcation, innate to the normal dispersion regime, which was found to result in the formation of Turing patterns composed of alternating fields of orthogonal polarisation. This bifurcation structure extends to a homogeneous background of a symmetric VDS, resulting in a multitude of symmetry broken VDS solutions. Of particular interest, is a SSB bifurcation of the VDS resulting in the formation of Turing patterns on the homogeneous background from which the soliton hangs.

When considering multiple simultaneous VDSs along the cavity round trip, SSB Turing patterns are found to form in the intervals between adjacent VDSs. As the Turing patterns grow in amplitude, VDSs are ‘pushed’ along the resonator, increasing their separation until an equidistant equilibrium distance is reached. In other words, the SSB of VDSs induce long range repulsive interactions between adjacent VDSs, mediated by the Turing patterns. The motion of the VDSs represents a spontaneous self-organisation phenomenon, which results in the formation of a regularly spaced soliton crystal. The ‘self-crystallisation’ of a RSC was previously demonstrated for VDSs of the ring resonator in Chapter 3, where in comparison, the Turing patterns of the FP resonator present with a higher wavenumber and longer amplitude saturation distance, which results in an increased range of the repulsive interaction between VDSs in the FP cavity. Hence, the FP resonator is more congruent to the formation for RSCs and more robust to changes in solitons number. RSCs originate spontaneously from a random distribution of VDS, without the need of a perturbation [40–44], offering new degrees of control, and a simple implementation, relevant for applications in RSC generation [123–126]. The generalisation of this process to the FP resonator increases the accessibility of this phenomenon for practical application. RSCs produce a frequency comb with smooth spectral profile and an increased line spacing when compared to a random distribution of cavity solitons. As such, a RSC may be used to emulate smaller cavity sizes while avoiding the associated experimental limitations.

Finally, we characterise the formation of VDBSs. These solutions form in regimes of highly symmetry broken HSSs, in which, the circulating power in one polarisation component is significantly larger than that other. With suitable perturbation, a dark soliton forms in the high power polarisation component, which is coupled to a bright soliton that forms in the low power component. Previous methods for the generation of VDBSs make use of bichromatic driving of a ring resonator [140], such that the two frequency components may operate in distinct regimes of group velocity dispersion, with one laser operating in the anomalous dispersion regime, generating a bright soliton, while the other operates in the normal dispersion regime, supporting a dark soliton through cross-phase modulation. In our system, the bright and dark solitons are formed in regimes of identical normal dispersion, and are composed of switching fronts which connect two high power plateaus and two low power plateaus. SFs lock to form solitons due to the interaction of oscillatory tails which appear on the approach to the plateaus of intermediary power. VDBS of the FP resonator undergo a Hopf bifurcation when scanning the detuning, resulting in breathing dynamics. We found that well separated VDBSs, located such that they do not interact via the local dynamics at the tails, experience oscillation-phase dependent interaction through the nonlocal coupling. We observed in simulation a pair of well separated dynamical VDBSs move as to oscillate exactly out of phase with overlapping limit cycle trajectories. This is unlike the synchronous dynamics of single component dark cavity solitons of the FP model in Chapter 5. Conversely, in the limit of a large cavity round trip time, the VDBS dynamics found to approach synchronisation. In general, short cavities display anti-synchronous dynamics, long cavities display synchronous dynamic, and intermediate cavities display nontrivial dynamics. These regimes are consequence of competition between real valued and complex valued integral terms.

Chapter 7

Conclusion

In this thesis, we studied the generation of temporal cavity solitons and frequency combs in high finesse ring and Fabry-Pérot resonators with; orthogonal polarisation field components, counterpropagating field components or a combination of the two. The theoretical and numerical results presented in this thesis offer interesting phenomenon of for future experimental consideration at parameter values achievable in current devices.

In Chapter 3, long-range interactions between dark vectorial temporal cavity solitons were induced by the formation of patterns via spontaneous symmetry breaking of orthogonally polarised fields in ring resonators. Turing patterns of alternating polarisations form between adjacent solitons, pushing them apart so that a random distribution of solitons along the cavity length move spontaneously towards equal equilibrium distances, the soliton crystal, without any the need for perturbation from mode crossings or external modulation. We seen that enhancement of the frequency comb is achieved through the spontaneous formation of regularly spaced soliton crystals, ‘self-crystallisation’, with greater power and spacing of the spectral lines for increasing soliton numbers. Partial self-crystallisation is also achievable in long cavities, allowing one to build crystal sections with controllable numbers of cavity solitons separated by intervals of pattern solutions of controllable length. Finally, we characterised vectorial dark-bright solitons found in regimes of large symmetry breaking. Such solutions are formed from switching fronts, which connect two bistable HSSs of high power and two HSSs of low power, locking due to the interaction of oscillatory tails.

In Chapter 4, we characterised the formation of robust stationary states formed by light plateaus separated by two local switching fronts in only one of two counterpropagating fields in ring resonators with normal dispersion. Such states are due to global cross coupling and allow for frequency combs to switch from one field to the other by simply tuning the input laser frequency. Exact expressions for the distance between fronts and for plateau powers were provided in excellent agreement with simulations. These demonstrate an unusual high degree of control over pulse and plateau duration in one of the fields upon changes of one of the input laser frequencies. We identified a wide parameter region in which light plateaus are self-starting and are the only stable solution. For certain values of the detunings we found multistable states of plateaus with switching fronts, slowly oscillating homogeneous states and non-oscillating homogeneous states of the counterpropagating fields. Robustness and multistability of these unusual single-field

front solutions were provided in parameter ranges that are experimentally achievable in a wide variety of ring resonators.

In Chapter 5, the ranges of existence and stability of dark cavity-soliton stationary states in a Fabry-Pérot resonator with a Kerr nonlinear medium and normal dispersion were determined. The Fabry-Pérot configuration introduces nonlocal coupling that shifts the cavity detuning by the round trip average power of the intracavity field. When compared with ring resonators described by the Lugiato-Lefever equation, nonlocal coupling leads to strongly detuned dark cavity solitons that exist over a wide range of detunings. This shift is a consequence of the counterpropagation of intracavity fields inherent to Fabry-Pérot resonators. In contrast with ring resonators, the existence and stability of dark soliton solutions are dependent on the size and number of solitons in the cavity. We investigated the effect of nonlocal coupling of Fabry-Pérot resonators on multiple dark solitons, and we demonstrated long-range interactions and synchronisation of temporal oscillations.

In Chapter 6, we generalised the Fabry-Pérot model to include polarisation considerations by resolving the intracavity field into counter-rotating orthogonal polarisations. Following from Pitois et al. [55], we modelled the interaction of the four intracavity fields with four partial differential equations (two forward propagating with orthogonal polarisations, two backward propagating with orthogonal polarisations) coupled through the Kerr nonlinearity. Inspired from the methods of Cole et al. [48], we then combined forward and backward propagating field to arrive at two integro-partial differential equations which model this system. Linear stability analysis of the HSSs revealed a codimension-2 bifurcation, composed of two distinct SSB bifurcations, corresponding to symmetry broken HSSs and Turing patterns of alternating polarisation. This bifurcation structure extends to the symmetric VDSs which were found to undergo a Turing bifurcation. Similar to the VDSs of the ring resonator, Turing patterns of alternating polarisations form between adjacent VDSs, pushing them apart so that a random distribution of solitons along the cavity length spontaneously reaches equal equilibrium distances. As such, the ‘self-crystallisation’ mechanism may be generalised to the FP model, and utilised for the formation of a regular soliton crystal. It is found that the wavenumber and amplitude saturation distance of the Turing pattern were much larger for the FP model. As such, the FP resonator is more congruent to the formation of robust regular soliton crystals due to a longer repulsive interaction distances. We concluded this chapter by discussing the formation of VDBSs in larger symmetry broken regimes. VDBS were found to undergo a Hopf bifurcation when scanning the detuning, which display nontrivial oscillations due to long range interaction originating from the nonlocal coupling.

Appendix A

Linear Stability Analysis of Counterpropagating Light in Ring Resonators

A.1 Linear stability analysis of the modal amplitudes

We begin our investigation by performing linear stability analysis on the homogeneous stationary states. Here, we perform our linearisation about the modal amplitudes of the counterpropagating model, Eqs. (4.11), which we rewrite here,

$$\begin{aligned} \partial_t f_\mu &= S\delta_{\mu,0} - (1 + i\theta_F)f_\mu + ik_\mu^2 f_\mu \\ &+ i \sum_{\mu',\mu'',\mu'''} \delta_{\mu,\mu'+\mu''-\mu'''} f_{\mu'} f_{\mu''} (f_{\mu'''})^* + 2if_\mu \sum_{\mu'} b_{\mu'} (b_{\mu'})^*, \end{aligned} \quad (\text{A.1})$$

$$\begin{aligned} \partial_t b_\mu &= S\delta_{\mu,0} - (1 + i\theta_B)b_\mu + ik_\mu^2 b_\mu \\ &+ i \sum_{\mu',\mu'',\mu'''} \delta_{\mu,\mu'+\mu''-\mu'''} b_{\mu'} b_{\mu''} (b_{\mu'''})^* + 2ib_\mu \sum_{\mu'} f_{\mu'} (f_{\mu'})^*, \end{aligned} \quad (\text{A.2})$$

where the expansion of the forward and backward field envelopes are defined

$$F(\tau, t) = \sum_{\mu=-\infty}^{\infty} f_\mu(t) e^{-ik_\mu(t-\tau)}, \quad B(\tau, t) = \sum_{\mu=-\infty}^{\infty} b_\mu(t) e^{-ik_\mu(t+\tau)}, \quad (\text{A.3})$$

for modal amplitudes $f_\mu(t), b_\mu(t)$ with wavenumber $k_\mu = 2\pi\mu/\tau_R$ and mode number μ . Within the modal formalism, the homogeneous stationary states of Eqs. (A.1) and (A.2) correspond to $f_{\mu,s} = f_s \delta_{\mu,0}$, $b_{\mu,s} = b_s \delta_{\mu,0}$ where $\delta_{\mu,0}$ is the Kronecker delta defined as

$$\delta_{\mu,0} = \begin{cases} 1, & \text{if } \mu = 0, \\ 0, & \text{if } \mu \neq 0. \end{cases} \quad (\text{A.4})$$

We introduce a linear perturbation of the form,

$$f_\mu = f_s \delta_{\mu,0} + \delta f_\mu, \quad b_\mu = b_s \delta_{\mu,0} + \delta b_\mu, \quad (\text{A.5})$$

to Eqs. (A.1) and (A.2), such that, we obtain linearised equations in terms of the perturbations $\delta f_\mu, \delta b_\mu$ with,

$$\begin{aligned} \partial_t \delta f_\mu &= -(1 + i\theta_F) \delta f_\mu + ik_\mu^2 \delta f_\mu \\ &\quad + 2i\{|f_s|^2 + |b_s|^2\} \delta f_\mu + i(f_s)^2 (\delta f_{-\mu})^* + 2i\delta_{\mu,0} \{f_s (b_s)^* \delta b_0 + (\delta b_0)^* f_s b_s\}, \end{aligned} \quad (\text{A.6})$$

$$\begin{aligned} \partial_t \delta b_\mu &= -(1 + i\theta_B) \delta b_\mu + ik_\mu^2 \delta b_\mu \\ &\quad + 2i\{|b_s|^2 + |f_s|^2\} \delta b_\mu + i(b_s)^2 (\delta b_{-\mu})^* + 2i\delta_{\mu,0} \{b_s (f_s)^* \delta f_0 + (\delta f_0)^* b_s f_s\}. \end{aligned} \quad (\text{A.7})$$

We note that the self-phase Kerr modulation may be expanded as,

$$\begin{aligned} &\sum_{\mu', \mu'', \mu'''} i\delta_{\mu, \mu' + \mu'' - \mu'''} (f_{\mu'} f_{\mu''} (f_{\mu'''}^*) - f_{\mu', s} f_{\mu'', s} (f_{\mu''', s})^*) \\ &= \sum_{\mu', \mu'', \mu'''} i\delta_{\mu, \mu' + \mu'' - \mu'''} \{f_{\mu', s} f_{\mu'', s} (\delta f_{\mu'''}^*) + f_{\mu', s} \delta f_{\mu''} (f_{\mu''', s})^* + \delta f_{\mu'} f_{\mu'', s} (f_{\mu''', s})^*\} \\ &= i\left\{ \sum_{\mu'''} \delta_{\mu, -\mu'''} (f_s)^2 (\delta f_{\mu'''}^*) + \sum_{\mu''} \delta_{\mu, \mu''} |f_s|^2 \delta f_{\mu''} + \sum_{\mu'} \delta_{\mu, \mu'} |f_s|^2 \delta f_{\mu'} \right\} \\ &= i\{(f_s)^2 (\delta f_{-\mu})^* + 2|f_s|^2 \delta f_\mu\}, \end{aligned} \quad (\text{A.8})$$

and similarly, the cross-phase Kerr modulation,

$$\begin{aligned} &2if_\mu \sum_{\mu'} b_{\mu'} (b_{\mu'})^* - 2if_{\mu, s} \sum_{\mu'} b_{\mu', s} (b_{\mu', s})^* \\ &= 2if_{\mu, s} \sum_{\mu'} \{(b_{\mu', s})^* \delta b_{\mu'} + (\delta b_{\mu'})^* b_{\mu', s}\} + 2i\delta f_\mu \sum_{\mu'} b_{\mu', s} (b_{\mu', s})^* \\ &= 2if_s \delta_{\mu, 0} \sum_{\mu'} \delta_{\mu', 0} \{(b_s)^* \delta b_{\mu'} + (\delta b_{\mu'})^* b_s\} + 2i\delta f_\mu \sum_{\mu'} \delta_{\mu', 0} |b_s|^2 \\ &= 2i\delta_{\mu, 0} \{f_s (b_s)^* \delta b_0 + (\delta b_0)^* f_s b_s\} + 2i|b_s|^2 \delta f_\mu. \end{aligned} \quad (\text{A.9})$$

In particular, it is noted that only the cross-phase Kerr modulation contains terms proportional to the Kronecker delta. This is due to the fact that this term governs the interaction of counterpropagating components.

Without the loss of generality, we may assume the homogeneous stationary states are real, such that, we write Eqs. (A.6) and (A.7) in terms of the the real and imaginary parts of the perturbations, with,

$$\begin{pmatrix} \partial_t \text{Re}(\delta f_\mu) \\ \partial_t \text{Im}(\delta f_\mu) \\ \partial_t \text{Re}(\delta b_\mu) \\ \partial_t \text{Im}(\delta b_\mu) \end{pmatrix} = \begin{pmatrix} -1 & -A_1 & 0 & 0 \\ B_1 & -1 & \delta_{\mu, 0} C & 0 \\ 0 & 0 & -1 & -A_2 \\ \delta_{\mu, 0} C & 0 & B_2 & -1 \end{pmatrix} \begin{pmatrix} \text{Re}(\delta f_\mu) \\ \text{Im}(\delta f_\mu) \\ \text{Re}(\delta b_\mu) \\ \text{Im}(\delta b_\mu) \end{pmatrix}, \quad (\text{A.10})$$

where

$$\begin{aligned} A_1 &= k_\mu^2 - \theta_F + f_s^2 + 2b_s^2, & B_1 &= k_\mu^2 - \theta_F + 3f_s^2 + 2b_s^2, & C &= 4f_s b_s, \\ A_2 &= k_\mu^2 - \theta_B + 2f_s^2 + b_s^2, & B_2 &= k_\mu^2 - \theta_B + 2f_s^2 + 3b_s^2. \end{aligned}$$

The characteristic equation of the Jacobian matrix of Eq. (A.10) is,

$$[(1 + \lambda)^2 + A_1 B_1][(1 + \lambda)^2 + A_2 B_2] - \delta_{\mu,0} A_1 A_2 C^2 = 0, \quad (\text{A.11})$$

form which we determine the eigenspectrum

$$\lambda(k_\mu) = -1 \pm \frac{\sqrt{-A_1 B_1 - A_2 B_2 \pm Q}}{\sqrt{2}}, \quad (\text{A.12})$$

$$Q = \sqrt{(A_1 B_1 - A_2 B_2)^2 + 4\delta_{\mu,0} A_1 A_2 C^2}. \quad (\text{A.13})$$

The significance of these eigenvalues is discussed in Section 4.3 of the main text.

A.2 Linear stability of homogeneous stationary states to step function perturbations

Here we investigate the linear stability of homogeneous stationary states F_s, B_s to inhomogeneous perturbations in fast time at zero dispersion ($\beta = 0$). The nonlocality of the counterpropagating system means that local perturbations will result in changes to the unperturbed regions, and therefore have an implicit dependence on the entirety of the field. It is necessary to track the evolution of the entire field to determine the susceptibility of the homogeneous stationary states to bifurcation along the longitudinal coordinate. We do so by considering the field part wise in fast time

$$F(\tau, t) = F_1(t)T(\tau/\tau_R)T(\Delta_F - \tau/\tau_R) + F_2(t)T(\tau/\tau_R - \Delta_F)T(1 - \tau/\tau_R), \quad (\text{A.14})$$

$$B(\tau, t) = B_1(t)T(\tau/\tau_R)T(\Delta_B - \tau/\tau_R) + B_2(t)T(\tau/\tau_R - \Delta_B)T(1 - \tau/\tau_R), \quad (\text{A.15})$$

such that

$$|F|^2 = |F_1|^2 T(\tau/\tau_R)T(\Delta_F - \tau/\tau_R) + |F_2|^2 T(\tau/\tau_R - \Delta_F)T(1 - \tau/\tau_R), \quad (\text{A.16})$$

$$|B|^2 = |B_1|^2 T(\tau/\tau_R)T(\Delta_B - \tau/\tau_R) + |B_2|^2 T(\tau/\tau_R - \Delta_B)T(1 - \tau/\tau_R), \quad (\text{A.17})$$

where $T(\tau)$ represent the Heaviside step function which has value 1 for $\tau \geq 0$, and 0 for $\tau < 0$, and Δ_F, Δ_B are the normalised durations in fast time occupied by F_1, B_1 . The part wise fields F_1 and F_2 (B_1 and B_2) represent two separate domains of fast time which experience different homogeneous perturbations of the same HSS, such that the perturbation over the round trip is inhomogeneous. We consider a linear perturbation to

the homogeneous stationary solution of the form

$$\begin{aligned} F_1(t) &= F_s + f_1(t), & F_2(t) &= F_s + f_2(t), \\ B_1(t) &= B_s + b_1(t), & B_2(t) &= B_s + b_2(t). \end{aligned}$$

The average field powers under this formulation are

$$\langle |F|^2 \rangle = \Delta_F |F_1|^2 + (1 - \Delta_F) |F_2|^2, \quad (\text{A.18})$$

$$\langle |B|^2 \rangle = \Delta_B |B_1|^2 + (1 - \Delta_B) |B_2|^2. \quad (\text{A.19})$$

The evolution of the F_1 and F_2 components are not explicitly dependent on each other as we have neglected dispersion. As such we describe the evolution of the F field as separate ODEs for F_1, F_2 (likewise for the B field). Hence this system is described by the four ODEs

$$\frac{dF_1}{d\tau} = S_F - (1 + i\theta_F)F_1 + i(|F_1|^2 + \nu[\Delta_B|B_1|^2 + (1 - \Delta_B)|B_2|^2])F_1, \quad (\text{A.20})$$

$$\frac{dF_2}{d\tau} = S_F - (1 + i\theta_F)F_2 + i(|F_2|^2 + \nu[\Delta_B|B_1|^2 + (1 - \Delta_B)|B_2|^2])F_2, \quad (\text{A.21})$$

$$\frac{dB_1}{d\tau} = S_B - (1 + i\theta_B)B_1 + i(|B_1|^2 + \nu[\Delta_F|F_1|^2 + (1 - \Delta_F)|F_2|^2])B_1, \quad (\text{A.22})$$

$$\frac{dB_2}{d\tau} = S_B - (1 + i\theta_B)B_2 + i(|B_2|^2 + \nu[\Delta_F|F_1|^2 + (1 - \Delta_F)|F_2|^2])B_2. \quad (\text{A.23})$$

Without loss of generality, we adjust the phase of S_F, S_B such that F_s, B_s are real. We have that the real and imaginary components of the perturbation evolve as

$$\begin{pmatrix} \dot{f}_{1,r} \\ \dot{f}_{1,i} \\ \dot{f}_{2,r} \\ \dot{f}_{2,i} \\ \dot{b}_{1,r} \\ \dot{b}_{1,i} \\ \dot{b}_{2,r} \\ \dot{b}_{2,i} \end{pmatrix} = \begin{pmatrix} -1 & A_1 & 0 & 0 & 0 & 0 & 0 & 0 \\ -B_1 & -1 & 0 & 0 & -\Delta_B C & 0 & -(1 - \Delta_B)C & 0 \\ 0 & 0 & -1 & A_1 & 0 & 0 & 0 & 0 \\ 0 & 0 & -B_1 & -1 & -\Delta_B C & 0 & -(1 - \Delta_B)C & 0 \\ 0 & 0 & 0 & 0 & -1 & A_2 & 0 & 0 \\ -\Delta_F C & 0 & -(1 - \Delta_F)C & 0 & -B_2 & -1 & 0 & 0 \\ 0 & 0 & 0 & 0 & 0 & 0 & -1 & A_2 \\ -\Delta_F C & 0 & -(1 - \Delta_F)C & 0 & 0 & 0 & -B_2 & -1 \end{pmatrix} \begin{pmatrix} f_{1,r} \\ f_{1,i} \\ f_{2,r} \\ f_{2,i} \\ b_{1,r} \\ b_{1,i} \\ b_{2,r} \\ b_{2,i} \end{pmatrix} \quad (\text{A.24})$$

where $\dot{f} = df/dt, \dot{b} = db/dt$ and

$$\begin{aligned} A_1 &= F_s^2 + \nu B_s^2 - \theta_F, & B_1 &= 3F_s^2 + \nu B_s^2 - \theta_F, & C &= 2\nu F_s B_s, \\ A_2 &= B_s^2 + \nu F_s^2 - \theta_B, & B_2 &= 3B_s^2 + \nu F_s^2 - \theta_B. \end{aligned}$$

The corresponding eigenvalue equation is then

$$0 = [(\lambda+1)^2 + A_1 B_1][(\lambda+1)^2 + A_2 B_2] \left\{ [(\lambda+1)^2 + A_1 B_1][(\lambda+1)^2 + A_2 B_2] - A_1 A_2 C^2 \right\}. \quad (\text{A.25})$$

Eq. (A.25) yields two distinct sets of eigenvalues, which account for different instability phenomena. Firstly, this results in the known eigenvalues of homogeneous perturbation of the homogeneous stationary states [96]

$$\lambda = -1 \pm \frac{\sqrt{-A_1 B_1 - A_2 B_2 \pm Q}}{\sqrt{2}}, \quad (\text{A.26})$$

$$Q = \sqrt{(A_1 B_1 - A_2 B_2)^2 + 4A_1 A_2 C^2}, \quad (\text{A.27})$$

corresponding to eigenvalues (4.16) for $k_\mu = 0$. Accompanying these eigenvalues, Eq. (A.25) yields

$$\lambda_F = -1 \pm \sqrt{-A_1 B_1}, \quad (\text{A.28})$$

$$\lambda_B = -1 \pm \sqrt{-A_2 B_2}. \quad (\text{A.29})$$

These eigenvalues are indicative of instability of either the F field (λ_F) or the B field (λ_B) due to fast time inhomogeneous perturbations and are a consequence of the global coupling of the counterpropagating field. Such eigenvalues are not present in locally coupled field, such as the copropagating fields of Chapter 3. This eigenspectrum is mathematically identical to those seen for the single field ring resonator (Lugiato-Lefever equation) with parameter values $P_F, \tilde{\theta}_F$ and $P_B, \tilde{\theta}_B$ respectively. It is important to note that this instability is predicted with the assumption of zero group velocity dispersion. Nonetheless, this instability is found to extend into the normal dispersion regime (but not the anomalous regime). As such, F_1 and F_2 do not need to be continuous regions of fast time. They represent the total proportion of the field perturbed below or above the stationary solution, and as such, the above eigenvalues are appropriate for a perturbation with random fast time variations (which would have width $\Delta_F \approx 0.5$ on average, assuming equal weighting). Likewise for the B field.

In the regime of local coupling, the two copropagating fields are coupled by Kerr cross-phase modulation. As such, a local perturbation of one of the fields will only effect the corresponding local region of the other field. If we introduce a step function perturbation to the homogeneous stationary states F_s, B_s with size Δ of the form $F = F_s + fT(\tau/\tau_R)T(\Delta - \tau/\tau_R)$, $B = B_s + bT(\tau/\tau_R)T(\Delta - \tau/\tau_R)$, the perturbations f, b will evolve identically to a homogeneous perturbation of the entire field. This results in the eigenvalues given by Eq. (A.26) of homogeneous perturbation of the homogeneous stationary states [96]. Non-locality in the counterpropagating system introduces an implicit dependence on the power of the entire field. This allows the system to access inhomogeneous states of the single LLE, and introduces four additional eigenvalues indicative of instability only in the presence of an inhomogeneous fast time component.

A.3 Linear stability of plateaus connected by step functions

In numerical simulations, we observe that stationary switching fronts (SF) form in only one field at any a given time, with the other field remaining homogeneous. Using a similar framework as in Appendix A.2, we can simply do the analysis by considering a homogeneous F field with an inhomogeneous B field. We describe the B field as the part

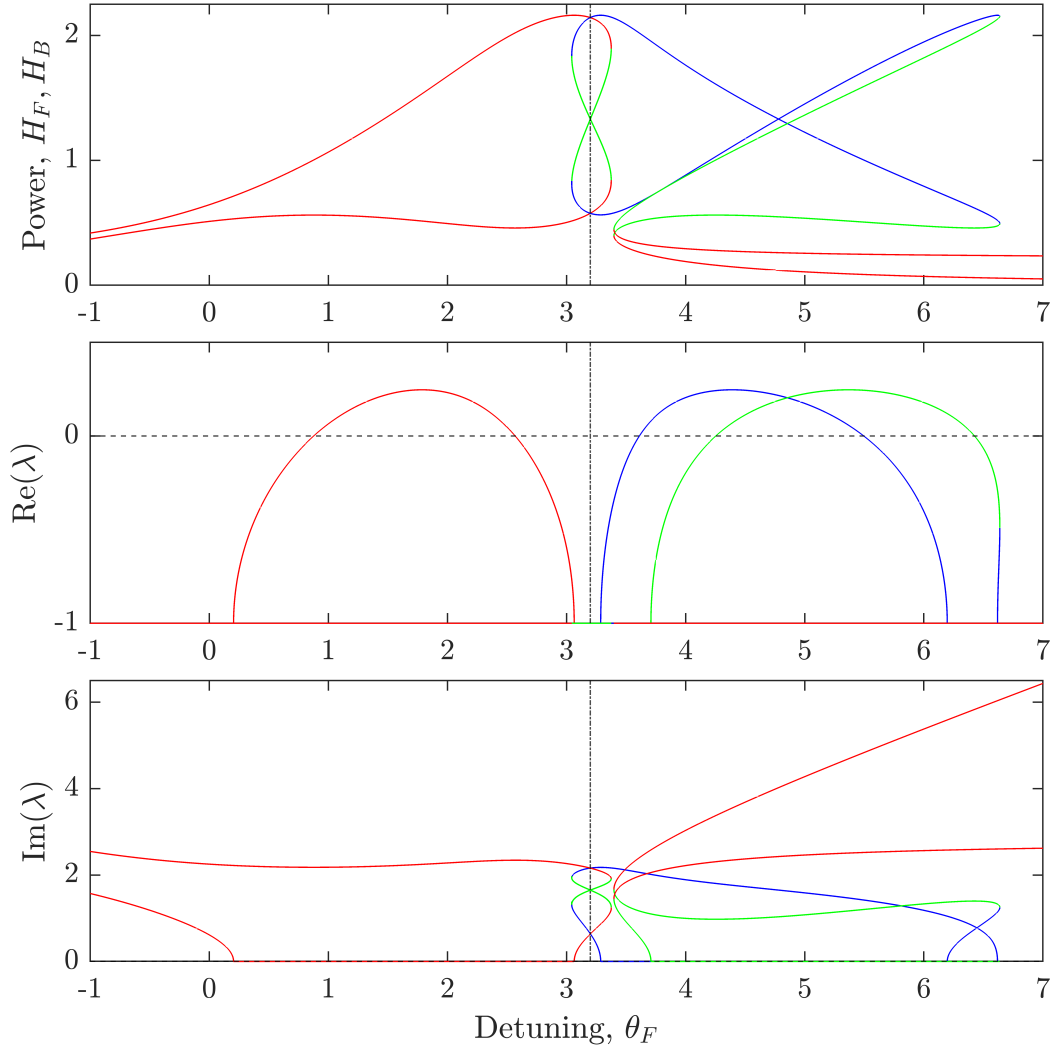


Figure A.1: (a) Homogeneous stationary solutions when scanning θ_F with parameter values $P_F = P_B = 2.1609, \theta_B = 3.2$. Distinct solutions branches are indicated by different colours. The real (b) and imaginary (c) components of the eigenvalues (A.28) and (A.29) indicate instability of the highest power branch of HSS for $\theta_F > \theta_B$ (blue), and instability of the sole HSS for $\theta_F < \theta_B$ (red). This instability results in the formation of two SF stationary states.

wise function in terms of the higher and lower power homogeneous state B^+ , B^- connected by the step functions (an approximation of very steep SFs), and the F field as a single homogeneous function. At zero dispersion we have

$$B = B^-(t)T(\tau/\tau_R)T(\Delta_B - \tau/\tau_R) + B^+(t)T(\tau/\tau_R - \Delta_B)T(1 - \tau/\tau_R), \quad (\text{A.30})$$

where Δ is the normalised front separation. Therefore,

$$|F(t)|^2 = |F(t)|^2, \quad (\text{A.31})$$

$$|B(t)|^2 = |B^-(t)|^2T(\tau/\tau_R)T(\Delta_B - \tau/\tau_R) + |B^+(t)|^2T(\tau/\tau_R - \Delta_B)T(1 - \tau/\tau_R), \quad (\text{A.32})$$

and the average field power is

$$\langle |F|^2 \rangle = |F|^2, \quad (\text{A.33})$$

$$\langle |B|^2 \rangle = \Delta_B |B^-|^2 + (1 - \Delta_B) |B^+|^2. \quad (\text{A.34})$$

As the B field is part wise and the F field is homogeneous, the evolution of the F, B fields is described by the three ODEs,

$$\frac{d}{dt}F = S_F - (1 + i\theta_F)F + i(|F|^2 + \nu[\Delta_B |B^-|^2 + (1 - \Delta_B) |B^+|^2])F, \quad (\text{A.35})$$

$$\frac{d}{dt}B^+ = S_B - (1 + i\theta_B)B^+ + i(|B^+|^2 + \nu|F|^2)B^+, \quad (\text{A.36})$$

$$\frac{d}{dt}B^- = S_B - (1 + i\theta_B)B^- + i(|B^-|^2 + \nu|F|^2)B^-. \quad (\text{A.37})$$

We introduce a linear perturbation to the system that is longitudinally inhomogeneous in the B field and homogeneous in the F field,

$$F = F_s + f, \quad (\text{A.38})$$

$$B^+ = B_s^+ + b^+, \quad B^- = B_s^- + b^-, \quad (\text{A.39})$$

where F_s is the stationary homogeneous solution of the F field and B_s^+ , B_s^- are the two stationary plateau states connected by the SFs. Without loss of generality, we adjust the phase of S_F, S_B such that F_s, B_s are real. We have that the real and imaginary components of the perturbations evolve as

$$\frac{d}{dt} \begin{pmatrix} f_r \\ f_i \\ b_r^+ \\ b_i^+ \\ b_r^- \\ b_i^- \end{pmatrix} = \begin{pmatrix} -1 & A & 0 & 0 & 0 & 0 \\ -B & -1 & -(1 - \Delta_B)C_1 & 0 & -\Delta_B C_2 & 0 \\ 0 & 0 & -1 & A_1 & 0 & 0 \\ -C_1 & 0 & -B_1 & -1 & 0 & 0 \\ 0 & 0 & 0 & 0 & -1 & A_2 \\ -C_2 & 0 & 0 & 0 & -B_2 & -1 \end{pmatrix} \begin{pmatrix} f_r \\ f_i \\ b_r^+ \\ b_i^+ \\ b_r^- \\ b_i^- \end{pmatrix}, \quad (\text{A.40})$$

where

$$\begin{aligned}
 A &= F_s^2 + \nu \langle |B_s|^2 \rangle - \theta_F, & B &= 3F_s^2 + \nu \langle |B_s|^2 \rangle - \theta_F, & C_1 &= 2\nu F_s B_s^+ \\
 A_1 &= (B_s^+)^2 + \nu F_s^2 - \theta_B, & B_1 &= 3(B_s^+)^2 + \nu F_s^2 - \theta_B, & C_2 &= 2\nu F_s B_s^- \\
 A_2 &= (B_s^-)^2 + \nu F_s^2 - \theta_B, & B_2 &= 3(B_s^-)^2 + \nu F_s^2 - \theta_B.
 \end{aligned}$$

This results in the characteristic polynomial

$$\begin{aligned}
 0 &= [(\lambda + 1)^2 + A_2 B_2] \left\{ [(\lambda + 1)^2 + AB][(\lambda + 1)^2 + A_1 B_1] - 2\Delta_B A A_1 C_1^2 \right\} \\
 &+ [(\lambda + 1)^2 + A_1 B_1] \left\{ [(\lambda + 1)^2 + AB][(\lambda + 1)^2 + A_2 B_2] - 2(1 - \Delta_B) A A_2 C_2^2 \right\}, \quad (\text{A.41})
 \end{aligned}$$

which is composed of the product of terms indicative of fast time instability

$$\Lambda_n^\pm = \lambda + 1 \pm \sqrt{-A_n B_n}, \quad (\text{A.42})$$

and eigenvalues indicative of temporal instability (in the curly brackets)

$$L_n^{(\pm, \pm)} = \lambda + 1 \pm \frac{\sqrt{-AB - A_n B_n \pm Q_n}}{\sqrt{2}}, \quad (\text{A.43})$$

$$Q_n = \sqrt{(AB - A_n B_n)^2 + (-1)^n (1 - n - \Delta_B) 8 A A_n C_n^2}. \quad (\text{A.44})$$

This expression has similar form to the characteristic polynomial of the HSS seen in appendix A.2 and will become identical when $\Delta_B = 0, 1$. In simulation, we observe that the SF solutions are susceptible to damped oscillations under perturbation. These oscillations grow in the range $3.5 < \theta_F < 6.3$ and the SF solutions are unstable. This instability range is predicted by eigenvalues (A.41), which are evaluated numerically in Fig. A.2.

If we instead consider a perturbation with inhomogeneous fast time component $b^\pm(\tau, t)$ to the stationary plateaus B_s^\pm of the SF solution that does not change the average power of the field $\langle |B_s^\pm + b^\pm(\tau, t)|^2 \rangle = \langle |B_s^\pm|^2 \rangle$, then the resulting eigenvalues are

$$\begin{aligned}
 \lambda &= -1 \pm \sqrt{-AB}, & \text{for the forward field,} \\
 \lambda_n &= -1 \pm \sqrt{-A_n B_n}, & \text{for the backward field.}
 \end{aligned}$$

These eigenvalues are indicative of the longitudinal stability along the respective plateaus, and suggests that temporal (longitudinal homogeneous) instability of the stationary states of counterpropagating fields is observed when the average powers of the fields is perturbed. Otherwise the fields exhibit an identical eigenspectrum to that of the LLE with effective detuning as defined in Section 4.5. In particular, the eigenvalues of the SF solution at stationary separation, as calculated in Section 4.5, are those of a single LLE at Maxwell

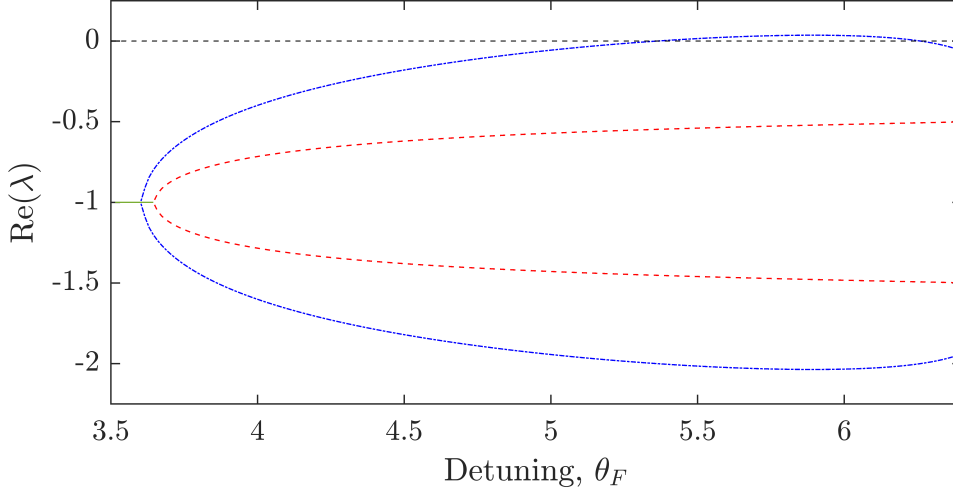


Figure A.2: Real component of eigenvalues of the zero dispersion SF solutions for changing θ_F with parameter values $P_F = P_B = 2.1609, \theta_B = 3.2$. The six eigenvalues are calculated numerically (six roots of Eq. (A.41)), where each branch of the blue dot dashed line represent the real part of a complex conjugate pair of solutions, the red dashed lines are real solutions.

point,

$$\lambda^+ = -1 \pm \sqrt{(\Theta_{\text{MP}} - Y_B^+)(3Y_B^+ - \Theta_{\text{MP}})}, \quad (\text{A.45})$$

$$\lambda^- = -1 \pm \sqrt{(\Theta_{\text{MP}} - Y_B^-)(3Y_B^- - \Theta_{\text{MP}})}. \quad (\text{A.46})$$

This is expected due to the one to one correspondence of the counterpropagating SF solution to the stationary states of the LLE. We note that these eigenvalues are independent of the detuning values. This is due to the fact that SF solutions of the counterpropagating system map to a single parameter value (the Maxwell point Θ_{MP}) of the analogues LLE. When changing θ_F , we move through the multi-stability of SF states found at the Maxwell point. The eigenvalues of the forward field are

$$\lambda = -1 \pm \sqrt{(\tilde{\theta}_F - Y_F)(3Y_F - \tilde{\theta}_F)} \quad (\text{A.47})$$

where $\tilde{\theta}_F = \theta_F - \nu \langle |B_s|^2 \rangle$ is the effective detuning, which is dependent on the detuning values (or more specifically the front separation Δ).

A.4 Self starting two switching front stationary states when scanning detuning

In Fig. A.3, we hold constant $\theta_B = 3.2$ and scan θ_F over the point of parameter symmetry $\theta_F = \theta_B$. We start in Fig. A.3(a)-(b) by increasing θ_F , where at $\theta_F \approx 0.9$, we see the

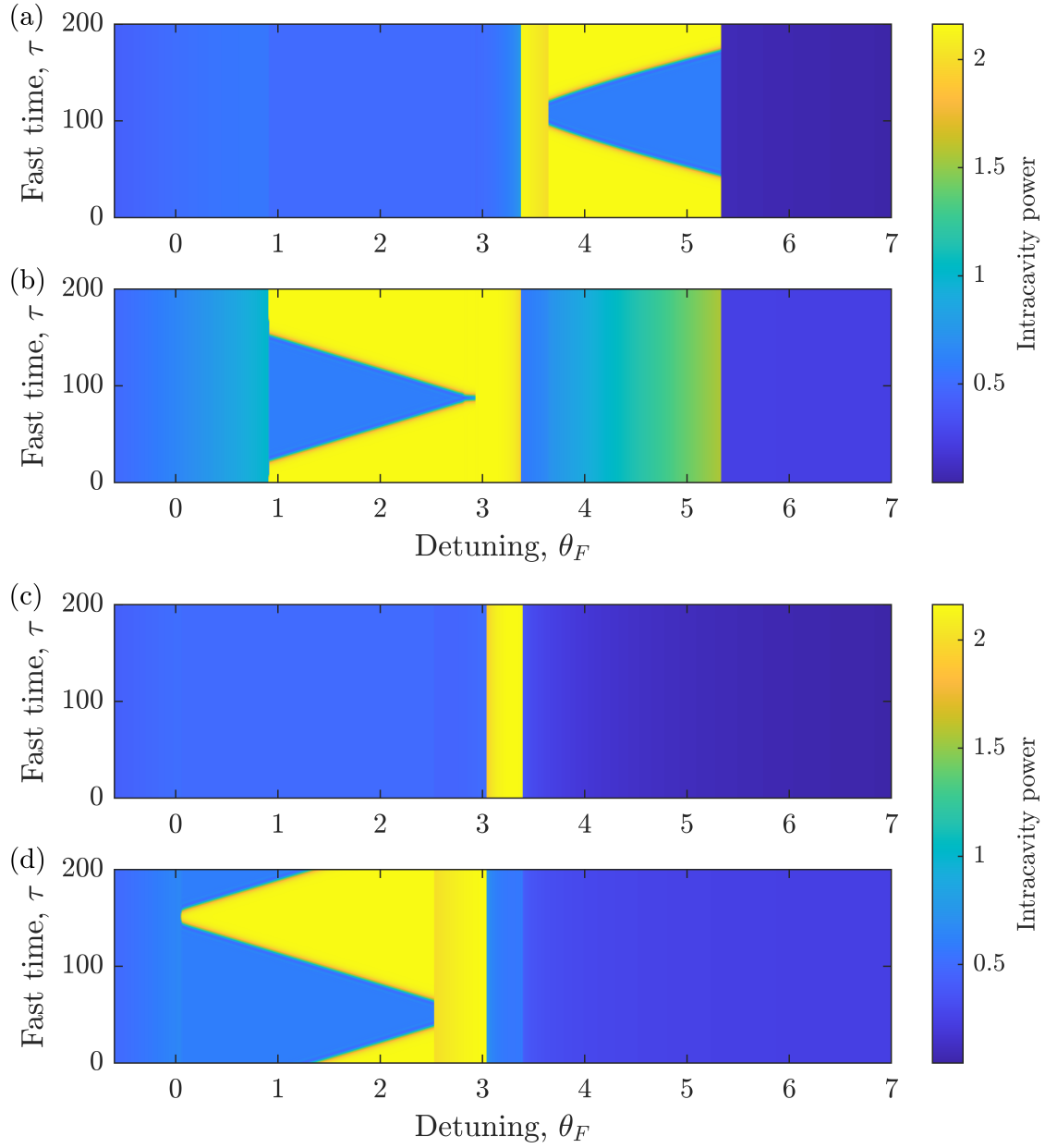


Figure A.3: Scans of the detuning, θ_F , for $S = 1.47, \theta_B = 3.2$. Forward (a) and backward (b) field intracavity power when gradually increasing θ_F over slow time. Switching front solutions arise spontaneously due to instability of the homogeneous solutions, where it can be seen that switching front solutions can be induced to switch propagation direction by increasing θ_F over the point of symmetry $\theta_F = \theta_B$. Forward (c) and backward (d) field intracavity power when gradually decreasing θ_F over slow time. No switching front solutions for $\theta_F > \theta_B$ due to bistability with a stable low power homogeneous stationary state.

spontaneous formation of a two switching front (SF) stationary state in the backward propagating field (b). This value of θ_F coincides with the beginning of a fast time instability of the homogeneous stationary state (HSS) as shown in Fig. A.1. As θ_F is increased, the separation of the SFs decreases linearly with θ_F , until the SFs collide and annihilate, resulting in symmetry broken HSSs. As θ_F moves over symmetry, the high and low power HSS suddenly switch fields due to a hysteresis of the HSS near symmetry, before entering another regime of fast time instability of the HSS at $\theta \approx 3.6$, as shown in Fig. A.1. This results in a two SF stationary solution in the forward propagating field. As θ_F is increased further, the separation of the SFs increases nonlinearly with θ_F , until the two SF solution becomes unstable to slow time oscillations of the plateaus at $\theta_F \approx 5.36$, as predicted by the eigenvalues shown in Fig. A.2. Fig. A.3(a) and (b) demonstrate a change in the direction of propagation of the frequency comb when scanning the detuning of one of the fields (θ_F in this case) over symmetry.

If we now reverse the direction of the scan, in Fig. A.3 (c)-(d), we remain on the low power HSS branch until we approach parameter symmetry. This reveals a large range of bistability between the low power HSS and the two SF stationary solutions. The field remains as symmetry broken HSS until $\theta_F \approx 2.55$. Here, we re-encounter the fast time instability of the HSS, which results in the formation of a two SF stationary state. As θ_F is decreased further, the SF separation increases linearly until the SFs collide and annihilate, and the system move towards the sole homogeneous stationary solution. Comparing (b) and (d), we see that the interval in which two SF stationary states occupy extends in both directions outside of the of fast time instability region. This results in a bistability of HSSs and two SF stationary states in the vicinity of the fast time instability.

A.5 Fast time dynamics of plateau solutions

Here we investigate the conditions required for the formation of exponentially localised stationary solutions of Eqs. (4.11) which approach plateau solutions (fixed points) as $\tau \rightarrow \pm\infty$. In particular, we wish to describe the heteroclinic cycles (two switching front stationary solutions) so prolific in the bidirectionally driven ring resonator. We assume the backwards field has flat profile such that Eqs. (4.11) can be written as

$$\partial_\tau U = \tilde{V}, \quad \partial_\tau V = \tilde{U}, \quad (\text{A.48})$$

$$\partial_\tau \tilde{U} = -(\theta_F - 2Y_B)U - V + UV^2 + U^3, \quad (\text{A.49})$$

$$\partial_\tau \tilde{V} = -(\theta_F - 2Y_B)V + U + VU^2 + V^3 - S, \quad (\text{A.50})$$

$$S^2 = Y_B^3 - 2(\theta_B - 2\langle U^2 + V^2 \rangle)Y_B^2 + [(\theta_B - 2\langle U^2 + V^2 \rangle)^2 + 1]Y_B. \quad (\text{A.51})$$

where the forward field presents the SF solutions with $F = U + iV$ and the backwards field is assumed homogeneous over the round trip with power Y_B . To study the stability of the plateaus in fast time, we introduce the linear perturbation $U = U_0 + \epsilon u, V = V_0 + \epsilon v$ to the fixed point U_0, V_0 . We continue with our previous assumption in which plateaus exist on desecrate intervals over the round trip and connected by step functions. To investigate the fast time stability of each plateau, we must appropriately evaluate the effect of the perturbation on the integral term. In what follows we assume that the

perturbation on the plateau has negligible effect on the average power of the full solution $\langle (U_0 + \epsilon u)^2 + (V_0 + \epsilon v)^2 \rangle = \langle U_0^2 + V_0^2 \rangle$. As a result, the perturbation does not effect the flat backward field. We find that this is a suitable assumption due to the robustness of the integral term to local inhomogeneity. Hence, the fast time stability of the plateaus can be understood by considering the Jacobian matrix

$$J = \begin{pmatrix} 0 & 0 & 1 & 0 \\ 0 & 0 & 0 & 1 \\ V^2 + 3U^2 - \theta + 2Y_B & -1 + 2UV & 0 & 0 \\ 1 + 2UV & U^2 + 3V^2 - \theta + 2Y_B & 0 & 0 \end{pmatrix}_{(U_0, V_0, Y_B)} \quad (\text{A.52})$$

where J is evaluated at a fixed point of Eqs. (5.28). This Jacobian provides eigenvalues of the form

$$\lambda = \pm \sqrt{(2Y_F - \theta_{\text{eff}}) \pm \sqrt{(Y_F^2 - 1)}}, \quad (\text{A.53})$$

where $Y_F = U_0^2 + V_0^2$ is the plateau power of the forward field and $\theta_{\text{eff}} = \theta - 2Y_B$ is the effective detuning of the forward field. This set of eigenvalues has identical form to those discussed in Chapter 4. As a result, the longitudinal stability of the plateaus is identical to the stability of the HSSs of the LLE. In numerical simulation, we find that the leading eigenvalue of (A.53) successfully predicts the approach of a SF solution to the high power and low power plateaus. In particular, eigenvalues (A.53) present a Hamiltonian Hopf bifurcation for $Y_F = 1$ ($\theta_{\text{eff}} > 2$). This predicts the decaying pattern which form on the approach to the low power plateau $Y_F < 1$ and a smooth exponential approach to the high power plateau $Y_F > 1$.

Appendix B

Linear Stability Analysis of the Fabry-Pérot Resonator

B.1 Linear stability analysis of homogeneous stationary states

Here, we perform linear stability analysis of the HSSs of the single field Fabry-Pérot model [48]. This is done to facilitate the discussion on the linear stability of the plateau solutions, performed in Section 5.5. We begin with the modal equations, which we rewrite here,

$$\begin{aligned} \partial_t f_\mu = & S\delta_{\mu,0} - (1 + i\theta_F)f_\mu + ik_\mu^2 f_\mu \\ & + i \sum_{\mu', \mu'', \mu'''} \delta_{\mu, \mu' + \mu'' - \mu'''} f_{\mu'} f_{\mu''} (f_{\mu'''})^* + 2if_\mu \sum_{\mu'} f_{\mu'} (f_{\mu'})^*, \end{aligned} \quad (\text{B.1})$$

for modal amplitude $f_\mu(t)$ with wavenumber $k_\mu = 2\pi\mu/\tau_R$, mode number μ and Kronecker delta $\delta_{\mu,0}$. These modal amplitudes are related to field envelope $\psi(\tau, t)$ via the modal expansion

$$\psi(\tau, t) = \sum_{\mu=-\infty}^{\infty} f_\mu(t) e^{ik_\mu \tau} \quad (\text{B.2})$$

defined over the cavity round trip $-\tau_R/2 \leq \tau \leq \tau_R/2$. Details of which can be found in the main text (Section 5.3).

We introduce a linear perturbation of the form,

$$f_{\mu,s} = \psi_s \delta_{\mu,0} + \delta f_\mu, \quad (\text{B.3})$$

about the HSS $\psi_s \delta_{\mu,0}$. When inserted into Eq. (B.1), we obtain linearised equations in terms of the perturbation δf_μ , with,

$$\begin{aligned} \partial_t \delta f_\mu = & -(1 + i\theta)\delta f_\mu + ik_\mu^2 \delta f_\mu \\ & + 4i|\psi_s|^2 \delta f_\mu + i\psi_s^2 (\delta f_{-\mu})^* + 2i\delta_{\mu,0} \{ |\psi_s|^2 \delta f_0 + (\delta f_0)^* \psi_s^2 \}. \end{aligned} \quad (\text{B.4})$$

We note that the self-phase Kerr modulation may be expanded as,

$$\begin{aligned}
 & \sum_{\mu', \mu'', \mu'''} i \delta_{\mu, \mu' + \mu'' - \mu'''} (f_{\mu'} f_{\mu''} (f_{\mu'''}^*) - f_{\mu', s} f_{\mu'', s} (f_{\mu''', s})^*) \\
 = & \sum_{\mu', \mu'', \mu'''} i \delta_{\mu, \mu' + \mu'' - \mu'''} \{ f_{\mu', s} f_{\mu'', s} (\delta f_{\mu'''}^*) + f_{\mu', s} \delta f_{\mu''} (f_{\mu''', s})^* + \delta f_{\mu'} f_{\mu'', s} (f_{\mu''', s})^* \} \\
 = & i \{ \sum_{\mu'''} \delta_{\mu, -\mu'''} \psi_s^2 (\delta f_{\mu'''}^*) + \sum_{\mu''} \delta_{\mu, \mu''} |\psi_s|^2 \delta f_{\mu''} + \sum_{\mu'} \delta_{\mu, \mu'} |\psi_s|^2 \delta f_{\mu'} \} \\
 = & i \{ (\psi_s)^2 (\delta f_{-\mu})^* + 2 |\psi_s|^2 \delta f_{\mu} \}, \tag{B.5}
 \end{aligned}$$

and similarly, the cross-phase Kerr modulation,

$$\begin{aligned}
 & 2i f_{\mu} \sum_{\mu'} f_{\mu'} (f_{\mu'})^* - 2i f_{\mu, s} \sum_{\mu'} f_{\mu', s} (f_{\mu', s})^* \\
 = & 2i f_{\mu, s} \sum_{\mu'} \{ (f_{\mu', s})^* \delta f_{\mu'} + (\delta f_{\mu'})^* f_{\mu', s} \} + 2i \delta f_{\mu} \sum_{\mu'} f_{\mu', s} (f_{\mu', s})^* \\
 = & 2i \psi_s \delta_{\mu, 0} \sum_{\mu'} \delta_{\mu', 0} \{ \psi_s^* \delta f_{\mu'} + (\delta f_{\mu'})^* \psi_s \} + 2i \delta f_{\mu} \sum_{\mu'} \delta_{\mu', 0} |\psi_s|^2 \\
 = & 2i \delta_{\mu, 0} \{ |\psi_s|^2 \delta f_0 + (\delta f_0)^* \psi_s^2 \} + 2i |\psi_s|^2 \delta f_{\mu}, \tag{B.6}
 \end{aligned}$$

where in particular, notice that only the cross-phase Kerr modulation contains terms proportional to the Kronecker delta. This is due to the fact that this term governs the interaction of counterpropagating components.

Without the loss of generality, we may assume the HSSs are real, such that, we write Eq. (B.4) in terms of real and imaginary parts,

$$\begin{pmatrix} \partial_t \text{Re}(\delta f_{\mu}) \\ \partial_t \text{Im}(\delta f_{\mu}) \end{pmatrix} = \begin{pmatrix} -1 & -A \\ B + 4\delta_{\mu, 0} \psi_s^2 & -1 \end{pmatrix} \begin{pmatrix} \text{Re}(\delta f_{\mu}) \\ \text{Im}(\delta f_{\mu}) \end{pmatrix}, \tag{B.7}$$

where $A = k_{\mu}^2 - \theta + 3\psi_s^2$ and $B = k_{\mu}^2 - \theta + 5\psi_s^2$. The characteristic polynomial of the Jacobian matrix of Eq. (B.7) is

$$\lambda^2 + 2\lambda + c_{\mu} = 0, \tag{B.8}$$

where

$$c_{\mu} = 1 + k_{\mu}^4 - 2(\theta - 4\psi_s^2)k_{\mu}^2 + \theta^2 + 15\psi_s^4 - 8\psi_s^2\theta - 4\delta_{\mu, 0}\psi_s^2(3\psi_s^2 - \theta). \tag{B.9}$$

This results in the eigenspectrum

$$\lambda(k_{\mu}) = -1 \pm \sqrt{1 - c_{\mu}}. \tag{B.10}$$

For $\mu = 0$, the eigenvalues are

$$\lambda = -1 \pm \sqrt{(\psi_s^2 - \theta)(\theta - 3\psi_s^2)} \tag{B.11}$$

and are mathematically identical to the eigenvalues of the Lugiato-Lefever equation. They

predict the typical stability of bistable HSSs, wherein solution which satisfy $\partial S^2/\partial H < 0$ are unstable. As a consequence, the middle HSS of the tilted Lorentzian resonance is unstable. In the case of $\mu \neq 0$, eigenvalues (B.10) become

$$\lambda = -1 \pm \sqrt{4\psi_s^2\theta_{\text{eff}} - 3\psi_s^4 - \theta_{\text{eff}}^2 + 2(\theta_{\text{eff}} - 2\psi_s^2)k_\mu^2 - k_\mu^4}. \quad (\text{B.12})$$

These eigenvalues were first derived in [48] and predict the onset of modulation instability at $H = 1$ ($\theta_{\text{eff}} > 2$), which is discussed in the main text in the context of plateaus and exponentially localised solutions (Section 5.5). Eq. (B.12) is written in terms of the effective detuning $\theta_{\text{eff}} = \theta - 2\psi_s^2$ for clearer comparison with the eigenvalues of Section 5.5. We note that the eigenvalues (B.10) may be obtained using an analogous perturbation to the envelope $\psi(\tau, t)$ of the form

$$\psi = \psi_s + \epsilon a e^{ik_\mu\tau + \Omega t} \quad (\text{B.13})$$

as seen in the main text, with wavenumber $k_\mu = 2\pi\mu/\tau_R$, growth/decay rate Ω and $\epsilon \ll 1$.

B.2 Linear stability analysis of plateau states connected by step functions

In Section 5.5, we discuss the growth/decay rate of Turing patterns on the plateau solutions, characterising the approach and exit of exponentially localised solutions to and from the plateau. Here, we present the derivation of the eigenspectrum 5.38 as presented in Section 5.5.

As motivated in Section 5.5, we consider with the coupled equations (5.35), which we rewrite here as

$$\partial_t \psi_{u,l} = S - (1 + i\theta)\psi_{u,l} + i(|\psi_{u,l}|^2 + 2[\Delta\langle|\psi_l|^2\rangle + (1 - \Delta)\langle|\psi_u|^2\rangle])\psi_{u,l} - i\partial_\tau^2 \psi_{u,l}. \quad (\text{B.14})$$

This equation describes the upper and lower plateaus, $\psi_u(\tau, t)$ and $\psi_l(\tau, t)$, occupying intervals over the round trip time τ_R of size $\tau_R(1 - \Delta)$ and $\tau_R\Delta$, respectively, and connected by step functions. The integral coupling terms are evaluated over their respective domains as

$$\langle|\psi_l|^2\rangle = \int_{-\tau_R/2}^{\tau_R(\Delta-1/2)} |\psi_l(\tau, t)|^2 d\tau, \quad \langle|\psi_u|^2\rangle = \int_{\tau_R(\Delta-1/2)}^{\tau_R/2} |\psi_u(\tau, t)|^2 d\tau. \quad (\text{B.15})$$

We introduce a perturbations

$$\psi_{u,l} = \psi_{u,l}^s + \epsilon_{u,l}(\tau, t) = \psi_{u,l}^s + \epsilon a_{u,l} e^{ik_{u,l}\tau + \Omega_{u,l}t} \quad (\text{B.16})$$

to each plateau respectively, where $k_{u,l}$ is the fast time wavenumber acting on the plateaus with growth/decay rate $\Omega_{u,l}$. The perturbation is assumed to be periodic over the plateau domain (with $k_u = 2\pi n_u/\tau_R(1 - \Delta)$ and $k_l = 2\pi n_l/\tau_R\Delta$), with mode numbers $n_{u,l}$ and $\epsilon \ll 1$. In this case, we consider perturbations that are sinusoidal ($k_{u,l} \neq 0$), such that the integral terms are evaluated as $\langle|\psi_{u,l}|^2\rangle = \langle|\psi_{u,l}^s|^2\rangle = |\psi_{u,l}^s|^2$. Inserting the perturbations

(B.16) into Eqs. (B.14) yields the linearised equations

$$\partial_t \epsilon_{u,l} = -(1 + i\theta_{\text{eff}} - ik_{u,l}^2)\epsilon_{u,l} + 2i|\psi_{u,l}^s|^2 \epsilon_{u,l} + i(\psi_{u,l}^s)^2 \epsilon_{u,l}^*, \quad (\text{B.17})$$

where we have defined the effective detuning $\theta_{\text{eff}} = \theta - 2\Delta|\psi_l^s|^2 - 2(1 - \Delta)|\psi_u^s|^2$. As the coupling between the two plateaus is parametrised by the phase insensitive real number Δ , we may assume that S may be adjusted such that the stationary plateaus $\psi_{u,l}^s$ are mutually real. The real and imaginary components of the perturbations become,

$$\begin{pmatrix} \partial_t \text{Re}(\epsilon_u) \\ \partial_t \text{Im}(\epsilon_u) \\ \partial_t \text{Re}(\epsilon_l) \\ \partial_t \text{Im}(\epsilon_l) \end{pmatrix} = \begin{pmatrix} -1 & -A_u & 0 & 0 \\ B_u & -1 & 0 & 0 \\ 0 & 0 & -1 & -A_l \\ 0 & 0 & B_l & -1 \end{pmatrix} \begin{pmatrix} \text{Re}(\epsilon_u) \\ \text{Im}(\epsilon_u) \\ \text{Re}(\epsilon_l) \\ \text{Im}(\epsilon_l) \end{pmatrix}, \quad (\text{B.18})$$

where

$$\begin{aligned} A_u &= k_u^2 - \theta_{\text{eff}} + (\psi_u^s)^2, & B_u &= k_u^2 - \theta_{\text{eff}} + 3(\psi_u^s)^2, \\ A_l &= k_l^2 - \theta_{\text{eff}} + (\psi_l^s)^2, & B_l &= k_l^2 - \theta_{\text{eff}} + 3(\psi_l^s)^2. \end{aligned}$$

This yields the characteristic equation

$$[(\Omega_u + 1)^2 + A_u B_u][(\Omega_l + 1)^2 + A_l B_l] = 0 \quad (\text{B.19})$$

with eigenspectrum

$$\Omega_{u,l} = 1 \pm \sqrt{-A_{u,l} B_{u,l}} \quad (\text{B.20})$$

as presented in its expanded form in Section 5.5 (Eq. 5.38).

Appendix C

Numerical Methods

In this appendix, we present the integration methods utilised to obtain the numerical results of this thesis. Simulations were performed using both explicit and implicit methods, where explicit integration methods allow for the calculation of the next time step from the current step, whereas, an implicit integration method has the next time step defined in terms of both the current and future time step. The generalised Lugiato-Lefever equations of (integro-partial differential equation form) found ubiquitously within this thesis were evaluated primarily through direction numerical integration via the Fourier split-step method (Appendix C.2). Although the standard Split-Step Fourier method is explicit for partial differential equation (such as the single field Lugiato-Lefever equation), in the presence of counterpropagating field components, this method is implicit in its calculation of the integral terms. As such, we also implement the explicit Crank-Nicolson method (Appendix C.3) to verify our results.

C.1 Constraints on simulation step sizes

Before we move onto the integration methods, we consider the constraint on the maximum step size applicable for both integration methods. To select an appropriate step size in the slow time and fast time we utilise the Nyquist-Shannon criterion for sampling signals. The Nyquist-Shannon sampling theorem states that a signal can be perfectly reconstructed from its samples if it is sampled at a rate at least twice its highest frequency component. Quantitatively, the Nyquist-Shannon criterion for the temporal step is

$$dt \leq \frac{1}{2f_{\max}}, \quad (\text{C.1})$$

for largest slow time frequency f_{\max} . The dominant contributions on this timescale are from the dispersion and Kerr nonlinearity. We must select f_{\max} to accommodate with the phenomenon we wish to simulate. In general, we may characterise the largest frequency through the dispersion time, with $f_{\max} \sim 1/t_{\text{disp}}$. The dispersion time $t_{\text{disp}} = \sqrt{L\beta_2}$ characterises the broadening of a pulse envelope in slow time as it travels the cavity length L due to chromatic dispersion, where β_2 is the group velocity dispersion.

Likewise to insure stability along the longitudinal coordinate, the grid spacing in fast

time must satisfy the Nyquist-Shannon criterion

$$d\tau \leq \frac{\pi}{\omega_{\max}}. \quad (\text{C.2})$$

Here, ω_{\max} correspond to the frequency of the cavity mode with largest mode number we wish to simulate.

C.2 Fourier split-step integration method for nonlocally coupled Lugiato-Lefever equations

The split-step Fourier method is commonly used for the numerical integration of nonlinear partial differential equations with periodic boundary conditions [167–169], such as the Lugiato-Lefever equation. Here, we adapt the split-step Fourier method for the integration of coupled integro-partial differential equations which describe counterpropagating fields $F(\tau, t), B(\tau, t)$ in a ring resonator (as discussed in Chapter 4), which we rewrite here as

$$\partial_t F = S_F - (1 + i\theta_F) + i(|F|^2 + \nu\langle|B|^2\rangle) - i\beta_2\partial_\tau^2 F \quad (\text{C.3})$$

$$\partial_t B = S_B - (1 + i\theta_B) + i(|B|^2 + \nu\langle|F|^2\rangle) - i\beta_2\partial_\tau^2 B, \quad (\text{C.4})$$

where θ_F, θ_B are the cavity detunings, S_F, S_B are the input field, ν is the coupling between fields (typically taking the value $\nu = 2$) and β_2 is the group velocity dispersion.

We begin by expressing the integro-partial differential equations in terms of linear and nonlinear operators,

$$\partial_t F = [\hat{\mathcal{L}}_F + \hat{\mathcal{N}}_F]F + S_F, \quad (\text{C.5})$$

$$\partial_t B = [\hat{\mathcal{L}}_B + \hat{\mathcal{N}}_B]B + S_B, \quad (\text{C.6})$$

where

$$\begin{aligned} \hat{\mathcal{L}}_F &= -(1 + i\theta_F) - i\beta_2\partial_\tau^2, & \hat{\mathcal{N}}_F &= i(|F|^2 + \nu\langle|B|^2\rangle), \\ \hat{\mathcal{L}}_B &= -(1 + i\theta_B) - i\beta_2\partial_\tau^2, & \hat{\mathcal{N}}_B &= i(|B|^2 + \nu\langle|F|^2\rangle). \end{aligned}$$

The formally exact solutions to (C.5) and (C.6) over the slow time step dt are

$$X(\tau, t + dt) = e^{dt(\hat{\mathcal{L}}_X + \hat{\mathcal{N}}_X)}X(\tau, t) + S_X \int_0^{dt} e^{(dt-s)(\hat{\mathcal{L}}_X + \hat{\mathcal{N}}_X)} ds. \quad (\text{C.7})$$

following from Duhamel’s principle, where X may represent either F, B and we have assumed $\hat{\mathcal{L}}_X$ and $\hat{\mathcal{N}}_X$ are slow time independent. The objective of the split-step method is to approximate the solution of Eqs. (C.5) and (C.6) by applying linear $\hat{\mathcal{L}}_{F,B}$ and nonlinear $\hat{\mathcal{N}}_{F,B}$ operators sequentially to advance the fields F, B in slow time. From Eq. (C.7), we see that this amounts to the assumption that we may resolve $\exp(dt[\hat{\mathcal{L}}_{F,B} + \hat{\mathcal{N}}_{F,B}])$ as the product of $\exp(dt\hat{\mathcal{L}}_{F,B})$ and $\exp(dt\hat{\mathcal{N}}_{F,B})$. As operators $\hat{\mathcal{L}}_{F,B}$ and $\hat{\mathcal{N}}_{F,B}$ do not commute, the exponent separation introduces an error associated with their commutativity, which may be quantified following from the Baker–Campbell–Hausdorff formula. Considering

first order contributions $\mathcal{O}(dt^2)$ over small slow time steps, the contribution of the commutator error is small and we may capture the leading-order dynamics of both operators as $\exp(dt[\hat{\mathcal{L}}_{F,B} + \hat{\mathcal{N}}_{F,B}]) \approx \exp(dt\hat{\mathcal{L}}_{F,B})\exp(dt\hat{\mathcal{N}}_{F,B})$, where further details may be found in [167, 168].

We introduce the discretisation of the slow time and fast time variables, with $F(\tau_j, idt) = F_j^i$, $B(\tau_j, idt) = B_j^i$. The field variables are period over the fast time interval $0 \leq \tau \leq \tau_R$ with round trip τ_R , which is now divided into N equal subintervals as

$$\tau_j = \tau_R \frac{j}{N}, \quad \text{for } j = 0, 1, 2, \dots, N-1, \quad (\text{C.8})$$

with the corresponding reciprocal space (Fourier space)

$$k_\mu = \begin{cases} \frac{2\pi}{\tau_R} \mu, & \text{for } 0 \leq \mu < N/2, \\ \frac{2\pi}{\tau_R} (\mu - N), & \text{for } N/2 \leq \mu < N. \end{cases} \quad (\text{C.9})$$

Linear component

We now begin the split-step integration by selecting the Linear component to advance forward in slow time. For the small slow time interval dt , the linear equations are

$$X_j^{i,(\hat{\mathcal{L}}_X)} = e^{dt\hat{\mathcal{L}}_X} X_j^i, \quad (\text{C.10})$$

where X_j^i may represent either F_j^i, B_j^i . These equation can be solve in the Fourier domain by defining the discrete Fourier transform

$$\mathcal{F}_\mu[X_j] = \hat{X}_\mu = \frac{1}{N} \sum_{j=0}^{N-1} X_j e^{-ik_\mu \tau_j} \quad (\text{C.11})$$

with the inverse discrete Fourier transform

$$\mathcal{F}_j^{-1}[\hat{X}_\mu] = X_j = \sum_{\mu=-N/2}^{N/2-1} \hat{X}_\mu e^{ik_\mu \tau_j}. \quad (\text{C.12})$$

where, in practice, these transforms can be performed via the fast Fourier transform (FFT) algorithm. Advancement of Eq. (C.10) in slow time becomes

$$X_j^{i,(\hat{\mathcal{L}}_X)} = \mathcal{F}_j^{-1} \left\{ \mathcal{F}_\mu \left[X_j^i e^{\hat{\mathcal{L}}_X dt} \right] \right\} \quad (\text{C.13})$$

$$= \mathcal{F}_j^{-1} \left\{ \hat{X}_\mu^i e^{-dt(1+i\theta_X - i\beta_2 k_\mu^2)} \right\}, \quad (\text{C.14})$$

where we have made use of the relationship $\mathcal{F}_\mu[\partial_t^2 X_j] = -k_\mu^2 \hat{X}_\mu$ during the evaluation of the linear operator.

Nonlinear component

We now evaluate the nonlinear component with respect to the solutions of the linear component $F_j^{i,(\hat{\mathcal{L}}_F)}, B_j^{i,(\hat{\mathcal{L}}_B)}$ by means of the 2nd order Runge-Kutta method [169]. Here, it is noted that the input fields $S_{F,B}$ are incorporated into the Runge-Kutta nonlinear step. Generally, the input field may be placed into either linear and nonlinear evaluations, but incorporating $S_{F,B}$ in $\hat{\mathcal{N}}_{F,B}$ offers computational simplicity. This is because the driving terms are constant in real space but non-diagonal in Fourier space (corresponding to the central comb line with $\mathcal{F}[S_{F,B}] = S_{F,B}\delta_{\mu,0}$) and therefore requires an additional convolution operation each integration time step, should it be incorporated into $\hat{\mathcal{L}}_{F,B}$. The integral of Eq. (C.7) may be approximated as $\int_0^{dt} \exp[(dt-s)(\hat{\mathcal{L}}_X + \hat{\mathcal{N}}_X)] S_X ds \approx dt S_X$, assuming dt is small, such that, we obtain an expression for the future time step as

$$F_j^{i+1} = F_j^{i,(\hat{\mathcal{L}}_F)} + k_j^{i,(F2)} + \mathcal{O}(dt^2), \quad (\text{C.15})$$

$$B_j^{i+1} = B_j^{i,(\hat{\mathcal{L}}_B)} + k_j^{i,(B2)} + \mathcal{O}(dt^2), \quad (\text{C.16})$$

with

$$k_j^{i,(F2)} = dt \left[S_F + i \left(\left| F_j^{i,(\hat{\mathcal{L}}_F)} + \frac{k_j^{i,(F1)}}{2} \right|^2 + \nu \left\langle \left| B_j^{i,(\hat{\mathcal{L}}_B)} + \frac{k_j^{i,(B1)}}{2} \right|^2 \right\rangle \right) \left(F_j^{i,(\hat{\mathcal{L}}_F)} + \frac{k_j^{i,(F1)}}{2} \right) \right], \quad (\text{C.17})$$

$$k_j^{i,(B2)} = dt \left[S_B + i \left(\left| B_j^{i,(\hat{\mathcal{L}}_B)} + \frac{k_j^{i,(B1)}}{2} \right|^2 + \nu \left\langle \left| F_j^{i,(\hat{\mathcal{L}}_F)} + \frac{k_j^{i,(F1)}}{2} \right|^2 \right\rangle \right) \left(B_j^{i,(\hat{\mathcal{L}}_B)} + \frac{k_j^{i,(B1)}}{2} \right) \right], \quad (\text{C.18})$$

where

$$k_j^{i,(F1)} = dt \left[S_F + i \left(\left| F_j^{i,(\hat{\mathcal{L}}_F)} \right|^2 + \nu \left\langle \left| B_j^{i,(\hat{\mathcal{L}}_B)} \right|^2 \right\rangle \right) \left(F_j^{i,(\hat{\mathcal{L}}_F)} \right) \right], \quad (\text{C.19})$$

$$k_j^{i,(B1)} = dt \left[S_B + i \left(\left| B_j^{i,(\hat{\mathcal{L}}_B)} \right|^2 + \nu \left\langle \left| F_j^{i,(\hat{\mathcal{L}}_F)} \right|^2 \right\rangle \right) \left(B_j^{i,(\hat{\mathcal{L}}_B)} \right) \right]. \quad (\text{C.20})$$

and the integral terms are evaluated as

$$\langle |X_j^i|^2 \rangle = \sum_{j=0}^{N-1} \frac{1}{N} |X_j^i|^2 - \frac{1}{2N} |X_0^i|^2 - \frac{1}{2N} |X_{N-1}^i|^2. \quad (\text{C.21})$$

Eqs. (C.15) and (C.16) form the recurrence relations which we use to simulate the counterpropagation of light in ring resonators.

To summarise this split-step Fourier method, we first advance the fields of initial condition F^i, B^i at time $t = idt$ according to the linear component [Eq. (C.14)] to obtain $F^{i,(\hat{\mathcal{L}}_F)}, B^{i,(\hat{\mathcal{L}}_B)}$. We then use $F^{i,(\hat{\mathcal{L}}_F)}, B^{i,(\hat{\mathcal{L}}_B)}$ as initial conditions for the nonlinear component, which is solved by Runge-Kutta methods [Eqs. (C.15) and (C.16)] to advance the fields to next step $t = (i+1)dt$.

Through a suitable redefinition of $k_j^{i,(F1)}$, $k_j^{i,(F2)}$, $k_j^{i,(B1)}$, $k_j^{i,(B2)}$, we use this method to simulate all generalised Lugiato-Lefever equations seen throughout this thesis.

C.3 Crank-Nicolson integration method for nonlocally coupled Lugiato-Lefever equations

The Crank-Nicolson method is a finite difference method first developed for numerical evaluation of partial differential equations of the heat-conduction type [170], for which it is unconditionally stable. Here we adapt this model for use in our models of Kerr resonators of ring and Fabry-Pérot geometries. We do so to verify the results of the Fourier split-step integration method of the previous section. Many of the models presented in this thesis are of integro-partial differential equation form. Integral terms are evaluated implicitly during the split-step integration. The Crank-Nicolson method allows us to evaluate the integral terms explicitly allowing us to verify the validity of our results obtained from split step simulation. Considering a system of general form

$$\partial_t u(\tau, t) = \Phi(\tau, t, u, \partial_\tau u, \partial_\tau^2 u), \quad (\text{C.22})$$

the Crank-Nicolson utilises a combination of the explicit forward Euler step and the implicit backwards Euler step in time t , given by

$$\frac{u_j^{i+1} - u_j^i}{dt} = \Phi_j^i(\tau, t, u, \partial_\tau u, \partial_\tau^2 u), \quad \text{forward Euler step}, \quad (\text{C.23})$$

$$\frac{u_j^{i+1} - u_j^i}{dt} = \Phi_j^{i+1}(\tau, t, u, \partial_\tau u, \partial_\tau^2 u), \quad \text{backward Euler step}, \quad (\text{C.24})$$

where we have introduced the discretisation $u(jd\tau, idt) = u_j^i$, and Φ_j^i evaluated in $jd\tau, idt, u_j^i$. Hence, the Crank-Nicolson method can be written as

$$\frac{u_j^{i+1} - u_j^i}{dt} = \frac{1}{2} [\Phi_j^i(\tau, t, u, \partial_\tau u, \partial_\tau^2 u) + \Phi_j^{i+1}(\tau, t, u, \partial_\tau u, \partial_\tau^2 u)]. \quad (\text{C.25})$$

This represents a second order integration method in time $\mathcal{O}(dt^2)$ and space $\mathcal{O}(d\tau^2)$.

Crank-Nicolson method for counterpropagating light in ring resonators

First we consider two counter propagating fields in a ring resonator, which evolve according to the nonlocally coupled LLE's which we restate here,

$$\partial_\tau F = S_F - (1 + i\theta_F)F + i(|F|^2 + \nu|B|^2)F - i\partial_\tau^2 F, \quad (\text{C.26})$$

$$\partial_\tau B = S_B - (1 + i\theta_B)B + i(|B|^2 + \nu|F|^2)B - i\partial_\tau^2 B. \quad (\text{C.27})$$

Focusing on the forward field equation (C.26), the Crank-Nicolson discretisation is

$$\frac{F_j^{i+1} - F_j^i}{dt} = -i \left[\frac{F_{j-1}^i - 2F_j^i + F_{j+1}^i}{2(d\tau)^2} + \frac{F_{j-1}^{i+1} - 2F_j^{i+1} + F_{j+1}^{i+1}}{2(d\tau)^2} \right] + f_j^i(F, B), \quad (\text{C.28})$$

with fast time step $\tau = jd\tau$ and slow time step $t = idt$, and

$$f_j^i(F, B) = S_F - (1 + i\theta_F)F_j^i + i(|F_j^i|^2 + \nu\langle |B_j^i|^2 \rangle)F_j^i. \quad (\text{C.29})$$

Although the Crank-Nicolson method is inherently implicit due to the backwards Euler step (C.24), we may rearrange the terms of Eq. (C.28) to produce an explicit relationship to evaluate F_j^{i+1} . Rearranging Eq. (C.28), we express the future time step ($i+1$) in terms of the current step time step (i), with

$$\begin{aligned} \frac{i}{2(d\tau)^2}F_{j-1}^{i+1} + \left[\frac{1}{dt} - \frac{i}{(d\tau)^2} \right] F_j^{i+1} + \frac{i}{2(d\tau)^2}F_{j+1}^{i+1} = \\ - \frac{i}{2(d\tau)^2}F_{j-1}^i + \left[\frac{1}{dt} - \frac{i}{(d\tau)^2} \right] F_j^i - \frac{i}{2(d\tau)^2}F_{j+1}^i + f_j^i(F, B). \end{aligned}$$

which may be expressed as the relations

$$aF_n^{i+1} + bF_1^{i+1} + aF_2^{i+1} = a^*F_n^i + b^*F_1^i + a^*F_2^i + f_1^i(F, B), \quad \text{for } j = 1, \quad (\text{C.30})$$

$$aF_{j-1}^{i+1} + bF_j^{i+1} + aF_{j+1}^{i+1} = a^*F_{j-1}^i + b^*F_j^i + a^*F_{j+1}^i + f_j^i(F, B), \quad \text{for } j = 2, \dots, n-1, \quad (\text{C.31})$$

$$aF_{n-1}^{i+1} + bF_n^{i+1} + aF_1^{i+1} = a^*F_{n-1}^i + b^*F_n^i + a^*F_1^i + f_n^i(F, B), \quad \text{for } j = n, \quad (\text{C.32})$$

where

$$a = -\frac{i}{2(d\tau)^2}, \quad b = \left[\frac{1}{dt} + \frac{i}{(d\tau)^2} \right]. \quad (\text{C.33})$$

This allows us to impose periodic boundary conditions, as can be seen in Eqs. (C.30) and (C.32). Writing Eqs. (C.30), (C.31), (C.32) in terms of matrices, we arrive at

$$AF^{i+1} = A^*F^i + f^i \quad (\text{C.34})$$

with

$$\begin{pmatrix} b & a & \cdots & \cdots & \cdots & a \\ a & b & a & & & \vdots \\ \vdots & a & b & a & & \vdots \\ \vdots & & \ddots & \ddots & \ddots & \vdots \\ \vdots & & & & & a \\ a & \cdots & \cdots & \cdots & a & b \end{pmatrix} \begin{pmatrix} F_1^{i+1} \\ F_2^{i+1} \\ F_3^{i+1} \\ \vdots \\ \vdots \\ F_n^{i+1} \end{pmatrix} = \begin{pmatrix} b^* & a^* & \cdots & \cdots & \cdots & a^* \\ a^* & b^* & a^* & & & \vdots \\ \vdots & a^* & b^* & a^* & & \vdots \\ \vdots & & \ddots & \ddots & \ddots & \vdots \\ \vdots & & & & & a^* \\ a^* & \cdots & \cdots & \cdots & a^* & b^* \end{pmatrix} \begin{pmatrix} F_1^i \\ F_2^i \\ F_3^i \\ \vdots \\ \vdots \\ F_n^i \end{pmatrix} + \begin{pmatrix} f_1^i \\ f_2^i \\ f_3^i \\ \vdots \\ \vdots \\ f_n^i \end{pmatrix}.$$

Hence, we obtain explicit relations for F^{i+1} and B^{i+1} ,

$$F^{i+1} = A^{-1}A^*F^i + A^{-1}f^i(F, B), \quad (\text{C.35})$$

$$B^{i+1} = A^{-1}A^*B^i + B^{-1}f^i(B, F), \quad (\text{C.36})$$

which we may solve numerically using matrix multiplication methods.

Crank-Nicolson method for Fabry-Pérot resonators

This integration method may be generalised to any of the system studied in this thesis through a suitable redefinition of f . For instance, a suitable recurrence relation for the fields of counter-rotating polarised components of the Fabry-Pérot presented in Chapter 6 is

$$\psi_{\pm}^{i+1} = A^{-1}A^*\psi_{\pm}^i + A^{-1}f_{\pm}^i(\psi_+, \psi_-), \quad (\text{C.37})$$

where

$$\begin{aligned} f_{\pm}^i(\psi_+, \psi_-) = & S - (1 + i\theta)\psi_{\pm}^i \quad (\text{C.38}) \\ & + i\frac{2}{3}\left(|\psi_{\pm}^i|^2\psi_{\pm}^i + 2|\psi_{\mp}^i|^2\psi_{\pm}^i + 2\langle|\psi_{\pm}^i|^2\rangle\psi_{\pm}^i + 2\langle|\psi_{\mp}^i|^2\rangle\psi_{\pm}^i + 2\langle\psi_{\pm}^i(\psi_{\mp}^i)^*\rangle\psi_{\mp}^i\right), \end{aligned}$$

and the matrix A is defined as before. Similarly, for the single field Fabry-Pérot of Chapter 5, we have

$$\psi^{i+1} = A^{-1}A^*\psi^i + A^{-1}f^i(\psi), \quad (\text{C.39})$$

where

$$f^i(\psi) = S - (1 + i\theta)\psi^i + i\left(|\psi^i|^2 + 2\langle|\psi^i|^2\rangle\right)\psi^i. \quad (\text{C.40})$$

Bibliography

- [1] J. Kerr, A new relation between electricity and light: Dielectrified media birefringent, *The London, Edinburgh, and Dublin Philosophical Magazine and Journal of Science*, **50**, 337–348, (1875).
- [2] J. Kerr, A new relation between electricity and light: Dielectrified media birefringent, (second paper), *The London, Edinburgh, and Dublin Philosophical Magazine and Journal of Science*, **50**, 446–458, (1875).
- [3] A. Pasquazi et al., Micro-combs: A novel generation of optical sources, *Phys. Rep.*, **729**, 1–81, (2018).
- [4] J. Pfeifle et al., Coherent terabit communications with microresonator Kerr frequency combs, *Nat. Photon.*, **8**, 375–380, (2014).
- [5] J. Pfeifle et al., Optimally coherent Kerr combs generated with crystalline whispering gallery mode resonators for ultrahigh capacity fiber communications, *Phys. Rev. Lett.*, **114**, 093902, (2015).
- [6] M.-G. Suh et al., Microresonator soliton dual-comb spectroscopy, *Sci.*, **354**, 600–603, (2016).
- [7] A. Dutt et al., On-chip dual-comb source for spectroscopy, *Sci. Adv.*, **4**, e1701858, (2018).
- [8] Christian Reimer et al., Generation of multiphoton entangled quantum states by means of integrated frequency combs, *Sci.*, **351**, 1176–1180, (2016).
- [9] M. Kues et al., Quantum optical microcombs, *Nat. Photon.*, **13**, 170–179, (2019).
- [10] J. L. Hall, Nobel Lecture: Defining and measuring optical frequencies, *Rev. Mod. Phys.*, **78**, 1279–1295, (2006).
- [11] P. Del’Haye et al., Optical frequency comb generation from a monolithic microresonator, *Nat.*, **450**, 1214–1217, (2007).
- [12] S. Coen and M. Erkintalo, Temporal cavity solitons in Kerr media, in *Nonlinear optical cavity dynamics: from microresonators to fiber lasers* edited by P. Grelu (John Wiley & Sons, New York, 2015), pp. 11–40.
- [13] G. L. Oppo and W. J. Firth, Theory and application of cavity solitons in photonic devices, *Phil. Trans. R. Soc. A*, **382**, 20230336, (2024).

- [14] T. J. Kippenberg, R. Holzwarth, and S. A. Diddams, Microresonator-based optical frequency combs, *Sci.*, **332**, 555–559, (2011).
- [15] A. J. Scroggie et al., Pattern formation in a passive Kerr cavity, *Chaos, Solitons & Fractals*, **4**, 1323–1354, (1994).
- [16] W. J. Firth and A. J. Scroggie, Optical bullet holes: robust controllable localized states of a nonlinear cavity, *Phys. Rev. Lett.*, **76**, 1623, (1996).
- [17] F. Leo et al., Temporal cavity solitons in one-dimensional Kerr media as bits in an all-optical buffer, *Nat. Photon.*, **4**, 471–476, (2010).
- [18] T. Herr et al., Temporal solitons in optical microresonators, *Nat. Photon.*, **8**, 145–152, (2014).
- [19] B. Garbin et al., Experimental and numerical investigations of switching wave dynamics in a normally dispersive fibre ring resonator, *The European Physical Journal D*, **71**, 1-8, (2017).
- [20] X. Xue, et al., Mode-locked dark pulse Kerr combs in normal-dispersion microresonators, *Nat. Photon.*, **9**, 594-600, (2015).
- [21] X. Xue et al., Microresonator Kerr frequency combs with high conversion efficiency, *Laser & Photon. Rev.*, **11**, 1600276, (2017).
- [22] X. Xue et al., Normal-dispersion microcombs enabled by controllable mode interactions, *Laser & Photon. Rev.*, **9**, L23-L28, (2015).
- [23] E. Nazemosadat et al., Switching dynamics of dark-pulse Kerr frequency comb states in optical microresonators, *Phys. Rev. A*, **103**, 013513, (2021).
- [24] L. A. Lugiato and R. Lefever, Spatial dissipative structures in passive optical systems, *Phys. Rev. Lett.*, **58**, 2209, (1987).
- [25] S. A. Akhmanov et al., Self-focusing and diffraction of light in a nonlinear medium, *Sov. Phys.*, **10**, 609, (1968).
- [26] M. Haelterman et al., Dissipative modulation instability in a nonlinear dispersive ring cavity, *Opt. Commun.*, **91**, 401–407, (1992).
- [27] L. A. Lugiato et al., From the Lugiato-Lefever equation to microresonator-based soliton Kerr frequency combs, *Phil. Trans. R. Soc. A.*, **376**, 20180113, (2018).
- [28] F. Castelli et al., The LLE, pattern formation and a novel coherent source, *The European Physical Journal D*, **71**, 1–16, (2017).
- [29] T. Wildi et al., Dissipative Kerr solitons in integrated Fabry–Pérot microresonators, *Optica*, **10**, 650–656, (2023).
- [30] J. Heebner, G. Rohit and T. A. Ibrahim, *Optical Microresonators: Theory, Fabrication, and Applications* edited by A. W. T. Rhodes (Springer, London, 2008).

- [31] I. Chremmos, O. Schwelb and N. Uzunoglu, *Photonic microresonator research and applications* edited by A. W. T. Rhodes (Springer, London, 2010).
- [32] G. P. Agrawal, *Nonlinear fiber optics*, (Springer, London, 2013).
- [33] L. Lugiato, F. Prati and M. Brambilla, *Nonlinear optical systems*, (Cambridge University Press, Cambridge, 2015).
- [34] A. Ghatak and K. Thyagarajan, *An Introduction to Fiber Optics*, (Cambridge University Press, Cambridge, 1998).
- [35] P. Parra-Rivas et al., Dark solitons in the Lugiato-Lefever equation with normal dispersion, *Phys. Rev. A*, **93**, 063839, (2016).
- [36] J. B. Geddes et al., Polarisation patterns in a nonlinear cavity, *Opt. Commun.*, **111**, 623, (1994).
- [37] D. N. Christodoulides and R. I. Joseph, Vector solitons in birefringent nonlinear dispersive media, *Opt. Lett.*, **13**, 53–55, (1988).
- [38] L. Hill, et al., Effects of self-and cross-phase modulation on the spontaneous symmetry breaking of light in ring resonators, *Phys. Rev. A*, **101**, 013823, (2020).
- [39] G. N. Campbell, et al., Frequency comb enhancement via the self-crystallization of vectorial cavity solitons, *Opt. Express*, **32**, 37691-37702, (2024).
- [40] D. C. Cole et al., Soliton crystals in Kerr resonators, *Nat. Photon.*, **11**, 671–676, (2017).
- [41] W. Wang et al., Robust soliton crystals in a thermally controlled microresonator, *Opt. Lett.*, **43**, 2002–2005, (2018).
- [42] M. Karpov et al., Dynamics of soliton crystals in optical microresonators, *Nat. Phys.*, **15**, 1071–1077, (2019).
- [43] G. Lin and T. Sun, Mode crossing induced soliton frequency comb generation in high-Q yttria-stabilized zirconia crystalline optical microresonators, *Photon. Res.*, **10**, 731–739, (2022).
- [44] L. Zhizhou et al., Synthesized soliton crystals, *Nat. Commun.*, **12**, 3179, (2021).
- [45] N. M. Kondratiev and V. E. Lobanov, Modulational instability and frequency combs in whispering-gallery-mode microresonators with backscattering, *Phys. Rev. A*, **101**, 013816, (2020).
- [46] D. V. Skryabin. Hierarchy of coupled mode and envelope models for bi-directional microresonators with Kerr nonlinearity. *OSA Continuum*, **3**:1364-1375, (2020).
- [47] W. J. Firth, L. Columbo and A. J. Scroggie, Proposed resolution of theory-experiment discrepancy in homoclinic snaking, *Phys. Rev. Lett.*, **99**, 104503, (2007).

- [48] D. C. Cole et al., Theory of Kerr frequency combs in Fabry-Pérot resonators, *Phys. Rev. A*, **98**, 013831, (2018).
- [49] L. Hill et al., Symmetry broken vectorial kerr frequency combs from Fabry-Pérot resonators, *Commun. Phys.*, **7**, 82, (2024).
- [50] T. Bunel et al., 28 THz soliton frequency comb in a continuous-wave pumped fiber Fabry-Pérot resonator, *APL Photon.*, **9**, 010804, (2024).
- [51] T. Bunel et al., Observation of modulation instability Kerr frequency combs in a fiber Fabry-Pérot resonator, *Opt. Lett.*, **48**, 275–278, (2023).
- [52] T. Bunel et al., Broadband Kerr frequency comb in fiber Fabry-Pérot resonators induced by switching waves, *Phys. Rev. A*, **109**, 063521, (2024).
- [53] E. Obrzud, S. Lecomte, and T. Herr, Temporal solitons in microresonators driven by optical pulses, *Nat. Photon.*, **11**, 600–607, (2017).
- [54] P. Parra-Rivas et al., Origin and stability of dark pulse Kerr combs in normal dispersion resonators, *Opt. Lett.*, **41**, 2402–2405, (2016).
- [55] S. Pitois, G. Millot, and S. Wabnitz, Nonlinear polarization dynamics of counter-propagating waves in an isotropic optical fiber: theory and experiments, *JOSA B*, **18**, 432–443, (2001).
- [56] G. N. Campbell et al., Dark solitons in Fabry-Pérot resonators with Kerr media and normal dispersion, *Phys. Rev. A*, **108**, 033505, (2023).
- [57] Lord Rayleigh, The problem of the whispering gallery, *The London, Edinburgh, and Dublin Philosophical Magazine and Journal of Science*, **20**, 1001–1004, (1910).
- [58] D. G. Rabus, C. Sada, *Integrated ring resonators* edited by W. T. Rhodes (Springer, London, 2007).
- [59] V. Ilchenko, A. Matsko, Optical resonators with whispering-gallery modes - Part II: Applications, *IEEE J. Sel. Top. Quantum Electron.*, **12**, 15–32, (2006).
- [60] A. N. Oraevsky, Whispering-gallery waves, *Quantum electronics*, **32**, 377, (2002).
- [61] J. Sarma and K. A. Shore, Electromagnetic theory for optical disc resonators, *IEE Proceedings J (Optoelectronics)*, **132**, 325–330, (1985).
- [62] T. Hansson, D. Modotto and S. Wabnitz, Analytical approach to the design of microring resonators for nonlinear four-wave mixing applications, *Journal of the Optical Society of America B*, **31**, 1109–1117, (2014).
- [63] B. Min, L. Yang and K. Vahala Perturbative analytic theory of an ultrahigh-Q toroidal microcavity, *Phys. Rev. A*, **76**, 013823, (2007).
- [64] G. B. Arfken, H. J. Weber and F. E. Harris, *Mathematical methods for physicists: a comprehensive guide*, seventh edition, (Elsevier, London, 2011), pp. 643–713.

- [65] M. Oxborrow, Traceable 2-D finite-element simulation of the whispering-gallery modes of axisymmetric electromagnetic resonators, *IEEE Transactions on Microwave Theory and Techniques*, **55**, 1209-1218, (2007).
- [66] B. Garbin et al., Asymmetric balance in symmetry breaking, *Phys. Rev. Res.*, **2**, 023244, (2020).
- [67] G. Xu et al., Spontaneous symmetry breaking of dissipative optical solitons in a two-component Kerr resonator, *Nat. Commun.*, **12**, 4023, (2021).
- [68] N. Moroney et al., A Kerr polarization controller, *Nat. Commun.* **13**, 398, (2022).
- [69] A. B. Matsko, Whispering-gallery-mode resonators as frequency references. I. Fundamental limitations, *J. Opt. Soc. Am. B*, **24**, 1324-1335, (2007).
- [70] N. M. Kondratiev, M. L. Gorodetsky, Thermorefractive noise in whispering gallery mode microresonators: Analytical results and numerical simulation, *Phys. Lett. A*, **382**, 2265-2268, (2018).
- [71] J. Warren et al., Hertz-linewidth semiconductor lasers using CMOS-ready ultra-high-Q microresonators, *Nat. Photon.*, **15**, 346–353, (2021).
- [72] L. Grigory et al., Platicon microcomb generation using laser self-injection locking, *Nat. Commun.*, **13**, 1771, (2022).
- [73] H. Wang, et al., Self-regulating soliton switching waves in microresonators, *Phys. Rev. A*, **106**, 053508, (2022).
- [74] S.-P. Yu et al., A continuum of bright and dark-pulse states in a photonic-crystal resonator, *Nat. Commun.*, **13**, 3134, (2022).
- [75] A. Ø. Svela et al., Coherent suppression of backscattering in optical microresonators, *Light Sci. Appl.*, **13**, 204, (2020).
- [76] M. Cai, O. Painter and K. J. Vahala, Observation of critical coupling in a fiber taper to a silica-microsphere whispering-gallery mode system, *Phys. Rev. Lett.*, **85**, 74, (2000).
- [77] K. Ikeda, Multiple-valued stationary state and its instability of the transmitted light by a ring cavity system, *Opt. Commun.*, **30**, 257-261, (1979).
- [78] T. Tobias et la., Universal formation dynamics and noise of Kerr-frequency combs in microresonators, *Nat. Photon.*, **6**, 480–487, (2012).
- [79] C. Godey et al., Stability analysis of the spatiotemporal Lugiato-Lefever model for Kerr optical frequency combs in the anomalous and normal dispersion regimes, *Phys. Rev. A*, **89**, 063814, (2014).
- [80] D. Gomila, A. J. Scroggie, and W. J. Firth, Bifurcation structure of dissipative solitons, *Physica D: Nonlinear Phenomena*, **227**, 70–77, (2007).

- [81] J. Burke A. Yochelis, and E. Knobloch, Classification of spatially localized oscillations in periodically forced dissipative systems, *SIAM Journal on Applied Dynamical Systems*, **7**, 651–711, (2008).
- [82] M. Haragus and G. Iooss, Local bifurcations, center manifolds, and normal forms in infinite-dimensional dynamical systems, (Springer, 2011).
- [83] A. R. Champneys, Homoclinic orbits in reversible systems and their applications in mechanics, fluids and optics, *Physica D: Nonlinear Phenomena*, **112**, 158–186, (1998).
- [84] P. Colet et al., Formation of localized structures in bistable systems through nonlocal spatial coupling. I. General framework, *Phys. Rev. E*, **89**, 012914, (2014).
- [85] G. Iooss and M.-C. Pérouème, Perturbed homoclinic solutions in reversible 1: 1 resonance vector fields, *Journal of differential equations*, **102**, 62–88, (1993).
- [86] G. Xu et al., Breathing dynamics of symmetry-broken temporal cavity solitons in Kerr ring resonators, *Opt. Lett.*, **47**, 1486–1489, (2022).
- [87] L. Quinn et al., Random number generation using spontaneous symmetry breaking in a Kerr resonator, *Opt. Lett.*, **48**, 3741–3744, (2023).
- [88] S. Coen et al., Nonlinear topological symmetry protection in a dissipative system, *Nat. Commun.*, **15**, 1398, (2024).
- [89] L. Quinn et al., Towards a novel coherent Ising machine using symmetry breaking in a Kerr resonator, In *AI and Optical Data Sciences IV*, page PC1243806. SPIE, (2023).
- [90] J. Fatome et al., Observation of polarization Faticons in a fibre Kerr resonator, in *Conference on Lasers and Electro-Optics/Europe (CLEO/Europe 2023) and European Quantum Electronics Conference (EQEC 2023)*, paper pd.2_7, (2023).
- [91] T. Huang et al., Coexistence of nonlinear states with different polarizations in a Kerr resonator, *Phys. Rev. A*, **109**, 013503, (2024).
- [92] A. E. Kaplan and P. Meystre, Enhancement of the sagnac effect due to nonlinearly induced nonreciprocity, *Opt. Lett.*, **6**, 590–592, (1981).
- [93] A.E. Kaplan and P. Meystre, Directionally asymmetrical bistability in a symmetrically pumped nonlinear ring interferometer, *Opt. Commun.*, **40**, 229–232, (1982).
- [94] E. M. Wright et al., Theory of the nonlinear sagnac effect in a fiber-optic gyroscope, *Phys. Rev. A*, **32**, 2857, (1985).
- [95] L. Del Bino et al., Symmetry breaking of counter-propagating light in a nonlinear resonator, *Sci. Rep.*, **7**, 43142, (2017).

- [96] M. T. M. Woodley et al., Universal symmetry-breaking dynamics for the Kerr interaction of counterpropagating light in dielectric ring resonators, *Phys. Rev. A*, **98**, 053863, (2018).
- [97] M. T. M. Woodley et al., Self-switching Kerr oscillations of counterpropagating light in microresonators, *Phys. Rev. Lett.*, **126**, 043901, (2021).
- [98] A. V. Andrianov and E. A. Anashkina, Bidirectional Raman soliton-like combs with unidirectional pump in a spherical microresonator, *Opt. Lett.*, **49**, 2301–2304, (2024).
- [99] M. Zhang et al., Strong interactions between solitons and background light in Brillouin-Kerr microcombs, *Nat. Commun.*, **15**, 1661, (2024).
- [100] C. Cui, L. Zhang, and L. Fan, Control spontaneous symmetry breaking of photonic chirality with reconfigurable anomalous nonlinearity, *preprint arXiv:2208.04866*, (2022).
- [101] R. D. D. Bitha et al., Bifurcation analysis of complex switching oscillations in a Kerr microring resonator, *Phys. Rev. E*, **108**, 064204, (2023).
- [102] A. Ghosh et al., Phase Symmetry Breaking of Counterpropagating Light in Microresonators for Switches and Logic Gates, *preprint arXiv:2407.16625*, (2024).
- [103] G. N. Campbell et al., Dark Temporal Cavity Soliton Pairs in Fabry-Pérot Resonators with Normal Dispersion and Orthogonal Polarizations, *CLEO/Europe and EQEC*, paper ef_p.3, (2023).
- [104] L. Hill, G.-L. Oppo, and P. Del’Haye, Multi-stage spontaneous symmetry breaking of light in Kerr ring resonators, *Commun. Phys.*, **6**, 208, (2023).
- [105] Y. Rah, and K. Yu, Demonstration of spontaneous symmetry breaking in self-modulated ring resonators, *Phys. Rev. Res.*, **6**, 013234, (2024)
- [106] A. Ghosh et al., Four-field symmetry breakings in twin-resonator photonic isomers, *Phys. Rev. Res.*, **5**, L042012, (2023).
- [107] K. W. Cheah et al., Spontaneous symmetry breaking of non-Hermitian coupled nano-cavities, *Research Square preprint*, (2023).
- [108] A. Ghosh et al., Controlled light distribution with coupled microresonator chains via Kerr symmetry breaking, *Photon. Res.*, **12**, 2376-2389, (2024).
- [109] A. Pal et al., Linear and nonlinear coupling of twin-resonators with Kerr nonlinearity, *preprint arXiv:2404.05646*, (2024).
- [110] L. Massai et al., Pure circularly polarized light emission from waveguide microring resonators, *preprint Appl. Phys. Lett.*, **121**, (2022).
- [111] W. Wang et al., Self-locked orthogonal polarized dual comb in a microresonator, *Photon. Res.*, **6**, 363–367, (2018).

- [112] C. Bao et al., Orthogonally polarized frequency comb generation from a Kerr comb via cross-phase modulation, *Opt. Lett.*, **44**, 1472–1475, (2019).
- [113] Z. Wu et al., Coexistence of multiple microcombs in monochromatically pumped Si₃N₄ microresonators, *Opt. Lett.*, **47**, 1190–1193, (2022).
- [114] T. Hansson, M. Bernard, and S. Wabnitz, Modulational instability of nonlinear polarization mode coupling in microresonators, *JOSA B*, **35**, 835–841, (2018).
- [115] R. Suzuki, et al., Theoretical study on dual-comb generation and soliton trapping in a single microresonator with orthogonally polarized dual pumping, *IEEE Photonics Journal*, **11**, 1–11, (2018).
- [116] M. Haelterman, S. Trillo, and S. Wabnitz, Polarization multistability and instability in a nonlinear dispersive ring cavity, *JOSA B*, **11**, 446–456, (1994).
- [117] G. N. Campbell et al., Counterpropagating light in ring resonators: Switching fronts, plateaus, and oscillations, *Phys. Rev. A*, **106**, 043507, (2022).
- [118] A. M. Turing, The chemical basis of morphogenesis, *Phil. Trans. R. Soc. Lond. B*, **237**, 37–72, (1952).
- [119] N. N. Rosanov and G. V. Khodova., Diffractive autosolitons in nonlinear interferometers, *JOSA B*, **7**, 1057–1065, (1990).
- [120] G.-L. Oppo, A. J. Scroggie, and W. J. Firth, From domain walls to localized structures in degenerate optical parametric oscillators, *Journal of Optics B: Quantum and Semiclassical Optics*, **1**, 133, (1999).
- [121] G.-L. Oppo, A. J. Scroggie, and W. J. Firth, Characterization, dynamics and stabilization of diffractive domain walls and dark ring cavity solitons in parametric oscillators, *Phys. Rev. E* **63**, 066209, (2001).
- [122] S. Fujii and T. Tanabe. Dispersion engineering and measurement of whispering gallery mode microresonator for Kerr frequency comb generation, *Nanophotonics*, **9**, 1087–1104, (2020).
- [123] J. Federici and L. Moeller. Review of terahertz and subterahertz wireless communications, *Journal of Appl. Phys.*, **107**, (2010).
- [124] J. Riemensberger et al., Massively parallel coherent laser ranging using a soliton microcomb, *Nat.*, **581**, 164–170, (2020).
- [125] X. Xu et al., Advanced rf and microwave functions based on an integrated optical frequency comb source, *Opt. Express*, **26**, 2569–2583, (2018).
- [126] J. Hu et al., Reconfigurable radiofrequency filters based on versatile soliton microcombs, *Nat. Commun.*, **11**, 4377, (2020).

- [127] V. V. Afanasjev, E. M. Dianov, and V. N. Serkin, Nonlinear pairing of short bright and dark soliton pulses by phase cross modulation, *IEEE journal of quantum electronics*, **25**, 2656–2664, (1989).
- [128] S. Trillo, et al., Optical solitary waves induced by cross-phase modulation, *Opt. Lett.*, **13**, 871–873, (1988).
- [129] M. Lisak, A. Höök, and D. Anderson, Symbiotic solitary-wave pairs sustained by cross-phase modulation in optical fibers, *JOSA B*, **7**, 810–814, (1990).
- [130] A. V. Buryak, Y. S. Kivshar, and D. F. Parker, Coupling between dark and bright solitons, *Phys. Lett. A*, **215**, 57–62, (1996).
- [131] V. V. Afanasyev, et al., Dynamics of coupled dark and bright optical solitons, *Opt. Lett.*, **14**, 805–807, (1989).
- [132] Y. S. Kivshar, et al., Symbiotic optical solitons and modulational instability, *Physica Scripta*, **44**, 195, (1991).
- [133] V. V. Afanas'ev, et al., Nonlinear pairing of light and dark optical solitons, *JETP Lett.*, **48**, 638–642, (1988).
- [134] D. N. Christodoulides, Black and white vector solitons in weakly birefringent optical fibers, *Phys. Lett. A*, **132**, 451–452, (1988).
- [135] X. Hu et al., Observation of incoherently coupled dark-bright vector solitons in single-mode fibers, *Opt. Express*, **27**, 18311–18317, (2019).
- [136] C. Becker et al., Oscillations and interactions of dark and dark–bright solitons in Bose–Einstein condensates, *Nat. Phys.*, **4**, 496–501, (2008).
- [137] C. Hamner et al., Generation of dark-bright soliton trains in superfluid–superfluid counterflow, *Phys. Rev. Lett.*, **106**, 065302, (2011).
- [138] Th. Busch, and J. R. Anglin, Dark-bright solitons in inhomogeneous Bose-Einstein condensates, *Phys. Rev. Lett.*, **87**, 010401, (2001).
- [139] S. Zhang et al., Spectral extension and synchronization of microcombs in a single microresonator, *Nat. Commun.*, **11**, 6384, (2020).
- [140] S. Zhang et al., Dark-bright soliton bound states in a microresonator, *Phys. Rev. Lett.*, **128**, 033901, (2022).
- [141] D. V. Strekalov, and N. Yu, Generation of optical combs in a whispering gallery mode resonator from a bichromatic pump, *Phys. Rev. A*, **79**, 041805, (2009).
- [142] T. Hansson, and S. Wabnitz, Bichromatically pumped microresonator frequency combs, *Phys. Rev. A*, **90**, 013811, (2014).
- [143] H. Taheri, A. B. Matsko, and L. Maleki, Optical lattice trap for Kerr solitons, *The European Physical Journal D*, **71**, 1–13, (2017).

- [144] C. Bao et al., Dual-pump generation of high-coherence primary Kerr combs with multiple sub-lines, *Opt. Lett.*, **42**, 595–598, (2017).
- [145] W. Wang et al., Dual-pump Kerr micro-cavity optical frequency comb with varying FSR spacing, *Sci. Rep.*, **6**, 28501, (2016).
- [146] R. J. Weiblen, and I. Vurgaftman, Bichromatic pumping in mid-infrared microresonator frequency combs with higher-order dispersion, *Opt. Express*, **27**, 4238–4260, (2019).
- [147] I. Coddington, N. Newbury, and W. Swann, Dual-comb spectroscopy, *Optica*, **3**, 414–426, (2016).
- [148] D. Turaev, A. G. Vladimirov, and S. Zelik, Long-range interaction and synchronization of oscillating dissipative solitons, *Phys. Rev. Lett.*, **108**, 263906, (2012).
- [149] Z. Fan and D. V. Skryabin, Soliton blockade in bidirectional microresonators, *Opt. Lett.*, **45**, 6446–6449, (2020).
- [150] P. C Fife and J. B. McLeod, The approach of solutions of nonlinear diffusion equations to travelling front solutions, *Archive for Rational Mechanics and Analysis*, **65**, 335–361, (1977).
- [151] N. N. Rosanov, *Spatial hysteresis and optical patterns*, Springer Science & Business Media, (2002).
- [152] P Couillet, J Lega, B Houchmandzadeh, and J Lajzerowicz, Breaking chirality in nonequilibrium systems, *Phys. Rev. Lett.*, **65**, 1352, (1990).
- [153] M. Gilles et al., Polarization domain walls in optical fibres as topological bits for data transmission, *Nat. photon.*, **11**, 102–107, (2017).
- [154] B. Garbin et al., Dissipative polarization domain walls in a passive coherently driven Kerr resonator, *Phys. Rev. Lett.*, **126**, 023904, (2021).
- [155] L. Del Bino et al., Microresonator isolators and circulators based on the intrinsic nonreciprocity of the Kerr effect, *Optica*, **5**, 279–282, (2018).
- [156] L. Del Bino, N. Moroney, and P. Del’Haye, Optical memories and switching dynamics of counterpropagating light states in microresonators, *Opt. Express*, **29**, 2193–2203, (2021).
- [157] F. Copie et al., Interplay of polarization and time-reversal symmetry breaking in synchronously pumped ring resonators, *Phys. Rev. Lett.*, **122**, 013905, (2019).
- [158] C. Schelte et al., Tunable Kerr frequency combs and temporal localized states in time-delayed Gires–Tournois interferometers, *Opt. Lett.*, **44**, 4925–4928, (2019).
- [159] E. R. Koch et al., Square-wave generation in vertical external-cavity Kerr-Gires–Tournois interferometers, *Opt. Lett.*, **47**, 4343–4346, (2022).

- [160] K. Y. Yang et al., Broadband dispersion-engineered microresonator on a chip, *Nat. Photon.*, **10**, 316–320, (2016).
- [161] C. Fabry and A. Pérot, A Multipass Interferometer, *Annales de Chimie et de Physique*, **16**, 115, (1899).
- [162] N. Ismail et al., Fabry-Pérot resonator: spectral line shapes, generic and related Airy distributions, linewidths, finesses, and performance at low or frequency-dependent reflectivity, *Opt. Express*, **24**, 16366–16389, (2016).
- [163] M. R. Islam et al., Chronology of Fabry-Pérot interferometer fiber-optic sensors and their applications: a review, *Sensors*, **14**, 7451–7488, (2014).
- [164] M. Marconi et al., How lasing localized structures evolve out of passive mode locking, *Phys. Rev. Lett.*, **112**, 223901, (2014).
- [165] W. J. Firth et al., Analytic instability thresholds in folded Kerr resonators of arbitrary finesse, *Phys. Rev. A*, **103**, 023510, (2021).
- [166] E. Knobloch, Spatial localization in dissipative systems, *conmatphys*, **6**, 325–359, (2015).
- [167] P. Suarez, and P. U. Su, An introduction to the split step Fourier method using MATLAB, *ResearchGate*, (2016).
- [168] G. M. Muslu, and H. A. Erbay, A split-step Fourier method for the complex modified Korteweg-de Vries equation, *Computers & Mathematics with Applications*, **45**, 503–514, (2003).
- [169] J. M. Sanz-Serna, and M. P. Calvo, *Numerical hamiltonian problems*, (Dover Publications, New York, 2018)
- [170] J. Crank, and P. Nicolson, A practical method for numerical evaluation of solutions of partial differential equations of the heat-conduction type, *Cambridge University Press*, **43**, 50–67, (2016).